

**Ballistic Transport in
One-Dimensional Magnetic
Nanojunctions:
A First-Principles
Wannier Function Approach**

Dissertation
zur Erlangung des Doktorgrades
der Mathematisch-Naturwissenschaftlichen Fakultät
der Christian-Albrechts Universität zu Kiel

vorgelegt von

Björn Hardrat

aus Hamburg

Kiel

2012

Referent/in:
Koreferent/in:

Prof. Dr. Stefan Heinze
Prof. Dr. Yuriy Mokrousov

Tag der mündlichen Prüfung:
Zum Druck genehmigt:

20.11.2012
20.11.2012

gez. Prof. Dr. Wolfgang J. Duschl, Dekan

Zusammenfassung

Die Entdeckung des Riesenmagnetwiderstandes (engl. GMR) durch Grünberg und Fert [1, 2] begründete das Feld der Spintronik, das die Entwicklung von Bauteilen mit hohen Schaltraten bei niedrigem Energieverbrauch verspricht, da nicht nur die Ladung eines Elektrons, sondern zusätzlich auch dessen Spin-Freiheitsgrad berücksichtigt wird. Durch die fortwährende Miniaturisierung zu nanoskaligen Strukturen kann die Größe solcher Bauteile kleiner als die mittlere freie Weglänge eines Elektrons werden. In diesem Bereich passieren die Elektronen ein Bauteil "ballistisch", das heißt, ohne Änderung ihres Impulses oder ihrer Energie durch unelastische Streuprozesse. Die hierbei auftretenden Effekte, wie z.B. die Quantisierung des Leitwerts oder spinabhängige Transportphänomene, sind quantenmechanischem Ursprungs. In dieser Arbeit wird ein neuartiger, theoretischer Ansatz vorgestellt, um den Quantentransport durch solche nanoskaligen, spintronischen Systeme zu berechnen.

In Übereinstimmung mit der grundlegenden Geometrie moderner Experimente, wie z.B. dem spinpolarisierten Rastertunnelmikroskop (SP-RTM, engl. SP-STM), werden eindimensionale Nanokontakte durch eine Streuregion beschrieben, die durch Zuleitungen mit zwei makroskopischen Elektroden verbunden ist. Die elektronischen und magnetischen Eigenschaften solch eines Nanokontakts werden anhand von Dichtefunktionaltheorie (DFT) mit der sehr präzisen Full-Potential Linearized Augmented Plane-Wave (engl. FLAPW) Methode in der Implementierung des FLEUR-Codes bestimmt. Der Quantentransport wird im Landauer-Formalismus mit Nichtgleichgewichtsgreensfunktionen (engl. NEGF) im Bereich der linearen Reaktion für kleine Biasspannungen berechnet. Da die NEGF Methode auf einem lokalisierten Basissatz beruht, werden Wannierfunktionen (engl. WFs) benutzt, um die elektronische Struktur der FLAPW-Rechnungen auf einen Tight-Binding-artigen Hamiltonoperator abzubilden. Wannierfunktionen bieten zudem zuverlässige Rahmenbedingungen, um den benötigten Rechenaufwand anhand der neuentwickelten "Locking-Technique" zu reduzieren.

Der erste wichtige Aspekt, der mit der neuen Transportmethode untersucht wird, ist der Einfluss der Spin-Bahn Kopplung (engl. SOC) auf den Leitwert. Durch die Spin-Bahn Kopplung kann die Magnetisierungsrichtung den Leitwert stark beeinflussen, was z.B. im ballistischen anisotropen Magnetwiderstand (engl. BAMR) resultiert. Die Spin-Bahn Kopplung ermöglicht es Elektronen zudem, zwischen den Spin-Kanälen zu wechseln und kann daher Spin-Flip Streuprozesse hervorrufen. Diese Effekte werden anhand einer magnetischen Co Störstelle in einem nichtmagnetischen Pt Monodraht und einer nichtmagnetischen Pt Störstelle in einem ferromagnetischen Co Monodraht analysiert. Es wird z.B. gezeigt, dass der ballistische anisotrope Magnetwiderstand, der bei perfekten Drähten auftritt, durch eine Störstelle in den konventionellen anisotropen Magnetwiderstand (engl. AMR) übergeht.

Der zweite wichtige Aspekt, der Einfluss komplexer, nichtkollinear Spinstrukturen auf den ballistischen Leitwert, wird in einem Nanokontakt untersucht, der aus zwei halbunendlichen, magnetischen Co Monodrähten mit magnetischen Mn Spitzenatomen besteht, die vom Tunnel- in den Kontaktbereich gebracht werden. Im Kontaktbereich kann durch konkurrierende Austauschwechselwirkungen ein stabiler, nichtkollinearer Zustand entstehen, der kennzeichnende Leitwert- und Magnetwiderstandsignaturen besitzt.

Abstract

The discovery of the giant magnetoresistance (GMR) effect by Grünberg and Fert [1, 2] initiated the field of spintronics, which holds high promise for future devices of high speed and low power consumption by not only utilizing the charge of the electron in an electronic device but also its spin degree of freedom. With the ongoing miniaturization to nano-scale structures, their size becomes eventually smaller than the mean free path of an electron. In this regime an electron is 'ballistically' transmitted through a nanocontact without changing its momentum or its energy due to inelastic scattering processes. The emerging effects, e.g. the quantization of conductance and spin-dependent transport phenomena, are of quantum mechanical nature. In this thesis, a novel theoretical approach is introduced to calculate quantum transport for such nano-scale spintronic systems.

In accordance to the basic geometry of state-of-the-art experiments, based e.g. on the spin-polarized scanning tunneling microscope (SP-STM), those one-dimensional nanojunctions are treated as a scattering region connected to two macroscopic electrodes by leads. The electronic and magnetic properties of such a nanojunction are described by density functional theory (DFT) within the high-precision full-potential linearized augmented plane-wave (FLAPW) method, as implemented in the FLEUR code. The quantum transport calculations are performed within the Landauer formalism based on non-equilibrium Green's functions (NEGF) in the linear response regime for small bias voltages. Since the NEGF method relies on a localized basis set, Wannier functions (WFs) are used to map the electronic structure of the FLAPW calculations onto a tight-binding like Hamiltonian. They also provide a reliable framework to save a considerable amount of computational effort within the newly employed "locking-technique".

The first important aspect studied with the novel transport code is the influence of spin-orbit coupling (SOC) on quantum transport. Due to SOC the magnetization direction can strongly influence the conductance, resulting in e.g. the ballistic anisotropic magnetoresistance (BAMR). SOC also allows electrons to switch between both spin-channels and, thus, can be responsible for spin-flip scattering processes. These effects are investigated for a magnetic Co impurity in a nonmagnetic Pt monowire and for a nonmagnetic Pt impurity in a ferromagnetic Co monowire. It is e.g. shown, that due to the presence of an impurity the BAMR which occurs for a perfect wire changes to the conventional anisotropic magnetoresistance (AMR).

The second important aspect studied is the effect of complex non-collinear spin-structures on ballistic conductance, which is investigated in a nanojunction consisting of two semi-infinite ferromagnetic Co monowires with magnetic Mn apex atoms, brought from the tunneling- to the contact-regime. A stable non-collinear solution occurs in the contact regime due to competing exchange interactions, which results in distinctive fingerprints in the conductance or magnetoresistance.

Contents

1	Introduction	1
2	Theory of Ballistic Transport	9
2.1	Ohm's Law or the 'Top-Down' Approach	11
2.2	Quantized Conductance or the 'Bottom-Up' Approach	13
2.3	Length, Cross-Section and Scattering	15
2.4	The NEGF Approach to Ballistic Transport	18
3	Density Functional Theory (DFT)	29
3.1	The Born-Oppenheimer Approximation	30
3.2	The Hohenberg-Kohn Theorems	32
3.3	The Kohn-Sham Equations	35
3.4	Spin Density Functional Theory	38
3.5	Exchange-Correlation Potentials	40
3.6	Calculation of the Total Energy	41
3.7	The Self-Consistency Cycle	41
3.8	Effective Models of Magnetism	43
4	The FLAPW Method	49
4.1	The Generalized Eigenvalue Problem	49
4.2	Plane Waves	50
4.3	The APW Method	51
4.4	The LAPW Method	52
4.5	The FLAPW Method	53
4.6	FLAPW for One-Dimensional Systems	55
4.7	Non-Collinear Magnetism within the FLAPW Method	57
4.8	Relativistic Description	59
4.9	The Brillouin Zone Integration	61
5	Wannier Functions	63
5.1	Maximally Localized Wannier Functions (MLWFs)	64
5.2	First-Shot Wannier Functions (FSWFs)	66
5.3	Constructing FSWFs within the FLAPW Method	68
5.4	Constructing MLWFs within the FLAPW Method	69
5.5	The Wannier Representation of the FLAPW Hamiltonian	71

5.6	FLAPW Wannier Functions for Systems with SOC	74
5.7	FLAPW Wannier Functions for Non-Collinear Spin-Structures	75
6	Implementation of Ballistic Transport within FLAPW	79
6.1	The General Transport Problem Revisited	80
6.2	Surface Green's Functions	82
6.3	Construction of the Transport Hamiltonian	85
6.4	The Locking-Technique	89
6.5	Ballistic Transport Calculations within FLAPW Wannier Functions	92
6.6	Pt Monowires with a Single Broken Bond	96
6.6.1	FSWFs versus MLWFs	97
6.6.2	Conductance and Transmission	100
6.6.3	The Locking Technique	101
6.6.4	Decomposition of Transmission and Density-of-States	105
6.6.5	Conductance upon Bond-Stretching	108
6.6.6	The Effects of Spin-Orbit Coupling on Ballistic Transport	109
6.7	Ferromagnetic Co Monowires	113
6.7.1	The Magnetoresistance	114
7	Ballistic Scattering on Impurities with SOC	119
7.1	Magnetic Impurity in a Non-Magnetic Wire	120
7.1.1	The $\text{Pt}_{\text{inf}} - \text{Co} - \text{Pt}_{\text{inf}}$ Junction	122
7.1.2	The Ballistic Anisotropic Magnetoresistance (BAMR)	125
7.2	Non-magnetic Impurity in a Ferromagnetic Wire	127
7.2.1	The $\text{Co}_{\text{inf}} - \text{Pt} - \text{Co}_{\text{inf}}$ Junction	128
7.2.2	Magnetoresistance: BAMR vs AMR	134
8	Ballistic Transport in Nanojunctions with Non-Collinear Magnetic Order	139
8.1	Non-Collinear Magnetism in Mn Monowires	140
8.1.1	Non-Collinear MLWFs of Mn Monowires	141
8.2	The $\text{Co}_{\text{inf}} - \text{Mn} - \text{Mn} - \text{Co}_{\text{inf}}$ Junction	145
8.2.1	The Tunneling-to-Contact Regime	148
8.2.2	Non-Collinear Magnetic States of the Junction in Contact Regime	151
8.2.3	Ballistic Conductance of Non-Collinear Magnetic States of the Junction	154
8.2.4	Model-Based Analysis of the Non-Collinear Ballistic Conductance	157
8.2.5	Fingerprints of Non-Collinear Magnetic States in Ballistic Conductance Experiments	160
9	Summary	167

Nomenclature

a	anti-bonding states
AMR	anisotropic magnetoresistance
AP	antiparallel
APW	augmented plane-wave
b	bonding states
BAMR	ballistic anisotropic magnetoresistance
DFT	density functional theory
FLAPW	full-potential linearized augmented plane-wave
FSWFs	first-shot Wannier functions
GFs	Green's functions
GGA	generalized gradient approximation
GMR	giant magnetoresistance
IR	interstitial region
LAPW	linearized augmented plane-wave
LDA	local density approximation
LSDA	local spin density approximation
MAE	magneto-crystalline anisotropy energy
MLWFs	maximally localized Wannier functions
MR	magnetoresistance
MT	muffin-tin
NEGF	non-equilibrium Green's function
NN	nearest neighbor
P	parallel
SOC(r)	SOC with out-of-chain quantization axis
SOC(z)	SOC with in-chain quantization axis
SP-STM	spin-polarized scanning-tunneling microscope
SR	scalar-relativistic
TEM	transmission electron microscope
VR	vacuum region
WFs	Wannier functions

1 Introduction

Science is driven by the formulation of new theories that are constantly challenged by experiments, allowing to improve subsequent, more general theories in accordance to the obtained experimental results. Thereby, scientific research creates knowledge and leads to a more and more fundamental understanding of nature. This evolution of ideas and the consequential improvement of technical applications has, for example, led to the ever shrinking sizes of modern electronic devices, as described by the phenomenological Moore's law for integrated circuits, stating that the number of transistors on an commercial integrated circuit doubles approximately every two years. Although being a rule of thumb, Moore's law is surprisingly accurate for mapping the success and progress in that particular field. Starting from a typical gate length of $10\ \mu\text{m}$ in 1970, gate lengths of 28 nm in commercial products have been reached in 2011. For the future the International Technology Roadmap for Semiconductors of 2011 [3] proposes nanowire metal-oxide-semiconductor field-effect transistors for scaling devices below 10 nm gate lengths. Such a metal-oxide-semiconductor nanowire represents the current limit of the present day semiconductor technology and is pushing towards the atomic limit.

At this particular frontier of physics, starting from the 1980's, a new field of solid state physics and engineering has evolved over the last decades, nanoscience and nanotechnology, as, e.g, necessary for the development and fabrication of the mentioned integrated circuits or present day hard discs. Those devices employ novel effects, such as the Giant Magnetoresistance (GMR), independently discovered 1989 by Grünberg and Fert [1, 2], for which they were awarded the 2007 Nobel Prize in physics. The discovery of the Giant Magnetoresistance can be recognized as the birth of the field of spin transport electronics, so-called spintronics. This effect demonstrates not only the importance of the spin degree of freedom on transport properties, but also the microscopic structure, the material composition and the quantum mechanical nature of the charge carriers can give rise to novel, unexpected and sometimes gigantic effects.

Smaller device sizes than the 10 nm for metal-oxide-semiconductor monowires can e.g. be achieved in metal junctions. The feasibility of such metal based junctions has been impressively demonstrated by mechanically-controllable break-junction experiments [4] or spin-polarized scanning-tunneling microscope (SP-STM) investigations [5–8]. In such measurements the central observable is the contact or tunneling conductance. The advent of such experiments sparked and inspired a lot of theoretical investigations about the structural, electronic, magnetic and transport

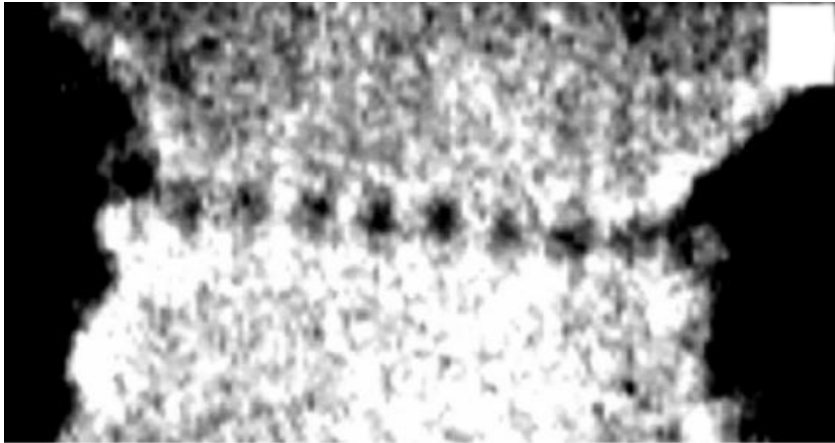


Figure 1.1: High-resolution TEM image of a mechanically controllable Au-break junction, displaying the left and right leads (dark areas left and right) with a monoatomic Au chain consisting of 10 Au atoms in the center (dark dots between the leads). This picture impressively demonstrates, how a nanocontact geometry locally looks like. Image taken from [4]

properties [9–12].

An impressive example of the lower limit of producibility of metal monowires can be seen in Figure 1.1, showing a high-resolution transmission electron microscope (TEM) picture of a mechanically-controllable Au break junction. There are 10 Au atoms forming a monoatomic wire between two thicker Au electrodes. It has been demonstrated in break-junction and STM experiments, that the conductance is quantized in that regime [13–15]. Nanoscale and atomic scale devices, such as the mentioned Au monowires in a break junction, are considerably smaller than the typical mean free path of an electron, reaching the so-called ballistic transport regime, where inelastic scattering processes on the conductance are negligible.

There are also novel spin-dependent transport effects in this regime, e.g. recent theoretical investigations [16] and experiments [14] reported conductance jumps upon rotating the magnetization direction with respect to the flowing current due to the spin-orbit coupling, coined the ballistic anisotropic magnetoresistance (BAMR). An interesting question is, how an impurity affects the BAMR. By introducing a small perturbation, e.g., such as a stretched central bond in a Ni nanowire it has been shown that the conductance jumps can be smoothed out [17], resulting in the conventional anisotropic magnetoresistance (AMR) effect.

Similar two-terminal junctions in the ballistic transport regime can be created in (SP-)STM experiments. Figure 1.2 shows a STM measurement of triangular Co island adatoms on a Cu(111) substrate. Additional adatoms, which appear as white protrusions, have been deposited on the Co island. Starting from this setup the SP-STM tip is approached towards the adatom, measuring the conductance from the

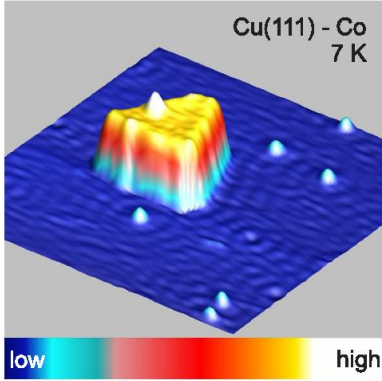


Figure 1.2: Pseudo three-dimensional constant current STM image of the typical system for a tunneling-to-contact STM experiment, showing a triangular Co island on a Cu(111) surface. Additional atoms, appearing as protrusions, can be deposited on the Co island to investigate various setups for such experiments. STM picture taken at $V = 100$ mV, $I = 100$ pA, the size is 24.5 nm \times 24.5 nm. Picture taken from [5]

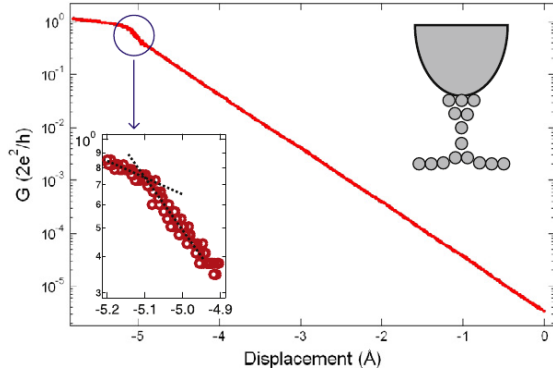


Figure 1.3: Conductance versus displacement for a single adsorbed Cu atom on a Cu(111) surface acquired at 8 K by tunneling-to-contact STM experiments. In the lower inset a close-up view of the transition between the tunneling and contact regime is shown, in the upper inset a illustration of the tip-atom contact, describing a typical transport geometry in such a experiment. Picture taken from [6]

tunneling to the contact regime. Another example of an STM contact experiment in the ballistic regime is shown in Figure 1.3, where a Cu adatom on a Cu(111) surface is contacted with an STM tip and retracted. In the conductance versus tip displacement curve the contact regime appears for tip displacements smaller than -5.1 Å (shown in the inset of Figure 1.3).

It has been reported that, in a similar setup, the spin-direction of Co adatoms on one monolayer Mn on W(110) can be individually imaged and manipulated by SP-STM [18]. The Mn monolayer exhibits a spin-spiral state on W(110), that allows to tune the spin-direction of a Co adatom due to the exchange coupling to the substrate by moving it laterally. This experimental setup provides the opportunity to investigate the effect of non-collinear magnetic order on ballistic transport as well as the angular dependence of the BAMR if a nonmagnetic tip is used. Note that in such an experiment the exchange coupling between the magnetic SP-STM tip and the magnetic adatom might not be negligible and could additionally influence the spin-direction of the Co adatoms.

These non-trivial experimental setups with a large amount of internal degrees of freedom, competing interactions and structural, electronic and magnetic

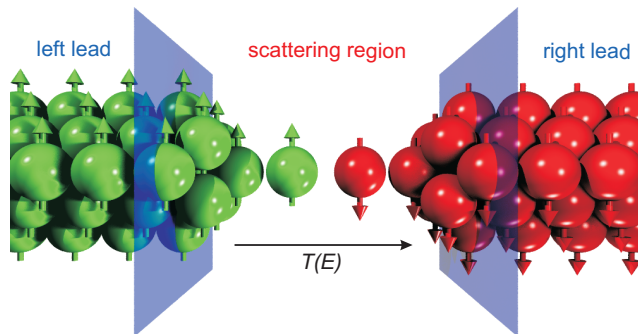


Figure 1.4: Schematic sketch of a magnetic two terminal Landauer-Büttiker transport setup: As scattering region is connected by a left and a right lead. Electrons are transmitted through the scattering region with a energy dependent transmission probability $T(E)$. The transmission probability will depend on the internal degrees of freedom, like shape and magnetic order.

effects make a theoretical study indispensable. Such a theoretical model, preferably derived from *first-principles*, i.e. free of parameters, can then be compared to the experimental outcome.

The most common theoretical approach to describe quantum transport in nanoscale systems is the Landauer-Büttiker method [19–21], that can be applied to a two probe setup consisting of a central scattering region, and two leads (See Fig. 1.4). The famous Landauer formula connects the transmission probability of an electron with the conductance through a ballistic nanojunction. Beyond the standard Landauer setup, it is possible to leave the ballistic regime in the leads by introducing two additional outer lead regions and reach the non-ballistic regime in the electrodes [22]. There are two main groups of approaches to solve the quantum mechanical transport problem by calculating the transmission: wave-function and Green’s functions (GFs) based methods, which are equivalent in the case of non-interacting electrons [23].

The wave function based approaches for ballistic transport in one-dimensional systems utilize the transfer matrix method [24–29], Lippman-Schwinger equations [30, 31] or wave function matching [32]. GF methods are usually based on Keldysh, Kadanoff and Baym’s non-equilibrium Green’s functions [33, 34]. Besides the standard non-interacting electrons approach it is possible to incorporate inelastic scattering effects, such as scattering on vibrations [35, 36], or correlation effects through self-energies [37]. Another way of calculating quantum transport is based on the Kubo approach, as formulated by Baranger and Stone [38], which relates the current to the dynamical polarization [39–41].

Based on these two general types of approaches, all implementations rely on different descriptions of the electronic structure of the device. There are semi-empirical approaches based on tight-binding Hamiltonians [24, 25, 31, 42, 43] and combined

semi-empirical and density functional theory (DFT) approaches, describing the scattering region by DFT and the leads by a free electron gas (jellium) [26, 28, 30]. A typical problem of the Landauer setup is to describe the semi-infinite leads with *ab-initio* accuracy, commonly used methods include non-hermitian self-energies [39, 44–57] or the GFs embedding method [58] as introduced by Inglesfield [59]. *Ab-initio* quantum transport codes treat leads and scattering regions with *ab-initio* accuracy.

Among the reported implementations with *ab-initio* accuracy, various DFT codes have been used. GF methods normally need a localized basis sets, such as Gaussian [47, 55], localized orbitals [45, 46, 48, 51, 60] or wavelets [49]. The other class of methods is based on more precise plane-wave methods [29, 49, 50, 58]. The latter provide more accurate results at the cost of a larger number of basis functions and therefore limit the size of treatable systems. One way of combining both approaches, plane waves and GFs, in order to benefit from each methods' particular strength, are Wannier functions [61]. Especially the maximally localized Wannier functions [62] (MLWFs) are well-defined and optimal as a minimal real space basis set [50, 56]. For low-dimensional devices and shrinking system sizes, the accuracy of electronic structure description becomes crucial, requiring a high precision DFT scheme, preferably based on an all-electron full-potential description. One of the most accurate DFT schemes is based on DFT and the full-potential linearized augmented plane-wave method (FLAPW), as e.g. implemented in the FLEUR-code [63]. This particular code is capable of describing one- [64], two- [65] and three-dimensional systems with SOC [66], non-collinear magnetism [67] and Wannier functions [68]. These are ideal prerequisites for a ballistic transport code.

There are only few other known approaches that were reported to include spin-orbit coupling [17, 69–71]. There are transport codes able to handle non-collinear magnetic order in nanojunctions, based on the $s - d$ model for the non-collinear electronic structure [72, 73], one-dimensional model Hamiltonians [74], the Korringa-Kohn-Rostoker approach [75] or *ab-initio* DFT [76]. However, to the authors knowledge there are no non-collinear ballistic transport calculations based on FLAPW or of obtaining Wannier functions for non-collinear magnetic systems reported on¹.

In this thesis an implementation of a ballistic transport code is reported for conductance calculations through one-dimensional nanoscale junctions. This novel approach has the aim to provide an accurate description in particular for magnetic systems including complex spin structures and SOC effects. It is based on the all-electron FLAPW method and the transmission function needed to obtain the

¹There are other ballistic transport implementations based on the FLEUR-Code [29, 58] and other FLAPW based codes available [77], capable of a Wannier transformation and that include spin-orbit coupling [78], in principal allowing to calculate ballistic transport with spin-orbit coupling (SOC) or with non-collinear spin-structures, but, to the authors knowledge, no results have been reported yet.

conductance with the Landauer formalism is calculated with the aid of the non-equilibrium Green's function (NEGF) method within the linear response regime for small bias voltages based on equilibrium properties. The electronic structure from the FLAPW calculation is mapped to a tight-binding like Hamiltonian via Wannier functions (WFs) [68], which provide a minimal, localized basis set. Thereby the accuracy of the FLAPW calculation is transferred to the transport calculation performed within the NEGF approach [79]. WFs are capable of describing complex electronic structures as caused by e.g. incorporating SOC and can be extended to complex magnetic systems exhibiting non-collinear magnetic order [80], as demonstrated in this thesis. WFs additionally allow to avoid the use of large unit cells and systematic errors in the leads, caused by scattering states, by combining multiple smaller unit cell calculations into one ballistic transport calculation via the locking-technique. The underlying one-dimensional FLAPW method [64] is specifically tailored to efficiently treat one-dimensional nanojunctions without employing supercells, resulting in a significant speed-up of the calculations.

The newly developed code is applied to study ballistic transport through model-type nanojunctions with focus on systems with SOC or non-collinear magnetic order. The effect of SOC is investigated with respect to the difference to the scalar-relativistic (SR) (I.e. without SOC) approximation. Emerging novel effects such as e.g. spin-scattering events and the BAMR or AMR are demonstrating the importance of considering the coupled spin- and orbital space to capture a realistic description of quantum transport.

In the present literature the focus on ballistic transport through non-collinear nanojunctions lies on investigations of domain wall structures and the spin-torque effect [74–76]. The SP-STM geometry has successfully been described based on a $s - d$ model for the non-collinear electronic structure [73]. Within this thesis non-collinear magnetic order is studied based on *first-principles* in a SP-STM- or magnetic break-junction-like geometry from the tunneling to the contact regime. Non-collinearity can be induced by frustration of exchange interaction between the magnetic moments of tip and sample atoms. The non-collinear magnetic order can significantly influence the conductance through such systems, suggesting the possibility to identify the magnetic order in the nanojunction by its fingerprints in the conductance or magnetoresistance.

This thesis is structured as follows:

A brief introduction on transport theory and the NEGF formulation of the Landauer formula within linear response is given in chapter 2. In chapter 3 DFT is described, which sparked a breakthrough in the understanding of the electronic and magnetic structure of real condensed matter from *first-principles*. In chapter 4 the concept of the FLAPW method is explained, which ranks among the most general, applicable and accurate implementations of DFT. In chapter 5 an approach to combine the NEGF Landauer transport method with the FLAPW method by Wannier

functions is proposed, including subtle effects such as spin-orbit coupling and non-collinear magnetic order. In chapter 6 the construction of the transport Hamiltonian and the implementation of the NEGF ballistic transport method is presented. It is applied to two test systems: Nonmagnetic Pt and ferromagnetic Co monowires. The results are compared to those obtained within a scattering approach in combination with a pseudopotential method for the electronic structure [69, 81]. In chapter 7 ballistic transport on impurities with spin-orbit coupling is treated for two types of model systems: A ferromagnetic Co impurity in a non-magnetic Pt wire and a Pt impurity in a ferromagnetic Co monowire. In chapter 8 the effect of non-collinear magnetic order on quantum transport is studied on a model system consisting of two semi-infinite ferromagnetic Co wires terminated with a single Mn atom, brought from the tunneling to the contact regime. Finally, chapter 9 concludes with a summary and an outlook.

2 Theory of Ballistic Transport

The modeling of electron transport has a long tradition concerning both technical applications and the fundamental understanding of the phenomena that emerge in connection with it, starting from the discovery of Ohm's law [82] in 1826 that first shed light on the electric conductance even before the responsible particle, the electron, was discovered:

$$I = GV \tag{2.1}$$

Ohm's law (Eqn. (2.1)) states, that the current I between two contacts in an isotropic medium is proportional to the applied potential difference V between those contacts with a constant of proportionality G (see Figure 2.1), called the conductance.

The conductance is the inverse of the resistance $R = G^{-1}$. This very fundamental and well-known macroscopic theory in combination with semi-classical microscopic models such as the Drude model, incorporating electrons as charge carriers, are successfully applied to electron transport in a wide range of lengthscales, but fails in the transition to nanoscale contacts, explicitly when the junction size becomes small enough for electrons to pass without dissipating energy and losing their phase coherence. In this regime, the electrons can be considered to 'ballistically' shoot through the junctions (thus, it is called ballistic regime), and to be sensitive to quantum effects. A key phenomenon of this regime is the occurrence of a quantized conductance, experimentally first discovered in semiconductor heterostructures [83] and recently also in e.g. Co nanocontacts [14], exhibiting a conductance quantum G_0 :

$$G_0 = \frac{2e^2}{h} = (12.9k\Omega)^{-1} \tag{2.2}$$

The conductance quantum itself is a fundamental constant of all materials. The conductance changes in quantized steps of G_0 with the width of a nanojunction and, thus, the number of available conducting states [83].

A theoretical approach to describe quantum transport in the ballistic regime is the Landauer-Büttiker formalism [19–21], that relates the probability of an electron to be transmitted through a nanojunction and its conductance quantum with the total conductance. Cutting edge theoretical and experimental investigations sparked increasing interest on the influence of the spin degree of freedom, spin-orbit coupling and non-collinear magnetic order on the ballistic transport properties by e.g. studying the spin-dependent contact conductance with the spin-polarized scanning-tunneling microscope (SP-STM) [5], the ballistic transport through domain wall structures, the spin-torque effect [74–76] or spin-orbit coupling related

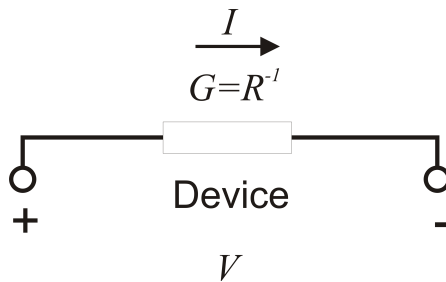


Figure 2.1: Current I and conductance $G = R^{-1}$ through a generic macroscopic device with applied potential difference V .

effects such as the ballistic anisotropic magnetoresistance (BAMR) in magnetic break-junctions [14, 16, 17].

A predictive theory of ballistic transport therefore inevitably needs a versatile quantum mechanical framework, that allows to describe spin-dependent phenomena, complex electronic and magnetic structures and that is at the same time capable of treating a system out of equilibrium and thus describing non-equilibrium phenomena such as the conductance at finite bias. A commonly used method that fulfills all those requirements can be built on non-equilibrium Green's functions (NEGFs). Green's functions are usually preferred to the more familiar concept of wave functions since they possess richer properties and are open for extension, such as incorporating inelastic scattering [35, 36] or correlation effects through self-energies [37]. The NEGF formalism introduced in this chapter follows an approach by Datta [84] and is used to treat nanojunctions within the linear response regime for small bias voltages, based on equilibrium properties ($V = 0$). The electronic structure of the nanojunction is constructed of a yet unspecified tight-binding Hamiltonian that is modified to include the injection, extraction and excitations of electrons. The resulting open quantum system consists of two electrodes, considered to be ideal non-reflecting reservoirs at different electro-chemical potentials, attached to a scattering region by leads. The effect of the leads is included in the scattering region in terms of self-energies, describing e.g. the energy level broadening due to the coupling to the leads within an effective Hamiltonian. The approach results in an elegant expression for the transmission probability and the conductance in the spirit of the Landauer formula.

In this chapter a short overview over the classical transport theory is given, following a 'top-down' approach, to illustrate why the classical or semi-classical picture fails in the ballistic regime. The origin of the conductance quantum is then derived within a 'bottom-up' approach based on a simple one-dimensional electron gas model before the intrinsic lengthscales of ballistic transport are discussed. Advancing to the NEGF formalism, the fundamental concepts of an open quantum system are introduced and the NEGF expression for the Landauer formula is derived.

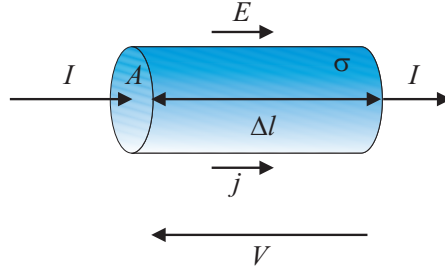


Figure 2.2: Current I and current density j through a isotropic cylindrical conductor with conductivity σ , length $\Delta l = l_2 - l_1$, cross-sectional area A for an applied electric field E in direction of the cylinder, resulting in a potential difference V .

2.1 Ohm's Law or the 'Top-Down' Approach

To understand the difference between classical and quantum conductance it is useful to begin from macroscopic quantities in a 'top-down' approach and investigate, why the transition to the nanoscale within this theory fails. Starting from a much more general formulation of Ohm's law Eq. (2.1), there is a direct proportionality of the current density $\mathbf{j}(\mathbf{r})$ and an applied electric field $\mathbf{E}(\mathbf{r})$ at a given coordinate \mathbf{r} , described by the conductivity tensor $\boldsymbol{\sigma}$:

$$\mathbf{j}(\mathbf{r}) = \boldsymbol{\sigma}\mathbf{E}(\mathbf{r}) \quad (2.3)$$

Assuming isotropic materials, the conductivity tensor $\boldsymbol{\sigma}$ can be replaced by a scalar conductivity σ . As a result current density and the electric field are aligned parallel. For a cylindrical conductor along the z -direction with length l , cross-sectional area A and the constant electric field $\mathbf{E}(\mathbf{r}) = E\hat{\mathbf{e}}_z$ (see Fig 2.2), the potential difference V between left (l_1) and right (l_2) side can be expressed as

$$V = - \int_{l_1}^{l_2} d\mathbf{l} \cdot \mathbf{E} = E\Delta l \quad (2.4)$$

The current density $\mathbf{j}(\mathbf{r}) = j\hat{\mathbf{e}}_z$ is constant and equal to the current divided by the cross-sectional area A :

$$j = \frac{I}{A} \quad (2.5)$$

By substituting $\mathbf{E}(\mathbf{r}) = E\hat{\mathbf{e}}_z$, $\boldsymbol{\sigma} = \sigma$ for an isotropic material, $\mathbf{j}(\mathbf{r}) = j\hat{\mathbf{e}}_z$ from Eqn. (2.5) and $E = \frac{V}{\Delta l}$ from Eqn. (2.4) in equation 2.3

$$I = \frac{\sigma A}{\Delta l} V \quad (2.6)$$

the dependence of the conductance G through the cylindrical conductor on its size can be determined by comparing Eqn. (2.6) to the first formulation of Ohm's law

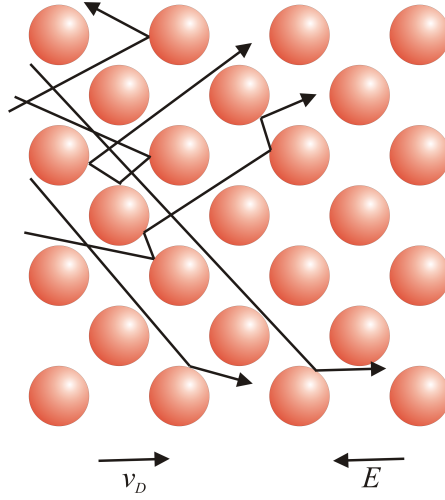


Figure 2.3: Electron transport within the Drude model: Electrons, described as a kinetic gas, collide with the rigid atoms, resulting in a non-zero drift velocity v_D for an applied electric field $\mathbf{E} = E\hat{e}_z$

(Eqn. 2.1):

$$G = \frac{\sigma A}{l} \quad (2.7)$$

In this description a shrinking size of the conductor ($A \rightarrow 0, l \rightarrow 0$) does not lead to the quantized conductance, which is observed in experiments [14, 83].

A semi-classical, atomistic transport description is the Drude model, proposed in 1900 [85, 86]. In the Drude model a conductor, e.g. a metal, is described by gas theory. The electrons are treated as a free electron gas with mass m_e and charge e that move between the rigid bulk ions (see Figure 2.3). For a constant electric field $\mathbf{E} = E\hat{e}_z$ the electrons experience a force $\mathbf{F}_{el} = -e\mathbf{E}$ and are scattered due to collisions between electrons and the bulk ions occurring within a mean free time of τ . The equation of motion of the electrons in z -direction is accordingly:

$$m_e \dot{v} + \frac{m_e}{\tau} v = -eE \quad (2.8)$$

The mean free time τ is of quantum mechanical origin and has to be determined by quantum mechanical methods, the Drude model is therefore a semi-classical approach. For the steady state ($\dot{v} = 0$) the drift velocity of the electrons v_D becomes:

$$v_D = -\frac{e\tau}{m} E \quad (2.9)$$

The current density j can now be determined including the electron density n as

$$j = -env_D \quad (2.10)$$

leading to a conductivity σ of

$$\sigma = \frac{j}{E} = \frac{e^2 \tau n}{m_e} \quad (2.11)$$

This model results in an atomistic description of the conductivity e.g. in isotropic metals, but does not resolve the problem of a quantized conductance (Eqn. (2.7)), similar to Ohm's law (Eqn. (2.3)). Concluding, the Drude model fails to describe electrons that pass the device faster than in the mean free time τ or devices that are smaller than the related mean free path.

2.2 Quantized Conductance or the 'Bottom-Up' Approach

As has been pointed out in the previous sections, an appropriate description of a nanocontact, small enough to avoid inelastic scattering events cannot be obtained within a classical or semi-classical picture. Following a bottom-up approach, a simple model of a single moded free electron gas, confined in a one-dimensional geometry, is introduced to investigate the origin of the quantized conductance. Assuming that the electrons maintain their phase coherence and pass the device in a constant current, quantum transport can be described by the time-independent Schrödinger equation:

$$-\frac{\hbar}{2m_e} \frac{d^2}{dz^2} \psi(z) = E\psi(z) \quad (2.12)$$

Without loss of generality the junction runs along the z -direction. The wave functions can be described by plane waves $\psi(z) = e^{ikz} / \sqrt{\Omega}$ with the wave vector $k = k_z$ and the energy eigenvalues E . The result is a quadratic energy dispersion for $E(k)$:

$$E(k) = \frac{\hbar^2 k^2}{2m_e} \quad (2.13)$$

The group velocity for a general energy dispersion $E(\mathbf{k})$ is defined as

$$\hbar \mathbf{v}(\mathbf{k}) = \nabla_{\mathbf{k}} E(\mathbf{k}) \quad (2.14)$$

for a single moded wire. The group velocity of a one-dimensional electron gas is therefore:

$$v(k) = \frac{1}{\hbar} \frac{\partial E(k)}{\partial k} = \frac{\hbar k}{m_e} \quad (2.15)$$

The current I through a wire with length l is carried by the states having a negative group velocity (compared to the current direction) and a negative charge $-e$, thus resulting in a positive current (see Figure 2.4):

$$I = \frac{-e}{l} \sum_{v(k) < 0} v(k). \quad (2.16)$$

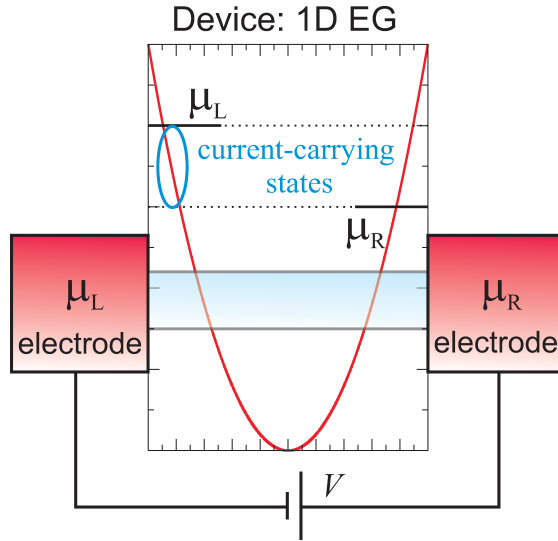


Figure 2.4: One-dimensional free electron gas between two electrodes, left L and right R , with the electro-chemical potentials μ_L and μ_R . The states with negative group velocity, located between μ_L and μ_R , contribute to the positive net current, carried by the negatively charged electrons.

Combining Eqn. (2.15) and Eqn. (2.16) results in an expression for the current based on the derivative $\frac{\partial E(k)}{\partial k}$ of the energy dispersion:

$$I = -\frac{-e}{l} \sum_{v(k) < 0} \frac{1}{\hbar} \frac{\partial E(k)}{\partial k} \quad (2.17)$$

The summation in Eqn. (2.17) can be replaced by an integration over k for continuous states:

$$I = e \int \frac{dk}{2\pi} \frac{1}{\hbar} \frac{\partial E(k)}{\partial k} = \frac{e}{h} \int dE \quad (2.18)$$

Each mode of a quantum wire carries the current of $\frac{e}{h}$ per unit energy. In equilibrium there is no current since all states with positive and negative group velocity are equally occupied and all contributions cancel out pair-wise. To obtain a current, a potential difference V has to be applied between two electrodes connected to the system, changing the occupation of the energy levels in a range of $\mp(eV/2)$ around the Fermi level E_F . Note, that for a positive Voltage the electrons are attracted from the right electrode, as shown in Figure 2.4. The details of this non-equilibrium state depend on the coupling of the one-dimensional system with the left (L) and right (R) electrodes and are left out at this point. The current is caused by a net negative group velocity of electrons (charge $-e$) flowing from the left electrode to the right electrode in an energy region $\mu_R = E_F - (eV/2) < E < \mu_L = E_F + (eV/2)$, as shown in Figure 2.4. This results, according to Eqn. (2.16) and Eqn. (2.17), to a

positive net current, flowing from right electrode (plus) to the left (minus) electrode. The current can be determined by integrating Eqn. (2.18) over the energy region $\mu_R < E < \mu_L$:

$$I = \frac{2e}{h}(\mu_L - \mu_R) \rightarrow I = \frac{2e^2}{h}V \quad (2.19)$$

Here the factor of 2 accounts for the double spin-occupation of the states. A comparison with Ohm's law (Eqn. (2.1)) yields the conductance quantum G_0 ,

$$G_0 = \frac{2e^2}{h} \quad (2.20)$$

as stated in Eqn. (2.2).

2.3 Length, Cross-Section and Scattering

The previous sections stated that there is a conductance quantum of G_0 for nanojunctions that are smaller than the mean free path of an electron and in the phase coherent regime¹. However, these relevant lengthscales have not been quantified yet for the systems considered in this thesis. The lateral size or cross-section plays another important role, leading to multiple modes or sub-bands. The concept of the Landauer formalism is then briefly introduced for multi-moded nanojunctions by linking transmission and reflection probabilities due to scattering on impurities to the conductance.

First, the typical length of a junction in the ballistic transport regime has to be determined. In general, electrons will exhibit ballistic conduction when the length of the junction l is smaller than the mean free path l_{MFP} (see Figure 2.5). For electrons l_{MFP} can be expressed by Matthiessen's rule:

$$\frac{1}{l_{\text{MFP}}} = \frac{1}{l_{\text{impurity}}} + \frac{1}{l_{\text{defect}}} + \frac{1}{l_{\text{el-el}}} + \frac{1}{l_{\text{aph}}} + \frac{1}{l_{\text{oph}}^e} + \frac{1}{l_{\text{oph}}^a} + \dots \quad (2.21)$$

where $l_{\text{impurity/defect}}$ describes the mean length an electron travels before an elastic scattering event occurs at impurities or defects, $l_{\text{el-el}}$ the electron-electron scattering length, l_{aph} describes the acoustic phonon emission and absorption and $l_{\text{oph}}^{e/a}$ the emission (e) and absorption (a) of optical phonons. All those quantities strongly depend on the material and its metalicity (the mean free path is usually longer in semiconductors) and on its purity. l_{MFP} can be divided into two distinct parts, the elastic mean free path and the phase coherence length.

The first two contributions of Eqn. (2.21) can be grouped into the elastic mean free path l_{elas} , the distance an electron travels before changing its momentum. Such

¹A theoretical description of ballistic transport can include e.g. electron-electron scattering, which destroys the phase but is energy conserving (cf. [87]). In the following, the phase coherent ballistic transport regime is considered.

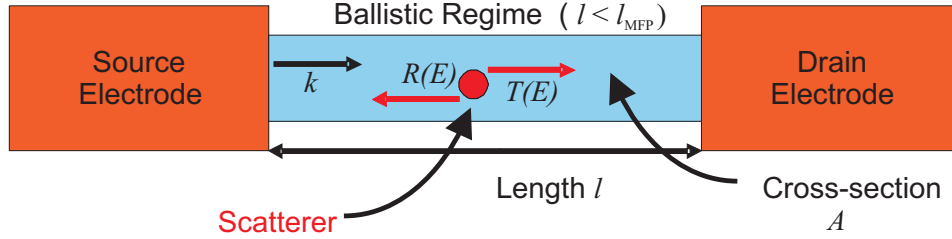


Figure 2.5: Sketch of a ballistic scattering process: Electrons are emitted from the source electrode on the left side with the wave vector k . The electrons enter the junction with length l , considerably shorter than the mean free path l_{MFP} , and have to be described in the ballistic regime. A scatterer (red circle) in the junction disrupts the propagation of the electron, leading to an energy dependent transmission function $T(E)$ and reflection function $R(E)$.

momentum changing processes can e.g. be connected to elastic scattering on defects or impurities. In magnetic transition metals, investigated in this work, it is usually of the order of a few atoms $l_{\text{elas}} \approx 10 - 20 \text{ \AA}$ [88].

The following contributions of Eqn. (2.21) determine the decoherence length l_ϕ . l_ϕ is the average distance an electron travels before a scattering event changes its energy. Processes related to this length are inelastic ones such as e.g. electron-electron scattering or scattering on phonons. The decoherence length macroscopically determines the conductance of a bulk material and related to the distance an electron travels in the mean free time, introduced in Eqn. (2.9) for the Drude model in the previous section. In those inelastic scattering processes the quantum mechanical phase is not conserved. There are no coherent quantum interference effects in junctions exceeding l_ϕ . The phase coherent length in metal heterostructures at low temperatures is usually of the order of $l_\phi \approx 100 - 200 \text{ \AA}$ [89].

For the discussion of the influence of the cross-section A of a nanojunction on the conductance, the free electron gas model introduced in section 2.2 will be laterally further constrained. A confinement of the electrons e.g. in a quadratic box ($A = a^2$), discussed in many textbooks (i.e. [90]), results in a one-dimensional dispersion in z -direction (Eqn. (2.13)) and the occurrence of quantized sub-bands. The reason for these sub-bands are additional modes n_x and n_y of the electron wave function, obtained by fulfilling the boundary conditions of a vanishing wavefunction outside of the box $A = a^2$:

$$E_{n_x, n_y} = \frac{\hbar^2}{8m_e a^2} (n_x^2 + n_y^2) \quad (2.22)$$

Depending on the electron density of the system and the size of the cross-sectional area, there can be multiple modes M present at the Fermi level, which contribute to the conductance with G_0 . Eqn. (2.19) has to be modified accordingly:

$$G = G_0 M \quad (2.23)$$

Changing the cross-sectional area A yields to a varying number of conducting states, Eqn. (2.23) therefore explains the presence of the experimentally found quantized conductance steps [83].

Another important effect is the presence of a scatterer in a junction and its influence on the conductance. While the previous description allows to calculate the current by simply counting the available modes or bands M and holds for perfect systems, the presence of an impurity makes the theoretical treatment of ballistic transport a non-trivial task. Such an impurity reflects incoming electrons of the mode m ($m = 1, \dots, M$) of one lead to mode m' ($m' = 1, \dots, M'$) in the other lead with a reflection probability $R_{mm'}(E)$. Only the fraction of transmitted electrons contribute to the conductance with G_0 (cf. Figure 2.5). The transmission probability $T_{mm'}(E) = 1 - R_{mm'}(E)$ of electrons can be obtained from the reflection probability and vice versa. $T_{mm'}(E)$, $R_{mm'}(E)$ and, thus, the conductance $G(E)$ are energy dependent functions depending on the electronic structure of the scatterer. Since only transmitted electrons contribute to the current $T_{mm'}(E)$ has to be factored into Eqn. (2.23) to obtain the conductance for a system with impurities (interface regions or defects):

$$G(E) = G_0 \sum_m \sum_{m'} T_{mm'}(E) = G_0 T(E) \quad (2.24)$$

This expression relates the total electron transmission function $T(E)$ to the conductance $G(E)$. The current I through such a two-terminal nanojunction in contact with two electrodes with distinct Fermi functions $f_{L/R}(E)$ can be calculated by the famous Landauer formula [19, 20]:

$$I = \frac{e}{h} \int dE T(E) [f_L(E) - f_R(E)] \quad (2.25)$$

Eqn. (2.24) briefly introduces the framework more complex nanojunctions can be understood with. It holds for perfect (in this case $T(E)$ equals the number of available states $M(E) = M'(E)$ at a given energy E), single- or multi-moded junctions (cf. Eqn. (2.2) and Eqn. (2.23)) and is applicable to more complex systems including scatterers or inequivalent leads ($M(E) \neq M'(E)$). The calculation of the transmission function $T(E)$ and of the conductance $G(E)$ provides a challenge for nanojunctions with complex electronic and magnetic structure and is the aim of the present thesis. The conductance obtained for the two-terminal geometry (cf. Figure 2.5), a quantum mechanical nanojunction in contact with two macroscopic electrodes, is the total conductance of the system rather than the conductance of the nanojunction. Therefore the Landauer formula relates not only the measured conductance to the transmission probability of electrons and the number of of transmission channels, it also includes the contact resistance caused by the coupling of a quantum mechanical system to macroscopic reservoirs. It is possible to extend

the Landauer formula to four-terminal measurements, e.g. by the multi-terminal Büttiker formalism [21].

2.4 The NEGF Approach to Ballistic Transport

In order to obtain the transmission function $T(E)$ and the conductance $G(E)$ for non-trivial systems based on *first-principles* electronic structure calculations, a quantum mechanical framework for such calculations is necessary. The method introduced in this thesis is based on non-equilibrium Green's functions (NEGF) and follows an approach by Datta [84]. This approach starts from a general two-terminal setup of a nanojunction as shown in Figure 2.6 as fundamental geometry. A nanojunction consists within this description of a central nanoscale conductor or scattering region and two leads (blue region in Figure 2.5) in contact with two electrodes (red regions in Figure 2.5) that are out of equilibrium, providing two distinct electro-chemical potentials μ_L and μ_R . One electrode keeps filling the nanojunction with electrons while the other one extracts them, leading to a steady current. The electrodes are considered to be ideal reservoirs, which means they are capable of providing or accepting enough uncorrelated electrons to maintain the steady current and they do not reflect incoming electrons.

For the quantum mechanical description of the nanojunction the wave function $\psi(\mathbf{r})$ of the system is expressed by a set of orthonormal basis functions $u_n(\mathbf{r})$:

$$\psi(\mathbf{r}) = \sum_n \psi_n u_n(\mathbf{r}) \quad (2.26)$$

where the ψ_n are the expansion coefficients. By substituting Eqn. (2.26) into the Schrödinger equation

$$\hat{H}\psi(\mathbf{r}) = E\psi(\mathbf{r}) \quad (2.27)$$

where \hat{H} is the Hamiltonian and E an energy eigenvalue, one obtains:

$$\hat{H} \sum_n \psi_n u_n(\mathbf{r}) = E \sum_n \psi_n u_n(\mathbf{r}) \quad (2.28)$$

Multiplying with $u_m^*(\mathbf{r})$ and integrating over all \mathbf{r} yields to

$$\sum_n H_{mn} \psi_n = E \sum_n \psi_n \quad (2.29)$$

which can be written as a matrix equation

$$\mathbf{H}\psi = E\psi \quad (2.30)$$

where the orthonormality condition

$$\int d^3r u_m^*(\mathbf{r})u_n(\mathbf{r}) = \delta_{mn} \quad (2.31)$$

was applied, resulting in the matrix elements:

$$H_{mn} = \int d^3r u_m^*(\mathbf{r})\hat{H} u_n(\mathbf{r}) \quad (2.32)$$

Given these matrix elements, it is straight-forward to calculate the eigenvalues and eigenvectors and therefore to solve the Schrödinger equation. The matrix representation of the Schrödinger equation (Eqn. (2.32)) can be used to construct the Hamiltonian of a nanojunction in an intuitive way: By additionally requiring that the $u_n(\mathbf{r})$ are localized tight-binding like basis functions, the $u_n(\mathbf{r})$ can be assigned to a individual atoms or bonds in real space. This characteristic can be exploited to construct the Hamiltonian matrix of the nanojunction atom-wise, following the set-up shown in Figure 2.6:

$$\mathbf{H} = \begin{pmatrix} \mathbf{H}_L & \mathbf{H}_{LS}^\dagger & \mathbf{0} \\ \mathbf{H}_{LS} & \mathbf{H}_S & \mathbf{H}_{SR} \\ \mathbf{0} & \mathbf{H}_{SR}^\dagger & \mathbf{H}_R \end{pmatrix}, \quad (2.33)$$

Each of the the three regions is described by a separate Hamiltonian matrix, the interaction between a lead and the scattering region is included by introducing coupling matrices $\mathbf{H}_{LS/SR}$. The leads are considered to be far away from each other in order to avoid lead-lead interaction. This condition can be always achieved for localized tight-binding like basis functions by choosing the scattering region to be large enough and, thus, avoiding an overlap between basis functions of the leads. The matrices of the leads $\mathbf{H}_{L/R}$ and the coupling matrices $\mathbf{H}_{LS/SR}$ describe the semi-infinite leads and the coupling to those leads and are therefore semi-infinitely large. Due to the semi-infiniteness of the leads the dimension of the Hamiltonian (Eqn. (2.33)) is infinitely large, which presents a conceptual difficulty for the solution of Eqn. (2.33) or related systems. The idea to overcome this problem is basically to use the finite-sized matrix of the scattering region \mathbf{H}_S , which contains all the relevant information about scattering potential, and to replace the effect of the leads using the concept of self-energies, obtainable from an open quantum system description, introduced in the following section.

The Open Quantum System

The Hamiltonian matrix of the two-probe nanojunction (cf. Figure 2.6 and Eqn. (2.33)) constitutes a quantum system that provides resonant energies given by the eigenvalues of the Schrödinger equation. Within this description no electron

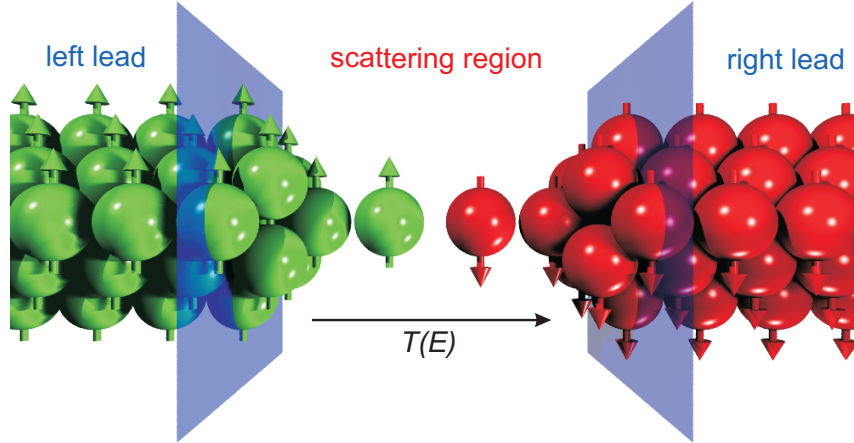


Figure 2.6: Geometry of a non-equilibrium open system, used for ballistic transport calculations. The open system consists of three different regions, the left lead (L), the right lead (R) and the scattering region (S). Electrons with energy E are transmitted through the scattering region with a transmission probability described by the transmission function $T(E)$.

transport processes can occur. The system has to be extended to an open system, allowing electrons to be injected into the system, to excite scattering states and then be retracted from the system, leading to a Schrödinger-like equation for open nanojunction based on its Hamiltonian matrix Eqn. (2.33):

$$\begin{pmatrix} (E - i\eta)\mathbf{I}_L - \mathbf{H}_L & \mathbf{H}_{LS}^\dagger & \mathbf{0} \\ \mathbf{H}_{LS} & E\mathbf{I}_S - \mathbf{H}_S & \mathbf{H}_{SR} \\ \mathbf{0} & \mathbf{H}_{SR}^\dagger & (E - i\eta)\mathbf{I}_R - \mathbf{H}_R \end{pmatrix} \begin{pmatrix} \phi_L + \chi_L \\ \psi_S \\ \phi_R + \chi_R \end{pmatrix} = \begin{pmatrix} \mathbf{S}_L \\ 0 \\ \mathbf{S}_R \end{pmatrix} \quad (2.34)$$

Here $\eta > 0$ is a small positive quantity representing the extraction of electrons from the open system by adding a small value on the imaginary axis, $\mathbf{S}_{L/R}$ describes the injection of electrons, in the spirit of an eccentric, resulting in excited scattering states $\chi_{L/R}$ in the leads. The $\phi_{L/R}$ are the solutions of this equation for the isolated leads (with $\mathbf{H}_{LS} = \mathbf{0}$ and $\mathbf{H}_{SR} = \mathbf{0}$) and ψ_S the states in the scattering region, respectively. The \mathbf{I} are unity matrices, the indices $L; S; R$ denote the region a matrix is defined in and, thus, its size.

Although these modifications to the Hamiltonian of the nanojunction seem to be minor, the result is a fundamental change in the point of view; \mathbf{H} is not hermitian any more and E no longer an eigenvalue, but an independent variable representing the energy of excitation from external sources. Unlike Eqn. (2.33), Eqn. (2.34) has complex eigenvalues and the imaginary part of the eigenvalues both broadens the density of states and gives the eigenstates a finite lifetime.

The open system Eqn. (2.34) can now be used to derive the NEGF transport formalism. The aim of the further approach is to eliminate all lead related contribu-

tions in Eqn. (2.34) and to express the transport processes in terms of the scattering region's Hamiltonian and states.

In the case of isolated leads ($\mathbf{H}_{LS/SR} = \mathbf{0}$), electrons cannot be transmitted into the scattering region and therefore no scattering states $\chi_{L/R}$ are present in the leads. From Eqn. (2.34)) the following expressions for the two leads in this limit are derived

$$[(E + i\eta)\mathbf{I}_{L/R} - \mathbf{H}_{L/R}]\phi_{L/R} = \mathbf{G}_{L/R}(E)\phi_{L/R} = \mathbf{S}_{L/R} \quad (2.35)$$

with the retarded Green's function (referred to as Green's function in the following) of the isolated leads:

$$\mathbf{G}_{L/R}(E) = [(E + i\eta)\mathbf{I}_{L/R} - \mathbf{H}_{L/R}]^{-1} \quad (2.36)$$

Bringing the leads back into contact with the scattering region by allowing $\mathbf{H}_{LS/SR}$ to have non-zero matrix elements, the scattering states $\chi_{L/R}$ (Eqn. (2.34)) can be expressed in terms of the Green's function of the isolated leads:

$$\chi_{L/R} = \mathbf{G}_{L/R}(E)\mathbf{H}_{LS/SR}^\dagger\psi_S \quad (2.37)$$

Eqn. (2.37) can now be used to replace the $\chi_{L/R}$ from the open system Eqn. (2.34) by the states of the scattering region ψ_S

$$(E\mathbf{I}_S - \mathbf{H}_S - \mathbf{H}_{LS}^\dagger\mathbf{G}_L(E)\mathbf{H}_{LS} - \mathbf{H}_{SR}^\dagger\mathbf{G}_R(E)\mathbf{H}_{SR})\psi_S = \mathbf{S} \quad (2.38)$$

with $\mathbf{S} = \mathbf{S}_L + \mathbf{S}_R$. Expressions for the $\mathbf{S}_{L/R}$ can be obtained by comparing Eqn. (2.38) with Eqn. (2.34):

$$\mathbf{S}_{L/R} = \mathbf{H}_{LS/SR}\phi_{L/R} \quad (2.39)$$

Eqn. (2.38) is a much more convenient formulation of the open system than Eqn. (2.34) since all effects of the leads are included by their self-energies

$$\Sigma_{L/R}(E) = \mathbf{H}_{LS/SR}^\dagger\mathbf{G}_{L/R}(E)\mathbf{H}_{LS/SR} \quad (2.40)$$

and scattering processes can be described based on the scattering region that, as mentioned before, includes all relevant information about the scattering potential itself. The self-energies are complex-valued energy dependent matrices containing all the details of the electronic structure of the leads and their coupling to the scattering region.

The Green's function of the scattering region, including the influence of the leads by their self-energies, is now given by:

$$\mathbf{G}_S(E) = [E\mathbf{I}_S - \mathbf{H}_S - \Sigma_L(E) - \Sigma_R(E)]^{-1}. \quad (2.41)$$

Formally Eqn. (2.41) is the Green's function of an effective Hamiltonian with the self-energies as external potentials. The self-energies of the semi-infinite leads are

finite-sized matrices, but still depend on semi-infinite quantities. However, it is possible to replace the leads Green's functions $\mathbf{G}_{L/R}(E)$ by its finite-sized surface Green's functions $\mathbf{g}_{L/R}(E)$ that is described by the localized states in the leads that are interacting with the scattering region, the semi-infiniteness is then included by a recursive scheme, discussed in chapter 6.2. Given such surface Green's functions and the resulting finite-sized self-energies $\Sigma_{L/R}(E)$, the open quantum system (Eqn. (2.34)) can be treated within the effective finite-sized Green's function of the scattering region (Eqn. (2.41)).

Non-Equilibrium's Description of an Open Quantum System

As stated at the end of chapter 2.2, the conductance through a junction is a non-equilibrium problem. The framework to inject, extract and excite electrons in an open system was discussed in the previous section, in this section the open system is extended to leads out of equilibrium with two distinct Fermi functions $f_{L/R}(E)$.

One possible way to describe non-equilibrium systems is by their density matrix ρ . In equilibrium the density matrix can be expressed by states ψ and the global Fermi function of the system $f_0(E)$ by performing a summation over all eigenstates α , which can be replaced by an integration over the energy for continuous states:

$$\begin{aligned} \rho &= \sum_{\alpha} f_0(E_{\alpha}) \psi_{\alpha} \psi_{\alpha}^{\dagger} \\ &= \int \frac{dE}{2\pi} \mathbf{G}^c(E) \end{aligned} \quad , \quad (2.42)$$

where $\mathbf{G}^c(E)$ is the correlation function, the matrix version of the electron density per unit energy. In equilibrium $[\mathbf{G}^c(E)]_{\text{eq}}$ is related to the spectral function $\mathbf{A}(E)$ by the global Fermi function $f_0(E)$

$$[\mathbf{G}^c(E)]_{\text{eq}} = \mathbf{A}(E) f_0(E) \quad (2.43)$$

where $\mathbf{A}(E)$ is the matrix version of the density of states per unit energy:

$$\mathbf{A}(E) = 2\pi\delta(E\mathbf{I} - \mathbf{H}) \quad (2.44)$$

The spectral function can additionally be used to calculate the density of states $D(E)$ of the system, used later in the ballistic transport implementation in chapter 6.5:

$$D(E) = \frac{1}{2\pi} \text{Tr}[\mathbf{A}(E)] \quad (2.45)$$

In the non-equilibrium case two leads have different electro-chemical potentials and two distinct Fermi functions $f_L(E)$ and $f_R(E)$ exist. As an assumption, one part of the spectral function $\mathbf{A}_L(E)$ is considered in equilibrium with lead L and a part of the spectral function $\mathbf{A}_R(E)$ is considered in equilibrium with lead R . The next

assumption is that these two partial spectral functions can be added up to the total spectral function:

$$\mathbf{A}(E) = \mathbf{A}_L(E) + \mathbf{A}_R(E) \quad (2.46)$$

By weighting the partial spectral functions $\mathbf{A}_{L/R}(E)$ with the according Fermi functions $f_{L/R}(E)$, the non-equilibrium correlation function is derived (cf. Eqn. (2.43)):

$$[\mathbf{G}^c(E)]_{\text{neq}} = \mathbf{A}_L(E)f_L(E) + \mathbf{A}_R(E)f_R(E) \quad (2.47)$$

Now an expression for the non-equilibrium density matrix has to be found for the open system (Eqn. (2.34)), based on the states of the scattering region ψ_S , which can be expressed by the scattering regions Green's function $\mathbf{G}_S(E)$ (Eqn. (2.41)) as:

$$\psi_S = \mathbf{G}_S(E)\mathbf{S} \quad (2.48)$$

Following the upper part of Eqn. (2.42), the density matrix is a sum over all states ($\psi_S\psi_S^\dagger$) in the scattering region, weighted by Fermi functions. Accordingly, $\psi_S\psi_S^\dagger$ has to be determined from Eqn. (2.48):

$$\psi_S\psi_S^\dagger = \mathbf{G}_S(E)\mathbf{S}\mathbf{S}^\dagger\mathbf{G}_S^\dagger(E) \quad (2.49)$$

In this equation, only the total electron injection rate related part $\mathbf{S}\mathbf{S}^\dagger$ is yet unknown. The total injection rate $\mathbf{S} = \mathbf{S}_L + \mathbf{S}_R$ is equal to the sum of the local injection rates $\mathbf{S}_{L/R}$ at each lead, given by Eqn. (2.39),

$$\begin{aligned} \mathbf{S}\mathbf{S}^\dagger = & \mathbf{H}_{LS}\phi_L\phi_L^\dagger\mathbf{H}_{LS}^\dagger + \mathbf{H}_{SR}\phi_R\phi_R^\dagger\mathbf{H}_{SR}^\dagger + \\ & \mathbf{H}_{LS}\phi_L\phi_R^\dagger\mathbf{H}_{SR}^\dagger + \mathbf{H}_{SR}\phi_R\phi_L^\dagger\mathbf{H}_{LS}^\dagger \end{aligned} \quad (2.50)$$

where the last two parts of the sum can be neglected due to the decoupling of the leads by construction (cf. Eqn. (2.33)). Thus, $\mathbf{S}\mathbf{S}^\dagger$ can be further simplified:

$$\mathbf{S}\mathbf{S}^\dagger = \mathbf{S}_L\mathbf{S}_L^\dagger + \mathbf{S}_R\mathbf{S}_R^\dagger = \mathbf{H}_{LS}\phi_L\phi_L^\dagger\mathbf{H}_{LS}^\dagger + \mathbf{H}_{SR}\phi_R\phi_R^\dagger\mathbf{H}_{SR}^\dagger \quad (2.51)$$

The non-equilibrium density matrix ρ can now be derived for the open system from $\psi_S\psi_S^\dagger$ (Eqn. (2.49)) by using this expression for $\mathbf{S}\mathbf{S}^\dagger$. The electrons in the lead L/R are distributed according the Fermi functions $f_{L/R}(E)$ in a continuous distribution described by the partial spectral function $\mathbf{A}_{L/R}(E)$ (Eqn. (2.56)), $\phi_{L/R}\phi_{L/R}^\dagger$ in Eqn. (2.51) can thus be replaced by this integral expression in case of continuous states:

$$\phi_{L/R}\phi_{L/R}^\dagger \rightarrow \int \frac{dE}{2\pi} f_{L/R}(E)\mathbf{A}_{L/R} \quad (2.52)$$

The result is the non-equilibrium density matrix ρ and the correlation function $\mathbf{G}^c(E)$ for the non-equilibrium open system:

$$\begin{aligned}\rho &= \int \frac{dE}{2\pi} [G^c(E)]_{\text{neq}} \\ &= \int \frac{dE}{2\pi} ([\mathbf{G}_S(E)\mathbf{\Gamma}_L(E)\mathbf{G}_S^\dagger(E)]f_L(E) + [\mathbf{G}_S(E)\mathbf{\Gamma}_R(E)\mathbf{G}_S^\dagger(E)]f_R(E))\end{aligned}\quad (2.53)$$

The correlation function of an open quantum system (Eqn. (2.4)) can be separated into two parts, each in equilibrium with one lead (cf. Eqn. (2.47)):

$$[G^c(E)]_{\text{neq}} = [\mathbf{G}_S(E)\mathbf{\Gamma}\mathbf{G}_S^\dagger(E)]f_L(E) + [\mathbf{G}_S(E)\mathbf{\Gamma}_R\mathbf{G}_S^\dagger(E)]f_R(E)\quad (2.54)$$

Here, the $\mathbf{\Gamma}_{L/R}(E)$ are broadening matrices:

$$\begin{aligned}\mathbf{\Gamma}_{L/R}(E) &= i[\mathbf{\Sigma}_{L/R}(E) - \mathbf{\Sigma}_{L/R}^\dagger(E)] \\ &= \mathbf{H}_{LS/SR}\mathbf{A}_{L/R}(E)\mathbf{H}_{LS/SR}^\dagger\end{aligned}\quad (2.55)$$

The $\mathbf{\Gamma}_{L/R}(E)$ describe the energy level broadening in the scattering region caused by the contact to the lead and the transfer rates of electrons from the leads into the scattering region. The broadening matrices are obtained from the the self-energies $\mathbf{\Sigma}_{L/R}(E)$ (Eqn. (2.40)).

Further studying ballistic transport processes in electronically and magnetically complex nanojunctions usually requires additional insight into the electronic properties of a system, such as provided by the density of states. To calculate the density of states of the open system (cf. Eqn. (2.45)) an expression for the partial spectral function $\mathbf{A}_{L/R}(E)$ has to be found. Such an expression can be obtained by comparing the non-equilibrium correlation functions in Eqn. (2.53) to Eqn. (2.47):

$$\mathbf{A}_{L/R}(E) = \mathbf{G}_S(E)\mathbf{\Gamma}_{L/R}(E)\mathbf{G}_S^\dagger(E)\quad (2.56)$$

The open system's Hamiltonian matrix, derived from a ground state electronic structure (Eqn. (2.33)), does not contain the modified potential in the scattering region due to the applied bias voltage in the non-equilibrium case. One way such a finite bias can be taken into account within the NEGF formalism is to solve the electrostatic problem to obtain the modified potential based on the non-equilibrium electron density. The non-equilibrium electron density can be calculated from the diagonal elements of the density matrix (Eqn. (2.53)) by performing a contour integral over the complex energy plane. Since the shape of the modified potential affects the non-equilibrium electron density and the non-equilibrium electron density modifies the potential by its charge density, this problem has to be solved self-consistently.

A detailed description of such an approach e.g. within density functional theory (DFT) based on norm-conserving pseudopotentials and numerical atomic orbitals with finite range is described in [48].

Such a self-consistent approach requires a simultaneous description of the electronic structure and the NEGFs by localized orbitals, not achievable within the intrinsically delocalized FLAPW wave functions (chapter 4) used within this thesis. However, most experimental measurements performed in the regime of ballistic transport do not rely on high bias voltages and are especially sensitive to the Fermi level. For those small bias voltages ballistic transport can be described in the linear-response regime. In this approximation the effect of the bias voltage on the total potential is considered to be small, the Hamiltonian matrix of the system (Eqn. (2.33)) is evaluated for zero bias voltage and can be extended to a small bias voltages by assigning two distinct Fermi functions $f_{L/R}(E)$ to the leads. Expressions for the ballistic transmission probabilities and the ballistic conductance within in the linear response regime are derived in the next section. A DFT based approach that includes a finite bias voltage within a maximally localized Wannier function (MLWFs) representation can be e.g. found in [91].

Transmission and Conductance

After introducing the concept of an open system, described by an effective Green's function of the scattering region (section 2.4) and incorporating non-equilibrium effects into this framework in the previous chapter, both concepts are combined to calculate the ballistic conductance within the NEGF approach in the linear response regime.

The current through an open system is given by the time rate of change of the electron's probability density:

$$I = -e \frac{d}{dt} \text{Tr}[\psi_S \psi_S^\dagger] = -e \frac{d}{dt} \text{Tr}[\psi_S^\dagger \psi_S] \quad (2.57)$$

The current flow $I_{L/R}$ between the lead L/R and the scattering region S can be calculated from the time-dependent version of the Schrödinger-like equation of the open system (Eqn. (2.34)) [84]:

$$I_{L/R} = \frac{e}{i\hbar} \left[\text{Tr}[\psi_S^\dagger \mathbf{H}_{LS/SR} \phi_{L/R} - \phi_{L/R}^\dagger \mathbf{H}_{LS/SR}^\dagger \psi_S] \right. \\ \left. - \text{Tr}[\chi_{L/R}^\dagger \mathbf{H}_{LS/SR}^\dagger \psi_S - \psi_S^\dagger \mathbf{H}_{LS/SR} \chi_{L/R}] \right] \quad (2.58)$$

The first trace represents the current inflow $I_{L/R}^{\text{in}}$ and the second trace the current outflow $I_{L/R}^{\text{out}}$ at the interface L/R between lead and scattering region.

$I_{L/R}^{\text{in}}$ can be further simplified by applying Eqn. (2.48) and Eqn. (2.39) and the following representation of the total spectral function

$$\mathbf{A}(E) = i[\mathbf{G}_S(E) - \mathbf{G}_S^\dagger(E)] \quad (2.59)$$

to the first part of Eqn. (2.58):

$$I_{L/R}^{\text{in}}(E) = \frac{e}{i\hbar} \text{Tr}[\mathbf{S}^\dagger \mathbf{G}_S^\dagger(E) \mathbf{S}_{L/R} - \mathbf{S}_{L/R}^\dagger \mathbf{G}_S(E) \mathbf{S}] = \frac{e}{\hbar} \text{Tr}[\mathbf{S}_{L/R} \mathbf{S}_{L/R}^\dagger \mathbf{A}(E)] \quad (2.60)$$

For the last step $\mathbf{S} = \mathbf{S}_L + \mathbf{S}_R$ and $\mathbf{S}_L \mathbf{S}_R^\dagger = \mathbf{S}_R \mathbf{S}_L^\dagger = 0$ (cf. Eqn. (2.51)) was used. $\mathbf{S}_{L/R} \mathbf{S}_{L/R}^\dagger$ can be again evaluated for continuous states by the integral expression Eqn. (2.52). Eqn. (2.60) results in combination with the broadening matrix (Eqn. (2.55)) into the total current inflow [84]:

$$I_{L/R}^{\text{in}} = \frac{e}{\hbar} \int \frac{dE}{2\pi} f_{L/R}(E) \text{Tr}[\mathbf{\Gamma}_{L/R} \mathbf{A}(E)] \quad (2.61)$$

A similar result to Eqn. (2.60) can be found for the current outflow by applying Eqn. (2.37) and Eqn. (2.55) to the second part of Eqn. (2.58) [84]:

$$I_{L/R}^{\text{out}}(E) = \frac{e}{\hbar} \text{Tr}[\psi_S \psi_S^\dagger \mathbf{\Gamma}_{L/R}] \quad (2.62)$$

The total contribution of the $\psi_S \psi_S^\dagger$ for continuous states is known from the density matrix (Eqn. (2.53)) and for the total current outflow it can be replaced by an energy integration over the correlation function $\mathbf{G}^c(E)$ (Eqn. (2.54)):

$$I_{L/R}^{\text{out}} = \frac{e}{\hbar} \int \frac{dE}{2\pi} \text{Tr}[\mathbf{\Gamma}_{L/R} \mathbf{G}^c(E)] \quad (2.63)$$

The total current $I_{L/R}$ through the lead L/R is given by the difference of all inflowing and outflowing currents. For a steady state the total current flowing from the left lead L equals the current arriving at the right lead:

$$I = I_L = -I_R \quad (2.64)$$

As a result a steady total current $I_{L/R}$ needs only to be determined for one interface region. The expression of total current

$$I_{L/R} = \frac{e}{\hbar} \int \frac{dE}{2\pi} \tilde{I}_{L/R} \quad (2.65)$$

has already the shape of the Landauer formula (Eqn. (2.25))

$$I = \frac{e}{h} \int dE T(E) [f_L(E) - f_R(E)] \quad (2.66)$$

with the transmission function $T(E)$. The dimensionless partial currents of Eqn. (2.65) can be expressed by the inflowing and outflowing partial currents (Eqn. (2.61) and Eqn. (2.63)):

$$\tilde{I}_{L/R} = \text{Tr}[\mathbf{\Gamma}_{L/R}\mathbf{A}(E)]f_{L/R}(E) - \text{Tr}[\mathbf{\Gamma}_{L/R}\mathbf{G}^c(E)] \quad (2.67)$$

As a check of consistency the partial currents diminish in the equilibrium case ($\tilde{I}_{L/R} = 0$) with Eqn. (2.43) and the global Fermi function $f_0(E) = f_{L/R}(E)$. In the non-equilibrium case the partial currents have to be calculated with the non-equilibrium correlation function (Eqn. (2.54)) and the spectral function Eqn. (2.56) of non-equilibrium open system:

$$\begin{aligned} \tilde{I}_{L/R} &= \text{Tr}[\mathbf{\Gamma}_L\mathbf{G}_S\mathbf{\Gamma}_L\mathbf{G}_S^\dagger]f_L(E) \\ &\quad + \text{Tr}[\mathbf{\Gamma}_L\mathbf{G}_S\mathbf{\Gamma}_R\mathbf{G}_S^\dagger]f_L(E) \\ &\quad - \text{Tr}[\mathbf{\Gamma}_L\mathbf{G}_S\mathbf{\Gamma}_L\mathbf{G}_S^\dagger]f_L(E) \\ &\quad - \text{Tr}[\mathbf{\Gamma}_L\mathbf{G}_S\mathbf{\Gamma}_R\mathbf{G}_S^\dagger]f_R(E) \\ &= \text{Tr}[\mathbf{\Gamma}_L\mathbf{G}_S\mathbf{\Gamma}_R\mathbf{G}_S^\dagger][f_L(E) - f_R(E)] \end{aligned} \quad (2.68)$$

By comparing the total current Eqn. (2.65), Eqn. (2.67) and Eqn. (2.66) the transmission function $T(E)$ can be related to the dimensionless currents $T(E) = \tilde{I}_{L/R}(E)$. The resulting expression is the transmission function $T(E)$ based on the NEGF approach within linear response:

$$T(E) = \text{Tr}[\mathbf{\Gamma}_L\mathbf{G}_S(E)\mathbf{\Gamma}_R\mathbf{G}_S^\dagger(E)] \quad (2.69)$$

Based on the Landauer formula Eqn. (2.66), the conductance

$$G(E) = G_0T(E) \quad (2.70)$$

can be derived from the transmission function $T(E)$. Single channel transmission functions can be obtained by restricting the trace operation of Eqn. (2.69) to the according states.

The NEGF method introduced in this chapter allows to efficiently calculate the transmission function of electrons through a nanojunction as far as the electronic structure of such a junction can be described by a tight-binding like Hamiltonian. The transmission function (Eqn. (2.69)) and the conductance (Eqn. (2.70)) are calculated within the linear response regime, which means that the Hamiltonian matrix Eqn. (2.33) and the corresponding Green's function based

quantities are evaluated for zero bias voltage. The current through a nanojunction is then obtained by the Landauer formula Eqn. (2.66) including a small bias voltage by applying two distinct Fermi functions $f_{L/R}(E)$ to the leads. The general approach can be applied to model experimental measurements that do not rely on high bias voltages and that are therefore sensitive to Fermi level properties.

3 Density Functional Theory (DFT)

Theoretical physics had enormous development early times in the last century. It started with the discovery of the particle-wave nature by Albert Einstein, Louis de Broglie and many others. The prediction of physical and chemical properties of a material, observable even at the macroscopic scale, such as for example the optical and magnetic properties of matter, requires a quantum mechanical description of the many-body system consisting of electrons and nuclei.

Beyond the macroscopic scale, reaching system sizes in the order of several nanometers, such as e.g. in nanojunctions described by the NEGF quantum transport method (chapter 2), the emergent phenomena, for example, the existence of a conductance quantum, are caused by the quantum mechanical nature of the electrons in the Coulomb potential of the, within the Born-Oppenheimer approximation, rigid nuclei. For a predictive theoretical formulation of such phenomena usually the complete knowledge of the Hamiltonian of the system, its eigenstates and its eigenvalues is implied. While it is rather simple to request such full knowledge, it is in general not an easy task to obtain it.

A full quantum mechanical treatment of a systems, even of rather simple ones such as non-magnetic Cu or Pt monowires, results in a very complex problem, not solvable analytically. Numerical approaches such as the total diagonalization of the Hamilton operator for a given set of electron wave functions reach their computational limits very quickly due the electrons inherent nature as indistinguishable Fermions. The total electron wave function is anti-symmetric as a consequence and has to be described mathematically by e.g. determinants of single electron wavefunctions, the so-called Slater determinants [92]. Slater determinants have the huge draw-back that the necessary memory to store them grows exponentially with the number of electrons N , resulting into what Walter Kohn named an *exponential wall* [93]. A complete quantum mechanical many-body description of realistic materials is therefore beyond reach within a total wave function representation and other approaches have to be found.

The density functional theory (DFT) [94–96] solves this problem very elegantly by uniquely mapping the many-body problem on a set of single electron equations, the so-called Kohn-Sham equations. Within the Kohn-Sham equations the electrons are treated within an effective potential, including the exchange interaction and electron correlation effects. Both, the quantum mechanical many-body problem and the Kohn-Sham equations result in identical electron densities $n(\mathbf{r})$. This is the name-defining quantity of the DFT and computationally much more feasible than

the total wave function due to its dependence on just one spatial coordinate instead of N . The central statement of DFT is that the ground state density defines uniquely all ground state observables, but most importantly the ground state energy. This theory is the basis of all modern *first-principles* (parameter-free) electronic structure calculation methods. The importance of this method was expressed by awarding Walter Kohn the Nobel Prize in chemistry in 1998.

3.1 The Born-Oppenheimer Approximation

The quantum mechanical treatment of a condensed matter system consisting of N electrons at the locations \mathbf{r}_i ($i = 1, \dots, N$) and M atomic nuclei at the locations \mathbf{R}_μ ($\mu = 1, \dots, M$) is based on the time-independent Schrödinger equation¹

$$\hat{H}(\mathbf{r}_1, \dots, \mathbf{r}_N, \mathbf{R}_1, \dots, \mathbf{R}_M) |\Psi(\mathbf{r}_1, \dots, \mathbf{r}_N, \mathbf{R}_1, \dots, \mathbf{R}_M)\rangle = E |\Psi(\mathbf{r}_1, \dots, \mathbf{r}_N, \mathbf{R}_1, \dots, \mathbf{R}_M)\rangle \quad (3.1)$$

In this equation all electrons have identical characteristics such as mass, charge and spin. As a result the eigenstates of $|\Psi(\mathbf{r}_1, \dots, \mathbf{r}_N, \mathbf{R}_1, \dots, \mathbf{R}_M)\rangle$ need to fulfill additional requirements. Identical particles cannot be distinguished in a measurement and therefore the expectation value of a measurement is invariant under the exchange of electrons:

$$\langle \hat{A} \rangle = \langle \dots \mathbf{r}_j \dots \mathbf{r}_k \dots | \hat{A} | \dots \mathbf{r}_j \dots \mathbf{r}_k \dots \rangle \stackrel{!}{=} \langle \dots \mathbf{r}_k \dots \mathbf{r}_j \dots | \hat{A} | \dots \mathbf{r}_k \dots \mathbf{r}_j \dots \rangle \quad (3.2)$$

Following this invariance, the eigenstates of identical particles must be either symmetric (bosons) or anti-symmetric (fermions). The focus of this work lies on the electronic structure of nanojunctions, hence particles of fermionic nature are further studied. The anti-symmetric wave-function of such fermions can be described in terms of Slater determinants [92]. Besides the huge conceptual problem for a computational treatment Slater determinants provide, since the required space to store such a determinant grows exponentially with the electron number N , the resulting problem cannot be solved analytically and additional approximations are necessary. One way to reduce the size of Eqn. (3.1) is the Born-Oppenheimer approximation, which separates the electron system and the system of atomic nuclei by a product ansatz:

$$|\Psi_{\text{total}}\rangle = |\Psi_{\text{electrons}}\rangle \cdot |\Psi_{\text{atomic nuclei}}\rangle \quad (3.3)$$

Additionally, due to the faster motion of the electrons compared to the nuclei because of their much smaller masses, it is assumed that the electron system instantly reacts

¹Even this very general description of a many body system includes approximations. For example, the nuclei are described as point-like objects, although they are not. However, the effect of such an approximation on the systems of interest in this thesis is negligible.

on a change of atomic coordinates from \mathbf{R}_μ to \mathbf{R}'_μ . This assumption is justified as long as

$$\left| \frac{\partial}{\partial \mathbf{R}_\mu} |\Psi_e(\dots, \mathbf{r}_i, \dots, \mathbf{R}_\mu, \dots)\rangle \right| \ll \left| \frac{\partial}{\partial \mathbf{r}_i} |\Psi_e(\dots, \mathbf{r}_i, \dots, \mathbf{R}_\mu, \dots)\rangle \right| \quad \forall i, \mu \quad (3.4)$$

is fulfilled. As a consequence, the Born-Oppenheimer approximation is especially suited for the description of ground state properties.

The many-electron system to solve depends therefore *parametrically* on the coordinates of the nuclei. Applying the Hamilton operator \hat{H} to the product ansatz of the Born-Oppenheimer approximation (Eqn. (3.3)) results in the following simplified problem:

System of electrons:

$$\hat{H}_e(\mathbf{r}_1, \dots, \mathbf{r}_N, \mathbf{R}_1, \dots, \mathbf{R}_M) |\Psi_e(\mathbf{r}_1, \dots, \mathbf{r}_N, \mathbf{R}_1, \dots, \mathbf{R}_M)\rangle = E_e |\Psi_e(\mathbf{r}_1, \dots, \mathbf{r}_N, \mathbf{R}_1, \dots, \mathbf{R}_M)\rangle \quad (3.5)$$

The Hamilton operator is given by

$$\hat{H}_e = \left(-\frac{\hbar^2}{2m} \sum_{i=1}^N \nabla^2 + \sum_{i=1}^N \sum_{\mu=1}^M \frac{e^2 Z_\mu}{|\mathbf{r}_i - \mathbf{R}_\mu|} + \frac{1}{2} \sum_{i \neq j} \frac{e^2}{|\mathbf{r}_i - \mathbf{r}_j|} \right) \quad (3.6)$$

with the number of nuclear charges Z_μ of the nucleus μ . Eqn. (3.6) consists of the kinetic energy operator of the electrons, and the Coulomb potentials caused by the nuclei and the other electrons.

System of atomic nuclei:

$$(\hat{T}_A + \hat{E}_{ii}) |\Psi_A(\mathbf{R}_1, \dots, \mathbf{R}_M)\rangle = (E_{\text{total}} - E_e) |\Psi_A(\mathbf{R}_1, \dots, \mathbf{R}_M)\rangle \quad (3.7)$$

Here \hat{T}_A is the operator of the kinetic energy of the system of the nuclei and $\hat{E}_{ii} = \sum_{\mu \neq \nu} \frac{e^2 Z_\mu Z_\nu}{|\mathbf{R}_\mu - \mathbf{R}_\nu|}$ describes the Coulomb interaction between the nuclei. The energy eigenvalues of the electron system $E_e(\mathbf{R}_1, \dots, \mathbf{R}_M)$ are a part of the potential for the motion of the nuclei. Since the nuclei are fixed the energy of the system of nuclei can be approximated by the Madelung constant $E_{\text{Mad}} = \sum_{\mu \neq \nu}^M \frac{e^2 Z_\mu Z_\nu}{|\mathbf{R}_\mu - \mathbf{R}_\nu|}$. For the total energy therefore follows:

$$E_{\text{total}} = E_e(\mathbf{R}_1, \dots, \mathbf{R}_M) + E_{\text{Mad}}(\mathbf{R}_1, \dots, \mathbf{R}_M) \quad (3.8)$$

In conclusion, for the determination of the ground state of a given many-body system the solution of the electron problem Eqn. (3.6) is of major interest. Despite all

made approximations, the problem stays analytically insolvable due to the exchange effects the electron-electron interaction. There are methods that are capable of solving those problem approximatively, such as e.g. the Hartree-Fock method (a textbook introduction of the Hartree-Fock method can be found e.g. in [97]), that self-consistently determines one optimal Slater determinant to describe the system. Within this method electron exchange effects are included, but the correlation of electronic motion is neglected. Additionally, the Hartree-Fock method includes a non-local part, resulting in an overall coupling of all electrons with identical spins in all bands of a condensed matter system, providing an additional computational burden. A powerful method to obtain the electronic structure of matter, relying on the electron density $n(\mathbf{r})$ rather than on the electron part of the total wave function (Eqn. (3.3)), is the density functional theory as formulated by Hohenberg and Kohn [94] and Kohn and Sham [95]. However, DFT is still based on the Hamiltonian of the electron system (Eqn. (3.6)) within Born-Oppenheimer approximation, but it is capable to include local exchange and electron correlations effects while staying computationally feasible.

3.2 The Hohenberg-Kohn Theorems

Starting from the electron Hamiltonian within Born-Oppenheimer approximation (Eqn. (3.6)), the density functional theory (DFT) is introduced in this section. The DFT is based on the theorems of Hohenberg and Kohn [94], which are first applied to non-magnetic and collinear spin-polarized systems and are then extended to general magnetic systems including non-collinear spin-structures.

Non-Magnetic Systems

The starting-point for quantum mechanics and the density functional theory is the idea, that although the total wave-function $\Psi(\mathbf{r}_1, \dots, \mathbf{r}_N)$ contains all relevant information about a system, it is yet possible to derive the ground state properties of a system without knowing the total wave-function. This has been shown first by Hohenberg and Kohn for non-degenerate ground states [94]. However, an extension to degenerate ground states is possible [96]. The density functional theory is based on two theorems, known as the Hohenberg-Kohn-Theorems:

Theorem 1 *The total energy of a system is an unique functional of the ground state electron density for any given external potential*

The ground state $|\Psi_0\rangle$ of a many-body problem with the Hamilton operator $\hat{H} = \hat{T} + \hat{U} + \hat{V}$ (cf. Eqn. (3.6)) is given by

$$\hat{H}|\Psi_0\rangle = (\hat{T} + \hat{U} + \hat{V})|\Psi_0\rangle = E_0|\Psi_0\rangle \quad (3.9)$$

where \hat{T} is the operator of the kinetic energy, \hat{U} the operator of the electron-electron-interaction, \hat{V} the operator of the interaction with an external potential $V(\mathbf{r})$ and E_0 is the ground state energy.

The Hamiltonian is characterized by its external potential $V(\mathbf{r})$, which is the only non-universal part. For a second many-body system with the external potential $V'(\mathbf{r})$ with $V(\mathbf{r}) \neq V'(\mathbf{r})$ the Hamilton operator \hat{H}' is given:

$$\hat{H}'|\Psi'_0\rangle = (\hat{T} + \hat{U} + \hat{V}')|\Psi_0\rangle = E'_0|\Psi'_0\rangle \quad (3.10)$$

By applying the Ritz variational principle

$$E_0 = \langle\Psi_0|\hat{H}|\Psi_0\rangle < \langle\Psi'_0|\hat{H}|\Psi'_0\rangle \quad (3.11)$$

which states that the energy is minimized for the ground state wave function, and then adding \hat{V} and subtracting \hat{V}' , results in the following equation:

$$\langle\Psi'_0|\hat{H}|\Psi'_0\rangle = \langle\Psi'_0|\hat{H}' + \hat{V} - \hat{V}'|\Psi'_0\rangle = E'_0 + \int d^3r n'_0(\mathbf{r})(V(\mathbf{r}) - V'(\mathbf{r})). \quad (3.12)$$

Here, the single particle electron density was used, defined as:

$$n(\mathbf{r}) = \langle\Psi|\sum_{i=1}^N \delta(\mathbf{r} - \mathbf{r}_i)|\Psi\rangle \quad (3.13)$$

By comparison of Eqn. (3.11) and Eqn. (3.12) one obtains:

$$E_0 < E'_0 + \int d^3r n'_0(\mathbf{r})(V(\mathbf{r}) - V'(\mathbf{r})) \quad (3.14)$$

By applying again the Ritz variational principle to the primed system

$$E'_0 = \langle\Psi'_0|\hat{H}'|\Psi'_0\rangle < \langle\Psi_0|\hat{H}'|\Psi_0\rangle \quad (3.15)$$

an analogous energy relation to Eqn. (3.11) can be found:

$$E'_0 < E_0 + \int d^3r n_0(\mathbf{r})(V'(\mathbf{r}) - V(\mathbf{r})) \quad (3.16)$$

For identical electron densities $n_0(\mathbf{r}) = n'_0(\mathbf{r})$ Eqn. (3.14) and Eqn. (3.16) results into

$$E_0 + E'_0 < E_0 + E'_0 \quad (3.17)$$

which cannot be fulfilled. As a consequence the electron densities are not identical $n_0(\mathbf{r}) \neq n'_0(\mathbf{r})$ for two different external potentials $V(\mathbf{r}) \neq V'(\mathbf{r})$. The electron system (Eqn. (3.5)) is therefore uniquely defined by the electron density $n_0(\mathbf{r})$ and

the external potential $V(\mathbf{r})$. In this case the total energy can be described as unique functional of the ground state electron density, as stated in *Theorem 1*:

$$E[n_0(\mathbf{r})] = T[n_0(\mathbf{r})] + U[n_0(\mathbf{r})] + V[n_0(\mathbf{r})] \quad (3.18)$$

Theorem 2 *The exact ground state electron density minimizes the energy functional $E[n(\mathbf{r})]$.*

Since the Hamilton system is uniquely defined by a given ground state electron density there is a functional relation between the ground density and the ground state and the excited states, respectively. For a given external potential $V(\mathbf{r})$ therefore follows

$$E_V = \langle \Psi[n(\mathbf{r})] | \hat{T} + \hat{U} + \hat{V} | \Psi[n(\mathbf{r})] \rangle \quad (3.19)$$

where $\Psi[n(\mathbf{r})]$ expresses the functional relation between $n(\mathbf{r})$ and the state $|\Psi\rangle$. The Ritz method states for two electron densities $n_0(\mathbf{r}) \neq n(\mathbf{r})$, with the ground state density $n_0(\mathbf{r})$, that

$$\langle \Psi[n_0(\mathbf{r})] | \hat{T} + \hat{U} + \hat{V} | \Psi[n_0(\mathbf{r})] \rangle < \langle \Psi[n(\mathbf{r})] | \hat{T} + \hat{U} + \hat{V} | \Psi[n(\mathbf{r})] \rangle \quad (3.20)$$

has to be fulfilled, or expressed differently:

$$E_V[n_0(\mathbf{r})] < E_V[n(\mathbf{r})] \quad (3.21)$$

The ground state electron density minimizes therefore, as claimed by theorem 2, the energy functional. Given the exact functional relation of the energy functional with respect to an arbitrary electron density, it would be possible to minimize that functional and obtain the ground state electron density. Unfortunately, the exact energy functional is yet unknown and an approximation has to be found.

Spin-Polarized Systems

Two similar theorems can be found for spin-polarized systems. In addition to the external potentials $V(\mathbf{r}) \neq V'(\mathbf{r})$, two external magnetic fields $\mathbf{B}(\mathbf{r}) \neq \mathbf{B}'(\mathbf{r})$ have to be considered for spin-polarized systems. The interaction of the system with the external potentials and magnetic fields can be described as

$$V_0 = \int d^3r (n_0(\mathbf{r})V(\mathbf{r}) - \mathbf{B}(\mathbf{r}) \cdot \mathbf{m}_0(\mathbf{r})) \quad (3.22)$$

with the ground state electron density $n_0(\mathbf{r})$ and the ground state magnetization density $\mathbf{m}_0(\mathbf{r})$. The ground state magnetization density results from the concept

of Pauli-spinors accounting for the electron spin (for definition see section 3.4, Eqn. (3.40)) As a result, expressions similar to Eqn. (3.14)

$$E_0 < E'_0 + \int d^3r n'_0(\mathbf{r})(V(\mathbf{r}) - V'(\mathbf{r})) - \int d^3r \mathbf{m}'_0(\mathbf{r}) \cdot (\mathbf{B}(\mathbf{r}) - \mathbf{B}'(\mathbf{r})) \quad (3.23)$$

and to Eqn. (3.16)

$$E'_0 < E_0 + \int d^3r n_0(\mathbf{r})(V'(\mathbf{r}) - V(\mathbf{r})) - \int d^3r \mathbf{m}_0(\mathbf{r}) \cdot (\mathbf{B}'(\mathbf{r}) - \mathbf{B}(\mathbf{r})). \quad (3.24)$$

can be obtained. Thus, the energy functional of spin-polarized systems is uniquely defined and minimized by the ground state electron density and the ground state magnetization density:

$$E_{V,\mathbf{B}}[n_0(\mathbf{r}), \mathbf{m}_0(\mathbf{r})] < E_{V,\mathbf{B}}[n(\mathbf{r}), \mathbf{m}(\mathbf{r})] \quad (3.25)$$

3.3 The Kohn-Sham Equations

As mentioned above, the exact expression for the energy functional is yet unknown. However, there is an approximation to the energy functional, introduced by Kohn and Sham [95], resulting into the powerful and versatile tool to calculate the electronic structure, density functional theory is nowadays. The idea is to separate the energy functional into its components:

$$E[n(\mathbf{r})] = T[n(\mathbf{r})] + U[n(\mathbf{r})] + V[n(\mathbf{r})] \quad (3.26)$$

Here, $T[n(\mathbf{r})]$ describes the kinetic part and $U[n(\mathbf{r})]$ the electron-electron interactions. Both functionals are universal, only the part of the external potential $V[n(\mathbf{r})]$ depends on the system and can be derived from Eqn. (3.9) and the ground state density (cf. Eqn. (3.13)),

$$V[n(\mathbf{r})] = \int d^3r n(\mathbf{r})V(\mathbf{r}) \quad (3.27)$$

for all other parts, $T[n(\mathbf{r})]$ and $U[n(\mathbf{r})]$, approximations are required. A good approximation to the electron-electron interaction can be found in the classical electromagnetism between two given electron distributions, the so-called Hartree term:

$$U_H[n(\mathbf{r})] = \frac{e^2}{2} \int d^3r \int d^3r' \frac{n(\mathbf{r})n'(\mathbf{r}')}{|\mathbf{r} - \mathbf{r}'|} \quad (3.28)$$

Since this term represents a classical approximation the quantum mechanical exchange and correlation effects are not included.

A precise determination of the kinetic energy is especially crucial for a physically feasible description. There are related methods, such as e.g. the Thomas-Fermi method [98, 99], where the inaccurate treatment of the kinetic energy leads to unphysical results². The following expression of the kinetic energy functional uses an electron density $n(\mathbf{r})$,

$$n(\mathbf{r}) = 2 \sum_{i=1}^N \psi_i^*(\mathbf{r})\psi_i(\mathbf{r}) \quad (3.29)$$

expressed in terms of non-interacting single-particle wave functions $\psi_i(\mathbf{r})$, where the factor of 2 accounts for the double spin-occupation of the orbitals. Within this approach the functional of the kinetic energy T_s can be determined by applying single-particle wave functions $\psi_i(\mathbf{r})$:

$$T_s[\psi[n(\mathbf{r})]] = -2 \sum_{i=1}^N \int d^3r \psi_i^*(\mathbf{r}) \frac{\hbar^2}{2m} \nabla^2 \psi_i(\mathbf{r}) \quad (3.30)$$

Since $T_s[\psi[n(\mathbf{r})]]$ depends on single-particle operators electron correlation effects are neglected by this description. It follows for the energy functional:

$$E[n(\mathbf{r})] = T_s[n(\mathbf{r})] + U_H[n(\mathbf{r})] + V[n(\mathbf{r})] + E_{xc}[n(\mathbf{r})] \quad (3.31)$$

All exchange (x) and correlation (c) effects mentioned before are included into the the unknown exchange-correlation functional $E_{xc}[n(\mathbf{r})]$:

$$E_{xc}[n(\mathbf{r})] = T_c[n(\mathbf{r})] + U_c[n(\mathbf{r})] + U_x[n(\mathbf{r})] \quad (3.32)$$

There are approximations to the exchange-correlation functional $E_{xc}[n(\mathbf{r})]$, such as e.g. the local density approximation (LDA) or the generalized gradient approximation (GGA) (cf. section 3.5), leading to excellent results for the ground state properties of a large class of materials.

Eqn. (3.31) can be solved by applying the variational principle. The variation of the energy functional has to be done while keeping the number of particles constant ($\int d^3r n(\mathbf{r}) = N$) by introducing the Lagrange multiplier μ and resulting in the following equations:

$$\begin{aligned} 0 &= \delta(E[n(\mathbf{r})]) - \mu \left(\int d^3r n(\mathbf{r}) - N \right) \\ &= \delta L[n(\mathbf{r})] = \int d^3r \frac{\delta L[n(\mathbf{r})]}{\delta n(\mathbf{r})} \delta n(\mathbf{r}) \end{aligned} \quad (3.33)$$

Eqn. (3.33) cannot be minimized directly, since $T_s[\psi[n(\mathbf{r})]]$ does not explicitly depend on the electron density. The minimization has to be performed with respect

²I.e., no molecular bonding has been found for N_2 molecule within the Thomas-Fermi method [100]

to the single-particle wave functions (or their complex conjugates), introduced in Eqn. (3.29):

$$0 = \int d^3r \frac{\delta L[\psi_i[n(\mathbf{r})]]}{\delta \psi_i(\mathbf{r})} \frac{\delta \psi_i(\mathbf{r})}{\delta n(\mathbf{r})} \delta n(\mathbf{r}) \Leftrightarrow 0 = \frac{\delta L[\psi_i[n(\mathbf{r})]]}{\delta \psi_i(\mathbf{r})} \frac{\delta \psi_i(\mathbf{r})}{\delta n(\mathbf{r})} \quad (3.34)$$

As an additional constraint, the single-particle wave functions have to be normalized ($\int d^3r |\psi_i(\mathbf{r})|^2 \stackrel{!}{=} 1$). The solution of Eqn. (3.34) can be determined by solving the **Kohn-Sham equations** :

$$\begin{aligned} \epsilon_i \psi_i(\mathbf{r}) &= \left(-\frac{\hbar^2}{2m} \nabla^2 + \underbrace{V(\mathbf{r}) + V_H(\mathbf{r}) + V_{xc}(\mathbf{r})}_{V_{\text{eff}}(\mathbf{r})} \right) \psi_i(\mathbf{r}) \\ &= \left(-\frac{\hbar^2}{2m} \nabla^2 + V_{\text{eff}}(\mathbf{r}) \right) \psi_i(\mathbf{r}) \end{aligned}$$

Here, is $V(\mathbf{r})$ the external potential, $V_H(\mathbf{r})$ the Hartree potential

$$V_H(\mathbf{r}) = e^2 \int d^3r' \frac{n(\mathbf{r}')}{|\mathbf{r} - \mathbf{r}'|} \quad (3.35)$$

and $V_{xc}(\mathbf{r})$ the exchange-correlation potential

$$V_{xc}(\mathbf{r}) = \frac{\delta E_{xc}[n(\mathbf{r})]}{\delta n(\mathbf{r})} \quad (3.36)$$

The Kohn-Sham equations are equivalent to single particle Schrödinger equations in an effective potential $V_{\text{eff}}(\mathbf{r})$. The solutions of the Kohn-Sham equation are connected by Eqn. (3.29) to the ground state density. It follows that the Kohn-Sham equations have to be solved self-consistently, since $V_H(\mathbf{r})$ and $V_{xc}(\mathbf{r})$ depend on the electron density, that itself depends on the solution of the Kohn-Sham equations. In principle, the Kohn-Sham equations map the numerically unsolvable quantum mechanical many-body problem of the electron system on a single-body problem with an effective potential with identical ground state densities. The single-particle wave functions $\psi_i(\mathbf{r})$ and energy eigenvalues ϵ_i formally possess no physical meaning. However, they can provide more insight into a given system by interpreting them as electron wave functions and energies, the latter used to determine e.g. band structures in periodic crystal structures³. Most importantly, the Kohn-Sham wave

³The Kohn-Sham equations are explicitly designed for ground state properties and do not contain excitations of any kind. For example, the correct description of semi-conductor band gaps or unoccupied states in molecules require more sophisticated approaches such as the *GW* approximation [101].

functions will be used as single-particle wave functions when calculating the quantum transport (cf. chapter 2 and chapter 6). This mean-field-like, one-electron approach is not able to describe pronounced many-body effects which may appear in in some cases during the transport process.

3.4 Spin Density Functional Theory

As mentioned in section 3.2, the Hohenberg-Kohn theorems are valid for spin-polarized systems. For those systems the energy functional has to be minimized for the ground state density $n_0(\mathbf{r})$ and additionally for the ground state magnetization density $\mathbf{m}_0(\mathbf{r})$:

$$E[n_0(\mathbf{r}), \mathbf{m}_0(\mathbf{r})] < E[n(\mathbf{r}), \mathbf{m}(\mathbf{r})] \quad (3.37)$$

The electron and magnetization densities can be expressed by two-component Pauli spinors:⁴

$$\boldsymbol{\psi}_i(\mathbf{r}) = \begin{pmatrix} \psi_{1,i}(\mathbf{r}) \\ \psi_{2,i}(\mathbf{r}) \end{pmatrix} \quad (3.38)$$

$$n(\mathbf{r}) = \sum_{i=1}^N |\boldsymbol{\psi}_i(\mathbf{r})|^2 \quad (3.39)$$

$$\mathbf{m}(\mathbf{r}) = \mu_B \sum_{i=1}^N \boldsymbol{\psi}_i^*(\mathbf{r}) \boldsymbol{\sigma} \boldsymbol{\psi}_i(\mathbf{r}) \quad (3.40)$$

Based on these quantities, the Kohn-Sham equations for the spin density functional theory can be derived. An equivalent way to describe electron and magnetization density are the four-component density matrices $\rho_{\alpha\beta}$ as introduced in the next section. Analogously to Eqn. (3.34), the **Kohn-Sham equations** for the spin density functional theory are:

$$\begin{aligned} \epsilon_i \boldsymbol{\psi}_i(\mathbf{r}) &= \left(-\frac{\hbar^2}{2m} \nabla^2 + \underbrace{V(\mathbf{r}) + V_H(\mathbf{r}) + V_{xc}(\mathbf{r})}_{V_{\text{eff}}(\mathbf{r})} + \boldsymbol{\sigma} \cdot \underbrace{(\mathbf{B}(\mathbf{r}) + \mathbf{B}_{xc}(\mathbf{r}))}_{\mathbf{B}_{\text{eff}}(\mathbf{r})} \right) \boldsymbol{\psi}_i(\mathbf{r}) \\ &= \left(-\frac{\hbar^2}{2m} \nabla^2 + \quad V_{\text{eff}}(\mathbf{r}) \quad + \boldsymbol{\sigma} \cdot \quad \mathbf{B}_{\text{eff}}(\mathbf{r}) \quad \right) \boldsymbol{\psi}_i(\mathbf{r}) \end{aligned}$$

⁴Pauli matrices : $\boldsymbol{\sigma} = (\underline{\sigma}_x, \underline{\sigma}_y, \underline{\sigma}_z)^T$ with $\underline{\sigma}_x = \begin{pmatrix} 0 & 1 \\ 1 & 0 \end{pmatrix}$, $\underline{\sigma}_y = \begin{pmatrix} 0 & -i \\ i & 0 \end{pmatrix}$, $\underline{\sigma}_z = \begin{pmatrix} 1 & 0 \\ 0 & -1 \end{pmatrix}$

In addition to the previously introduced exchange-correlation potential $V_{xc}(\mathbf{r})$, an exchange-correlation field $\mathbf{B}_{xc}(\mathbf{r})$ appears:

$$\mathbf{B}_{xc}(\mathbf{r}) = \frac{\delta E_{xc}[n(\mathbf{r}), \mathbf{m}(\mathbf{r})]}{\delta \mathbf{m}(\mathbf{r})} \quad (3.41)$$

In the spin-polarized case non-interacting Pauli spinors are calculated in an effective potential $V_{\text{eff}}(\mathbf{r})$ and an effective magnetic field $\mathbf{B}_{\text{eff}}(\mathbf{r})$. The components of those Pauli spinors can be related by Eqn. (3.38) and Eqn. (3.40) to the ground state electron density and the ground state magnetization density. It is possible to simplify the spin-polarized Kohn-Sham equations for the case of collinear magnetism, where the magnetization can be expressed by its value $m(\mathbf{r}) = |\mathbf{m}(\mathbf{r})| = n_{\uparrow}(\mathbf{r}) - n_{\downarrow}(\mathbf{r})$ along the collinear spin-direction. In this case both spin densities $n_{\sigma}(\mathbf{r})$ with the spin-directions $\sigma = \uparrow, \downarrow$ can be calculated independently in the effective potential and magnetic field.

The Density Matrix

An effective method to describe non-collinear magnetism within the Kohn-Sham approach is the density matrix $\rho_{\alpha\beta}$:

$$\boldsymbol{\rho} = \frac{1}{2}n\mathbf{I}_2 + \boldsymbol{\sigma} \cdot \mathbf{m} = \frac{1}{2} \begin{pmatrix} n + m_z & m_x - im_y \\ m_x + im_y & n - m_z \end{pmatrix} \quad (3.42)$$

Equivalently, an expression for the potential matrix \mathbf{V} can be found:

$$\mathbf{V} = V\mathbf{I}_2 + \mu_B\boldsymbol{\sigma} \cdot \mathbf{B} = \begin{pmatrix} V + \mu_B B_z & \mu_B(B_x - iB_y) \\ \mu_B(B_x + iB_y) & V - \mu_B B_z \end{pmatrix} \quad (3.43)$$

A comparison to Eqn. (3.38) to Eqn. (3.40) reveals that the following connection between both representations exists:

$$\rho_{\alpha\beta} = \sum_{i=1}^N \psi_{i,\alpha}^* \psi_{i,\beta} \quad (3.44)$$

It is possible to rewrite the Kohn-Sham equations by using the potential matrix Eqn. (3.43) to the following form:

$$\left(-\frac{\hbar^2}{2m}\nabla^2 + \mathbf{V} \right) \boldsymbol{\psi}_i = \epsilon_i \boldsymbol{\psi}_i \quad (3.45)$$

This representation demonstrates that the elements V_{12} and V_{21} of the potential matrix (Eqn. (3.43)) couple both spin channels. For collinear systems it is always

possible to chose the global spin-quantization axis in a way that the off-diagonal elements are zero $V_{12} = V_{21} = 0$. In this case both spin-channels are again decoupled and can be calculated separately, as mentioned in the previous section. For non-collinear systems Eqn. (3.45) has to be additionally diagonalized, resulting in an increased computational effort to solve general magnetic problems.

3.5 Exchange-Correlation Potentials

Up to now, no exact expression for the exchange-correlation potential and -field were reported, therefore approximations to them have to be made. One approximation is the so-called local density approximation (LDA) or local spin density approximation (LSDA) for the spin-polarized case. The exchange-correlation energy is approximated by the exchange energy of a homogeneous electron gas with a corresponding electron and magnetization density:

$$E_{xc}[n(\mathbf{r}), \mathbf{m}(\mathbf{r})] = \int d^3r n(\mathbf{r}) \epsilon_{xc}(n(\mathbf{r}), \mathbf{m}(\mathbf{r})) \quad (3.46)$$

As a consequence ϵ_{xc} is a function and not a functional of the electron density $n(\mathbf{r})$ and the value of the magnetization density $|\mathbf{m}(\mathbf{r})|$. With Eqn. (3.36) the exchange-correlation potential can be written as:

$$V_{xc}(\mathbf{r}) = \epsilon_{xc}(n(\mathbf{r}), |\mathbf{m}(\mathbf{r})|) + n(\mathbf{r}) \frac{\delta \epsilon_{xc}(n(\mathbf{r}), |\mathbf{m}(\mathbf{r})|)}{\delta n(\mathbf{r})} \quad (3.47)$$

The exchange-correlation field results with Eqn. (3.41) in:

$$\mathbf{B}_{xc} = n(\mathbf{r}) \frac{\delta \epsilon_{xc}(n(\mathbf{r}), |\mathbf{m}(\mathbf{r})|)}{\delta \mathbf{m}(\mathbf{r})} \hat{\mathbf{m}}(\mathbf{r}) \quad (3.48)$$

Although LDA and LSDA are might seem to be only valid for slowly varying densities, they have been applied with surprising success to inhomogeneous systems. However, LSDA based DFT results do not reproduce e.g. the magnetic properties and the bulk crystal structure of Fe [102]. For such systems and inhomogeneous systems, e.g. low dimensional systems with open surfaces, other approximations to the exchange-correlation potentials and fields may be useful and can be formulated, i.e. by including local gradients of the electron and magnetization density as well as higher order terms, resulting in the generalized gradient approximation (GGA) [103].

Parameters for these approximations can be found, for example, with Hartree-Fock calculations for the homogeneous electron gas, on Quantum-Monte-Carlo calculations (LDA, Vosko, Wilk and Nusair [104]) or on the Random Phase Approximation (LDA, Barth and Hedin [105]). In this work mainly the GGA as described by Perdew *et al.* is used [103].

3.6 Calculation of the Total Energy

The total energy is the most important ground state property since its variation reveals the ground state density. Further, depending on the parameters, such as e.g. the locations of the nuclei and the assumed magnetic configuration, the equilibrium configuration of an investigated system can be obtained by finding the minimal total energy in dependence on those parameters. It is therefore necessary to determine the total energy as precisely as possible. The total energy functional can be derived from Eqn. (3.8) and Eqn. (3.31):

$$E[n(\mathbf{r})] = T_s[n(\mathbf{r})] + U_H[n(\mathbf{r})] + V[n(\mathbf{r})] + E_{xc}[n(\mathbf{r})] + E_{\text{Mad}} \quad (3.49)$$

It is numerically favorable not to apply the operator ∇^2 directly to calculate of the kinetic part of the total energy, but to find a more convenient expression. This expression is obtainable from the following, rearranged Kohn-Sham equations:

$$-\frac{\hbar^2}{2m}\nabla^2\psi_i(\mathbf{r}) = \epsilon_i\psi_i(\mathbf{r}) - V_{\text{eff}}(\mathbf{r})\psi_i(\mathbf{r}) - \boldsymbol{\sigma} \cdot \mathbf{B}_{\text{eff}}(\mathbf{r})\psi_i(\mathbf{r}) \quad (3.50)$$

By applying $\int d^3r \psi_i(\mathbf{r})$ from the left side and summing the contributions of all occupied states

$$T_s[n(\mathbf{r})] = \sum_{i=1}^N \epsilon_i - \int d^3r n(\mathbf{r})V_{\text{eff}}(\mathbf{r}) - \int d^3r \mathbf{m}(\mathbf{r}) \cdot \mathbf{B}_{\text{eff}}(\mathbf{r}) \quad (3.51)$$

Eqn. (3.50) benefits from all needed quantities being available while iteratively solving the Kohn-Sham equations. It is not only possible to calculate the total energy for a converged electron density, approximations to the total energy are also available for every iteration step..

Another numerical difficulty is that the Hartree energy and the contributions of the nuclei to the Coulomb interaction can lead to singularities. Weinert, Wimmer and Freeman [106] have proven that those singularities do not appear for

$$V_{\text{ext}} = \sum_{\mu=1}^N \frac{e^2 Z^\mu}{|\mathbf{r} - \mathbf{R}_k|}, \quad \mathbf{B}_{\text{ext}} = \mathbf{0} \quad (3.52)$$

due to negating contributions of kinetic and potential energy.

3.7 The Self-Consistency Cycle

It is necessary to solve the Kohn-Sham equations self-consistently, as mentioned before in Section 3.3, due to the need of calculating simultaneously the electron density and the single-particle wave functions, which depend on each other. To solve

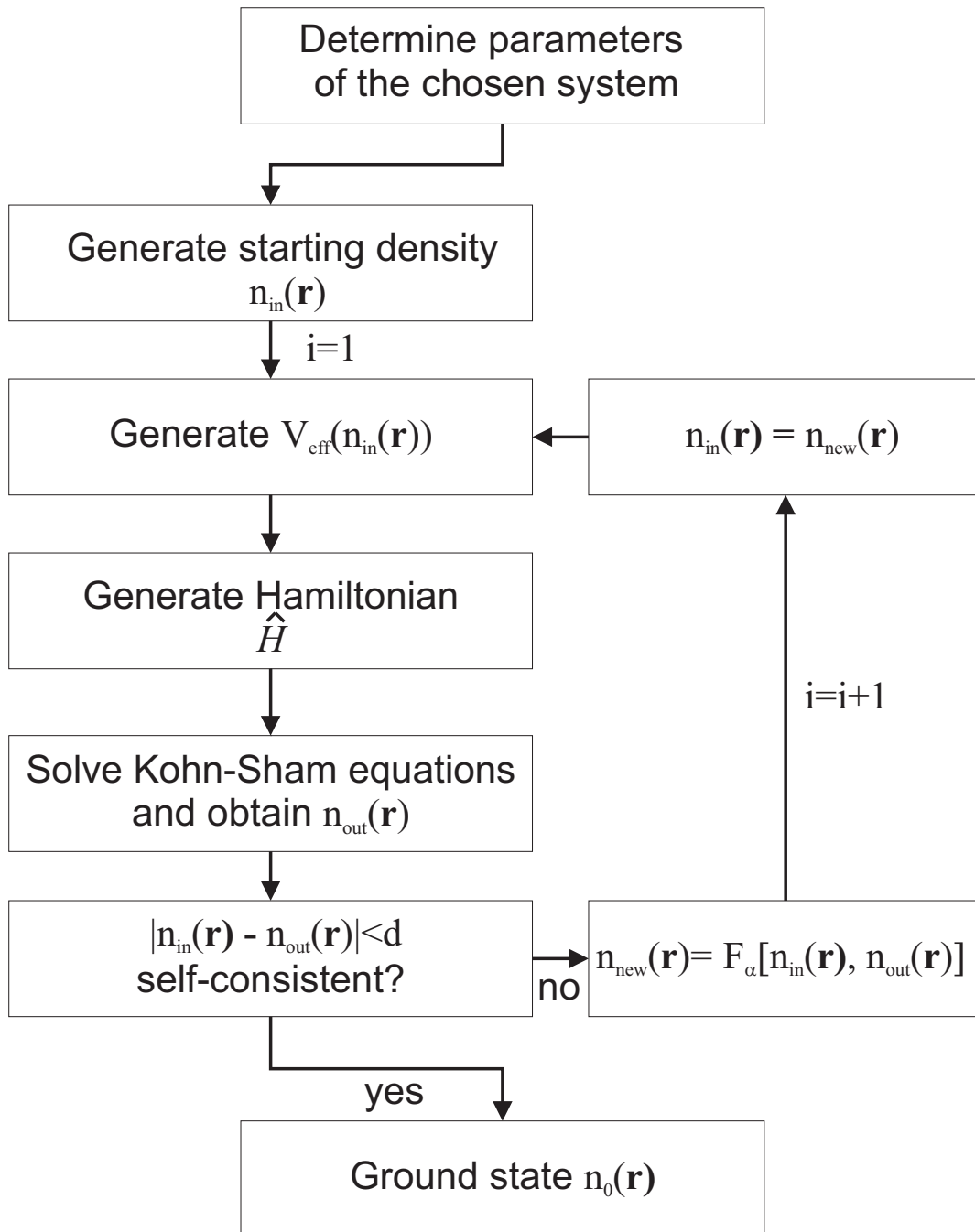


Figure 3.1: The DFT self-consistency cycle.

the Kohn-Sham equations for a given basis-set, one has to follow the self-consistency cycle displayed in Figure 3.1.

As the first step, the parameters of a system to be calculated have to be determined, such as e.g. the geometrical structure, the chemical composition, the lattice constants and collinear or non-collinear magnetization directions. In accordance to those parameters, a starting electron density $n_{\text{in}}(\mathbf{r})$, the effective potential $V_{\text{eff}}(n_{\text{in}}(\mathbf{r}))$ and the Hamiltonian \hat{H} are constructed, based on the Kohn-Sham equations (Eqn. (3.35)), which are solved in the next step. The resulting electron density $n_{\text{out}}(\mathbf{r})$, the Fermi energy E_F , magnetic moments, the total energy (cf. 3.6) and other quantities obtainable from eigenvalues and eigenvectors are then determined based on the single particle Kohn-Sham wave functions. The aim is to reach self-consistency ($n_{\text{in}}(\mathbf{r}) = n_{\text{out}}(\mathbf{r})$). An electron density, and thus the whole self-consistent problem, is regarded as converged when the difference between both electron densities $n_{\text{in}}(\mathbf{r})$ and $n_{\text{out}}(\mathbf{r})$ is smaller than a threshold d : $|n_{\text{in}}(\mathbf{r}) - n_{\text{out}}(\mathbf{r})| < d$. In case of not achieving self-consistency, a new density has to be calculated from $n_{\text{in}}(\mathbf{r})$ and $n_{\text{out}}(\mathbf{r})$, where typically both densities have to be considered for a fast convergence. There are different methods, ranging from simple mixing the electron densities $n_{\text{in}} = (1 - \alpha)n_{\text{in}} + \alpha n_{\text{out}}$ with an mixing parameter α to much more sophisticated methods such as e.g. Quasi-Newton-Raphson methods [107]. Since the convergence strongly depends on the used method it is typically recommended to use a method with a high order of convergence.

3.8 Effective Models of Magnetism

Since the effect of collinear and non-collinear magnetism on the conductance through many metal nanojunctions is discussed in this thesis a short introduction into effective models for magnetism can provide further insight into this very relevant topic. In the following the Stoner model of ferromagnetism, derived directly from spin-density functional theory, and the Heisenberg model of magnetism, applicable to e.g. investigate the origin of non-collinear spin-structures in terms of inter-atom exchange coupling, will be briefly introduced.

The Stoner Model of Ferromagnetism

In general, the magnetization density $m(\mathbf{r})$ is small compared to the electron density $n(\mathbf{r})$, therefore the exchange correlation potential V_{xc}^σ for the spin-polarized case can be linearized with respect to the non-spinpolarized case V_{xc} :

$$V_{\text{xc}}^\sigma(\mathbf{r}) = V_{\text{xc}}(\mathbf{r}) \mp \tilde{V}_{\text{xc}}(\mathbf{r})m(\mathbf{r}) \quad (3.53)$$

where $\sigma = \uparrow, \downarrow$ denotes the spin direction and higher order terms are neglected. $V_{\text{xc}}^\sigma(\mathbf{r})$ is decreased for the majority and increased for the minority spin electrons, providing

an attractive or repulsive potential, depending on the spin direction. Stoner introduced the exchange integral I to approximate this shift according to Eqn. (3.53) with

$$V_{\text{xc}}^{\sigma}(\mathbf{r}) \cong V_{\text{xc}}(\mathbf{r}) \mp \frac{1}{2}IM \quad (3.54)$$

where M is the net magnetic moment of an atom defined by an integration of the magnetization density over the volume V of an atom:

$$M = \int_V d^3r m(\mathbf{r}) \quad (3.55)$$

Compared to the non-spinpolarized case the eigenstates of the Kohn-Sham orbitals remain unchanged, since the effective potential has only been shifted by a constant, resulting in the following spin-dependent shift of the energy eigenvalues:

$$\epsilon_i^{\sigma} = \epsilon_i \mp \frac{1}{2}IM \quad (3.56)$$

The density of states for both spin-directions $n_{\sigma}^0(\mathbf{r})$ can be obtained from the non-magnetic density of states $n^0(\mathbf{r})$ as a consequence:

$$n_{\sigma}^0(\epsilon) = n^0(\epsilon \mp \frac{1}{2}IM) \quad (3.57)$$

The Fermi level E_F of the magnetic system can now be determined by

$$N = \int_{-\text{inf}}^{E_F} d\epsilon \left(n^0(\epsilon - \frac{1}{2}IM) + n^0(\epsilon + \frac{1}{2}IM) \right) \quad (3.58)$$

with the total number of electrons N . Analogously, the magnetic moment M of an atom is then given by

$$M = \int_{-\text{inf}}^{E_F} d\epsilon \left(n^0(\epsilon - \frac{1}{2}IM) - n^0(\epsilon + \frac{1}{2}IM) \right) \quad (3.59)$$

In the ferromagnetic case M has the same value for all atoms. The magnetic moment depends on the Fermi level taken from Eqn. (3.58), the Fermi level can therefore be expressed by the magnetic moment:

$$E_F = E_F(M) \quad (3.60)$$

By combining Eqn. (3.59) and Eqn. (3.60) the magnetic moment can be expressed as

$$M = F(M) \quad (3.61)$$

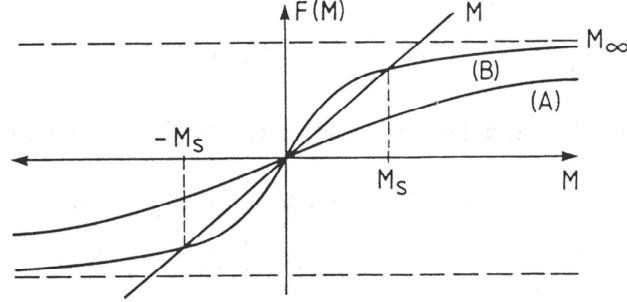


Figure 3.2: Graphical solution of Eqn. (3.61). Figure taken from [108].

$F(M)$ equals Eqn. (3.59) with an upper integral boundary $E_F(M)$ and fulfills the following relations:

$$\begin{aligned}
 (i) \quad & F(0) = 0 \\
 (ii) \quad & F'(M) > 0 \\
 (iii) \quad & F(M \rightarrow \pm\infty) \rightarrow \pm M_\infty \\
 (iv) \quad & F(M) = -F(-M)
 \end{aligned} \tag{3.62}$$

Figure 3.2 shows two possible curves consistent with (i) - (iv). In case (A) only the non-magnetic case $M = 0$ is a solution of Eqn. (3.61), for (B) the two ferromagnetic solutions $M = \pm M_S$ exist. To obtain a ferromagnetic solution, $F(M)$ has to increase more than linear ($F'(0) > 1$) at its origin, which leads to the Stoner criterion:

$$I n^0(E_F) > 1 \tag{3.63}$$

The existence of a ferromagnetic solution depends on the exchange integral I and the density of states $n^0(\mathbf{r})$ at the Fermi level. While I is basically an atomic quantity and depend on the nuclear number, the density of states is approximately proportional to the bandwidth W . The bandwidth depends strongly on the overlap between wave functions of neighboring atoms and is approximately proportional to the square root of the number of nearest neighbors \sqrt{N} and on the localization properties of the wave functions. Based on those values the Stoner model predicts bulk Fe, Co and Ni to be magnetic and explains the tendency of low-dimensional structures, e.g. thin films or nanowires, to exhibit magnetism not shown in their bulk phases due to the reduced bandwidth. The energy gain E_{Stoner} due to the creation of magnetic moment grows quadratically with the magnetic moment within the Stoner model:

$$E_{\text{Stoner}} = \frac{1}{2} I M^2 \tag{3.64}$$

The Stoner model can be generalized to arbitrary spin configurations such as e.g. antiferromagnetic order, as discussed in [108].

The Heisenberg Model for Localized Spins

Although the Stoner Model can be extended to arbitrary spin-configurations, a more applicable approach to study e.g. systems with non-collinear spin order in terms of effective Hamiltonians may be useful. Especially with respect to competing exchange interactions and the resulting frustration of exchange interaction a description based on e.g. the classical Heisenberg model [109]:

$$H_{\text{Heisenberg}} = - \sum_{i \neq j} J_{ij} \mathbf{S}_i \mathbf{S}_j \quad (3.65)$$

where the net spin-moments \mathbf{S} within the atomic volume at the lattice sites i and j are approximated by localized vectors and the interaction between the atoms is expressed in terms of the exchange constants J_{ij} . In localized spin systems the J_{ij} can be safely restricted to the nearest neighbor interaction, $J_1 \neq 0$, $J_{ij} = 0$ for all other neighbors, leading to a ferromagnetic $J_1 > 0$ and a antiferromagnetic $J_1 < 0$ solution of Eqn. (8.1). Although the Heisenberg model is a very basic model, it has been shown to be a valuable tool for the investigation of non-collinear magnetic order, even in itinerant systems where J_1 often dominates over neighbors further away. However, in such systems usually Heisenberg exchange constants beyond nearest neighbor and even higher order terms [110], such as e.g. the biquadratic

$$H_{\text{biq}} = - \sum_{ij} B_{ij} (\mathbf{S}_i \mathbf{S}_j)^2 \quad (3.66)$$

here restricted to neighboring spins i and j , and four-spin interaction,

$$H_{4s} = - \sum_{ijkl} K_{ijkl} [(\mathbf{S}_i \mathbf{S}_j)(\mathbf{S}_k \mathbf{S}_l) + (\mathbf{S}_i \mathbf{S}_l)(\mathbf{S}_k \mathbf{S}_j) - (\mathbf{S}_i \mathbf{S}_k)(\mathbf{S}_j \mathbf{S}_l)] \quad (3.67)$$

describing an interaction between four neighboring spins i , j , k and l , have to be considered. The Heisenberg model can additionally be extended by including interactions such as e.g. the spin-orbit coupling based Dzyaloshinskii-Moriya interaction, responsible e.g. for the chirality (rotation sense) of spin-spiral states in systems without inversion symmetry, for example in magnetic monolayer systems on metallic surfaces [111, 112]. Even highly complex magnetic structures such as e.g. an nanoscale skyrmion lattice, found in the Fe ML on Ir(111), can be successfully investigated in terms of the Heisenberg exchange parameters, including the higher order Heisenberg terms and the Dzyaloshinskii-Moriya interaction [113].

However, in the metallic monowires considered within this thesis, the Heisenberg model, as shown in Eqn. (8.1), is often sufficient to study e.g. non-collinear magnetic

order within an effective model. The the four-spin interactions is suppressed because there are only two neighboring spins in a chain geometry. The Dzyaloshinskii-Moriya interaction has only to be considered for systems with SOC without inversion symmetry. Only the biquadratic term (Eqn. (3.66)) could play a role for the systems under consideration in this thesis.

4 The FLAPW Method

Within density functional theory (DFT) (chapter 3), there are several methods to solve the Kohn-Sham equations to obtain the electronic structure of condensed matter. Basis-set based methods can be divided into three common approaches, plane waves, localized atomic orbitals and atomic sphere methods. Plane waves play an important role in modern DFT codes due to their simplicity and their perfect adaption to periodic structures, such as e.g. the monowires used to construct nanojunctions in this thesis. There are several drawbacks using plane waves, especially in the vicinity of atomic nuclei or at surfaces, where the general approach becomes inefficient due to the large number of waves necessary to describe those region with high accuracy. There are methods to resolve a part of such problems, e.g. with pseudo-potentials replacing the steep potential at the atomic nuclei. The method used in this thesis follows another approach, which combines plane waves with with the concept of atomic spheres, by solving the atom-like Kohn-Sham equation in spherical regions around each nucleus in terms of spherical harmonics and matches the solution to plane waves in the surrounding region. This method is called augmented plane-wave (APW) method, introduced by Slater [114].

In this thesis a full-potential method based on linearized augmented plane waves (LAPW) as implemented in the FLEUR code [63] (FLAPW) is used, known as one of the most precise implementation of DFT. This chapter introduces the FLAPW method starting from plane waves, introduces APWs and LAPWs and finally results into the FLAPW method. FLAPWs provide an accurate and efficient basis set that can be used to describe complex electronic or magnetic structures as found e.g. in non-collinear magnetic order [67] or systems with spin-orbit coupling (SOC) [66] and can be specifically tailored to treat one-dimensional systems [64], such as e.g. nanojunctions, efficiently by incorporating an additional surrounding vacuum region.

4.1 The Generalized Eigenvalue Problem

There are a variety of numerical techniques to solve the Kohn-Sham-equations (chapter 3), the by far most popular approach is by representing the wave function $\phi_{m\mathbf{k}}(\mathbf{r})$ by a set of N basis functions $\psi_{n\mathbf{k}}(\mathbf{r})$, that are eigenfunctions of lattice translation operators with a wave-vector \mathbf{k} .

$$\phi_{m\mathbf{k}}(\mathbf{r}) = \sum_n c_{n\mathbf{k}}^m \psi_{n\mathbf{k}}(\mathbf{r}) \quad (4.1)$$

The choices of a basis set and the approximations made to express the effective potential define different techniques to solve the Kohn-Sham-equations within DFT. Inserting the basis functions into the Kohn-Sham equations (Eqn. (3.35) in chapter 3.3) results in an eigenvalue problem for the eigenvalue $\epsilon_m(\mathbf{k})$ and the expansion coefficients $c_{n\mathbf{k}}^m$ for every \mathbf{k} :

$$(\mathbf{H}^{(\mathbf{k})} - \epsilon_m(\mathbf{k})\mathbf{S}^{(\mathbf{k})}) \mathbf{c}_{m\mathbf{k}} = \mathbf{0} \quad (4.2)$$

where the Hamiltonian matrix $\mathbf{H}^{(\mathbf{k})}$ is given by

$$H_{n'n}^{(\mathbf{k})} = \int d^3r \psi_{n'\mathbf{k}}(\mathbf{r}) \hat{H} \psi_{n\mathbf{k}}(\mathbf{r}) \quad (4.3)$$

with the Hamilton operator \hat{H} . Since a set of basis functions $\psi_{n\mathbf{k}}(\mathbf{r})$ has not necessarily to be orthogonal the overlap matrix $\mathbf{S}^{(\mathbf{k})}$ has to be introduced:

$$S_{n'n}^{(\mathbf{k})} = \int d^3r \psi_{n'\mathbf{k}}(\mathbf{r}) \psi_{n\mathbf{k}}(\mathbf{r}) \quad (4.4)$$

In case of an orthonormal basis set $\mathbf{S}^{(\mathbf{k})}$ is equal to the unity matrix \mathbf{I} . The generalized eigenvalue problem (Eqn. (4.2)) can be mapped onto a normal eigenvalue problem by decomposing the overlap matrix $\mathbf{S}^{(\mathbf{k})}$ by a Cholesky factorization. $\mathbf{H}^{(\mathbf{k})}$ and $\mathbf{S}^{(\mathbf{k})}$ are in general hermitian matrices with real eigenvalues. The computational time to solve Eqn. (4.2) scales with N^3 , an efficient basis set requiring only a small number of basis functions is therefore highly desirable.

4.2 Plane Waves

A very common basis set used for electronic structure calculations are plane waves:

$$\psi_{\mathbf{G}}(\mathbf{r}, \mathbf{k}) = \frac{1}{\sqrt{\Omega}} e^{i(\mathbf{G}+\mathbf{k})\mathbf{r}} \quad (4.5)$$

Here Ω is the volume of the unit cell and \mathbf{G} a vector from reciprocal space. $\mathbf{G} + \mathbf{k}$ are chosen to be within the first Brillouin zone to maintain orthogonality¹. Plane waves are often used because of their simplicity and their perfect adaption to periodic structures. They are already diagonal with respect to the operator of momentum and it easy to implement for this operator or operators including power sets of ∇ . However, plane waves have a serious drawback. The wave functions exhibit a strong

¹In chapter 5 this orthogonality of plane waves is explicitly used in the process of wannierization, $\mathbf{G} + \mathbf{k}$ lying in the first Brillouin zone will then be denoted as $[\mathbf{G} + \mathbf{k}]_{\text{BZ}}$. This notation is left out here for reasons of readability, $\mathbf{G} + \mathbf{k}$ is always meant to be in the first Brillouin zone in regard to the plane waves in this chapter.

oscillatory behavior in the vicinity of the atomic nuclei or in vacuum regions, resulting in a huge number of plane waves corresponding to a large cutoff \mathbf{G}_{\max} to describe a system correctly and thus making this approach inefficient. A possibility to work around this problem are pseudo-potential methods. In such methods the core potential is smoothed in a way that preserves the correct ground state density and properties of the system under investigation. Pseudo-potentials are not easily obtainable for transition metals and often lack the flexibility of full-potential methods like FLAPW, which possesses transferability, i.e. a high accuracy to describe in different chemical environments.

4.3 The APW Method

A natural way to treat electrons in the vicinity of the atomic nuclei are spherical harmonics, as proposed by Slater [114]. This approach leads to the augmented plane wave basis set (APW). The basic idea is to divide space into two different parts: Spherical regions centered at the nuclei called muffin-tins (MT) and an interstitial region (IR) between the muffin-tin spheres.

The potential $V(\mathbf{r})$ will be approximated as spherical symmetric in the muffin-tin spheres and constant in interstitial region:

$$V(\mathbf{r}) = \begin{cases} V_I^0 = \text{const} & \text{interstitial region} \\ V_{\text{MT}^\mu}(r) & \text{muffin-tin } \mu \end{cases} \quad (4.6)$$

The potential will be described in the muffin-tins by spherical harmonics $Y_L(\hat{\mathbf{r}})$, where L runs over the orbital and angular quantum numbers ($L = (l, m)$) and the coordinates are denoted relative to the atomic center $r = |\mathbf{r} - \mathbf{r}_\mu|$. Higher order multipole elements are usually neglected in the APW method ($l = 0$), resulting in a shape approximation to the potential. The wave functions are expressed as

$$\psi_{\mathbf{G}}(\mathbf{r}, \mathbf{k}) = \begin{cases} \frac{1}{\sqrt{\Omega}} e^{i(\mathbf{G}+\mathbf{k})\mathbf{r}} & \text{IR} \\ \sum_L A_L^{\mu\mathbf{G}}(\mathbf{k}) u_l(r) Y_L(\hat{\mathbf{r}}) & \text{MT}^\mu \end{cases} \quad (4.7)$$

where $u_l(r)$ is the solution of the separated radial part of the Schrödinger equation

$$\left\{ \frac{-\hbar^2}{2m} \frac{d^2}{dr^2} + \frac{\hbar^2}{2m} \frac{l(l+1)}{r^2} + V(r) - \epsilon_l \right\} r u_l(r) = 0 \quad (4.8)$$

with the band energies ϵ_l . The coefficients $A_L^{\mu\mathbf{G}}(\mathbf{k})$ are chosen such that Eqn. (4.7) is continuous at the boundary of the muffin-tin spheres. They can be calculated by expressing the interstitial region's plane waves at the boundary of the muffin-tin μ

with radius R_μ in spherical harmonics:

$$\begin{aligned} \frac{1}{\sqrt{\Omega}} e^{i(\mathbf{G}+\mathbf{k})\mathbf{r}} \Big|_{\partial\text{MT}^\mu} &= \frac{1}{\sqrt{\Omega}} e^{i(\mathbf{G}+\mathbf{k})(\mathbf{R}_\mu+\mathbf{r}-\mathbf{R}_\mu)} = \\ &= \frac{1}{\sqrt{\Omega}} e^{i(\mathbf{G}+\mathbf{k})\mathbf{R}_\mu} 4\pi \sum_L i^l j_l(R_\mu \cdot |\mathbf{k} + \mathbf{G}|) Y_L^*(\hat{\mathbf{e}}_{\mathbf{k}+\mathbf{G}}) Y_L(\hat{\mathbf{r}}) \end{aligned} \quad (4.9)$$

Here, the j_l are spherical Bessel functions. The comparison of Eqn. (4.9) with the muffin-tin part of Eqn. (4.7) results in the following coefficients $A_L^{\mu\mathbf{G}}(\mathbf{k})$:

$$A_L^{\mu\mathbf{G}}(\mathbf{k}) = \frac{1}{\sqrt{\Omega}} e^{i(\mathbf{G}+\mathbf{k})\mathbf{R}_\mu} \frac{4\pi i^l}{\sqrt{\Omega} u_l(R_\mu)} j_l(R_\mu \cdot |\mathbf{k} + \mathbf{G}|) Y_L^*(\hat{\mathbf{e}}_{\mathbf{k}+\mathbf{G}}) \quad (4.10)$$

For small or vanishing $u_l(R_\mu)$ numerical problems arise, since $A_L^{\mu\mathbf{G}}(\mathbf{k}) \propto \frac{1}{u_l(R_\mu)}$. This problem is called the asymptotic problem.

Additionally, because of the missing variational freedom for the determination of the radial functions, ϵ_l cannot be held fixed. The ϵ_l have to be equal to the band energies and the wave functions have to be known for the determination of the band energies and vice versa. This results in a non-linear problem that has to be additionally solved, resulting in an overall bigger computational effort.

4.4 The LAPW Method

The main numerical problems of the augmented plane wave method arise due to a lack of variational freedom. To circumvent those problems, the radial part of the APWs are linearized around the band energy ϵ_l resulting in so-called linearized augmented plane wave approach (LAPW) [115–117]:

$$u_l(\epsilon, r) = u_l(\epsilon_l, r) + \frac{\partial}{\partial \epsilon} u_l(\epsilon, r) \Big|_{\epsilon_l} (\epsilon - \epsilon_l) \quad (4.11)$$

The error in the wave function scales quadratically with the variation $(\epsilon - \epsilon_l)$ and this, due to the variational principle, the error determining the band energies is of order 4 [115, 116]. Therefore it becomes possible to describe solutions of the valence bands by a single linearization in energy for each orbital character l if the energy derivative is included in the basis set. The energy derivative $\frac{\partial}{\partial \epsilon} u_l(\epsilon_l, r)$ can be calculated from Eqn. (4.8):

$$\left\{ -\frac{\hbar^2}{2m} \frac{d^2}{dr^2} + \frac{\hbar^2}{2m} \frac{l(l+1)}{r^2} + V(r) - \epsilon_l \right\} r \frac{\partial}{\partial \epsilon} u_l(r) = r u_l(r) \quad (4.12)$$

The LAPW basis assumes the following form:

$$\psi_{\mathbf{G}}(\mathbf{r}, \mathbf{k}) = \begin{cases} \frac{1}{\sqrt{\Omega}} e^{i(\mathbf{G}+\mathbf{k})\mathbf{r}} & \text{IR} \\ \sum_L \left(A_L^{\mu\mathbf{G}}(\mathbf{k}) u_l(r) Y_L(\hat{\mathbf{r}}) + B_L^{\mu\mathbf{G}}(\mathbf{k}) \frac{\partial}{\partial \epsilon} u_l(r) Y_L(\hat{\mathbf{r}}) \right) & \text{MT}^\mu \end{cases} \quad (4.13)$$

The energy parameter ϵ_l is fixed for every angular momentum l . The $A_L^{\mu\mathbf{G}}(\mathbf{k})$ and $B_L^{\mu\mathbf{G}}(\mathbf{k})$ are calculated analogously to the APW basis set, but due to the additional variational freedom, it is possible to fulfill continuity of the wave function and of the first radial derivative ($\frac{\partial}{\partial r}$) at the boundary of each muffin-tin sphere ∂MT^μ :

$$\begin{aligned} \frac{1}{\sqrt{\Omega}} e^{i(\mathbf{G}+\mathbf{k})\mathbf{r}} \Big|_{\partial\text{MT}^\mu} &= \sum_L \left(A_L^{\mu\mathbf{G}}(\mathbf{k}) u_l(r) + B_L^{\mu\mathbf{G}}(\mathbf{k}) \frac{\partial}{\partial \epsilon} u_l(r) \right) \Big|_{\partial\text{MT}^\mu} Y_L(\hat{\mathbf{r}}) \\ \frac{1}{\sqrt{\Omega}} \frac{\partial}{\partial r} e^{i(\mathbf{G}+\mathbf{k})\mathbf{r}} \Big|_{\partial\text{MT}^\mu} &= \sum_L \left(A_L^{\mu\mathbf{G}}(\mathbf{k}) \frac{\partial}{\partial r} u_l(r) + B_L^{\mu\mathbf{G}}(\mathbf{k}) \frac{\partial}{\partial r} \frac{\partial}{\partial \epsilon} u_l(r) \right) \Big|_{\partial\text{MT}^\mu} Y_L(\hat{\mathbf{r}}) \quad (4.14) \end{aligned}$$

It is useful to require the $u_l(\epsilon, r)$ to be normalized

$$\int_0^{R_\mu} dr r^2 u_{l,\mu}^2(r) = 1 \quad (4.15)$$

and to chose $u_l(\epsilon, r)$ and $\frac{\partial}{\partial \epsilon} u_{l,\mu}(r)$ to be orthogonal

$$\int_0^{R_\mu} dr r^2 u_{l,\mu}(r) \frac{\partial}{\partial \epsilon} u_{l,\mu}(r) = 0 \quad (4.16)$$

to define $\frac{\partial}{\partial \epsilon} u_l(r)$ and $u_l(r)$ uniquely. The LAPW method solves the asymptotical problem of the APW method, since for $A_L^{\mu\mathbf{G}}(\mathbf{k})$ and $B_L^{\mu\mathbf{G}}(\mathbf{k})$, $u_l(\epsilon, r)$ and $\frac{\partial}{\partial \epsilon} u_l(r)$ do not longer appear in the numerator. Schrödinger type equations can be solved by diagonalization of the Hamiltonian matrix in the vicinity of the energy parameters. LAPWs are additionally capable of describing non-spherical potentials facilitating a possible full-potential description, introduced for the FLAPW method in the next section.

4.5 The FLAPW Method

Many APW or LAPW based methods use shape-approximations to the potential Eqn. (4.6)². It is nevertheless possible if not mandatory for an accurate treatment of a system to describe the potential without such shape-approximations, resulting into the FLAPW (full-potential linearized APW) method [119, 120]. Especially open structures, such as e.g. the monoatomic wires focused on in this work, ideally require such a precise description.

²There are APW and LAPW methods using a warped potential in the interstitial region [118]

The FLAPW Potential

The main idea behind the full potential augmented plane wave method (FLAPW), proposed by Wimmer *et al.* [120], is to use the LAPW basis set and additionally find a way of describing the full potential without shape approximations. The total Coulomb potential consists of the Hartree part $V_H(\mathbf{r})$ and the external potential $V_{\text{ext}}(\mathbf{r})$:

$$V_c(\mathbf{r}) = V_H(\mathbf{r}) + V_{\text{ext}}(\mathbf{r}) \quad (4.17)$$

The Hartree potential can be determined from the charge density by the following Poisson equation:

$$\nabla^2 V_H(\mathbf{r}) = 4\pi\epsilon_0\rho(\mathbf{r}) \quad (4.18)$$

The potential has to fulfill continuity at the the boundary of each the muffin-tin spheres ∂MT :

$$V_{\text{MT}}(r)|_{\partial\text{MT}} \stackrel{!}{=} V_{\text{IR}}(r)|_{\partial\text{MT}} \quad (4.19)$$

The treatment of the potential in the interstitial region is difficult in real space, while the Poisson equation is diagonal in reciprocal space,

$$\mathbf{G}^2 V_H = 4\pi\rho(\mathbf{G}) \quad (4.20)$$

leading to Fourier series for the total charge density

$$\rho(\mathbf{r}) = \sum_{\mathbf{G}} \rho_{\mathbf{G}} e^{i\mathbf{G}\cdot\mathbf{r}} \quad (4.21)$$

and for the potential in the interstitial region.

$$V_{\text{I}} = \sum_{\mathbf{G}\neq 0} \frac{4\pi\rho_{\mathbf{G}}}{\mathbf{G}^2} e^{i\mathbf{G}\cdot\mathbf{r}} = \sum_{\mathbf{G}\neq 0} V_{\text{I}}^{\mathbf{G}} e^{i\mathbf{G}\cdot\mathbf{r}} \quad (4.22)$$

The integration constant $v_{\mathbf{G}=0}$ is set to zero. The resulting Dirichlet problem can be solved by means of Green's functions [121]. Charge density $\rho(\mathbf{r})$ and potential $V(\mathbf{r})$ can be expressed as follows using spherical harmonics $Y_L(\hat{\mathbf{r}})$ within the muffin-tin spheres:

$$\rho(\mathbf{r}) = \begin{cases} \sum_{\mathbf{G}} \rho_{\text{I}}^{\mathbf{G}} e^{i\mathbf{G}\cdot\mathbf{r}} & \text{IR} \\ \sum_L \rho_L^{\mu}(r) Y_L(\hat{\mathbf{r}}) & \text{MT}^{\mu} \end{cases} \quad (4.23)$$

$$V(\mathbf{r}) = \begin{cases} \sum_{\mathbf{G}\neq 0} V_{\text{I}}^{\mathbf{G}} e^{i\mathbf{G}\cdot\mathbf{r}} & \text{IR} \\ \sum_L V_L^{\mu}(r) Y_L(\hat{\mathbf{r}}) & \text{MT}^{\mu} \end{cases} \quad (4.24)$$

There are numerical problems to calculate the potential in the muffin-tins because of the fast oscillatory behavior of the wave functions in the vicinity of the atomic nuclei, resulting in a very slowly converging Fourier series of the potential. This problem can be solved by the pseudo charge density method introduced by Weinert [121]. In this approach the charge density is replaced by a faster converging pseudo charge density $\tilde{\rho}$ resulting in an identical potential in the interstitial region [119, 121].

4.6 FLAPW for One-Dimensional Systems

So far only systems with three-dimensional translation symmetry have been discussed. It is still possible to describe quasi one-dimensional structures in a unit cell with three-dimensional periodicity within a super cell approach. In such a super cell calculation, e.g for a freestanding monowire, several parallel wires are described with a large inter-wire distance to avoid overlapping wave functions between wires from different unit cells. This approach is, while still possible to perform, computationally expensive since a large number of plane waves is necessary to capture the exponential decay of the wave function between the wires. In the spirit of the FLAPW method, an additional vacuum region (VR) is therefore introduced, describing the exponential decay by adapted wave functions. Mokrousov *et al.* [64] developed the FLAPW method for quasi one-dimensional systems, Krakauer *et al.* [65] proposed a similar approach for two-dimensional films. The vacuum region itself is defined to be outside of a cylinder with diameter D_{vac} (cf. Fig. 4.1 and Fig 4.2) and the wave function is described to be exponentially decaying in this region.

The interstitial region is again described by plane waves with a wave vector $\mathbf{G} = (\mathbf{G}_{\parallel}, G_z)$. In z direction periodic boundary conditions are applied, the wave vector k_z is situated within the one-dimensional Brillouin zone. In $x - y$ the plane waves of the interstitial region are restricted to a square lattice with the lattice constants \tilde{D} . To increase the variational freedom, \tilde{D} is chosen larger than D_{vac} . The description in the muffin-tin spheres remains unchanged, constituting the following set of basis functions:

$$\psi_{\mathbf{G}}(\mathbf{r}, k_z) = \begin{cases} \frac{1}{\sqrt{\Omega}} e^{i(\mathbf{G}+k_z)\mathbf{r}} & \text{IR} \\ \sum_m \left\{ A_m^{\mathbf{G}}(k_z) u_m^{G_z}(k_z, r) + B_m^{\mathbf{G}}(k_z) \frac{\partial}{\partial \epsilon} u_m^{\mathbf{G}}(k_z, r) \right\} e^{im\phi} e^{i(G_z+k_z)z} & \text{VR} \\ \sum_L \left(A_L^{\mu\mathbf{G}}(k_z) u_l(r) + B_L^{\mu\mathbf{G}}(k_z) \frac{\partial}{\partial \epsilon} u_l(r) \right) Y_L(\hat{\mathbf{r}}) & \text{MT}^{\mu} \end{cases} \quad (4.25)$$

The vacuum region is described in terms of cylindrical coordinates $\mathbf{r} = (r, \phi, z)$ and the summation over m extends to the maximal angular expansion parameter m_{max} (typically $m_{\text{max}} = 50$ is sufficient), which ensures a smooth transition of the wave functions from the interstitial to the vacuum region. The radial symmetric part of the potential $V_0(r)$ and the vacuum energy parameter ϵ_{vac} are determined at every iteration step to solve the radial Kohn-Sham equations, resulting into the vacuum radial basis functions $u_m^{G_z}(k_z, r)$ and its energy derivative $\frac{\partial}{\partial \epsilon} u_m^{\mathbf{G}}(k_z, r)$. The A and B coefficients for the vacuum region and the muffin-tins have to be determined by fulfilling continuity of the wave function and its energy derivative at the VR-IR and the IR-MT boundaries.

For the potential the routine described in chapter 4.5 has to be changed accord-

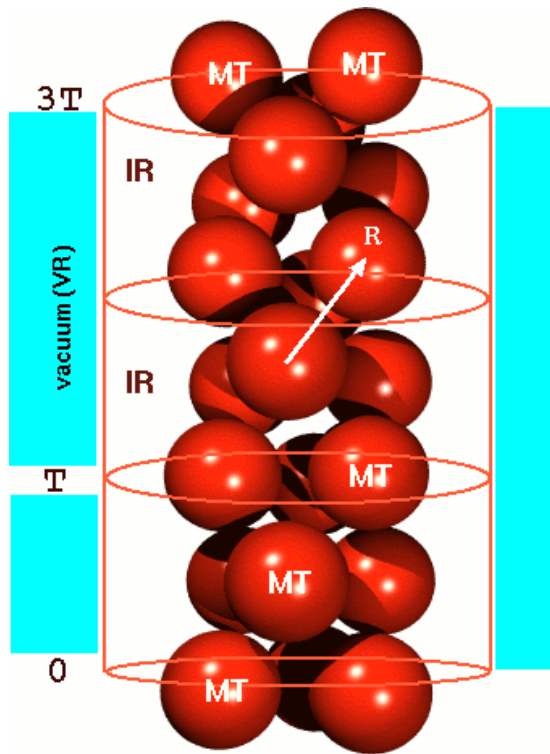


Figure 4.1:

Division of space for a one-dimensional FLAPW calculation. An additional vacuum region is introduced outside of a cylinder with radius D_{vac} and z -periodicity (T describes a translation in z -direction), an interstitial region (IR) inside of the cylinder and the muffin-tins (MT) around the atomic nuclei. Image taken from [64].

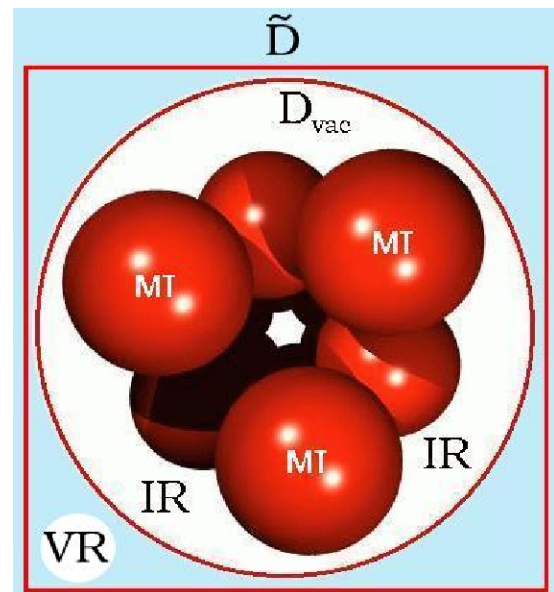


Figure 4.2:

$x - y$ -plane cut through a one-dimensional FLAPW calculation: Muffin-tins (MT) and interstitial region inside of the cylinder with radius D_{vac} , the vacuum region outside the cylinder and the fictitious in-plane square lattice with the lattice constant \tilde{D} . Image taken from [64].

ing to the newly introduced vacuum region: First, the Fourier components of the potential in the muffin-tin spheres and the vacuum potential, by solving a Poisson equation for the vacuum charge density, have to be obtained. Thereafter, the resulting Dirichlet problem for the interstitial-vacuum boundary region is solved by obtaining the Fourier components of the interstitial potential (compare with Eqn. (4.21)). With those components, the interstitial-muffin-tin region boundary problem is solved by Green's functions, as mentioned in chapter 4.5. An in-depth description of the one-dimensional FLAPW method can be found in [64].

4.7 Non-Collinear Magnetism within the FLAPW Method

Within the FLAPW method, it is possible to go beyond collinear magnetism and to treat the spin-dependent Kohn-Sham equations (chapter 3.4) for non-collinear spin structures [67]. As previously shown, both spin channels $\sigma = \uparrow, \downarrow$ can be separated for collinear magnetic calculations, resulting in two independently solvable problems. In this case the potential matrix \mathbf{V} becomes diagonal (compare Eqn. (3.43) in chapter 3.4) and the basis functions maintain the shape of non-magnetic calculations. The total charge density and the value of the magnetization density is expressed by the sum

$$n(\mathbf{r}) = n_{\uparrow}(\mathbf{r}) + n_{\downarrow}(\mathbf{r}) \quad (4.26)$$

or difference

$$|\mathbf{m}(\mathbf{r})| = n_{\uparrow}(\mathbf{r}) - n_{\downarrow}(\mathbf{r}) \quad (4.27)$$

of the two resulting spin densities $n_{\sigma}(\mathbf{r})$. The two spin-channels are only coupled by the effective potential and the exchange correlation field (see chapter 3.4). The implementation non-collinear magnetic order in the FLEUR-Code by Kurz *et al.* [67] follows the general spin-density functional theory framework introduced in chapter 3.4. The spin directions is described by the two-component spinor χ^g with the spinor components χ_{σ}^g ,

$$\chi_{\uparrow}^g = \begin{pmatrix} 1 \\ 0 \end{pmatrix} \text{ and } \chi_{\downarrow}^g = \begin{pmatrix} 0 \\ 1 \end{pmatrix} \quad (4.28)$$

where g denotes a global quantization axis. For the non-collinear Kohn-Sham equations, the magnetization density is generally not aligned in the direction of the global quantization axis, instead it points into a local quantization axis defined for every point in real space. Within the FLAPW approach used by FLEUR, the magnetization density is kept collinear in the muffin-tin spheres, pointing in direction of a local spin frame σ^{μ} of muffin-tin μ and is described as a continuous vector field in the interstitial region, as shown in Fig. 4.3.

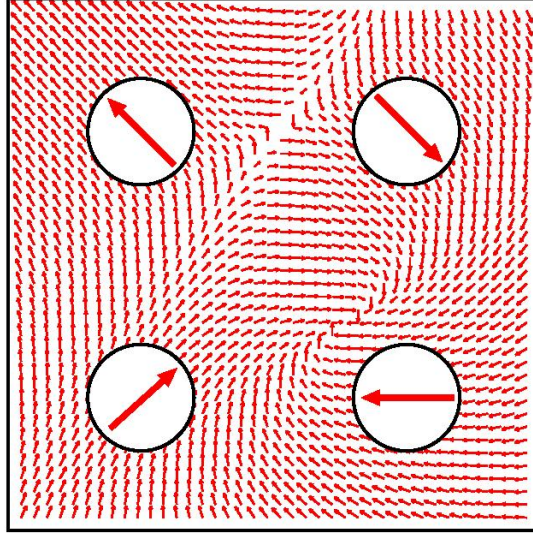


Figure 4.3: Cut through a non-collinear magnetization density with collinear magnetic moments in the muffin-tins (MT) pointing in direction of a local quantization axis σ^μ and the magnetization density of the interstitial region described as continuous vector field. Image taken from [67].

The representation of the basis functions within this approach can be expressed as follows:

$$\psi_{\mathbf{G}\sigma}(\mathbf{r}, \mathbf{k}) = \begin{cases} \frac{1}{\sqrt{\Omega}} e^{i(\mathbf{G}+\mathbf{k})\mathbf{r}} \chi_\sigma^g & \text{IR} \\ \sum_{\sigma L} \left(A_{L\sigma\sigma^\mu}^{\mu\mathbf{G}}(\mathbf{k}) u_{l\sigma}^{\sigma^\mu}(r) + B_{L\sigma\sigma^\mu}^{\mu\mathbf{G}}(\mathbf{k}) \frac{\partial}{\partial r} u_{l\sigma}^{\sigma^\mu}(r) \right) Y_L(\hat{\mathbf{r}}) \chi_\sigma^{\sigma^\mu} & \text{MT}^\mu \end{cases} \quad (4.29)$$

Here the $u_{l\sigma}^{\sigma^\mu}(r)$ and $\frac{\partial}{\partial r} u_{l\sigma}^{\sigma^\mu}(r)$ denote the solution of the radial Schrödinger equation in the local spin frame σ^μ . Both spins of a rotated local spin frame can now couple to both global spin directions. As a result, the coefficients $A_{L\sigma\sigma^\mu}^{\mu\mathbf{G}}(\mathbf{k})$ and $B_{L\sigma\sigma^\mu}^{\mu\mathbf{G}}(\mathbf{k})$ depend on the local and the global spin quantization axes. For the calculation of the coefficients a transformation from global spin frame g into the local spin frame of muffin-tin μ has to be found.

The local spin frames of the muffin-tins are described by the two Euler angles α and β . The two component spinor χ^g of non-collinear basis functions (Eqn. (4.29)) can be rotated by the unitary transformation \mathbf{U}_μ into a local spin frame of the muffin-tin μ :

$$\chi^{\mu g} = \begin{pmatrix} e^{i\frac{\alpha_\mu}{2}} \cos\left(\frac{\beta_\mu}{2}\right) & e^{-i\frac{\alpha_\mu}{2}} \sin\left(\frac{\beta_\mu}{2}\right) \\ -e^{i\frac{\alpha_\mu}{2}} \sin\left(\frac{\beta_\mu}{2}\right) & e^{-i\frac{\alpha_\mu}{2}} \cos\left(\frac{\beta_\mu}{2}\right) \end{pmatrix} \chi^g = \mathbf{U}_\mu \chi^g \quad (4.30)$$

It is necessary to reformulate the boundary conditions on the muffin-tin spheres ∂MT_μ with respect to a rotated local quantization axis. This is done by rotating the wave functions in the muffin-tins from the local into the the global quantization axis g , following Eqn. (4.30), by \mathbf{U}_μ^\dagger . The resulting boundary conditions, by demanding continuity of the wave function and its the first energy derivative between muffin-tin and interstitial wave functions, are

$$\frac{1}{\sqrt{\Omega}} e^{i(\mathbf{G}+\mathbf{k})\mathbf{r}} \Big|_{\partial\text{MT}^\mu} \chi_\sigma^g = \sum_L \mathbf{U}_\mu^\dagger \left(\begin{array}{c} A_{L\uparrow\sigma^\mu}^{\mu\mathbf{G}}(\mathbf{k}) u_{l\uparrow}^{\sigma^\mu}(r) + B_{L\uparrow\sigma^\mu}^{\mu\mathbf{G}}(\mathbf{k}) \frac{\partial}{\partial \epsilon} u_{l\uparrow}^{\sigma^\mu}(r) \\ A_{L\downarrow\sigma^\mu}^{\mu\mathbf{G}}(\mathbf{k}) u_{l\downarrow}^{\sigma^\mu}(r) + B_{L\downarrow\sigma^\mu}^{\mu\mathbf{G}}(\mathbf{k}) \frac{\partial}{\partial \epsilon} u_{l\downarrow}^{\sigma^\mu}(r) \end{array} \right) \Big|_{\partial\text{MT}^\mu} Y_L(\hat{\mathbf{r}}) \quad (4.31)$$

and

$$\begin{aligned} & \frac{1}{\sqrt{\Omega}} \frac{\partial}{\partial r} e^{i(\mathbf{G}+\mathbf{k})\mathbf{r}} \Big|_{\partial\text{MT}^\mu} \chi_\sigma^g \\ &= \sum_L \mathbf{U}_\mu^\dagger \left(\begin{array}{c} A_{L\uparrow\sigma^\mu}^{\mu\mathbf{G}}(\mathbf{k}) \frac{\partial}{\partial r} u_{l\uparrow}^{\sigma^\mu}(r) + B_{L\uparrow\sigma^\mu}^{\mu\mathbf{G}}(\mathbf{k}) \frac{\partial}{\partial r} \frac{\partial}{\partial \epsilon} u_{l\uparrow}^{\sigma^\mu}(r) \\ A_{L\downarrow\sigma^\mu}^{\mu\mathbf{G}}(\mathbf{k}) \frac{\partial}{\partial r} u_{l\downarrow}^{\sigma^\mu}(r) + B_{L\downarrow\sigma^\mu}^{\mu\mathbf{G}}(\mathbf{k}) \frac{\partial}{\partial r} \frac{\partial}{\partial \epsilon} u_{l\downarrow}^{\sigma^\mu}(r) \end{array} \right) \Big|_{\partial\text{MT}^\mu} Y_L(\hat{\mathbf{r}}) \quad (4.32) \end{aligned}$$

The A and B coefficients for muffin-tin μ in the non-collinear description can be calculated from expressions known from collinear calculations (Eqn. (4.14)) by including the rotation matrices \mathbf{U}_μ

$$A_{L\uparrow\sigma^\mu}^{\mu\mathbf{G}}(\mathbf{k}) = \chi_\uparrow^{gT} \mathbf{U}_\mu \chi_\uparrow^g A_{L\uparrow}^{\mathbf{G}}(\mathbf{k}) \quad (4.33)$$

$$B_{L\uparrow\sigma^\mu}^{\mu\mathbf{G}}(\mathbf{k}) = \chi_\uparrow^{gT} \mathbf{U}_\mu \chi_\uparrow^g B_{L\uparrow}^{\mathbf{G}}(\mathbf{k}) \quad (4.34)$$

$$A_{L\downarrow\sigma^\mu}^{\mu\mathbf{G}}(\mathbf{k}) = \chi_{\downarrow g}^T \mathbf{U}_\mu \chi_{\downarrow}^g A_{L\downarrow}^{\mathbf{G}}(\mathbf{k}) \quad (4.35)$$

$$B_{L\downarrow\sigma^\mu}^{\mu\mathbf{G}}(\mathbf{k}) = \chi_{\downarrow g}^{gT} \mathbf{U}_\mu \chi_{\downarrow}^g B_{L\downarrow}^{\mathbf{G}}(\mathbf{k}) \quad (4.36)$$

Given a general magnetic problem, the resulting solutions of the non-collinear Kohn-Sham equations are two-component spinors $\psi_{\mathbf{G}}(\mathbf{r}, \mathbf{k})$. The resulting particle density $n(\mathbf{r})$ and a scalar magnetization density $m(\mathbf{r})$ pointing into the local spin quantization axis can now be calculated, following Eqn. (3.38) to Eqn. (3.40) in chapter 3.4.

4.8 Relativistic Description

For a high precision description of the electronic structure, it is necessary to include relativistic effects since core and valence states can reach high kinetic energies, especially in the vicinity of the atomic nuclei. The importance of relativistic effects, like

the spin-orbit coupling (SOC) and the mass-velocity- and Darwin-terms, rises for heavier elements because of the higher core charge Z and the resulting steeper potential and higher kinetic energies. For heavier elements the spin density functional theory has to be extended to the relativistic density functional theory, resulting in single-particle Dirac-equation-like Kohn-Sham equations [122] (cf. chapter 3.4)

$$\{c\boldsymbol{\alpha} \cdot \hat{\mathbf{p}} + (\boldsymbol{\beta} - \mathbf{I})mc^2 + V_{\text{eff}}(\mathbf{r}) + \boldsymbol{\sigma} \cdot \mathbf{B}_{\text{eff}}(\mathbf{r})\}\Psi = \epsilon\Psi \quad (4.37)$$

with the velocity of light c , the electron mass m ,

$$\boldsymbol{\alpha} = \begin{pmatrix} 0 & \boldsymbol{\sigma} \\ \boldsymbol{\sigma} & 0 \end{pmatrix}$$

including the vector of Pauli matrices $\boldsymbol{\sigma} = (\underline{\sigma}_x, \underline{\sigma}_y, \underline{\sigma}_z)^T$ (for definition see chapter 3.4) and

$$\boldsymbol{\beta} = \begin{pmatrix} \mathbf{I}_2 & 0 \\ 0 & -\mathbf{I}_2 \end{pmatrix}$$

the 2×2 unity matrices \mathbf{I}_2 . The solution of this equation is a relativistic four-component wave function Ψ . In the fully-relativistic approach the Dirac equation is solved by expressing the spinor Ψ within the chosen basis set (section 4.4). While in principal necessary, this approach is extremely time-consuming, increasing the computational time needed e.g. for diagonalization by a factor of 64.

The Scalar-Relativistic Approximation and SOC

For lighter elements usually the so-called scalar-relativistic (SR) approximation is commonly used [123]. In this approximation the spin-orbit term is neglected and the spin and spatial coordinates become decoupled. This reduced the Hamiltonian matrix to two decoupled parts of half the size, which can be solved independently. Compared with the fully relativistic approach the SR approximation saves a factor of four of computational time. In the FLEUR-code [63] the wave functions of the muffin-tins are treated scalar-relativistically due to the typically higher kinetic energies, while interstitial and possible vacuum regions are treated non-relativistically. The relativistic radial functions are solved in the muffin-tin spheres, based on the Kohn-Sham-Dirac equations and only the large component of Ψ is matched to the non-relativistic wavefunctions at the MT-IR boundary, because the small component is already negligible at this distance from the nucleus. However, the small component is attached to the large component, and cannot be varied independently. This is a very sensible approximation, since inside the muffin-tin sphere the large component is still much bigger than the small component and plays a more important role and the two components are determined by solving the scalar relativistic equations³.

³Since the Kohn-Sham-Dirac equations do not *fundamentally* change the FLAPW method, this further complication is neglected.

Spin-orbit coupling (SOC) can then be included self-consistently in second variation. In this case the (approximated) SOC operator

$$\hat{H}_{\text{SOC}} = v(r) \boldsymbol{\sigma} \cdot \hat{\mathbf{L}} \quad (4.38)$$

is introduced in the subspace of eigenstates obtained without SOC. Here, $\hat{\mathbf{L}}$ is the angular momentum operator and $v(r)$ is a spherically symmetric function. $v(r)$ depends on the gradient of the spherically symmetric average potential (it is therefore larger for higher core charges Z) and decays fast for increasing distance r from the nucleus. A detailed description of the method implemented in FLEUR can be found in [66].

As a result of spin-orbit coupling, the spin quantum number s and angular momentum quantum numbers L couple to the total angular momentum quantum number j and its projection on a quantization axis m_j . s or l are no independent quantum numbers any more and, thus, both spin directions are coupled. The details of this coupling depend on a global spin-quantization axis for spin-polarized systems, which determines the magnetization direction with respect to the crystal field, resulting in effects such as e.g. an anisotropy energy between distinct magnetic orientations. SOC is important for atoms with a large nuclear charge due to the typically high kinetic energies in the vicinity of the nucleus or in low-dimensional systems, such as one-dimensional nanojunctions, where the reduced symmetry results in a large magneto-crystalline anisotropy energy (MAE) as the orbital moments become more significant [124–126].

4.9 The Brillouin Zone Integration

Previously, the the generalized eigenvalue problem (section 4.1) has been introduced and can now be solved based on the FLAPW basis set on a mesh of \mathbf{k} -points. One important aspect of the Kohn-Sham equations solved within the generalized eigenvalue description is that the equations can be solved independently for each \mathbf{k} -point. The electron density and any other quantity of a periodic crystal are depending on a summation over all \mathbf{k} and all occupied states:

$$n_{\sigma}(\mathbf{r}) = \sum_{i=1}^N \sum_{\mathbf{k}} |\psi_{\mathbf{G}\sigma}(\mathbf{r}, \mathbf{k})| \quad (4.39)$$

However, it is quite important to restrict calculations to few \mathbf{k} -points, since each corresponds to the set-up and the diagonalization of one eigenvalue problem. There are many methods to obtain optimal \mathbf{k} -point meshes for two or three dimensional structures such as the ones developed by Chadi-Cohen [127] or by Monkhorst-Pack [128]. For the one-dimensional systems focused on in this work, equidistant meshes along the direction of periodicity in the irreducibly part of the Brillouin zone are usually sufficient.

5 Wannier Functions

Wannier functions, first introduced by Wannier 1937 [61], can be seen as the Fourier transforms of a Bloch basis set, as e.g. provided by FLAPW (chapter 4). Bloch functions are the eigenfunctions of both the Hamiltonian and lattice translation operators and intrinsically delocalized. FLAPW Bloch functions do not provide a very efficient framework to study e.g. quantum transport within the previously introduced NEGF approach (chapter 2), due to their lack of localization and the typically rather large number of FLAPWs. However, the FLAPW method is among the most precise DFT implementations. One way to map the FLAPW electronic structure on a mathematically equivalent minimal and localized basis set are WFs. Similar to the δ -Function, that is the Fourier transform of a plane wave, the idea is to perform a unitary Fourier-type transformation back to real space and thus obtain a localized tight-binding like description within FLAPW.

This claim is not easily fulfilled, since Wannier functions are not defined uniquely due to an arbitrary phase factor applicable to any Bloch state. This phase factor strongly influences i.e. the localization properties of the Wannier functions, making it very difficult to achieve WFs with consistent spatial localization. What first seems as a serious draw-back can be used to uniquely define Wannier functions by imposing additional constraints, e.g. requiring maximal spatial localization, resulting into maximally localized Wannier functions (MLWFs) as proposed by Mazari and Vanderbilt [62]. MLWFs are one of the most popular approaches nowadays due to being mostly real, at least for collinear systems without spin-orbit coupling (SOC), and being optimally localized. Additionally, they provide a basis set of minimal size that maintains the accuracy of the underlying FLAPW electronic structure. MLWFs provide great insight into the aspect of localization of electrons in periodic potentials and are commonly used e.g. in modern theory of polarization [129–131], based on the displacement of the centers of MLWFs, bonding properties in disordered systems [132] or local correlations [133–135].

First-shot Wannier functions (FSWFs), based on projections of localized trial orbitals on the FLAPWs [68], are another, computationally less demanding approach to obtain WFs and typically serve as starting point for the MLWFs localization procedure. However, FSWFs are in contrast to MLWFs non-unique due to their strong dependence on the initial choice of the trial orbitals. Reasonable choices of trial orbital can still maintain the accuracy of FLAPW and most of the characteristics of MLWFs.

Recent experimental studies sparked interest on the transport properties of com-

plex electronic or magnetic systems, including effects such as e.g. spin-orbit coupling [14] or non-collinear spin-structures [18]. MLWFs or FSWFs obtained within the FLAPW method are among the most accurate choices to study this challenging field within the NEGF Landauer transport formalism including SOC [79] or non-collinear spin structures [80].

5.1 Maximally Localized Wannier Functions (MLWFs)

Wannier functions can be easily defined for a single isolated band, which does not become degenerate with any other band at any \mathbf{k} -point,

$$|W_{\mathbf{R}}\rangle = \frac{1}{\mathcal{N}} \sum_{\mathbf{k}} e^{-i\mathbf{k}\cdot\mathbf{R}} |\psi_{\mathbf{k}}\rangle \quad (5.1)$$

where \mathbf{R} is a lattice vector specifying the WFs unit cell and the Bloch functions $|\psi_{\mathbf{k}}\rangle$ are normalized with respect to the unit cell. The sum is performed over a uniform mesh of \mathcal{N} \mathbf{k} -point in the Brillouin zone. The $|W_{\mathbf{R}}\rangle$ constitute an orthonormal basis set:

$$\begin{aligned} \langle \psi_{\mathbf{k}} | \psi_{\mathbf{k}'} \rangle &= \mathcal{N} \delta_{\mathbf{k}, \mathbf{k}'} \\ \langle W_{\mathbf{R}} | W_{\mathbf{R}'} \rangle &= \delta_{\mathbf{R}, \mathbf{R}'} \end{aligned} \quad (5.2)$$

As mentioned before, the Wannier functions are not uniquely defined by Eqn. (5.1). For any given basis set there can be a \mathbf{k} -point dependent phase factor $\phi(\mathbf{k})$

$$|W_{\mathbf{R}}\rangle' = \frac{1}{\mathcal{N}} \sum_{\mathbf{k}} e^{-i\mathbf{k}\cdot\mathbf{R}} e^{i\phi(\mathbf{k})} |\psi_{\mathbf{k}}\rangle \quad (5.3)$$

resulting different sets of Wannier functions that can differ dramatically from each other, e.g. by their localization properties.

For a further use with minimal computational expense, e.g. by using a Wannier representation based tight-binding like Hamiltonian (see section 5.5) for the NEGF transport method used in this thesis (chapter 2), a unique definition of rapidly decaying WFs is desirable. In this case only few overlap matrix elements between the WFs have to be considered, resulting overall in a computationally inexpensive treatment (see chapter 6). One way to obtain such WFs is to require, in addition to Eqn. (5.1), maximal spatial localization, resulting into maximally localized Wannier functions (MLWFs) [62]. It has been shown that MLWFs are mostly real-valued¹, and possess optimal exponential decay properties and the maximal symmetry of the system [62].

¹The real-valuedness cannot always be preserved for more complex systems, such as those including SOC or non-collinear magnetism.

Before discussing the process of maximally localizing WFs, a more general formulation than Eqn. (5.1) has to be found that can be applied to e.g. metallic systems. The electronic structure of a transition metal monowire typically provides a group of non-isolated bands, thus becoming degenerate at certain \mathbf{k} -points. This increases the freedom of defining WFs further as bands may be mixed at every \mathbf{k} -point by the transformations $U_{mn}^{(\mathbf{k})}$,

$$|W_{\mathbf{R}n}\rangle = \frac{1}{N} \sum_{\mathbf{k}} e^{-i\mathbf{k}\cdot\mathbf{R}} \sum_{m=1}^M U_{mn}^{(\mathbf{k})} |\psi_{m\mathbf{k}}\rangle \quad (5.4)$$

where m is the band index of the Bloch state and n is the index of the Wannier function. The number of Bands M has to be larger or equal than the number of Wannier functions N . Maximally localizing the Wannier functions imposes a constraint on the set of $U_{mn}^{(\mathbf{k})}$ -matrices, that defines the MLWFs uniquely up to an arbitrary global phase [62]. The $U_{mn}^{(\mathbf{k})}$ -matrices are unitary in case of $M = N$ for an isolated group of bands and thus the correspondence between Bloch state and Wannier function eigenvalue spectra is exact. Many systems of interest, especially metallic systems, do not fulfill this requirement.

In this case the number of bands typically varies at each \mathbf{k} -point in a fixed energy interval and the bands have to be disentangled [136] to obtain an optimal subspace of energy bands $M = N$. Note, that the energy bands of this optimal subspace may not correspond to any of the original energy bands due to a mixing between states. However, bands can be included unchanged into the optimal subspace in an inner 'frozen energy window', as long as the number of bands in this window M_{frozen} does not exceed the number of Wannier functions N . Hence, the exact correspondence between the energy spectra of FLAPW and WFs can always be achieved, given a sufficiently large number N of WFs (cf. section 5.5).

The localization properties of a set of WFs can be expressed by their spread, which is defined as the sum over their expectation values second momenta:

$$\Omega = \sum_n |\langle \mathbf{r}^2 \rangle_n - (\langle \mathbf{r} \rangle_n)^2| \quad (5.5)$$

The spread describes the mean positional expectation value of electrons, minimizing the spread of a set of Wannier functions therefore localizes them. Wannier functions with the minimal spread are called maximally localized Wannier functions.

Marzari and Vanderbilt first proposed an efficient method to minimize the spread defined by Eqn. (5.5) for isolated and entangles groups of bands [62, 136]. The localization procedure of the FLEUR-code [63] uses the publicly available Wannier90-code [137]. Following the algorithm of Mazari and Vanderbilt, two quantities have to be obtained for the calculation of MLWFs: First, as a starting point, the projections of the Bloch functions on localized orbitals $|g_n\rangle$

$$A_{mn}^{(\mathbf{k})} = \langle \psi_{m\mathbf{k}} | g_n \rangle \quad (5.6)$$

and, secondly, for the iterative process that leads to MLWFs, the overlaps between the lattice-periodic parts $|u_{m\mathbf{k}}\rangle$

$$u_{m\mathbf{k}}(\mathbf{r}) = e^{-i(\mathbf{k}\cdot\mathbf{r})} \psi_{m\mathbf{k}}(\mathbf{r}) \quad (5.7)$$

between neighboring \mathbf{k} -points, \mathbf{k} and $\mathbf{k} + \mathbf{b}$:

$$M_{mn}^{(\mathbf{k},\mathbf{b})} = \langle u_{m\mathbf{k}} | u_{n\mathbf{k}+\mathbf{b}} \rangle \quad (5.8)$$

Based on the initial overlap matrices $M_{mn}^{(\mathbf{k},\mathbf{b})}$, the second momenta (Eqn. (5.5)) can be expressed as [62]

$$\begin{aligned} \langle \mathbf{r} \rangle_n &= -\frac{1}{N} \sum_{\mathbf{k},\mathbf{b}} w_{\mathbf{b}} \text{Im} \tilde{M}_{mn}^{(\mathbf{k},\mathbf{b})} \\ \langle \mathbf{r}^2 \rangle_n &= \frac{1}{N} \sum_{\mathbf{k},\mathbf{b}} w_{\mathbf{b}} \left[1 - |\tilde{M}_{mn}^{(\mathbf{k},\mathbf{b})}|^2 + (\text{Im} \tilde{M}_{mn}^{(\mathbf{k},\mathbf{b})})^2 \right] \end{aligned} \quad (5.9)$$

in every iteration step, where $w_{\mathbf{b}}$ is the weighting factor of \mathbf{b} . Eqn. (5.9) is only valid for uniform \mathbf{k} -point meshes. The weights $w_{\mathbf{b}}$ can be calculated from the continuity equations for $\langle \mathbf{r} \rangle_n$ and $\langle \mathbf{r}^2 \rangle_n$ by finite differences [62]. $\tilde{M}_{mn}^{(\mathbf{k},\mathbf{b})}$

$$\tilde{M}_{mn}^{(\mathbf{k},\mathbf{b})} = \sum_{m_1 m_2} (U_{m_1 m}^{(\mathbf{k})})^\dagger U_{m m_2}^{(\mathbf{k}+\mathbf{b})} M_{mn}^{(\mathbf{k},\mathbf{b})}. \quad (5.10)$$

is related to the initial $M_{mn}^{(\mathbf{k},\mathbf{b})}$ matrix by its $U_{mn}^{(\mathbf{k})}$ matrices, used to define a set of Wannier functions in Eqn. (5.4). For the iterative process of localization, $A_{mn}^{(\mathbf{k})}$ and $M_{mn}^{(\mathbf{k},\mathbf{b})}$ have to be calculated only once from the electronic structure, while the $U_{mn}^{(\mathbf{k})}$ are updated for every iteration step. The algorithm of the localization procedure [62] refines the $U_{mn}^{(\mathbf{k})}$ -matrices until the minimal spread and hence the MLWFs are found. The spread can be calculated by Eqn. (5.9) and Eqn. (5.5) for every iteration step and display the convergence behavior.

5.2 First-Shot Wannier Functions (FSWFs)

As discussed before, the localization process requires a starting point based on a Bloch function description given by the matrices $A_{mn}^{(\mathbf{k})}$ (cf. Eqn. (5.6)). $A_{mn}^{(\mathbf{k})}$ is obtained by projecting the Bloch functions $|\psi_{m\mathbf{k}}\rangle$ on a set of localized trial orbitals $|g_n\rangle$:

$$|\phi_{n\mathbf{k}}\rangle = \sum_m |\psi_{m\mathbf{k}}\rangle \langle \psi_{m\mathbf{k}} | g_n \rangle \quad (5.11)$$

The resulting $|\phi_{n\mathbf{k}}\rangle$ are not necessarily orthogonal, it is convenient to rewrite them into orthonormal form:

$$|\tilde{\psi}_{n\mathbf{k}}\rangle = \sum_m ((\mathbf{S}^{(\mathbf{k})})^{-\frac{1}{2}} |\phi_{m\mathbf{k}}\rangle \quad (5.12)$$

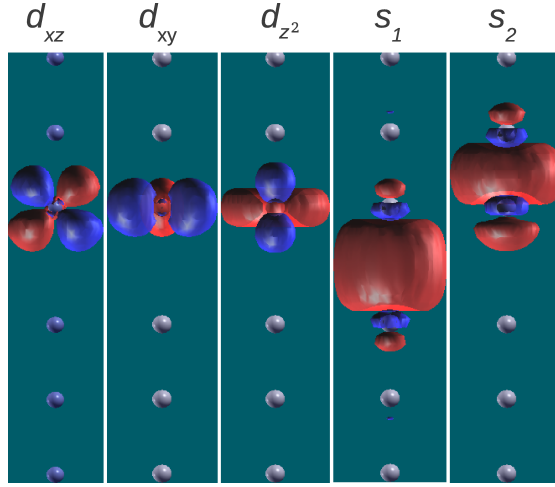


Figure 5.1: MLWFs for a Pt monowire with a stretched central bond, based on FSWFs constructed from d_{xz} -, d_{xy} -, d_{z^2} -, and s -trial orbitals. s_1 is centered on the stretched bond and s_2 on one bond in the wire. Image taken from [138]

with the overlap matrix $S_{mn}^{(\mathbf{k})} = \langle \phi_{m\mathbf{k}} | \phi_{n\mathbf{k}} \rangle$. The orthonormalized $|\tilde{\psi}_{n\mathbf{k}}\rangle$ can now be used to construct Wannier functions by applying Eqn. (5.1), the so-called first-shot Wannier functions (FSWFs):

$$|W_{\mathbf{R}n}\rangle = \frac{1}{\mathcal{N}} \sum_{\mathbf{k}} e^{-i\mathbf{k}\cdot\mathbf{R}} |\tilde{\psi}_{n\mathbf{k}}\rangle \quad (5.13)$$

FSWFs strongly depend on the initial choice of trial orbitals $|g_n\rangle$. Convenient choices of initial localized basis sets are e.g. Gaussians [62], the radial parts of hydrogen wave functions or the solution of the scalar relativistic equations of the radial symmetric FLAPW potential in the muffin-tins [68] (cf. chapter 4.5).

FSWFs constitute a legitimate set of Wannier functions and can be already very suitable to describe the electronic structure based on WFs, given a set of trial orbitals tailored to e.g. the symmetries of a specific system, which is done by restricting the localized trial orbitals $|g_n\rangle$ to functions of defined angular character. For example, the electrons of the valence and conduction bands of transition metal monowires can be described by one s - and five d -orbitals per spin and atom. To account for the cylindrical symmetry of such a monowire, the d -orbitals are chosen to be d_{xz} - and d_{yz} - orbitals (Δ_3 -symmetry), d_{xy} - and $d_{x^2-y^2}$ -orbitals (Δ_4 -symmetry) and d_{z^2} -orbitals ($s - d_{z^2} : \Delta_1$ -symmetry).

In Figure 5.1, the typical shape of such orbitals (d_{xz} , d_{xy} and d_{z^2}) is displayed for a Pt monowire with a stretched central bond (discussed in chapter 6.6). Note, that the shape of FSWFs Δ_1 -orbitals would differ significantly, since the s -orbitals are typically (but not necessarily) centered on the atoms (cf. chapter 6.6.1). Within this approach it is also possible to construct hybrid trial orbitals, such as e.g. sp^2 -

(i.e. for graphene) or sp^3 - (i.e. for diamond lattices) orbitals.

In addition, since FSWFs serve as the starting point to obtain MLWFs, such an adapted initial choice of localized basis functions can help to significantly improve the localization procedure. Although MLWFs are in principle unique, it is still possible to reach only a local minimum of spread, which can be prohibited by choosing the trial orbitals optimally.

5.3 Constructing FSWFs within the FLAPW Method

FSWFs have been defined for an arbitrary set of Bloch functions by Eqn. (5.6), Eqn. (5.12) and Eqn. (5.13). The aim is now to construct FSWFs from the FLAPW basis set. The central quantity to determine FSWFs is the $A_{mn}^{(\mathbf{k})}$ -matrix (Eqn. (5.6)), describing the projections on the localized trial functions $|g_n\rangle$. To obtain the matrix within FLAPW, the $|g_n\rangle$ are expressed by radial functions centered in a muffin-tin sphere μ :

$$g_n(\mathbf{r}) = \sum_L c_{nL} \tilde{u}_{nl}(r) Y_L(\hat{\mathbf{r}}) \quad (5.14)$$

Here, L runs over the orbital and angular quantum numbers, c_{nL} are the expansion coefficients depending on the trial function and their angular behavior, the $\tilde{u}_{nl}(r)$ are radial functions and $Y_L(\hat{\mathbf{r}})$ are spherical harmonics, denoted relative to the coordinate of the atomic center \mathbf{r}_μ .

For an arbitrary radial part $\tilde{u}_{nl}(r)$ the projection of the localized trial orbital $|g_n\rangle$ onto the FLAPW basis functions in the muffin-tin μ (cf. Eqn. (4.13) in chapter 4.4)

$$\psi_{m\mathbf{k}}(\mathbf{r})|_{\text{MT}^\mu} = \sum_L \left(A_{mL}^\mu(\mathbf{k}) u_{ml}^\mu(r) Y_L(\hat{\mathbf{r}}) + B_{mL}^\mu(\mathbf{k}) \frac{\partial}{\partial \epsilon} u_{ml}^\mu(r) Y_L(\hat{\mathbf{r}}) \right) \quad (5.15)$$

is obtained from Eqn. (5.6) and Eqn. (5.14),

$$\begin{aligned} A_{mn}^{(\mathbf{k})} = \sum_L c_{nL} \{ & (A_{mL}^\mu(\mathbf{k}))^* \int dr u_{ml}(r) \tilde{u}_{nl}(r) r^2 \\ & + (B_{mL}^\mu(\mathbf{k}))^* \int dr \frac{\partial}{\partial \epsilon} u_{ml}^\mu(r) \tilde{u}_{nl}(r) r^2 \} \end{aligned} \quad (5.16)$$

where the $A_{mL}^\mu(\mathbf{k})$ and $B_{mL}^\mu(\mathbf{k})$ are the expansion coefficients of the FLAPW basis set in the muffin-tin sphere μ and \mathbf{k} denotes a wave vector moved into the first Brillouin zone by a reciprocal lattice vector $\mathbf{G}(\mathbf{k}')$: $\mathbf{k} = \mathbf{k}' - \mathbf{G}(\mathbf{k}')$.

A convenient choice of the radial part of the trial function is $\tilde{u}_{nl}(r) = u_{nl}^\mu(r)$, where $u_{nl}^\mu(r)$ is the solution of the scalar relativistic equations of the radial symmetric FLAPW potential at the band energy for which the FSWFs is constructed.

Eqn. (5.16) can be further simplified due to the orthonormalization of $u_{nl}^\mu(r)$ and $\frac{\partial}{\partial \epsilon} u_{nl}^\mu(r)$ (cf. chapter 4.4, Eqn. (4.15) and Eqn. (4.16)):

$$A_{mn}^{(\mathbf{k})} = \langle \psi_{m\mathbf{k}} | g_n \rangle = \sum_L c_{nL} (A_{mL}^\mu(\mathbf{k}))^* \quad (5.17)$$

There are more sophisticated ways to construct FSWFs, i.e. by constructing them as a linear combination of two localized orbitals originating from different muffin-tin spheres to describe a bond [68]. This can be useful to describe s -orbitals to be rather centered on a bond and not on an atom, which can help speed up the localization procedure for MLWFs in some cases. However, trial orbitals centered on the atoms (Eqn. (5.17)) are often very suitable to obtain MLWFs or to precisely describe the electronic structure of transition metal wires in practice (see e.g. chapter 6.6.1).

5.4 Constructing MLWFs within the FLAPW Method

For the calculation of MLWFs, the most important quantity is the $M_{mn}^{(\mathbf{k},\mathbf{b})}$ -matrix (Eqn. (5.8)), which includes all important information about the spreads and WF's centers (Eqn. (5.5) and Eqn. (5.9)). The $M_{mn}^{(\mathbf{k},\mathbf{b})}$ -matrix is defined by the overlap between the lattice periodic part $u_{m\mathbf{k}}(\mathbf{r})$, related to a Bloch function by $u_{m\mathbf{k}}(\mathbf{r}) = \exp -i(\mathbf{k} \cdot \mathbf{r}) \psi_{m\mathbf{k}}(\mathbf{r})$ (Eqn. (5.7)), on the nearest neighbor \mathbf{k} -points \mathbf{k} and $\mathbf{k} + \mathbf{b}$:

$$M_{mn}^{(\mathbf{k},\mathbf{b})} = \int d^3r e^{i\mathbf{b} \cdot \mathbf{r}} \psi_{m\mathbf{k}}^*(\mathbf{r}) \psi_{n[\mathbf{k}+\mathbf{b}]_{\text{BZ}}}(\mathbf{r}) \quad (5.18)$$

Here, $[\mathbf{k} + \mathbf{b}]_{\text{BZ}}$ denotes that $\mathbf{k} + \mathbf{b}$ is shifted to the first Brillouin zone by a reciprocal lattice vector $\mathbf{G}(\mathbf{k})$. Since space is divided into interstitial region and muffin-tins by the FLAPW method (see chapter 4.5), $M_{mn}^{(\mathbf{k},\mathbf{b})}$ has to be calculated separately in both regions:

$$M_{mn}^{(\mathbf{k},\mathbf{b})} = M_{mn}^{(\mathbf{k},\mathbf{b})}|_{\text{IR}} + \sum_{\mu} M_{mn}^{(\mathbf{k},\mathbf{b})}|_{\text{MT}^{\mu}} \quad (5.19)$$

In case of a one-dimensional description an additional vacuum region (cf. chapter 4.6) contribution has to be added to Eqn. (5.19) (cf. section 5.4). In the muffin-tins the FLAPW basis functions are expanded into the radial basis functions $u_l(r)$, its energy derivative $\frac{\partial}{\partial \epsilon} u_l^\mu(r)$ and spherical harmonics $Y_L(\hat{\mathbf{r}})$ (cf. Eqn. (5.15)), $M_{mn}^{(\mathbf{k},\mathbf{b})}|_{\text{MT}}^\mu$

can be determined based on these quantities [68],

$$\begin{aligned}
 M_{mn}^{(\mathbf{k}+\mathbf{b})}|_{\text{MT}^\mu} = 4\pi e^{-i\mathbf{b}\mathbf{r}_\mu} \sum_{L,L'} & [(A_{mL}^\mu(\mathbf{k}))^* A_{nL'}^\mu([\mathbf{k}+\mathbf{b}]_{\text{BZ}}) t_{11}^\mu(\mathbf{b}, L, L') \\
 & + (A_{mL}^\mu(\mathbf{k}))^* B_{nL'}^\mu([\mathbf{k}+\mathbf{b}]_{\text{BZ}}) t_{12}^\mu(\mathbf{b}, L, L') \\
 & + (B_{mL}^\mu(\mathbf{k}))^* A_{nL'}^\mu([\mathbf{k}+\mathbf{b}]_{\text{BZ}}) t_{21}^\mu(\mathbf{b}, L, L') \\
 & + (B_{mL}^\mu(\mathbf{k}))^* B_{nL'}^\mu([\mathbf{k}+\mathbf{b}]_{\text{BZ}}) t_{22}^\mu(\mathbf{b}, L, L')]
 \end{aligned} \tag{5.20}$$

where \mathbf{r}_μ is the center of the muffin-tin sphere μ and L runs over the the orbital and angular quantum numbers. Explicit integral expressions for the matrix elements $t_{11}^\mu(\mathbf{b}, L'', L)$ and $t_{12}^\mu(\mathbf{b}, L'', L)$ including Gaunt coefficients can be found in [68].

The contribution for the interstitial region to the $M_{mn}^{(\mathbf{k},\mathbf{b})}$ -matrix, expanded in plane waves (cf. 4.4 and 4.6), can be determined as (cf. Eqn. (5.18)) [68]:

$$\begin{aligned}
 M_{mn}^{(\mathbf{k}+\mathbf{b})}|_{\text{IR}} = \frac{1}{\Omega} \sum_{\mathbf{G},\mathbf{G}'} & (c_{\mathbf{k}m}(\mathbf{G}))^* c_{[\mathbf{k}+\mathbf{b}]_{\text{BZ}}n}(\mathbf{G}') \\
 & \times \int d^3r e^{i([\mathbf{k}+\mathbf{b}]_{\text{BZ}}n+\mathbf{G}')\mathbf{r}} e^{-i(\mathbf{k}+\mathbf{G})\mathbf{r}} e^{i\mathbf{b}\cdot\mathbf{r}}
 \end{aligned} \tag{5.21}$$

The integration is performed over the interstitial region only by introducing a step function $\Theta(\mathbf{r})$, that cuts out the muffin-tin spheres, and its Fourier transform $\Theta_{\mathbf{G}}$, resulting into the final form of Eqn. (5.21),

$$M_{mn}^{(\mathbf{k}+\mathbf{b})}|_{\text{IR}} = \sum_{\mathbf{G},\mathbf{G}'} (c_{\mathbf{k}m}(\mathbf{G}))^* c_{[\mathbf{k}+\mathbf{b}]_{\text{BZ}}n}(\mathbf{G}') \Theta_{\mathbf{G}(\mathbf{k}+\mathbf{b})+\mathbf{G}-\mathbf{G}'} \tag{5.22}$$

where $\mathbf{G}(\mathbf{k}+\mathbf{b})$ is the reciprocal vector, that moves $\mathbf{k}+\mathbf{b}$ into the first Brillouin zone.

$M_{mn}^{(\mathbf{k},\mathbf{b})}$ for One-Dimensional FLAPW Calculations

As described in chapter 4.6 for one-dimensional FLAPW calculations, an additional vacuum region (VR) region is introduced outside of a cylinder with a radius $D_{\text{vac}}/2$ around the central z -axis. In this region the wave functions are described by exponentially decaying functions. Starting from the vacuum FLAPW functions (Eqn. (4.25)) and expressing plane waves in cylindrical coordinates ($\mathbf{r} = (z, r, \phi)$), the overlap matrix $M_{mn}^{(\mathbf{k},\mathbf{b})}|_{\text{VR}}$ can be determined similar to Eqn. (5.19) and

Eqn. (5.21) for the vacuum region by Eqn. (5.18) [68]:

$$\begin{aligned}
 M_{mn}^{(\mathbf{k}, \mathbf{b})}|_{\text{VR}} = & \sum_{\mathbf{G}, \mathbf{G}'} \sum_{p, p'} \int_{\text{VR}} d^3r e^{i(\mathbf{G}' - \mathbf{G}_z - \mathbf{G}_z(k_z + \mathbf{b}))} \\
 & \times e^{-i\mathbf{G}_{\parallel}(k_z + \mathbf{b})\mathbf{r}_{\parallel}} e^{i(p' - p)\phi} \Psi_{pp'G_z'}^{mnG_z}(k_z, [k_z + \mathbf{b}]_{\text{BZ}}, r)
 \end{aligned} \tag{5.23}$$

The function Ψ is constructed from products of the the solution of the radial equation of the vacuum and its energy derivative u and $\frac{\partial}{\partial \epsilon} u$ for a k_z -vector and its neighbor $k_z + \mathbf{b}$, where \mathbf{b} is not necessarily situated on the z -axis. Hence there can be a contribution in the plane perpendicular to the z -axis, denoted by a contribution belonging to a reciprocal space vector \mathbf{G}_{\parallel} and a positional vector \mathbf{r}_{\parallel} . p is an integer labeling a cylindrical angular harmonic needed for the construction of Eqn. (5.23) with help of the cylindrical Bessel functions J_p . In case of a one-dimensional FLAPW calculation the vacuum part $M_{mn}^{(\mathbf{k}, \mathbf{b})}|_{\text{VR}}$ Eqn. (5.23) has to be added to obtain the total overlap matrix $M_{mn}^{(\mathbf{k}, \mathbf{b})}$ Eqn. (5.19):

$$M_{mn}^{(\mathbf{k}, \mathbf{b})} = M_{mn}^{(\mathbf{k}, \mathbf{b})}|_{\text{IR}} + \sum_{\mu} M_{mn}^{(\mathbf{k}, \mathbf{b})}|_{\text{MT}^{\mu}} + M_{mn}^{(\mathbf{k}, \mathbf{b})}|_{\text{VR}} \tag{5.24}$$

5.5 The Wannier Representation of the FLAPW Hamiltonian

In this section, it is demonstrated, how a FLAPW electronic structure calculation (chapter 4) is mapped on a a tight-binding like Hamiltonian within Wannier representation. FSWFs and MLWFs can be obtained based on FLAPW basis functions, including the one-dimensional FLAPW geometry, based on the quantities derived in section 5.3 and 5.4. Each set of Wannier functions $|W_{n\mathbf{R}}\rangle$ is defined by its $U_{mn}^{(\mathbf{k})}$ -matrices (Eqn. (5.4)), provided by the `Wannier90`-code [137].

Written in terms of FLAPW basis functions $|\psi_{\mathbf{k}m}\rangle$, the Hamiltonian \hat{H}_{FLAPW} assumes the diagonal form

$$\hat{H}_{\text{FLAPW}} = \frac{1}{\mathcal{N}} \sum_{\mathbf{k}, m} \epsilon_m(\mathbf{k}) |\psi_{\mathbf{k}m}\rangle \langle \psi_{\mathbf{k}m}| \tag{5.25}$$

where the $\epsilon_m(\mathbf{k})$ are the eigenvalues of \hat{H}_{FLAPW} and \mathcal{N} is the number of \mathbf{k} -points. If the number of bands is equal to the number of WFs, the $U_{mn}^{(\mathbf{k})}$ -matrices in Eqn. (5.4) will be unitary. In this case Eqn. (5.4) and Eqn. (5.25) are resulting in

$$\hat{H}_{\text{WFs}} = \sum_{n\mathbf{R}_1} \sum_{n'\mathbf{R}_2} H_{n, n'}(\mathbf{R}_1 - \mathbf{R}_2) |W_{n\mathbf{R}_1}\rangle \langle W_{n'\mathbf{R}_2}| \tag{5.26}$$

which is, due to the being related by a unitary transformation, a mathematically equivalent formulation, e.g. with identical energy eigenvalue spectra. This equivalence still holds for states in the frozen energy window in case of disentanglement.

The hopping elements $H_{n,n'}(\mathbf{R}_1 - \mathbf{R}_2)$ between the Wannier orbitals n and n' at sites \mathbf{R}_1 and \mathbf{R}_2 are the central quantities obtained by a Wannier transformation and will later correspond to the matrix elements of the tight-binding like Hamiltonians in a quantum transport calculation (cf. chapter 6). The hopping elements quantify the hopping from Wannier orbital $|W_{n\mathbf{R}_1}\rangle$ to $|W_{n'\mathbf{R}_2}\rangle$:

$$H_{n,n'}(\mathbf{R}_1 - \mathbf{R}_2) = \langle W_{n\mathbf{R}_1} | \hat{H}_{\text{FLAPW}} | W_{n'\mathbf{R}_2} \rangle \quad (5.27)$$

By substituting Eqn. (5.25) into Eqn. (5.27),

$$H_{n,n'}(\mathbf{R}_1 - \mathbf{R}_2) = \frac{1}{\mathcal{N}} \sum_{m,\mathbf{k}} \epsilon_m(\mathbf{k}) \langle W_{n\mathbf{R}_1} | \psi_{m\mathbf{k}} \rangle \langle \psi_{m\mathbf{k}} | W_{n'\mathbf{R}_2} \rangle \quad (5.28)$$

and expressing $|W_{n\mathbf{R}_1}\rangle$ to $|W_{n'\mathbf{R}_2}\rangle$ by FLAPW functions and their $U_{mn}^{(\mathbf{k})}$ -matrices (Eqn. (5.4)), Eqn. (5.28) can be brought to its final form:

$$H_{n,n'}(\mathbf{R}_1 - \mathbf{R}_2) = \frac{1}{\mathcal{N}} \sum_{m,\mathbf{k}} \epsilon_m(\mathbf{k}) e^{i\mathbf{k}(\mathbf{R}_1 - \mathbf{R}_2)} (U_{mn}^{(\mathbf{k})})^* (U_{mn'}^{(\mathbf{k})}) \quad (5.29)$$

The Wannier representation can be used to interpolate a FLAPW band structure, given by the eigenvalues $\epsilon_m(\mathbf{k})$, as shown in Figure 5.3. For this interpolation, Eqn. (5.28) is evaluated at \mathbf{k} -points, which are not necessarily included in the FLAPW calculation, by Bloch-like functions,

$$|\tilde{\psi}_{m\mathbf{k}}\rangle = \frac{1}{\sqrt{\mathcal{N}}} \sum_{\mathbf{R}} e^{i\mathbf{k}\mathbf{R}} |W_{n\mathbf{R}}\rangle \quad (5.30)$$

resulting in the matrix elements $H_{nn'}^{(\mathbf{k})}$:

$$H_{nn'}^{(\mathbf{k})} = \frac{1}{\mathcal{N}} \sum_{\mathbf{R}_1, \mathbf{R}_2} H_{n,n'}(\mathbf{R}_1 - \mathbf{R}_2) e^{-i\mathbf{k}(\mathbf{R}_1 - \mathbf{R}_2)} = \sum_{\mathbf{R}} H_{n,n'}(\mathbf{R}) e^{-i\mathbf{k}\mathbf{R}} \quad (5.31)$$

Diagonalization of the matrix $\mathbf{H}^{(\mathbf{k})}$ yields to the interpolated eigenvalues $\epsilon(\mathbf{k})$.

In Figure 5.3 a comparison between a FLAPW bandstructure, its MLWFs representation and the interpolated bandstructure is given for a octahedral Pt wire (cf. Figure 5.2) with the in-chain unit cell size $d_z = 4.48$ bohr². Due to the presence of entangled bands the disentanglement procedure is applied in a frozen energy window including all occupied states up to the Fermi level. The correspondence between FLAPW and MLWFs representation is exact in the frozen energy window and even several meV above the Fermi level. Above the frozen energy window, both energy spectra are expectably not identical due to the mixed disentangled states. The quality of a Wannier function based interpolation of the bandstructure (Eqn. (5.31)) is

²1 bohr = $5.2917721092 \times 10^{-11}$ m (≈ 0.529 Å)

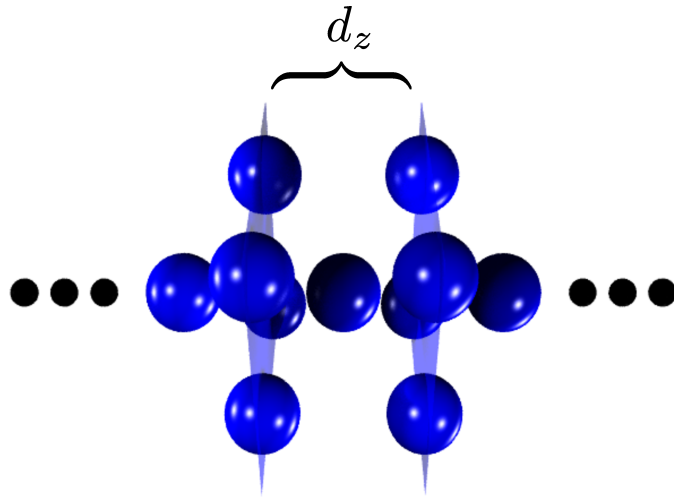


Figure 5.2:

Sketch of the unit cell, used for the bandstructure calculation of a Pt monowire with octahedral structure, with the in-chain unit cell size $d_z = 4.48$ bohr (Figure 5.3).

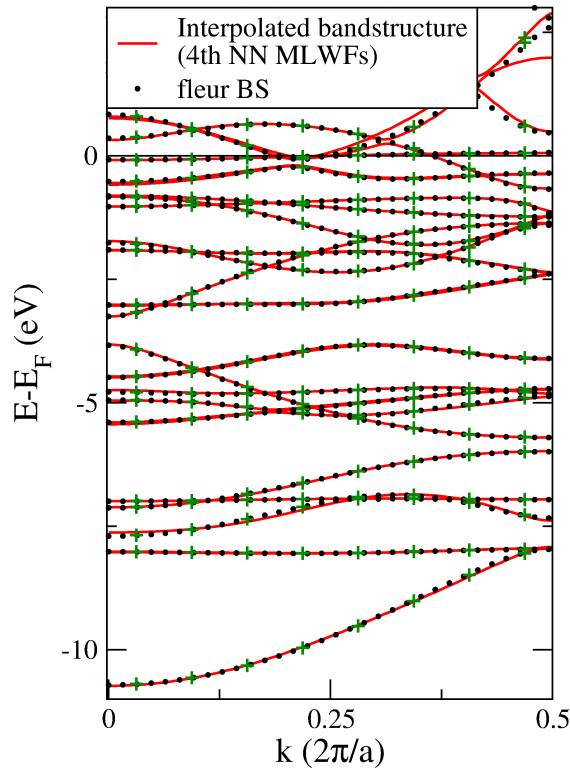


Figure 5.3:

Bandstructure of an octahedral Pt wire (see Figure 5.2), calculated with FLAPW (black dots) on a mesh of 32 k -points in the irreducible part of the Brillouin zone, The Wannier representation (green crosses) of the same calculation is based on MLWFs, determined on an equidistant mesh of 16 k -points in the whole BZ. The interpolation of the band structure (red lines) in 4th nearest neighbor (NN) is performed on a mesh of 161 k -points in the irreducible part of the Brillouin zone.

demonstrated for the frozen energy window on a very fine \mathbf{k} -point mesh (red lines) in Figure 5.3. The interpolation is very efficient compared to a full FLAPW calculation due to the rather small size of $\mathbf{H}^{(\mathbf{k})}$ and very precise if the \mathbf{k} -mesh, used to obtain the Wannier functions, is sufficiently fine. It additionally allows to evaluate \mathbf{k} -points, which were not captured by the FLAPW calculation and can additionally be used to e.g. calculate the Fermi surface. Similar interpolation schemes can be derived for operators other than the Hamiltonian [139–141].

5.6 FLAPW Wannier Functions for Systems with SOC

In case of spin-orbit coupling (SOC), the spin quantum number s and angular momentum quantum numbers L couple to the total angular momentum quantum numbers j and m_j (cf. chapter 4.8), s or l are no independent quantum numbers any more. As a consequence, there are interactions between both spin channels and the wave functions has to be described by a spinor with the two spin components $\psi_{\mathbf{k}m\sigma}$ ($\sigma = \uparrow, \downarrow$) [68]. The $A_{mn}^{(\mathbf{k})}$ -matrix can be calculated according to Eqn. (5.16) incorporating the coupled spin-channels [68]:

$$A_{mn}^{(\mathbf{k})} = \sum_L \sum_\sigma c_{nL\sigma} \times \left\{ (A_{mL\sigma}^\mu(\mathbf{k}))^* \int dr u_{l\sigma}^\mu(r) \tilde{u}_{l\sigma}(r) r^2 \right. \\ \left. + (B_{mL\sigma}^\mu(\mathbf{k}))^* \int dr \frac{\partial}{\partial \epsilon} u_{l\sigma}^\mu(r) \tilde{u}_{l\sigma}(r) r^2 \right\} \quad (5.32)$$

The $A_{mL\sigma}^\mu$ and $B_{mL\sigma}^\mu$ are the expansion coefficients of the FLAPW basis functions in the muffin-tin sphere μ . Localized orbitals $|g_n\rangle$ that are eigenstates of the projection of the spin operator onto the spin-quantization axis are a reasonable choice for weak to modest spin-orbit coupling. In this case $c_{nL\sigma}$ may only differ from zero for one spin component σ for any given n and each spin direction can be evaluated according to Eqn. (5.17). Choosing $\tilde{u}_{nl\sigma}(r) = u_{nl\sigma}^\mu(r)$ to be a solution of the radial symmetric FLAPW potential of the localized orbitals can further simplify this expression (cf. Eqn. (5.17)).

The $M_{mn}^{(\mathbf{k}, \mathbf{b})}$ -matrix can be obtained in accordance to Eqn. (5.18), including a summation over the coupled spin-directions:

$$M_{mn}^{(\mathbf{k}, \mathbf{b})} = \sum_\sigma \int d^3r e^{i\mathbf{b}\cdot\mathbf{r}} \psi_{m\mathbf{k}\sigma}^*(\mathbf{r}) \psi_{n[\mathbf{k}+\mathbf{b}]_{\text{BZ}}\sigma}(\mathbf{r}) \quad (5.33)$$

The spin index σ refers to the eigenstates of the projection of the spin-operator onto the spin quantization axis.

The Wannier representation of the Hamiltonian (see Eqn. (5.5)) has to be changed accordingly: Although Eqn. (5.26) remains valid, the SOC Wannier function $|\mathbf{W}_{\mathbf{R}}\rangle$

are two-component spinors. It is possible to additionally regard their projection onto the global spin-quantization axis:

$$|W_{\mathbf{R}\sigma}\rangle = |\sigma\rangle\langle\sigma|\mathbf{W}_{\mathbf{R}}\rangle \quad (5.34)$$

The hopping elements (Eqn. (5.28)) for SOC include interactions between both spin channels:

$$H_{nn'}^{\sigma\sigma'}(\mathbf{R}_1 - \mathbf{R}_2) = \frac{1}{\mathcal{N}} \sum_{m,\mathbf{k}} \epsilon_m(\mathbf{k}) \langle W_{\mathbf{R}_1 n \sigma} | \psi_{m\mathbf{k}} \rangle \langle \psi_{m\mathbf{k}} | W_{\mathbf{R}_2 n' \sigma'} \rangle \quad (5.35)$$

The corresponding real-space representation of the Hamiltonian for systems with SOC is now given analogously to Eqn. (5.26), including an additional summation over the spin channels:

$$\hat{H}_{\text{WFs}} = \sum_{n\mathbf{R}_1} \sum_{n'\mathbf{R}_2} \sum_{\sigma\sigma'} H_{n,n'}^{\sigma\sigma'}(\mathbf{R}_1 - \mathbf{R}_2) |W_{\mathbf{R}_1 n \sigma}\rangle \langle W_{\mathbf{R}_2 n' \sigma'}| \quad (5.36)$$

This representation of the Hamiltonian allows to further decompose it with respect to the two spin directions. Such a decomposition can provide additional insights into the spin-distribution of e.g. a conductance channel, helping to study SOC based effects significantly.

5.7 FLAPW Wannier Functions for Non-Collinear Spin-Structures

A novel way of using WFs is to extend them to general magnetic order within the FLAPW method [80] based on the description in chapter 4.7. A sketch of such a non-collinear spin structure with angles of 30° between the spin moments of adjacent atoms in a monowire geometry is shown in Figure 5.4. Within the FLAPW description of non-collinear magnetic order the spin moment is kept collinear in the muffin-tin spheres by introducing a local spin quantization axis σ^μ , pointing into the direction of the net spin moment. For non-collinear spin order, the local and the global quantization axis σ are not identical and the FLAPW basis functions are two-component spinors $\psi_{\mathbf{k}m}$ (see chapter 4.7, Eqn. (4.29)). The local quantization axes σ^μ can be rotated into the global frame with the unitary rotation matrices \mathbf{U}_μ^\dagger (chapter 4.7, Eqn. (4.30)). The result of this rotation is that the spin-up component of the local frame σ^μ couples into both spin channels of the global frame g , the same holds for the spin-down component. Both spin directions have to be treated at the same time, similar to a system with spin-orbit coupling (see section 5.6). The general framework to obtain WFs for spinors has already been discussed in section 5.6 for SOC. In the case of non-collinear magnetic order it is only necessary to find

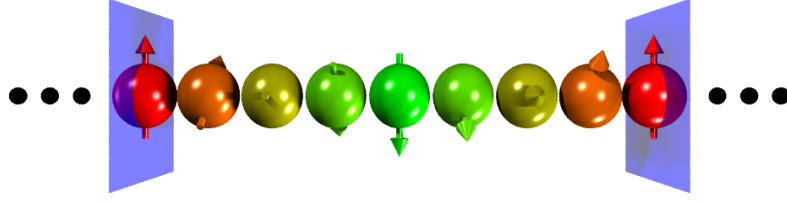


Figure 5.4: Sketch of non-collinear magnetic spin-structure in a monowire with 30° between adjacent magnetic moments. The direction of the net magnetic moment and hence the local spin frame σ^μ is displayed with arrows.

new expressions for the contributions related to the muffin-tin spheres for $A_{mn}^{(\mathbf{k})}$ (cf. Eqn. (5.16)) and $M_{mn}^{(\mathbf{k},\mathbf{b})}$ (cf. to Eqn. (5.19)).

Due to the intra-atomic collinearity it is reasonable in the non-collinear case to choose the localized trial orbitals $|g_n\rangle$ to be eigenstates of the projection of the spin-operator onto the local spin-quantization axis σ^μ . In this case $c_{nL\sigma\sigma^\mu}$ only differs from zero for one spin component σ for any given n and $A_{mn}^{(\mathbf{k})}$ can thus be obtained similar to the collinear magnetic case (Eqn. (5.16)) in local spin frame (chapter 4.7, Eqn. (4.29)):

$$A_{mn}^{(\mathbf{k})} = \sum_L c_{nL\sigma\sigma^\mu} \{ [A_{mL\sigma\sigma^\mu}^{(\mathbf{k})}]^* \int dr u_{ml\sigma}^{\sigma^\mu}(r) \tilde{u}_{nl\sigma}^{\sigma^\mu}(r) r^2 + [B_{mL\sigma\sigma^\mu}^{(\mathbf{k})}]^* \int dr \frac{\partial}{\partial \epsilon} u_{ml\sigma}^{\sigma^\mu}(r) \tilde{u}_{nl\sigma}^{\sigma^\mu}(r) r^2 \}. \quad (5.37)$$

Choosing again the radial part of the localized trial orbitals to be a solution of the radial symmetric FLAPW potential $\tilde{u}_{nl\sigma}^{\sigma^\mu}(r) = u_{nl\sigma}^{\sigma^\mu}(r)$ in the local spin-frame σ^μ , this expression can be further simplified according to Eqn. (5.17).

The contribution of MT^μ to the $M_{mn}^{(\mathbf{k},\mathbf{b})}$ matrix in Eqn. (5.19) can likewise be written as

$$M_{mn}^{(\mathbf{k},\mathbf{b})} |_{\text{MT}^\mu} = \sum_\sigma \int_{\text{MT}^\mu} d^3 r [\psi_{\mathbf{k}m\sigma\sigma^\mu}(\mathbf{r})]^* e^{-i\mathbf{b}\cdot\mathbf{r}} \psi_{\mathbf{k}+\mathbf{b}n\sigma\sigma^\mu}(\mathbf{r}) \quad (5.38)$$

where $\psi_{\mathbf{k}m\sigma\sigma^\mu} |_{\text{MT}^\mu}$ is the wave function in the local spin frame σ^μ of MT^μ (Eqn. (4.29) in chapter 4.7) with the spinor component $\sigma = \uparrow, \downarrow$. This expression can be calculated in either spin-frame, since the unitary rotation matrices \mathbf{U}_μ^\dagger do not change the sum (or trace) over both spin-directions. The most convenient choice is, as shown in Eqn. (5.38), the local spin-frame σ^μ . The computation of the $M_{mn}^{(\mathbf{k},\mathbf{b})}$ matrix for non-collinear systems reduces therefore to integrals for which explicit expressions have been given for the FLAPW method [68].

The Wannier representation of the Hamiltonian can be written according to

Eqn. (5.35)

$$H_{nn'}^{\sigma\sigma'}(\mathbf{R}_1 - \mathbf{R}_2) = \frac{1}{\mathcal{N}} \sum_{\mathbf{k}m} \epsilon_m(\mathbf{k}) \langle W_{\mathbf{R}_1 n \sigma} | \psi_{\mathbf{k}m} \rangle \langle \psi_{\mathbf{k}m} | W_{\mathbf{R}_2 n' \sigma'} \rangle \quad (5.39)$$

and Eqn. (5.36):

$$\hat{H}_{\text{WFs}} = \sum_{n\mathbf{R}_1} \sum_{n'\mathbf{R}_2} \sum_{\sigma\sigma'} H_{n,n'}^{\sigma\sigma'}(\mathbf{R}_1 - \mathbf{R}_2) |W_{n\mathbf{R}_1\sigma}\rangle \langle W_{n'\mathbf{R}_2\sigma'}| \quad (5.40)$$

The spin-decomposition based on WFs for a non-collinear system depends on the arbitrary choice of the global frame, since spin and positional space are not coupled and only the relative orientation of the spins is important. This is unlike SOC, where the absolute orientation of the quantization axis determines the magnetic orientation direction and couples the spin to the crystal field, leading to effects such as an anisotropy energy between different spin directions. A spin-decomposition of the WFs Hamiltonian preserves its physical meaning only for the special case of a collinear magnetic configurations within the non-collinear approach with parallel or antiparallel local and global spin frames and therefore collinear spin states. For the general non-collinear case, the WFs Hamiltonian can only be decomposed with respect to the orbital symmetry.

6 Implementation of Ballistic Transport within FLAPW

A state-of-the-art theoretical approach to calculate ballistic transport through nanojunctions with a complex electronic and magnetic structure relies on two ingredients:

- a transport method allowing to treat non-equilibrium open quantum systems
- an accurate *first-principles* electronic structure calculation method

In this chapter, an approach is introduced that fulfills both requirements: the first one by applying non-equilibrium Green's functions (NEGF) to calculate ballistic transport of two-terminal nanojunctions introduced in chapter 2, taking into account non-equilibrium within the linear response regime, the second one, by performing density functional theory (DFT) (chapter 3) electronic structure calculations of such nanojunctions, based on the full-potential linearized augmented plane-wave (FLAPW) method (chapter 4), known as one of the most precise implementations of DFT. The FLAPW method, as implemented in the FLEUR-code [63], provides an ideal framework to study electronic structures, including subtle effects such as e.g. spin-orbit coupling (SOC) [66] and non-collinear spin-structures [67] in one-dimensional geometry [64].

Due to the rather large number of FLAPW basis functions and their inherent delocalization a straight-forward combination between both methods is impossible to achieve. Wannier functions (WFs), as introduced in chapter 5, are proposed in this thesis as an interface to map the FLAPW wave functions and electronic structure on a tight-binding like Hamiltonian, while maintaining the benefits of both approaches. WFs can provide an efficient representation of the Hamiltonian if based on few well-localized Wannier orbitals. The localization of Wannier orbitals is crucial, since it is directly related to the number of neighbors, which have to be considered to construct the tight-binding like Hamiltonian while maintaining the accuracy of the FLAPW electronic structure and, thus, to the overall computational effort. Two types of WFs are considered within this thesis: First-shot Wannier functions (FSWFs) and maximally localized Wannier functions (MLWFs) [62]. While the uniquely-defined MLWFs naturally possess all the required characteristics, it is demonstrated in this chapter, that FSWFs can lead to an equally precise description of the electronic structure of the considered transition metal nanojunction within FLAPW accuracy for reasonable choices of trial orbitals. Given such a adapted set of trial orbitals,

FSWFs can be even regarded superior to MLWFs for ballistic transport calculations due to the known spin and orbital symmetry of each orbital, allowing to construct the required tight-binding like Hamiltonians in a straight-forward way. The implementation of FSWFs and MLWFs within the FLEUR-code [63] uses an interface to the publicly available Wannier90-code [137] and allows to treat nanojunctions including spin-orbit coupling (SOC) [68] and non-collinear spin-structures [80], which allows to perform transport studies on nanoscale metallic contacts incorporating such complex effects.

In this chapter, the setup and the calculation method for ballistic transport based on the FLAPW method is introduced and tests of the implementation are critically discussed for two-terminal nanojunctions, consisting of a scattering region connected to two macroscopic electrodes by leads. First, the determination of finite-sized self-energy matrices using surface Green's functions introduced, which allows to incorporate all effects of the leads on the scattering region. In the following, the construction of the tight-binding like Hamiltonians for leads and scattering region and their coupling matrices is described, based on a WFs representation. WFs open the possibility to combine multiple FLAPW electronic structure calculations, performed for the leads and the scattering region separately, with the newly developed locking-technique. This technique allows to accurately and efficiently calculate ballistic transport, while keeping the FLAPW system sizes computationally feasible. In addition, the locking-technique helps to avoid computational artifacts by accurately describing the leads as true periodic systems.

Furthermore, the Green's function based approach to calculate ballistic transport grants access to an orbital decomposition of the conductance or the locally and orbitally resolved density-of-states (DOS), which provide valuable tools to study ballistic transport.

All aspects of the new ballistic transport method are demonstrated on two test systems; (i) Nonmagnetic Pt monowires (section 6.6) and (ii) magnetic Co monowires (section 6.7), each with a stretched central bond, and compared to ballistic transport calculations based on a scattering approach and pseudopotentials [69, 81].

6.1 The General Transport Problem Revisited

As discussed in detail in chapter 2, all investigations will be based on the ground state Hamiltonian (cf. chapter 2.4, Eqn. (2.33)) of the open quantum system (see Figure 6.1):

$$\mathbf{H} = \begin{pmatrix} \mathbf{H}_L & \mathbf{H}_{LS}^\dagger & \mathbf{0} \\ \mathbf{H}_{LS} & \mathbf{H}_S & \mathbf{H}_{SR} \\ \mathbf{0} & \mathbf{H}_{SR}^\dagger & \mathbf{H}_R \end{pmatrix} \quad (6.1)$$

The all-electron FLAPW ground state Hamiltonian \hat{H}_{FLAPW} can be mapped onto localized Wannier functions $|W_{n\mathbf{R}_i}\rangle$ with the WFs index n at the position \mathbf{R} (cf.

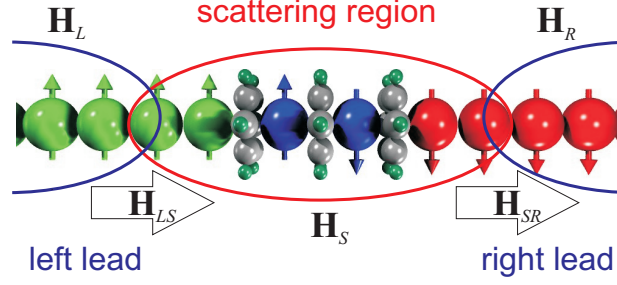


Figure 6.1: Geometry of a typical open quantum system for ballistic transport calculations, consisting of three different regions: The semi-infinite left and right leads, described by the semi-infinite Hamiltonian matrices $\mathbf{H}_{L/R}$ and the scattering region, described by the finite sized Hamiltonian matrix \mathbf{H}_S . The coupling between scattering region and the leads is expressed by the coupling matrices $\mathbf{H}_{LS/SR}$. While the semi-infinite leads resemble the electronic structure of a perfect periodic system, the scattering region includes the scatterer as well as the lead-scatterer interface region.

chapter 5.5)

$$\hat{H}_{\text{WFs}} = \sum_{n\mathbf{R}_1} \sum_{n'\mathbf{R}_2} H_{n,n'}(\mathbf{R}_1 - \mathbf{R}_2) |W_{n\mathbf{R}_1}\rangle \langle W_{n'\mathbf{R}_2}| \quad (6.2)$$

with the hopping elements

$$H_{n,n'}(\mathbf{R}_1 - \mathbf{R}_2) = \langle W_{n\mathbf{R}_1} | \hat{H}_{\text{FLAPW}} | W_{n'\mathbf{R}_2} \rangle \quad (6.3)$$

It has been shown in chapter 5 that this description applies for non-magnetic and magnetic (chapter 4.7) systems, including spin-orbit coupling or non-collinear magnetism (chapter 4.7 and chapter 5.7). The approach is held very general in this respect, the difference is the treatment of the spin degree of freedom. The spin channels can either be degenerate, as for non-magnetic calculations, be calculated independently for each spin direction, as for collinear magnetic calculations, or have to be considered simultaneously in one calculation, in the case of spin-orbit coupling or non-collinear spin-structures. Starting from a FLAPW calculation, the electronic structure is mapped on the WF's Hamiltonian (Eqn. (6.2)), which can in principle be used to calculate all quantities of the NEGF approach, introduced in chapter 2.4. For example, the self energies $\Sigma_{L/R}(E)$ (cf. chapter 2.4, Eqn. (2.40)) of the left (L) and right (R) leads, containing all details of the electronic structure of the leads and their coupling to the scattering region,

$$\Sigma_{L/R}(E) = \mathbf{H}_{LS/SR}^\dagger \mathbf{G}_{L/R}(E) \mathbf{H}_{LS/SR} \quad (6.4)$$

can be expressed by the Green's functions $\mathbf{G}_{L/R}(E)$ of the lead L or R (cf. chapter 2.4, Eqn. (2.36)),

$$\mathbf{G}_{L/R}(E) = [(E + i\eta)\mathbf{I}_{L/R} - \mathbf{H}_{L/R}]^{-1} \quad (6.5)$$

defined by the semi-infinite Hamiltonian matrices $\mathbf{H}_{L/R}$ of the leads. The broadening matrices $\mathbf{\Gamma}_{L/R}$ (chapter 2.4 Eqn. (2.55)), describing the effect of the broadening of the states in the scattering region due to interactions with the leads as well as the transfer rates of electrons originating from the leads into the scattering region, are given by:

$$\mathbf{\Gamma}_{L/R}(E) = i[\mathbf{\Sigma}_{L/R}(E) - \mathbf{\Sigma}_{L/R}^\dagger(E)] \quad (6.6)$$

The Green's function of the scattering region is thus defined by an effective Hamiltonian with self-energies (Eqn. (6.4)) acting as external potentials (cf. chapter 2.4, Eqn. (2.41)):

$$\mathbf{G}_S(E) = [E\mathbf{I}_S - \mathbf{H}_S - \mathbf{\Sigma}_L(E) - \mathbf{\Sigma}_R(E)]^{-1} \quad (6.7)$$

Based on those quantities the transmission function $T(E)$ within the Landauer formalism is obtained (Eqn. (2.69)):

$$T(E) = \text{Tr}[\mathbf{\Gamma}_L(E)\mathbf{G}_S(E)\mathbf{\Gamma}_R(E)\mathbf{G}_S^\dagger(E)] \quad (6.8)$$

The current

$$I = \frac{e}{h} \int dE T(E)[f_L(E) - f_R(E)] \quad (6.9)$$

and conductance

$$G(E) = \frac{2e^2}{h} T(E) \quad (6.10)$$

of a system can then be calculated. Although the road map to calculate ballistic transport based on FLAPW electronic structure is clear, there are still many technical problems to be solved. The leads and therefore their Green's functions $\mathbf{G}_{L/R}(E)$ are based on semi-infinite Hamiltonian matrices $\mathbf{H}_{L/R}$, the self energies and broadening matrices are therefore not obtainable within this description. Additionally, the FLAPW calculations are by construction periodic in real space, a characteristic not shared with the general transport setup (see Figure 6.1). The details of constructing an open quantum system from periodic FLAPW calculations are given below.

6.2 Surface Green's Functions

As has been discussed before, the Green's functions of the leads (Eqn. (6.5)) depend on the semi-infinite Hamiltonian matrices $\mathbf{H}_{L/R}$ and the self energies $\mathbf{\Sigma}_{L/R}$ (Eqn. (6.4)) and the broadening matrices $\mathbf{\Gamma}_{L/R}$ (Eqn. (6.6)) on semi-infinite coupling matrices $\mathbf{H}_{LS/SR}$. Following an approach by Datta [87], it is now illustrated

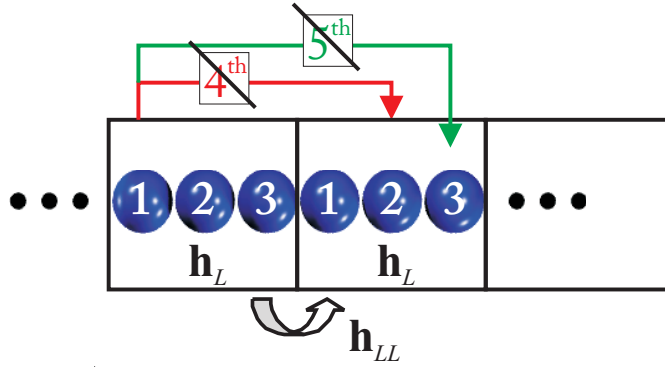


Figure 6.2: Separation of the left lead into identical principal layers consisting of 3 identical atoms described by the sub-matrix \mathbf{h}_L and the interaction sub-matrix \mathbf{h}_{LL} . Unbalanced interactions, like the 4th and 5th NN interactions, shown here for atom 1, have to be canceled.

how to construct finite-sized matrices to calculate the self energies $\Sigma_{L/R}$ and the broadening matrices $\Gamma_{L/R}$ within the surface Green's function technique.

Simply truncating the matrices $\mathbf{H}_{L/R}$ and $\mathbf{H}_{LS/SR}$ to finite size and then solving the problem would change the whole picture from an open quantum system with nonreflecting leads to a closed system with fully reflecting leads. Thus, a more elaborated method has to be found.

The first step is to consider the coupling matrix \mathbf{H}_{LS} only to be non-zero for a finite number of orbitals, constituting a principal layer. This assumption can, for example, be justified for a tight binding Hamiltonian based on localized basis functions, such as the WFs used in the present approach.

In case of a localized basis set, the overlap between orbitals of the scattering region and orbitals of the leads will rapidly decay with increasing distance. In fact, MLWFs and FSWFs, based on localized trial orbitals, will later be shown to decay exponentially in chapter 6.6.1, fulfilling therefore the claim of a rather small number neighbors with considerable interaction. Keeping in mind the idea of a principal layer at the interface between the lead scattering region, it is possible to continue this concept into the leads and construct e.g. the left leads Hamiltonian matrix \mathbf{H}_L from quadratic ($N \times N$) sub-matrices of principal layers \mathbf{h}_L and the interaction matrices \mathbf{h}_{LL} between principal layers, as shown in Figure 6.2:

$$\mathbf{H}_L = \begin{pmatrix} \ddots & & & \mathbf{0} \\ & \mathbf{h}_L & \mathbf{h}_{LL}^\dagger & \\ & \mathbf{h}_{LL} & \mathbf{h}_L & \mathbf{h}_{LL}^\dagger \\ \mathbf{0} & & \mathbf{h}_{LL} & \mathbf{h}_L \end{pmatrix}. \quad (6.11)$$

The expression for the right lead can be set up accordingly. In terms of the tight-binding like Hamiltonian, N describes the total number of orbitals, $N = n \times o$, where

n is the number of atoms in a principal layer and o the number of orbitals per atom. The resulting approximation is called the n^{th} nearest neighbor (NN) approximation. Such a principal layer still includes unbalanced hoppings, as illustrated in Figure 6.2. In a principal layer consisting e.g. of 3 identical atoms, the interaction between atom 1 of the present principal layer and atom 2 and 3 in the next principal layer are 4th and 5th NN hoppings, not available e.g. for atom 3. All those excess hoppings have to be set to zero in a practical calculation, otherwise the identical atoms would differ. Even though the difference might be small, not doing so would artificially enlarge the unit cell, leading to energy gaps at the zone boundary and a systematic error, discussed in section 6.6.3.

Assuming the leads to be ideal periodic structures, the block diagonal matrix Eqn. (6.11) can be constructed from identical $\mathbf{h}_{L/R}$ and $\mathbf{h}_{LL/RR}$ matrices, obtainable from an FLAPW calculations mapped on a WFs Hamiltonian

$$\hat{h}_{L/R} = \sum_{i,n} \sum_{j,m} H_{n,m}(\mathbf{R}_i - \mathbf{R}_j) |W_{n\mathbf{R}_i}\rangle \langle W_{m\mathbf{R}_j}| \quad (6.12)$$

where the indices i and j determine the atoms in one principal layer in the and n and m the orbital character of the WFs, and

$$\hat{h}_{LL/RR} = \sum_{i,n} \sum_{j,m} H_{n,m}(\mathbf{R}_i - \mathbf{R}_j) |W_{n\mathbf{R}_i}\rangle \langle W_{m\mathbf{R}_j}| \quad (6.13)$$

where the indices i and n determine the atoms and the orbital character of the WFs in one principal layer of the lead and the indices j and m in a neighboring principal layer. Within a single FLAPW calculation usually the outmost atoms, far away from the scatterer, are considered to be lead atoms. The draw-backs of this approach and an alternative solution will be discussed in section 6.4.

The matrix elements of the $\mathbf{h}_{L/R}$ and $\mathbf{h}_{LL/RR}$ matrices are given by the hopping elements $H_{n,m}(\mathbf{R}_i - \mathbf{R}_j)$

$$\langle W_{n\mathbf{R}_i} | \hat{h} | W_{m\mathbf{R}_j} \rangle = H_{n,m}(\mathbf{R}_i - \mathbf{R}_j) \quad (6.14)$$

by using the orthonormality condition of the WFs (cf. chapter 5, Eqn. (5.2)).

Based on this description of the leads, the finite sized ($N \times N$) surface Green's function $\mathbf{g}_{L/R}(E)$ can be determined by an recursive scheme within a Dyson equation treatment [142, 143]:

$$\begin{aligned} \mathbf{g}_{L/R}^{[0]}(E) &= [(E + i\eta)\mathbf{I}_{L/R} - \mathbf{h}_{L/R}]^{-1} \\ \mathbf{g}_{L/R}^{[1]}(E) &= [(E + i\eta)\mathbf{I}_{L/R} - \mathbf{h}_{L/R} - \mathbf{h}_{LL/RR}^\dagger \mathbf{g}_{L/R}^{[0]}(E) \mathbf{h}_{LL/RR}]^{-1} \\ &\vdots \\ \mathbf{g}_{L/R}^{[n]}(E) &= [(E + i\eta)\mathbf{I}_{L/R} - \mathbf{h}_{L/R} - \mathbf{h}_{LL/RR}^\dagger \mathbf{g}_{L/R}^{[n-1]}(E) \mathbf{h}_{LL/RR}]^{-1} \end{aligned} \quad (6.15)$$

Unfortunately, the convergence of Eqn. (6.15) is rather slow, the convergence can be improved by using a more efficient recursive scheme [144]. After obtaining the finite size surface Green's function, the open quantum system is reduced to a finite size problem within n^{th} NN approximation. Based on the surface Green's functions of the leads, now the self energies $\Sigma_{L/R}$ (Eqn. (6.4))

$$\Sigma_{L/R}(E) = \mathbf{h}_{LS/SR}^\dagger \mathbf{g}_{L/R}(E) \mathbf{h}_{LS/SR}, \quad (6.16)$$

and the broadening matrices $\Gamma_{L/R}(E_i)$ (Eqn. (6.6))

$$\Gamma_{L/R}(E) = i[\Sigma_{L/R}(E) - \Sigma_{L/R}^\dagger(E)] \quad (6.17)$$

can in principle be calculated based on the surface Green's function $\mathbf{g}_{L/R}(E)$ and finite sized coupling matrices $\mathbf{h}_{LS/SR}$ between the interacting principal layers of lead and scattering region. However, the finite sized coupling matrices $\mathbf{h}_{LS/SR}$ have yet to be defined.

6.3 Construction of the Transport Hamiltonian

According to Eqn. (6.4) to Eqn. (6.8)), it is necessary to define the open quantum system's Hamiltonian by determination of the matrices \mathbf{H}_S , \mathbf{H}_{LS} , \mathbf{H}_{SR} , \mathbf{H}_L and \mathbf{H}_R . The previous section shows, that it is not necessary to describe the open quantum system by the semi-infinite Hamiltonians $\mathbf{H}_{L/R}$ of the leads, but rather by the finite sized submatrices $\mathbf{h}_{L/R}$ and $\mathbf{h}_{LL/RR}$ of a principal layer and the resulting surface Green's functions. Additionally, by introducing principal layers the coupling matrices $\mathbf{H}_{LS/SR}$ can be replaced by finite sized matrices $\mathbf{h}_{LS/SR}$. Interactions beyond the outmost principal layers of scattering region and leads are neglected in this approach.

In this section the Hamiltonian \mathbf{H}_S of the scattering region and the coupling matrices \mathbf{h}_{LS} and \mathbf{h}_{SR} will be constructed, based on FLAPW electronic structure calculations and the resulting WFs hopping elements (cf. Eqn. (6.3) in chapter 5.5). First, the construction of the Hamiltonian matrix of the scattering region (see Figure 6.3) is treated. The WFs $|W_{n\mathbf{R}_i}\rangle$, defined by their band index n and their position \mathbf{R}_i , can now be used to describe the scattering region in real space. First, the atoms of the scattering region have to be identified. The scattering region has thereby to be chosen large enough not only to contain the scatterer, but also an scatterer-lead interface region to screen a possible interaction between scatterer and leads (see Figure 6.3) The preliminary result for \hat{H}_S can now be written down, based on its Hamiltonian,

$$\hat{H}_S = \sum_{i,n} \sum_{j,m} H_{n,m}(\mathbf{R}_i - \mathbf{R}_j) |W_{n\mathbf{R}_i}\rangle \langle W_{m\mathbf{R}_j}| \quad (6.18)$$

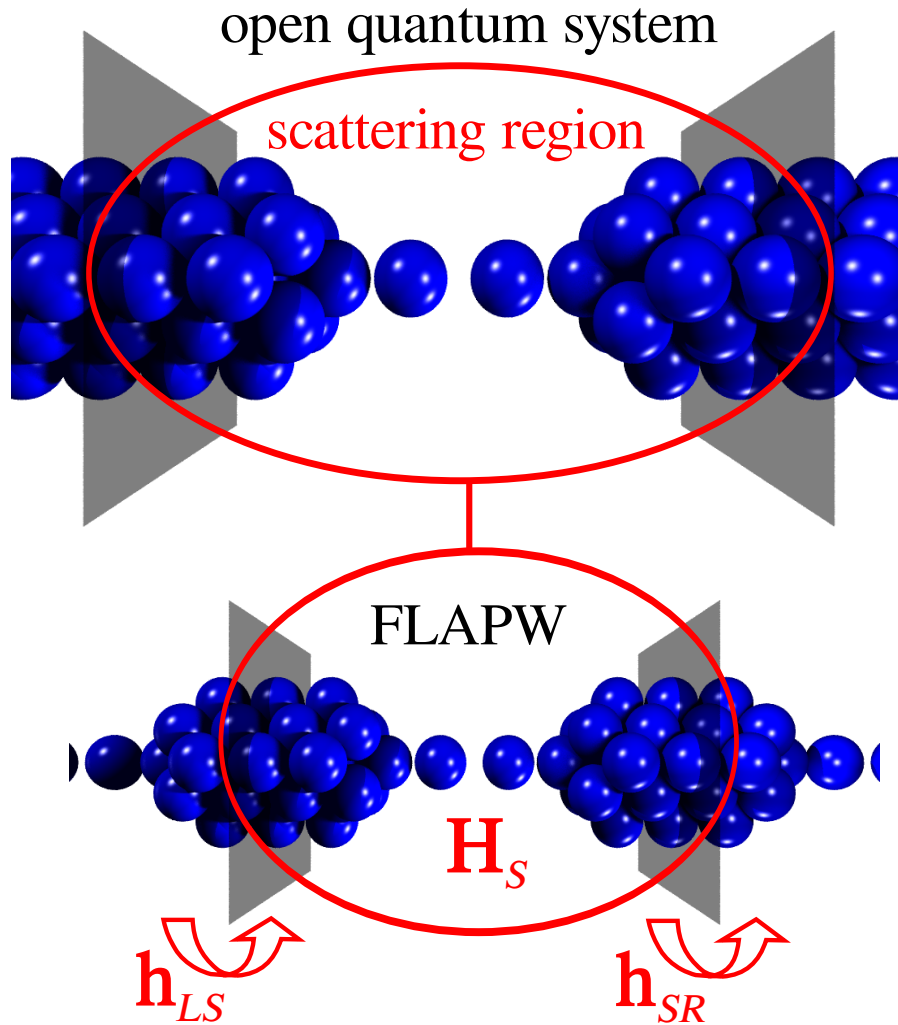


Figure 6.3: The scattering region's Hamiltonian matrix H_S is extracted from a FLAPW supercell calculation describing the geometric shape and magnetic properties of the scattering region of the open quantum system. To prevent a large systematic error, the scattering region contains the scatterer and an interface region to screen structural, electronic and magnetic effects on the leads.

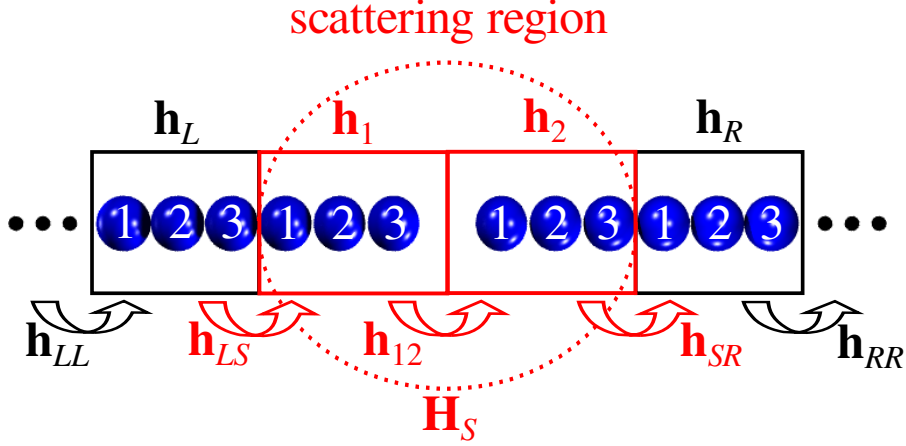


Figure 6.4: Description of a scattering region by two principal layers: The total scattering region's Hamiltonian \mathbf{H}_S is divided into two atom principal layers consisting of three atoms each, described by the sub-matrices $\mathbf{h}_{1/2}$ and the coupling matrix \mathbf{h}_{12} . The lead-scattering region coupling matrices $\mathbf{h}_{LS/SR}$ are evaluated between the connected principal layers of scattering region and lead.

where the indices i and j determine the atoms in the scattering region and n and m the orbital character of the WFs. Since the scattering region is described non-periodically there is no band index anymore, as in the underlying FLAPW calculation. The orbital character of a Wannier function is known from the trial orbital the Wannier function was projected on in case of first-shot Wannier functions (FSWFs) or from the spread of the orbital in case of maximally localized Wannier functions (MLWFs).

The matrix elements of the \mathbf{H}_S matrices are again obtained from the hopping elements $H_{n,m}(\mathbf{R}_i - \mathbf{R}_j)$

$$\langle W_{n\mathbf{R}_i} | \hat{H}_S | W_{m\mathbf{R}_j} \rangle = H_{n,m}(\mathbf{R}_i - \mathbf{R}_j) \quad (6.19)$$

by using the orthonormality condition of the WFs (cf. chapter 5, Eqn. (5.2)). Due to the exponential decay of the Wannier functions with distance it is only necessary to keep matrix elements up to a certain number of nearest neighbors, setting the rest of the elements to zero, as has been mentioned before in section 6.2.

A more flexible approach can be achieved by dividing the scattering region, too, into principal layers \mathbf{h}_l , with $l = 1, \dots, s$ and interaction matrices $\mathbf{h}_{l,l+1}$ between neighboring layers (see Figure 6.4) in a similar approach as used for the leads (Eqn. (6.11)):

$$\mathbf{H}_S = \begin{pmatrix} \mathbf{h}_1 & \mathbf{h}_{12}^\dagger & & \mathbf{0} \\ \mathbf{h}_{12} & \ddots & \ddots & \\ & \ddots & \mathbf{h}_{s-1} & \mathbf{h}_{(s-1)s}^\dagger \\ \mathbf{0} & & \mathbf{h}_{(s-1)s} & \mathbf{h}_s \end{pmatrix} \quad (6.20)$$

The sub-matrices are calculated according to Eqn. (6.18). For the on-site matrices, \mathbf{h}_l , the indices i and j will be restricted to atoms from the layer l . For the interaction matrices $\mathbf{h}_{l,l+1}$, the index i will be restricted to atoms from layer l and the index j will be restricted to atoms from the neighboring layer $l + 1$. In contrast to the leads principal layers (Eqn. (6.11)), the submatrices are usually not identical. \mathbf{H}_S is a sparse band matrix in this representation, which allows a computationally inexpensive treatment. While this approach is still capable of describing the system in terms of Eqn. (6.18) (with $s = 1$), the principal layers optimally contain only the number of atoms effectively interacting.

An ideal choice for the scattering regions principal layers is a description with the same size as the principal layers of the leads (see section 6.2), as shown in Figure 6.4, to maintain the same order of NN approximation. In this thesis, unless stated otherwise, n^{th} NN approximation means a n^{th} NN approximation to the electronic structure of the leads and the scattering region. There are still unbalanced hoppings, as shown in Figure 6.2 for the leads. Those excess hopping elements have to be set to zero to maintain an accurate and balanced Hamiltonian matrix, as described for the leads in section 6.2. Adapting the principal layer structure to the scattering region additionally minimizes the effort of canceling out those excess hopping elements. Furthermore this scheme preserves flexibility with respect to possible future extensions, such as e.g. a combination of separately calculated scatterers into one scattering region or inelastic scattering effects such as scattering on vibrations [35, 36] or correlation effects [37] based on self-energies.

Knowing the Hamiltonian \mathbf{H}_S of the scattering region, it is necessary to determine the coupling of the scattering region to the leads. Since the surface GFs of both leads and the scattering region are described by principal layers (See Eqn. (6.11) and Eqn. (6.20)), only the hopping elements between those layer need to be found, as shown in Figure 6.4. The finite sized \mathbf{h}_{LS} can now be extracted from the supercell calculation as

$$\hat{h}_{LS} = \sum_{i,n} \sum_{j,m} H_{n,m}(\mathbf{R}_i - \mathbf{R}_j) |W_{n\mathbf{R}_i}\rangle \langle W_{m\mathbf{R}_j}| \quad (6.21)$$

where the index i runs over the atoms included of the principal layer \mathbf{h}_1 of \mathbf{H}_S and the index j over the outmost principal layer of the left scattering region. n and m denote the Wannier orbitals of each atom.

The matrix elements of the \mathbf{h}_{LS} matrices are again obtained from the hopping elements $H_{n,m}(\mathbf{R}_i - \mathbf{R}_j)$

$$\langle W_{n\mathbf{R}_i} | \hat{h}_{LS} | W_{m\mathbf{R}_j} \rangle = H_{n,m}(\mathbf{R}_i - \mathbf{R}_j) \quad (6.22)$$

by using the orthonormality condition of the WFs (cf. chapter 5, Eqn. (5.2)). \mathbf{h}_{SR} can be constructed analogously.

Here, it is important to keep in mind, that the Hamiltonian matrix is constructed from one FLAPW calculation. The interaction matrix Eqn. (6.21) typically includes hoppings between identical unit cells due to the z -periodicity of the FLAPW

calculation. To prevent a significant systematical error, it is necessary to choose the scattering regions unit cell large enough to screen an unphysical inter-unit cell interaction.

6.4 The Locking-Technique

The accurate treatment of the leads within the approach described above constitutes a considerable challenge. Taken from a self-consistent supercell electronic structure calculation as they are, the sub-matrices $\mathbf{h}_{L/R}$ and $\mathbf{h}_{LL/RR}$ (section 6.2, Eqn. (6.11)) will contain deviations from "ideal"-lead matrix elements in a large vicinity of the scattering region. While some of these deviations are definitely physical in their origin due to a large decay length of one-dimensional charge perturbations caused by the scatterer, the rest of them will be a spurious artifact of the supercell approach owing to the fact that the leads as calculated are not intrinsically semi-infinite. This presents a considerable problem in particular when the leads have to be described with Hamiltonians beyond the 1st NN. In this case to describe the semi-infinite leads precisely, one would have to go to huge supercells so that the n atoms in the supercell describing the lead would be exactly identical, with n being the number of atoms in one principal layer (see Eqn. (6.11)). That condition is found impossible to achieve for non-trivial systems. Another approach of constructing a lead beyond 1st NN artificially from the outmost atoms of the scattering region by periodically expanding it is flawed, too, due to the unknown unperturbed hopping matrix elements beyond 1st NN. This is a serious problem, since the lead has to be described as precisely as possible to prevent a huge systematic error.

The basic idea to work around this problem is as simple as effective, namely matching the supercell hopping matrix elements to those of the true leads. Within this so-called "locking" technique, the leads are replaced by the perfect wires, providing correct self-energies and Fermi levels of the true infinite periodic system, while the supercell size is chosen large enough to describe the lead-scatterer interface region sufficiently well (cf. Figure 6.5). Within the presented transport approach this means that different parts of the Hamiltonian (Eqn. (6.18) and Eqn. (6.21)) are extracted from two different DFT calculations [145–147]: The \mathbf{H}_S and $\mathbf{h}_{LS/SR}$ coupling matrices are taken from the supercell calculation describing the scattering region, while the $\mathbf{h}_{L/R}$ and $\mathbf{h}_{LL/RR}$ sub-matrices, needed to determine the surface Green's functions (Eqn. (6.11) and Eqn. (6.15)), are taken from the calculation for the perfect leads. $\mathbf{h}_{L/R}$ and $\mathbf{h}_{LL/RR}$ can be determined according to Eqn. (6.12), Eqn. (6.13) and Eqn. (6.14). To achieve matching Fermi levels for lead and supercell calculations, it is additionally necessary to align the diagonal elements of the matrices $\mathbf{h}_{L/R}$ (Eqn. (6.11)) and \mathbf{H}_S (Eqn. (6.20)).

The main challenge in this approach is to match the Wannier functions originating from the periodic leads $|W_{n'\mathbf{R}'_i}\rangle$ to the Wannier functions of the lead atoms in the

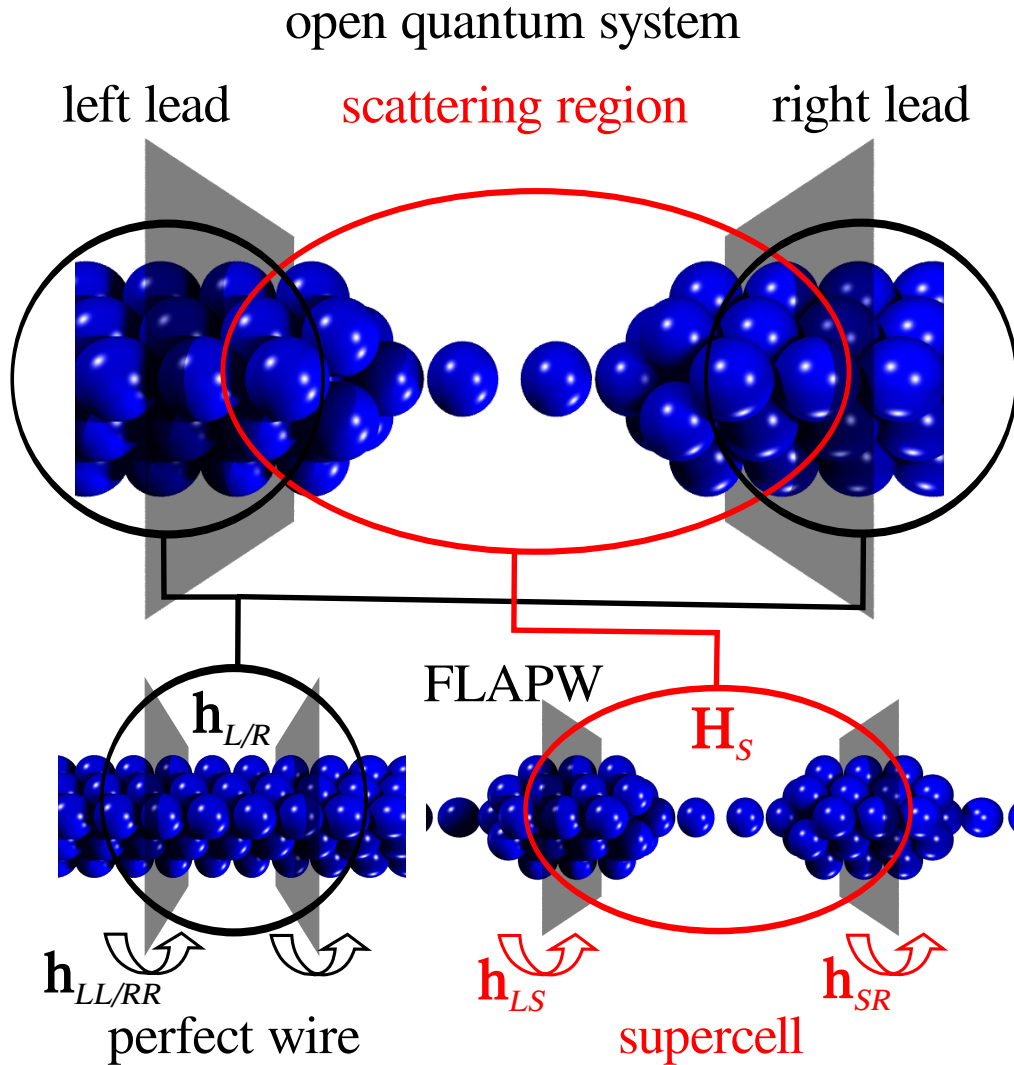


Figure 6.5: Schematic sketch of a ballistic transport calculation based on the WF's tight-binding Hamiltonian obtained from FLAPW calculations. The leads principal layer Hamiltonian matrices $\mathbf{h}_{L/R}$ and coupling matrices $\mathbf{h}_{LL/RR}$ are described separately by perfect wires to prevent deviations from their exact electronic structure, while the scattering region Hamiltonian matrix \mathbf{H}_S and the coupling matrices to the leads $\mathbf{h}_{LS/SR}$ are extracted from a supercell calculation. The supercell has to be large enough to reproduce the lead-scatterer interface region with the desired accuracy.

supercell calculation of the scattering region $|W_{n\mathbf{R}_i}\rangle$ (compare Eqn. (5.2)). This has to be done to ensure that the matrix elements of $\mathbf{h}_{LS/SR}$ (Eqn. (6.22)) are connected to the correct Wannier orbitals in the leads. In case of a large supercell, the properties of the outmost MLWFs of the supercell typically do not significantly differ from the periodic leads and one can assume orthonormality:

$$\langle W_{n'\mathbf{R}'_i} | W_{n\mathbf{R}_i} \rangle = \delta_{\mathbf{R}'\mathbf{R}} \delta_{n'n} \quad (6.23)$$

Here $\mathbf{R}_i = \mathbf{R}'_i$ is the location of a lead atom and $n = n'$ is the orbital index of the Wannier function. n and n' must have the same orbital symmetry and in case of coupled spin-channels the same spin-direction. In a practical calculation it is not necessary to evaluate Eqn. (6.23) explicitly, since $\mathbf{h}_{LS/SR}$ (Eqn. (6.21)) is constructed from the supercell calculation. However, a hopping element of $\mathbf{h}_{LS/SR}$ has to be assigned to a corresponding Wannier function in the leads (cf. Eqn. (6.11) and Eqn. (6.15)) with matching orbital character and spin-direction. For example, a hopping element evaluated in the scattering region supercell between a state of s -like character and spin direction 'up' and a d_{z^2} -like state with the same spin direction in the leads has to be matched to the according d_{z^2} -like spin-up state of the periodic lead calculation. Deviations from Eqn. (6.23) can result in computational artifacts, which are found to be negligible for reasonable supercell sizes (cf. section 6.6.3).

In case of MLWFs the localization procedure usually intermixes the Wannier functions and this information is usually lost. However, the orbital character and the location of MLWFs are identifiable by the their centers and spreads (cf. chapter 5.1) and MLWFs from leads and scattering region can be matched accordingly for non-magnetic and spin-polarized systems. For more complicated systems with coupled spin-channels, such as systems including SOC or non-collinear magnetic order, the spin of an individual MLWFs is unknown and the matching condition (Eqn. (6.23)) generally becomes unachievable¹.

For FSWFs the matching condition is generally easy to obtain, since the location, orbital character and the spin is known from the projection on the localized trial functions $|g_n\rangle$ (cf. chapter 5.3) Therefore, for systems with coupled spin channels FSWFs are often a much more convenient choice to calculate ballistic transport. The orthonormality condition (Eqn. (6.23)) can still be assumed for the non-unique FSWFs due to the construction of supercell and lead FSWFs from similar trial orbitals (cf chapter 5.3) . This is the case for sufficiently large supercells, where the the solution of the scalar relativistic equations of the radial symmetric FLAPW potential of the outmost muffin tins and, thus, the trial orbitals become leads-like. The locking-technique is further discussed in section 6.6.3 with respect to practical applications.

¹Usually there are multiple atoms in a principal layer with e.g. 12 different orbitals. Those 12 orbitals can be divided into groups of 2 orbitals with similar centers and spreads and unknown spin. All those spin characters have to be assigned correctly by chance to achieve the correct description, which is practically unachievable.

6.5 Ballistic Transport Calculations within FLAPW Wannier Functions

After discussing the construction of the transport Hamiltonian of the open quantum system, based on DFT (chapter 3) electronic structure calculations within the FLAPW method (chapter 4), mapped on a tight-binding like Hamiltonian by Wannier functions (chapter 5), now the ballistic transport can be calculated based on NEGFs within the linear response regime (chapter 2), as illustrated in Figure 6.6.

First, the FLAPW electronic structure of a nanojunction is calculated within the the FLEUR-code [63]. As mentioned before, it is in principle possible to construct the leads and the scattering region from one huge supercell calculation, while it is recommended to use the locking-technique, based on three separate FLAPW calculations for each region for precise results and reduced computational effort (cf. sections 6.4 and 6.6.3). Within FLAPW, the equilibrium configuration and the ground state electronic and magnetic properties of a nanojunction are determined, such as e.g. the total energy, magnetic moments and the Fermi level, which depend on the parameters of the calculation, such as e.g. the geometrical shape, magnetic configuration or the spin quantization axis in case of spin-orbit coupling (SOC), allowing first insights into the physical properties of the studied system.

The FLAPW electronic structure is then mapped by FSWFs or MLWFs on a tight-binding like Hamiltonian, provided by the Wannierization routines of FLEUR and Wannier90 [137]. The correspondence between FLAPW and Wannier function energy spectra (or bandstructures) can be controlled with respect to the the NN approximation of the tight-binding like Hamiltonian. A valuable tool to compare both representations is e.g. the Wannier function based interpolation procedure, introduced in chapter 5.5. For a sufficiently accurate representation, the Hamiltonian matrices $\mathbf{h}_{L/R}$, $\mathbf{h}_{LL/RR}$ (see chapter 6.2) are then constructed from the lead calculations and the $\mathbf{h}_{LS/SR}$ and \mathbf{H}_S (see chapter 6.3) from the supercell calculation.

NEGF ballistic transport calculations can now be performed within the linear response regime. All Hamiltonian matrices are therefore based on FLAPW ground state properties. Within the NEGF formalism, the energy E is no longer an eigenvalue, but an independent variable representing the energy of excitation from external sources. E has to be varied accordingly and the transport properties are solved on a equidistant discrete energy grid with the grid points E_i in this thesis. However, since the ballistic transport problem is independently solvable for every grid point, an extension to arbitrary energy grids or parallel computed grid-points is possible.

First, the surface Green's functions $\mathbf{g}_{L/R}(E_i)$ are determined from the submatrices $\mathbf{h}_{L/R}$, $\mathbf{h}_{LL/RR}$ (see section 6.2, Eqn. (6.15)). The surface Green's functions are then used to determine the the self energies $\Sigma_{L/R}(E_i)$, including the coupling matrices to the scattering region $\mathbf{h}_{LS/SR}$ (Eqn. (6.16)),

$$\Sigma_{L/R}(E) = \mathbf{h}_{LS/SR}^\dagger \mathbf{g}_{L/R}(E) \mathbf{h}_{LS/SR} \quad (6.24)$$

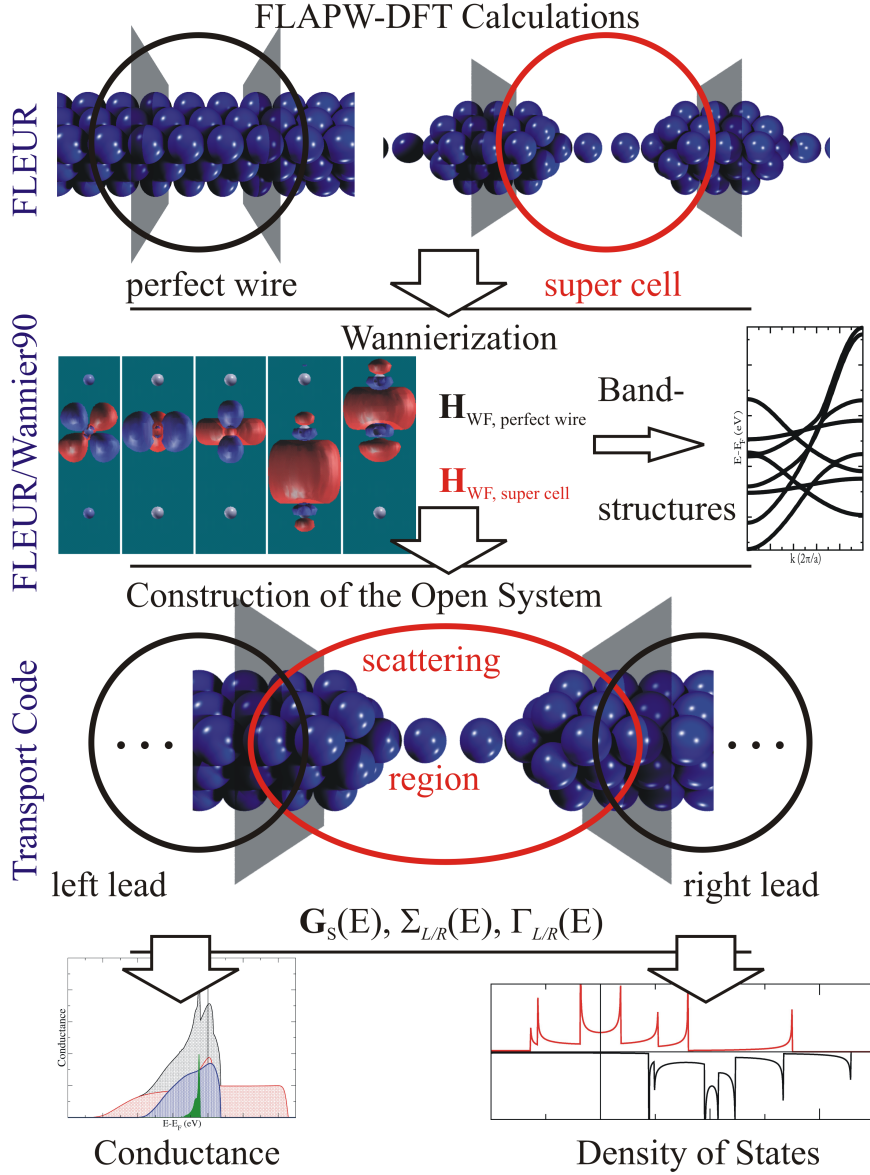


Figure 6.6: The ballistic transport method developed within this thesis. First, the FLEUR FLAPW calculations for electronic structure of the scattering region have to be performed, then the FLAPW Hamiltonian has to be transformed on the minimal tight-binding Wannier function Hamiltonian, as provided from the Wannierization routines of FLEUR and Wannier90. This mapping allows the check of the quality of the Wannier functions by comparing the bandstructures. Given a precise enough Wannier function tight-binding like Hamiltonian, the open quantum system for the ballistic transport calculation can be constructed, describing a scatterer between two semi-infinite leads exactly. The leads are treated in terms of finite-sized surface Green's functions, resulting in self energies $\Sigma_{L/R}(E)$ and broadening matrices $\Gamma_{L/R}(E)$ as effective lead-scattering region interaction. The conductance and the density of states and their orbital decompositions can then be calculated from the scattering region's Green's function $G_S(E)$.

and the broadening matrices $\mathbf{\Gamma}_{L/R}(E_i)$ (Eqn. (6.17))

$$\mathbf{\Gamma}_{L/R}(E_i) = i[\mathbf{\Sigma}_{L/R}(E_i) - \mathbf{\Sigma}_{L/R}^\dagger(E_i)] \quad (6.25)$$

The complex increment η (cf. Eqn. (6.15)) has to be chosen sufficiently small, which has to be checked by the convergence of the transmission function with respect to η . The complex valued self energies $\mathbf{\Sigma}_{L/R}(E_i)$ are necessary to determine the effective scattering regions Green's function (Eqn. (2.41) in chapter 2.4):

$$\mathbf{G}_S(E_i) = [E_i \mathbf{I}_S - \mathbf{H}_S - \mathbf{\Sigma}_L(E_i) - \mathbf{\Sigma}_R(E_i)]^{-1} \quad (6.26)$$

Eqn. (6.26) can be solved by sparse matrix inversion techniques [148] since \mathbf{H}_S is a sparse band matrix by construction (Eqn. (6.20)) and due to the well-localized Wannier functions (see section 6.3). Given $\mathbf{G}_S(E_i)$ and $\mathbf{\Gamma}_{L/R}(E_i)$, the transmission function $T(E_i)$ can be calculated by the expression found based on non-equilibrium Green's functions within the linear response regime (cf. chapter 2.4):

$$T(E_i) = \text{Tr}[\mathbf{\Gamma}_L(E_i) \mathbf{G}_S(E_i) \mathbf{\Gamma}_R(E_i) \mathbf{G}_S^\dagger(E_i)] \quad (6.27)$$

The trace operation of Eqn. (6.27) runs over all orbital and spin degrees of freedom of the Wannier functions. Subsets of Wannier functions with the same spin or orbital symmetry allows to decompose the transmission function with respect to such subsets and thereby provides distinct spin- and symmetry-related transmission channels.

Additional insight into the electronic structure of an open quantum system can be obtained by evaluating the total spectral function $\mathbf{A}(E) = \mathbf{A}_L(E) + \mathbf{A}_R(E)$, based on the partial spectral functions $\mathbf{A}_{L/R}(E)$ (cf. chapter 2.4, Eqn. (2.56)) at E_i :

$$\mathbf{A}(E_i) = \mathbf{G}_S(E_i) \mathbf{\Gamma}_L(E_i) \mathbf{G}_S^\dagger(E_i) + \mathbf{G}_S(E_i) \mathbf{\Gamma}_R(E_i) \mathbf{G}_S^\dagger(E_i) \quad (6.28)$$

According to chapter 2.4, the density of states (DOS) $D(E)$ at E_i can be calculated from Eqn. (2.45):

$$D(E_i) = \frac{1}{2\pi} \text{Tr}[\mathbf{A}(E_i)] \quad (6.29)$$

The trace operation runs over all orbital and spin degrees of freedom of the Wannier functions. Grouping those WFs into subsets by spin-direction, orbital symmetry and position allows to resolve the DOS with respect to each subset. It is important to note, that Eqn. (6.29) is the DOS of the open quantum system, which means the scattering region is coupled to semi-infinite leads, resulting e.g. in energy level broadening. A comparison to the DOS obtained from the FLAPW supercell calculation of the scattering region is given in section 6.6.4.

All these steps are repeated on a set of energy grid points $\{E_i\}$, usually

1401 energy grid points with energy steps of 0.01 eV are used within this thesis, unless stated otherwise, resulting in the transmission function $T(\{E_i\})$, which is evaluated in terms of the total conductance

$$G(\{E_i\}) = \frac{2e^2}{h}T(\{E_i\}) \quad (6.30)$$

on the given energy grid. The total calculation time to obtain the transmission function $T(\{E_i\})$ strongly depends on the number of Wannier functions in each region. It is typically in the order of seconds for small model systems up to a few minutes for the most demanding systems regarded², which is rather short compared to full FLAPW calculations and the Wannierization routines. However, due to the strong dependence of the calculational time on the number of Wannier functions and the use of an optimal set with the least possible number of electron orbitals per atom is recommended. For clarity, the parentheses in the expressions $T(\{E_i\})$ and $G(\{E_i\})$ will be dropped from hereon for calculational results.

²Intel Pentium Dual-Core CPU E5300 2.60GHz 4GB RAM

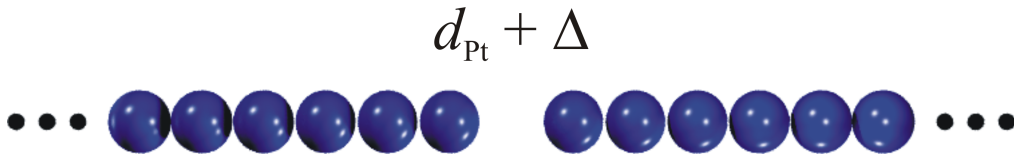


Figure 6.7: Sketch of a freestanding Pt monowire with a broken central bond. The Pt-Pt interatomic distance d_{Pt} is elongated by Δ at the central bond, simulating stepwise the bond-breaking process.

6.6 Pt Monowires with a Single Broken Bond

As first test system for the ballistic transport code, Pt monowires are investigated, which possess a single stretched bond that acts as a non-trivial scattering potential for electrons, as shown in Figure 6.7. In the following sections instructive applications are presented, which illustrate the quality and features of the ballistic transport code through a nanojunction, such as transmission functions and the closely related conductances, the density of states (DOS) and their orbital decompositions. These central quantities are powerful tools to understand quantum transport processes. Furthermore, the density of states of the open system will be discussed in comparison to super-cell based FLAPW density of states. The applicability of the locking technique is demonstrated and the quality of the MLWF (chapter 5.4) and the FSWF (chapter 5.3) representation of FLAPW electronic structure calculations will be discussed. Finally, spin-orbit coupling (SOC) is included into the ballistic transport calculations and the effect of SOC on the conductance is studied. Additionally, the obtained conductances in scalar-relativistic approximation and with SOC are compared to those obtained within a scattering approach in combination with a pseudopotential method for the electronic structure [69] and found to be in excellent agreement.

Parts of the results have been published in reference [79].

Computational Details

Non-magnetic 6 and 12 atom super cell calculations were performed within the FLEUR code [63] for Pt monowires with an interatomic distance of $d_{\text{Pt}} = 4.48 \text{ bohr}^3$ and a scattering potential due to a single bond stretched by $\Delta = 0.0, 0.34, 0.72, 1.22, 1.82$ and 2.52 bohr , respectively. The generalized gradient approximation (GGA) was applied to the exchange-correlation potential [103]. For calculations in the scalar-relativistic (SR) approximation, the irreducible part of the 1D Brillouin zone (BZ) was sampled by 6–10 k -points depending on the size of the super cell. For the 6 atom super cell, also calculations including spin-orbit coupling in second variation were performed. For calculations with SOC the whole 1D BZ was sampled by 24

³1 bohr = $5.2917721092 \times 10^{-11} \text{ m}$ ($\approx 0.529 \text{ \AA}$)

Pt MW	Ω_{MLWFs} (bohr ²)	Ω_{FSWFs} (bohr ²)
$s(\Delta_1)$	6.2	319.4
$d_{z^2}(\Delta_1)$	2.9	55.8
Δ_3	3.7	3.7
Δ_4	2.3	2.3

Table 6.1: Spreads (Ω) of MLWFs and FSWFs of a perfect Pt monowire with $d_{\text{Pt}} = 4.48$ bohr of orbitals belonging to the Δ_1 , Δ_3 and Δ_4 symmetry groups.

k -points. In all calculations, G_{max} was chosen to be 3.7 bohr^{-1} , which corresponds to approximately 200 basis functions per atom. The diameter of the cylindrical vacuum, D_{vac} , and the value of the in-plane auxiliary lattice constant, \tilde{D} [64], were set to 5.0 and 7.3 bohr, respectively (see chapter 4.6).

For the conductance calculations the locking technique was applied to a perfect monowire to describe the semi-infinite leads (see chapter 6.4). In the SR approximation FSWFs and MLWFs were generated on a mesh of 16 k -points in the whole BZ starting from one s - and 5 d -orbitals per atom in the super cell, based on solutions of the radial equation of the first-principles potentials as trial functions. In the calculations including SOC, MLWFs were generated on a 24 k -point mesh in the whole BZ based on 2 s - and 10 d -orbitals per atom due to the coupled spin channels. The energy bands were disentangled using the procedure described in [136]. For the SR calculations, the lowest 80 eigenstates are needed for 72 WFs for the 12 atom super cell and the lowest 44 eigenvalues per k -point for 36 WFs for the 6 atom super cell calculations. With SOC the lowest 80 eigenstates per k -point for 72 WFs were used.

6.6.1 FSWFs versus MLWFs

Before proceeding into the discussion of systems exhibiting complex magnetic behavior or SOC, it is insightful to examine the localization properties of typical MLWFs and FSWFs for a model system, such as an perfect Pt monowire, which will later be used as leads. While the MLWFs are uniquely defined and well known for their localization in real space, this is not necessarily the case for the FSWFs, which strongly depend on the initial choice of the trial orbitals. If the trial orbitals did not differ very much from the final result of the localization procedure or mimic the general behavior and symmetry of the system under investigation well, the difference in the spreads between the MLWFs and the FSWFs should be small.

The spreads of the Δ_1 (s and d_{z^2}), Δ_3 (d_{xz} and d_{yz}) and Δ_4 (d_{xy} and $d_{x^2-y^2}$) MLWFs and FSWFs of an infinite periodic Pt monowire with an interatomic spacing of 4.48 bohr are shown in table 6.1. The Δ_3 and Δ_4 spreads are 3.7 bohr^2 and 2.3 bohr^2 , respectively, in both representations. The situation is completely different, however, for the FSWFs constructed from the s - and d_{z^2} -like trial orbitals. In this case the difference in spread between the resulting FSWFs and the Δ_1 -like MLWFs is

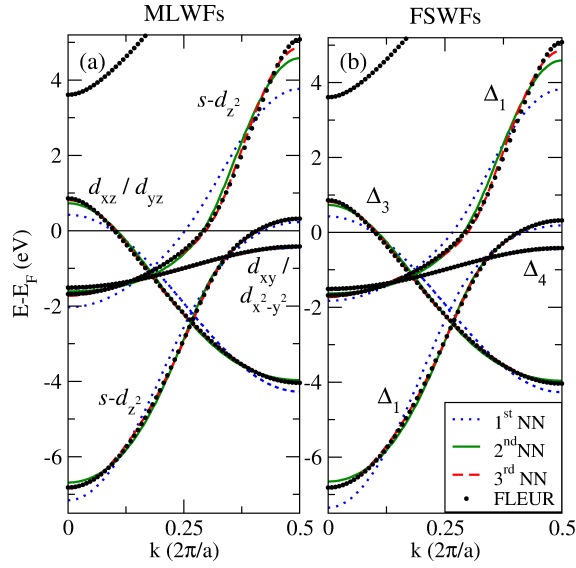


Figure 6.8: Comparison of the Pt monowire bandstructure in SR approximation calculated based on the FLAPW method (big black dots) and interpolated from the WF Hamiltonian based on (a) MLWFs and (b) FSWFs considering a limited number of nearest neighbors. In (a) the orbital character of the states is given and in (b) the bands are denoted according to their symmetry with respect to the chain geometry.

remarkable. While values of 2.9 and 6.2 bohr² are obtained for the spread of d_{z^2} -like and s -like MLWFs, respectively, the corresponding values constitute 55.8 and 319.4 bohr² for FSWFs. This indicates that the MLWFs differ significantly from the trial orbitals, and that for the one-dimensional cases the localization procedure mainly affects the orbitals localized along the direction of periodicity. The reason for the rather large spreads of the FSWFs can be found by comparing the FSWF centers to the MLWFs centers. In case of MLWFs the centers of the s -like WFs are located between the atoms, forming covalent bridge-like Wannier functions. Such Wannier functions are hard to construct directly from the atom-centered trial orbitals. The FSWFs constructed from the s - and d_{z^2} -like trial orbitals are, in contrast, located on the atoms, which causes a significantly larger spread [149].

As a result, there are two types of Wannier functions used in this thesis to setup the transport Hamilton matrices: MLWFs, which are by definition maximally localized and unique, and there are FSWFs, which in principal lack these properties, as shown for the Δ_1 symmetry orbitals of the perfect Pt wire. Although this presents in general a serious drawback for the latter, FSWFs can still be suitable to describe a system reasonably well. All Hamiltonians obtained by mapping to Wannier functions, which include the hopping matrix elements between all WFs are equivalent since all sets of Wannier functions are related by unitary transformations (cf. chapter 5.1). This

equivalence is lifted, however, since the Hamilton matrix will be truncated beyond a certain number of interacting nearest neighbors in a typical quantum transport calculation (see section 6.3).

In Figure 6.8, the Pt monowire bandstructure based on the FLAPW calculation and Slater-Koster interpolations (compare chapter 5.5, Eqn. (5.31)) of the bandstructure based on MLWFs and FSWFs are compared. The trial orbitals for the FSWFs are in this case chosen to be s - and d -like orbitals, centered on each atom and the MLWFs are obtained with these FSWFs as starting WFs using the localization procedure. While in first nearest neighbor (NN) approximation the interpolated bandstructures differ between the MLWFs and FSWFs approach, especially in the bandwidth of the more delocalized s and d_{z^2} orbitals, which also possess very large differences in their spreads (cf. table 6.1), already in second NN approximation both WFs basis sets describe the FLAPW bandstructure equally well. By increasing the considered number of neighbors to third NN approximation, the accuracy of the description increases with respect to the s -bandwidth. This can be expected, since the matrix elements $|H(\mathbf{R}_i - \mathbf{R}_j)|$ between Wannier functions i and j rapidly decay with increasing NN distance, as shown in Figure 6.9: MLWFs due to the localization procedure and FSWFs due to the construction from localized trial orbitals (cf. chapter 5). However, the most important part with respect to transport properties is the bandstructure in the vicinity of the Fermi level, which does not improve significantly with NN approximations above 2nd. For the more localized d_{xy} , $d_{x^2-y^2}$, d_{xz} and d_{yz} orbitals even the first NN description is sufficient as can be seen in the bandstructure and also from the hopping matrix elements as seen in Figure 6.9.

At least for a rather simple system such as a perfect Pt monowire the localization procedure used to obtain MLWFs obviously does not influence the more localized d -orbitals, as mentioned above. Only the s and d_{z^2} states are affected, but the decay of the hopping integrals is exponential irrespective of the Wannier representation, as shown in Figure 6.9. In such a case the electronic structure rapidly converges with increasing number of considered neighbors, the basis set remains optimally small and the ballistic transport calculations can be performed with minimal computational effort. For all considered transition metal wires, even those exhibiting complex magnetic order, a similar rate of decay, as shown for the Pt monowire in Figure 6.9, has been found. It is seldomly necessary to describe monowire systems beyond 2nd or 3rd NN due to the rapid decay of the tight-binding Hamiltonian matrix elements with increasing NN distance for FSWFs and MLWFs (Figure 6.9). For systems more complicated than a Pt monowire, the initial choice of trial orbitals may not be straightforward. In such a case the localization procedure to obtain MLWFs significantly improves the accuracy of the calculation, while for systems with more intuitive choices of orbitals or systems where the orbital character is known, FSWFs are an excellent and accurate alternative for a quantum transport calculation.

An example that both Wannier representations are indeed in excellent agreement with respect to the ballistic transport properties is shown below for a Pt monowire

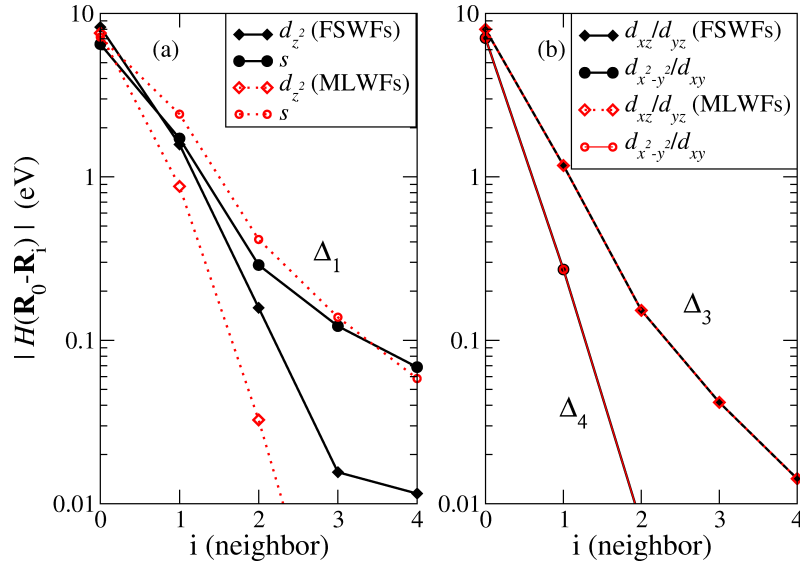


Figure 6.9: Real space hopping integrals between orbitals of the same type $|H(\mathbf{R}_i - \mathbf{R}_0)|$ as a function of the neighbor for a Pt monowire on a logarithmic scale. The hoppings were calculated both with MLWFs (open red symbols) and FSWFs (closed black symbols) for (a) s and d_{z^2} orbitals, and for (b) d_{xy} , $d_{x^2-y^2}$, d_{xz} and d_{yz} orbitals.

with one elongated bond in section 6.6.5.

6.6.2 Conductance and Transmission

Before focusing on more complex scattering potentials, first the characteristics and the typical shape of the energy dependent conductance and electron transmission will be discussed for the most simple system available at this point, the perfect Pt monowire. As derived in chapter 2, the conductance in case of a ballistic conductor is quantized with the conductance quantum $G_0 = 2e^2/h$ for a single spin-degenerate band. Further, the probability $T(E)$ for an electron to be transmitted through a junction and the conductance $G(E)$ have been shown to be connected (chapter 2.4, Eqn. (2.70)):

$$G(E) = \frac{2e^2}{h} T(E). \quad (6.31)$$

As a consequence, due to the absence of any scatterer in a perfect Pt monowire, every band contributes one G_0 to the conductance, resulting in the typical step-shape, shown in Figure 6.10. The general shape is caused by two very broad $s - d_{z^2}$ bands, ranging from -7 eV to -0.5 eV (depending on the NN approximation) and from -1.6 eV to 5 eV and Δ_3 and Δ_4 bands, which dominate the bandstructure, and hence the conductance, between -4 eV and 1 eV.

As expected from the previously calculated bandstructures, the 1st NN approximation is not precise enough for a good description of the conductance, while the

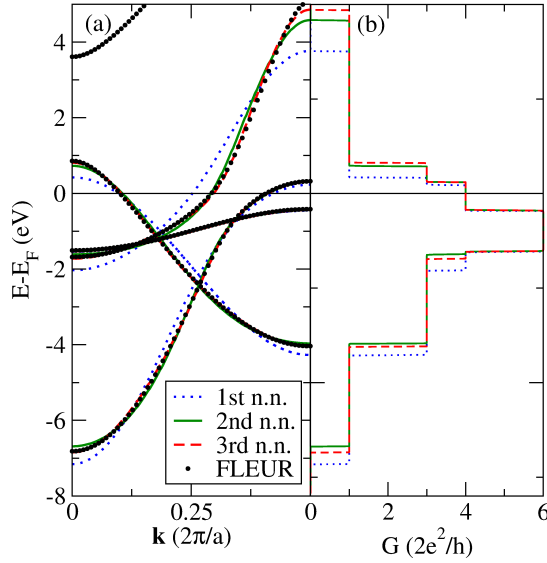


Figure 6.10: (a) Bandstructure for a perfect Pt monowire with $d_{\text{Pt}} = 4.48$ bohr. The bandstructures are derived from 1st (dotted blue lines), 2nd (solid green lines) and 3rd (dashed red lines) NN approximation tight-binding Hamiltonians. As a measure of the quality of the WFs Hamiltonian the FLAPW bandstructure (black dots) is displayed, too. (b) Corresponding conductances in 1st (dotted blue lines), 2nd (solid green lines) and 3rd (dashed red lines) NN approximation.

2nd and 3rd NN approximations already provide very good approximations of the conductance through a Pt monowire.

Another important aspect of perfect monowires is that they are used throughout this thesis as leads within the locking technique (cf. section 6.4). By introducing a scatterer into a perfect wire the transmission probability is reduced due to scattering processes. The lead conductances can therefore be regarded as an outer envelope for all conductance functions including a scatterer, given that the two leads are equal. For two inequivalent leads the maximal conductance is given by the inner envelope of both lead's conductance functions with matching orbital symmetry.

6.6.3 The Locking Technique

In the previous section the quality of the Wannier function representation of the Hamilton matrix with respect to the FLAPW electronic structure was discussed for perfect Pt monowires. In this section the applicability of locking technique will be demonstrated by further introducing a non-trivial scattering potential by elongating the central Pt bond by $\Delta = 0.72$ (cf. Figure 6.7). For this purpose, conductances are compared based on a rather small 6 atom and a 12 atom super cell FLAPW calculation for the scattering region. The perturbation induced by the central stretched bond decays only slowly with wire length in this one-dimensional

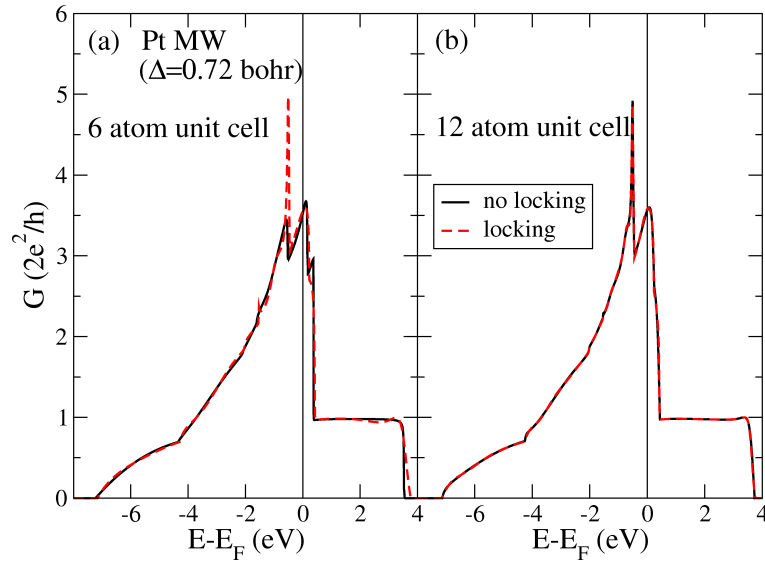


Figure 6.11: Conductance for a Pt monowire with a single bond stretched by $\Delta = 0.72$ bohr using MLWFs within the nearest-neighbor approximation for the transport Hamiltonian and (a) a 6 atom super cell and (b) a 12 atom super cell for the FLAPW calculation of the scattering region. The semi-infinite leads have been described using the super cell calculation (solid lines) or using the locking technique (dashed lines) with perfect Pt monowires as leads.

system and still has a larger effect on the end atoms in the 6 atom unit cell than in the rather large 12 atom unit cell. The quantum conductances obtained for both cases without applying the locking-technique, by constructing the semi-infinite leads from the end atoms of each super cell calculation in 1st NN approximation, are qualitatively similar, but still differ in key details such as e.g. a sharp peak just below the Fermi energy (compare Figure 6.11(a) and (b)).

In principle, all relevant information about the scattering potential are already included in the 6 atom unit cell calculation. The main difference compared to the 12 atom unit cell calculation is due to the perturbed electronic structure at the end atoms, resulting in deviations from the pure lead electronic structure in case of the smaller super cell. To eliminate this main error source, the leads are replaced by separate FLAPW calculations of perfect periodic Pt-monowires, describing the leads with maximal accuracy, e.g. without the perturbation due to the scatterer.

The conductances change as follows: While the conductance based on the 12 atom super cell calculation is nearly independent on how the lead was constructed, indicating the end atom to be very similar to a perfect leads atom as stated above, the result for the 6 atom calculation improves significantly upon using the locking technique and is almost indistinguishable from the calculation in the larger 12 atom super cell, while demanding significantly less computational resources. This demon-

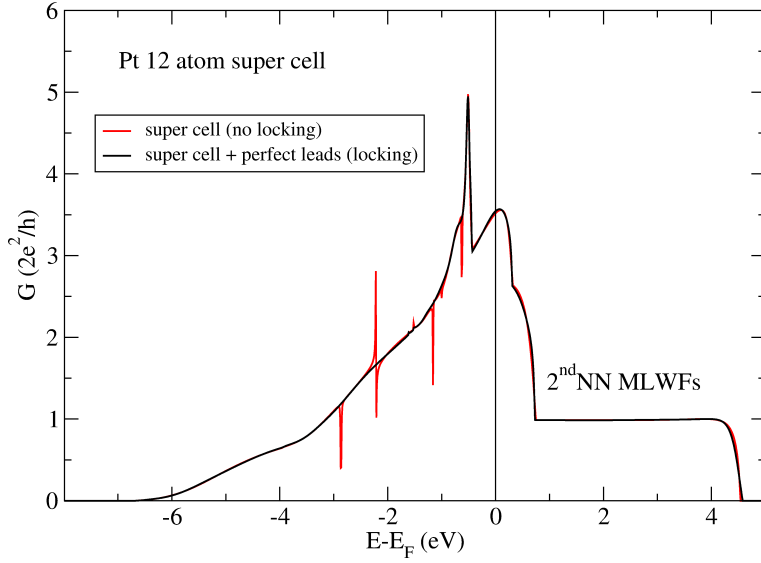


Figure 6.12: Conductance for the Pt monowire with a central elongated bond of $\Delta = 0.72$ bohr, calculated in a 12 atom super cell within 2nd NN approximation using MLWFs. Conductance obtained from a supercell calculation (solid red lines), including artificial peaks due to an inaccurate description of the leads from the super cell and the conductance obtained from a supercell calculation within the locking-technique (solid black lines) with perfect Pt leads, taken from a separate 6 atom unit cell FLAPW calculation of the perfect Pt leads.

strates the applicability and quality of the locking technique which allows to save a considerable amount of computational effort to calculate the ballistic transport properties of a nanojunction.

Another problem arises for the construction of a transport Hamiltonian for descriptions beyond 1st NN approximation without locking technique. While the lead constructed from a single super cell may converge to a true leads atom, as shown in Figure 6.11, typically neighboring atoms of non-trivial systems differ at least slightly due to the presence of a non-trivial scattering potential. Even such a slight perturbation lifts the equivalence of the identical lead atoms and thus artificially increases the periodicity of the leads. Even for a rather large 12 atom Pt supercell with one elongated central bond of $\Delta = 0.72$ bohr, which has previously been shown to have a lead-like end atoms, the inequivalency of two neighboring end atoms, assigned to be leads, results in spurious artificial peaks in the conductance, as shown in Figure 6.12. Those peaks are due to the gaps at the zone boundaries of the bandstructure, caused by two slightly inequivalent lead atoms. However, replacing the leads by perfect Pt monowires within the locking-technique solves this misconception in the description (cf. Figure 6.12)

Similar artifacts can be obtained for conductances based on Hamilton matrices

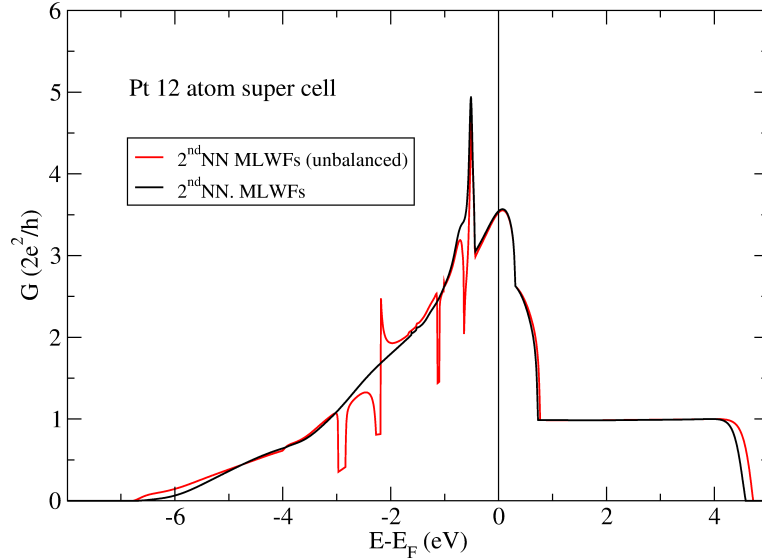


Figure 6.13: Conductance for the Pt monowire with a central elongated bond of $\Delta = 0.72$ bohr, calculated in a 12 atom super cell within 2^{nd} NN approximation using MLWFs and the locking-technique: The correct description without excess hoppings beyond 2^{nd} NN approximation (solid black line) and the result including those excess hoppings (solid red line) and the resulting artificial peaks.

containing unbalanced hoppings (cf. section 6.2, Figure 6.2), as shown in Figure 6.13. In this Figure the conductance is described in 2^{nd} NN approximation, based on principal layers of 2 atoms (cf. section 6.2) and section 6.3. While canceling all excess hoppings beyond 2^{nd} NN results in a consistent description, keeping an unbalanced Hamiltonian including e.g. the 3^{rd} NN hopping elements, resulting in artificial peaks due to the same reasons stated above.

Next, the accuracy of a conductance will be determined for a non-trivial scattering region with respect to the number of neighbors included. In Figure 6.14 (a) the conductances are presented, obtained in first, second, and third nearest-neighbor approximation based on the 12 atom super cell for the scattering region with one stretched bond of $\Delta = 0.72$ bohr. The main effect, which can be observed upon including more neighbors into the description, can be related to the previously shown bandstructures of the leads (cf. Figure 6.8 (a)). The conductance in the vicinity of the Fermi level does not change significantly with increasing number of considered neighbors. However, since the bandwidth of the lead's states strongly depend on the NN approximation, such effects can be seen in the conductance. For example, there is a shift between the 1^{st} NN and the $2^{\text{nd}}/3^{\text{rd}}$ NN conductances around 0.5 eV, which can be traced back to a similar shift in the Δ_3 band in the bandstructure (cf. left zone boundary in Figure 6.8 (b)). The increasing bandwidth and successive improvement of the Δ_1 band description with an increasing number of considered neighbors can be

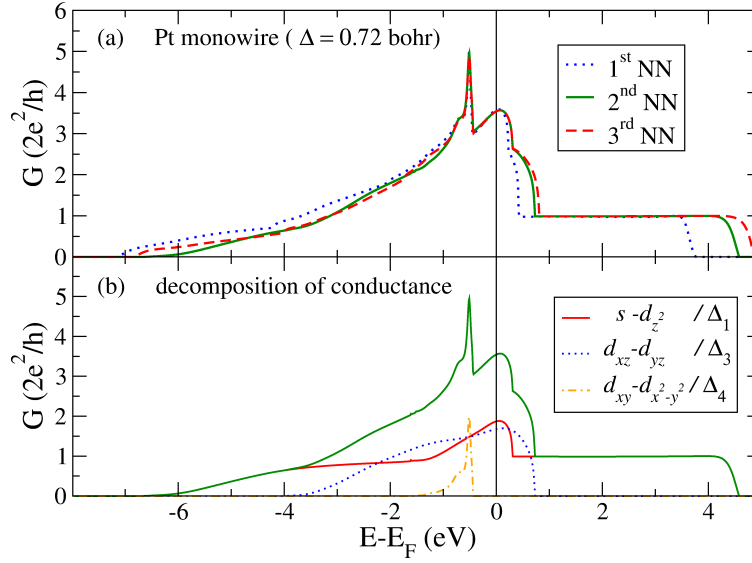


Figure 6.14: (a) Conductance for a Pt monowire with a single bond stretched by $\Delta = 0.72$ bohr based on a 12 atom super cell calculation using the first, second, and third nearest-neighbor approximation for the construction of the transport Hamiltonian from MLWFs and the locking technique to attach the leads. (b) Decomposition of the total conductance (solid line) for the second nearest-neighbor approximation into the contributions of the $s - d_{z^2}$ (Δ_1) (solid red line), the $d_{xz} - d_{yz}$ (Δ_3) (dotted blue line) and the $d_{xy} - d_{x^2-y^2}$ (Δ_4) (dashed-dotted orange line) channels.

likewise seen in Figure 6.14, resulting e.g. in an extended conductance above 4 eV for the 2nd and 3rd NN approximation. For an accurate description of quantum transport processes, a large number of NN (≥ 3) is preferable. However, since the focus of the present description is on the energy region around the Fermi level within the linear response regime, the 2nd NN approximation is already sufficient in absence of e.g. Δ_1 band edges in that particular energy region. Additionally, the convergence of the lead bandstructure with respect to the FLAPW electronic structure (cf. Figure 6.8) can give an estimation on the accuracy of the whole transport calculation, as long as the Wannier orbitals in the scattering region possess similar localization properties, which can be seen in their spreads.

6.6.4 Decomposition of Transmission and Density-of-States

While the contribution of distinct bands is easily identifiable in periodic junctions, such as the perfect Pt monowire, discussed in chapter 6.6.2, due to the known bandstructure, it is necessary to decompose the transmission function with respect to the orbital symmetry of the Wannier functions for non-trivial scattering potentials (cf. section 6.5). Such a decomposition of the transmission function or the conductance can provide additional insights into ballistic transport calculations.

In Figure 6.14 (b) such a decomposition is shown for the Pt monowire with a stretched central bond of $\Delta = 0.72$ bohr in 2nd NN approximation. The Δ_1 ($s - d_{z^2}$) states provide an almost perfectly conducting channel in a large energy range. Only far below the Fermi energy its value drops significantly below $2e^2/h$. In the vicinity of the Fermi energy two Δ_1 orbitals overlap, resulting in a broad peak in the conductance (cf. the bandstructure in Figure 6.8). The conductance of the more localized Δ_3 ($d_{xz} - d_{yz}$) states is situated around the Fermi level and possesses a smaller bandwidth than the Δ_1 channel. The Δ_4 ($d_{xy} - d_{x^2-y^2}$) orbitals only contribute in a small energy window, ranging from -0.5 to -1 eV below the Fermi level, due to being the most localized orbitals. The total conductance at the Fermi level is therefore nearly to the same extend due to Δ_1 and Δ_3 states.

Another important quantity, provided by the Green's function description of the open quantum system, is the locally and orbitally resolved density of states (DOS) (cf. section 6.5), as shown in Figure 6.15. Figure 6.15 (a) shows the Green's function DOS for perfect Pt leads and, below, the orbital decomposition into Δ_1 , Δ_3 and Δ_4 states that can be related to the Pt bandstructures in Figure 6.8. In Figure 6.15 (b) and (c) the DOS and its orbital decomposition of the Pt monowire with a central stretched bond of $\Delta = 0.72$ bohr for one Pt atom in contact with the leads and one Pt atom with an elongated bond in the center of the junction are displayed, respectively. In comparison, the DOS obtained based on FLAPW super cell calculations of the scattering region are displayed. Although the shape of the DOS is similar for the open quantum system and the super cells, there are e.g. additional oscillations in the FLAPW DOS between -4 eV and -2 eV beyond the Fermi level. These oscillations are caused by the finite size of the super cell, not including e.g. the effect of level broadening due to semi-infinite leads within the open quantum system (cf. chapter 2.4). The decomposition of the DOS of the open quantum system in the $s - d_{z^2}$, $d_{xz} - d_{yz}$ and the $d_{xy} - d_{x^2-y^2}$ channels allows further insight into the orbital character of the states of every atom.

The DOS of the lead atoms (cf. Figure 6.15 (a)) are by construction identical to the DOS of the perfect Pt MW (cf. Figure 6.14). The Pt atom in contact with the lead (cf. Figure 6.15 (b)) still exhibits DOS qualitatively similar to the perfect MW. The DOS of the central Pt atom in contact to the elongated bond (cf. Figure 6.15 (c)) displays e.g. a sharper Δ_4 peak and overall a smaller Δ_3 and Δ_4 bandwidth due to the reduced hybridization across the elongated bond.

The orbitally and locally resolved DOS is especially useful to investigate ballistic transport calculations in combination with the decomposition of the conductance for chemically more diverse nanojunctions, containing e.g. more than one type transition metal. In such nanojunctions the DOS of the open quantum system can help to identify conductance channels and effects of the orbital symmetry and the electronic structure on the conductance, such as e.g. an energy mismatch between symmetry related states on neighboring atoms, preventing electron transport for those states.

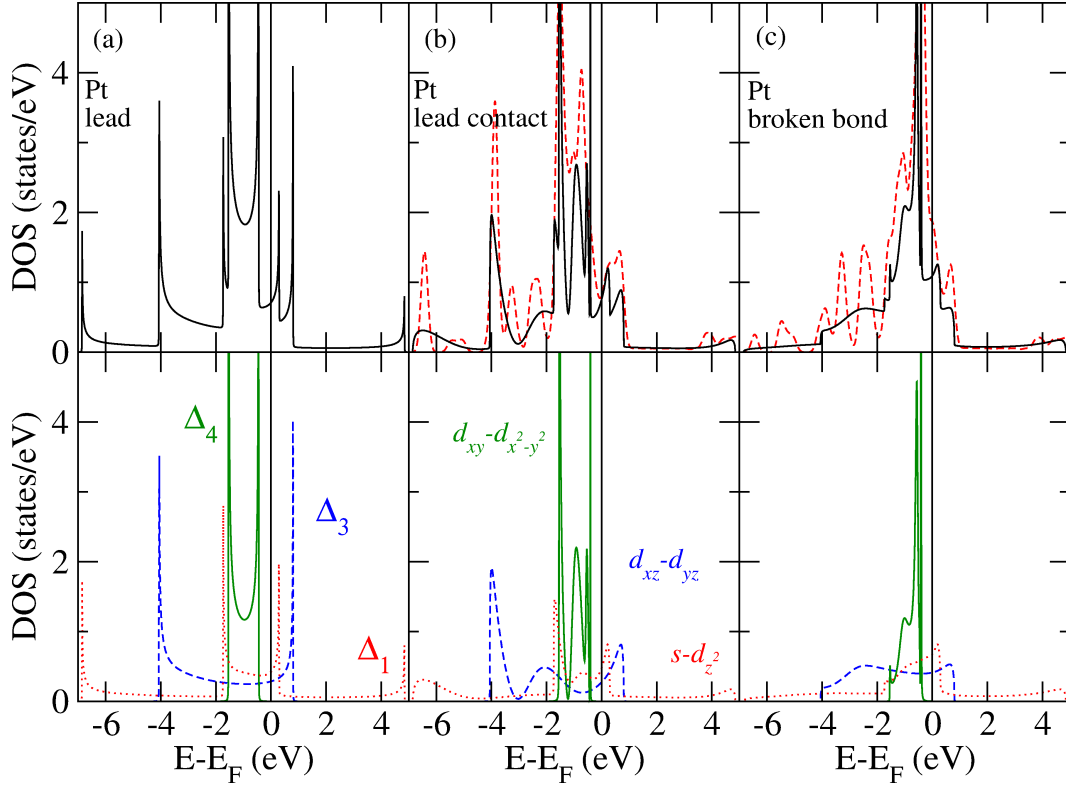


Figure 6.15: Density of states (DOS) of a Pt junction with one elongated central bond ($\Delta = 0.72$ bohr) calculated in a 6 atom super cell and locking-technique in 3rd NN approximation using MLWFs for (a) an atom in the lead, (b) the outmost atom of the scattering region in contact with the lead and (c) a Pt atom next to the broken bond. The upper graphs are the DOS for the open quantum system (solid black lines) and the DOS of the supercell calculated within the FLAPW method (dashed red lines). The lower graphs exhibit the orbital decomposition of the DOS into $s-d_{z^2}$ (Δ_1) (dotted red lines), $d_{xz}-d_{yz}$ (Δ_3) (dashed blue lines) and $d_{xy}-d_{x^2-y^2}$ (Δ_4) (solid green lines) channels within the NEGF description.

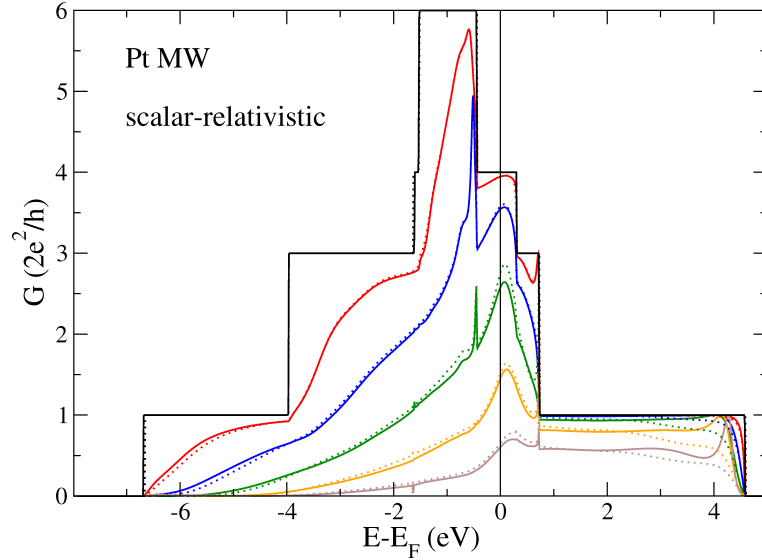


Figure 6.16: Conductance for a nonmagnetic Pt monowire in the scalar-relativistic approximation, i.e., neglecting spin-orbit coupling, with a single bond stretched by Δ . The second nearest-neighbor approximation has been used for the transport Hamiltonian. The WFs and hopping matrix elements have been constructed from a 12 atom super cell and the leads were described by the locking technique. Curves are shown for MLWFs (solid lines) and FSWFs (dotted lines) for $\Delta = 0.0, 0.34, 0.72, 1.22, 1.82$ and 2.52 bohr (from left to right).

6.6.5 Conductance upon Bond-Stretching

Finally, after presenting all important tools to investigate ballistic transport, the conductance of the Pt monowire can be calculated as a function of the length of the central bond, shown in Figure 6.16. For the conductance of a perfect Pt wire, the expected step-function shape is obtained with each band contributing one conductance quantum G_0 per spin within its bandwidth. Upon increasing the length of a single bond in the wire, mimicking e.g. break junctions or tunneling-to-contact STM experiments, the overlap between the Wannier orbitals across the gap decreases, especially for the more localized d -orbitals, and as a result the transmission drops dramatically. Accordingly, only the contribution originated from s - d_{z^2} states remain for large gap sizes, e.g. the sharp $d_{xy} - d_{x^2-y^2}$ peak at 0.5 eV vanishes above $\Delta = 1.82$ bohr (compare with Figure 6.15). Another important result of this calculation is that the Hamiltonians obtained with MLWFs and FSWFs provide nearly the same results, i.e., the trial orbitals based on the radial solutions of the FLAPW potential are evidently a reasonable choice for this system, as stressed in section 6.6.1.

A comparison between Figure 6.16 and Figure 6.17, where the transmission function of a Pt monowire with a central stretched bond of $\Delta = 0.38$ bohr is displayed, shows an excellent agreement between the NEGF and FLAPW ballistic transport

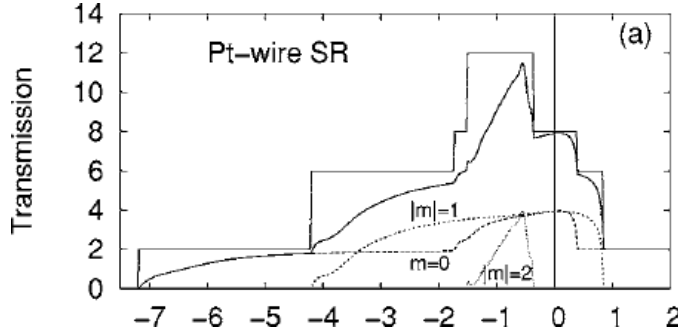


Figure 6.17: Transmission function for a Pt monowire, calculated within a scattering approach in combination with a pseudopotential method for the electronic structure, with $d_{\text{Pt}} = 4.48$ bohr (upper curve) and with an elongated central bond $\Delta = 0.38$ bohr (curve beneath) with decomposition into the orbital character $|m|$, taken from [69]. The definition of the transmission function here is based on the definition of conductance quantum as $G'_0 = e^2/h$, in contrast to the conductance quantum defined as $G_0 = 2e^2/h$ within this thesis, resulting in a factor of 2 difference between both representations (cf. Figure 6.16).

method, introduced in this thesis, and the scattering approach in combination with a pseudopotential method for the electronic structure [69].

6.6.6 The Effects of Spin-Orbit Coupling on Ballistic Transport

For heavy transition metals such as Pt, being a $5d$ transition metal with the nuclear charge of $Z = 78$, spin-orbit coupling plays an important role and has a significant impact on the electronic structure. As a result, the transport properties should be equally affected, since they are strongly related to the electronic structure. A suitable method to describe the quantum conductance in such systems has to be capable of treating SOC. The effect of SOC on the electronic structure, namely the coupling of the spin quantum number $s = \frac{1}{2}$ and angular momentum quantum number $l = 0, 1, 2, \dots$ to the total angular momentum quantum number $j = \frac{1}{2}, \frac{3}{2}, \frac{5}{2}, \dots$ can be seen in Figure 6.18. Compared to the scalar-relativistic calculation, in which SOC is neglected (cf. Figure 6.8), the bandstructure including SOC changes significantly, Figure 6.18. In the chain geometry, the states are eigenfunctions to the z -component (chain axis) of the total angular momentum and the bands can be classified by the absolute value of m_j as shown in Figure 6.18 (a). Thereby, spin-orbit coupling leads to several avoided crossings in the bandstructure, e.g. the $s - d_{z^2}$ and d_{xz}/d_{yz} -band around -3 eV below the Fermi level.

With respect to the scalar-relativistic bandstructure, significant shift of the d_{xy} and $d_{x^2-y^2}$ -bands towards the Fermi energy can be also observed. As this band touches the Fermi energy at $k = \frac{\pi}{a}$ the conductance jumps from $4G_0$ in the scalar-relativistic case to a value of $5G_0$. This very significant change in conduction by

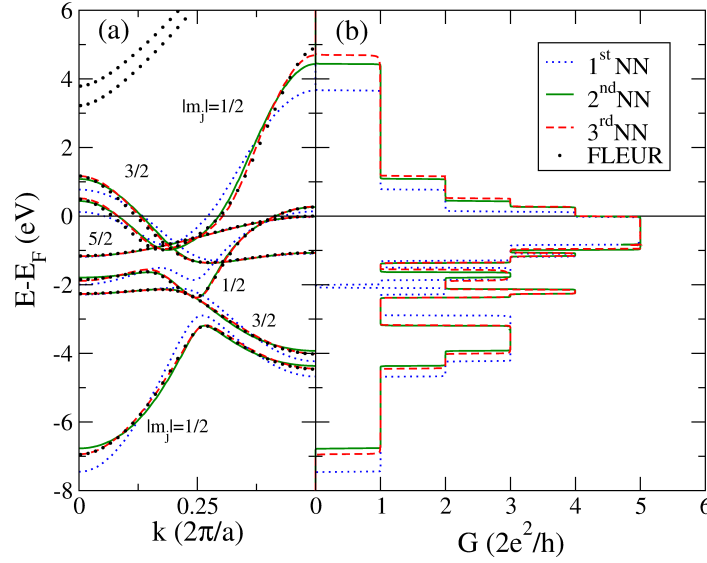


Figure 6.18: Bandstructure of an infinite nonmagnetic Pt monowire including spin-orbit coupling. (a) Bandstructure from the FLAPW calculation (big dots) and using the Hamiltonian from FSWFs within the first, second, and third nearest-neighbor approximation. (b) Conductance based on FSWFs for 1st (dotted line), 2nd (dashed line) and 3rd (solid line) NN approximation.

simply accounting for SOC already demonstrates the importance of SOC for quantum transport calculations in such systems. The convergence with respect to nearest neighbors considered is similar to the scalar-relativistic case, even though the systems electronic structure is more complex in this description and the hopping elements $H_{n,n'}^{\sigma\sigma'}(\mathbf{R}_i - \mathbf{R}_j)$ are in general not real valued any more. Again, already a 2nd NN approximation description reproduces the Pt SOC bandstructure quite accurately. The general shape of the conductance function in presence of SOC changes significantly, too, due to the lifted degeneracies of bands with different $|m_j|$ -values (see Figure 6.18 (b)).

While the conductance at the Fermi level is enhanced upon taking SOC into account, the degeneracy of the d_{xy} and $d_{x^2-y^2}$ -bands in the SR case leads to a higher conductance of $6G_0$ below the Fermi energy. Another key difference due to SOC is the larger number of steps which appear in the conductance as a result of the anti-crossings in the bandstructure, in particular, in the energy range of -3 eV to -1 eV below the Fermi level, leading to a area of significantly reduced conductance due to a huge anti-crossing in the hybridized $s - d_{z^2}$ bands. In Figure 6.19, also the evolution of the conductance is displayed upon stretching a single bond in the Pt monowire. Similar to the SR case, a rapid decrease of the conductance is observed due to more localized d -orbitals. However, due to the spin-orbit split bands there is a more pronounced peak structure in the conductance. In particular, a sharp

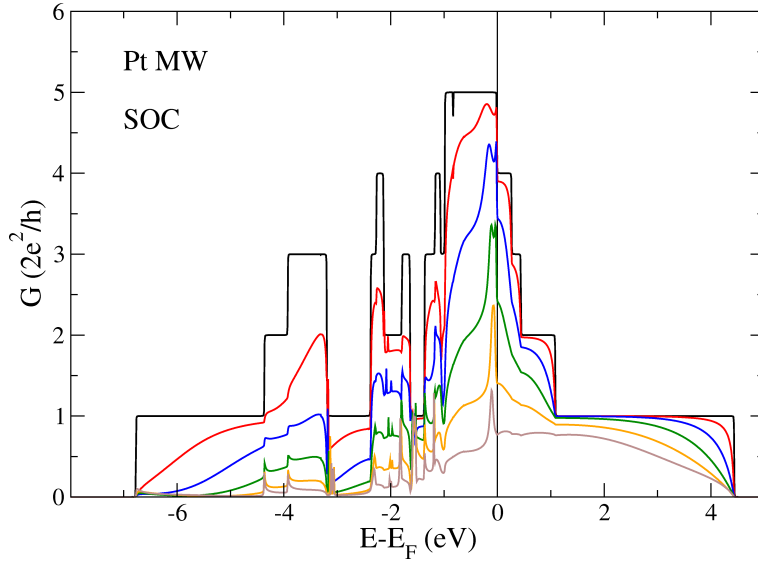


Figure 6.19: Conductance for a nonmagnetic Pt wire with a single stretched bond $d_{\text{Pt}} + \Delta$ including spin-orbit coupling calculated within a 6 atom super cell and using locking to semi-infinite Pt leads based on the Hamiltonian obtained from MLWFs in second nearest-neighbor approximation. From left to right: one bond stretched by $\Delta = 0.0, 0.34, 0.72, 1.22, 1.82$ and 2.52 bohr.

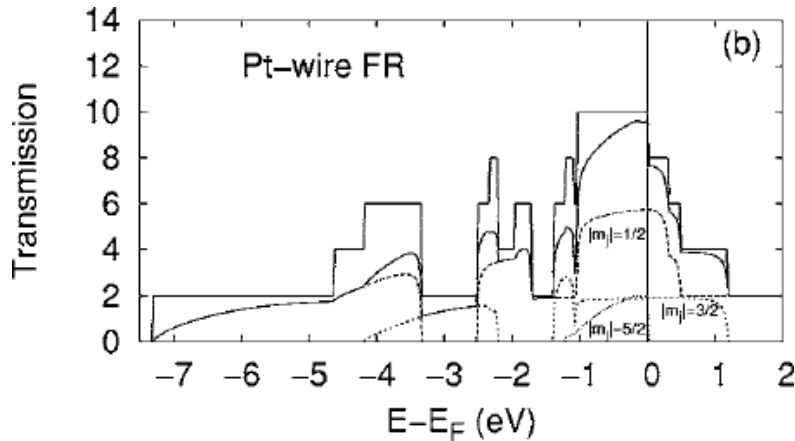


Figure 6.20: Transmission function obtained within a scattering approach in combination with a fully relativistic pseudopotential method for the electronic structure for a Pt monowire with $d_{\text{Pt}} = 4.48$ bohr (upper curve) and with an elongated central bond $\Delta = 0.38$ bohr (curve beneath) with decomposition into the orbital character $|m_j|$, taken from [69]. The definition of the transmission function here is based on the definition of conductance quantum as $G'_0 = e^2/h$, in contrast to the conductance quantum defined as $G_0 = 2e^2/h$ within this thesis, resulting in the factor 2 difference to Figure 6.19.

peak just below the Fermi energy is found which decays more slowly than in the SR calculation where it is located slightly lower in energy. The calculations of the conductance are in good agreement with those obtained based on fully relativistic ultrasoft pseudopotentials and a scattering approach to obtain the conductance [69], as shown in Figure 6.20 for a Pt monowire with a stretched central bond of $\Delta = 0.38$ bohr.

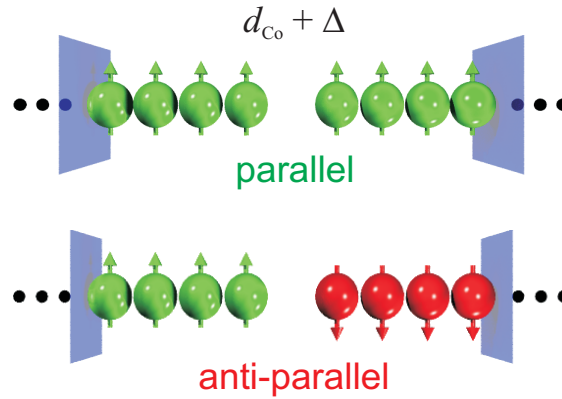


Figure 6.21: Sketch of the scattering regions of FM Co chains used to calculate the magnetoresistance: Two parallel FM Co chains with a central elongated bond ($d_{\text{Co}} + \Delta$) and two antiparallel FM Co chains with a central elongated bond.

6.7 Ferromagnetic Co Monowires

As a second test system, a ferromagnetic (FM) Co monowire with a central stretched bond, as sketched in Figure 6.21, is chosen. The ferromagnetism in the junction allows to investigate spin-polarized ballistic transport calculations and the analysis of ballistic magnetoresistance. The ballistic magnetoresistance is the difference in conductance achieved by switching the FM leads from parallel (P) to antiparallel (AP) alignment (see Figure 6.21). The general P vs AP setup can be achieved in a tunneling-to-contact spin-polarized STM experiment [5] or a magnetic break junction. The results of the antiparallel configuration can be compared to calculations performed by Smogunov *et al.* based on the scattering approach and pseudopotentials [81].

Parts of the results have been published in reference [79].

Computational Details

The ferromagnetic Co monowire was described within the FLEUR code [63] with a lattice constant of $d_{\text{Co}} = 4.15$ bohr and a single stretched bond in the center of the scattering region. This bond was successively stretched by values of $\Delta = 0.0, 0.45, 1.05, 1.85$ and 2.85 bohr. Two collinear magnetic configurations of the Co monowire were considered: either with parallel or antiparallel alignment of the Co spins on the left and on the right sides of the gap. Therefore, two calculations had to be performed: For the parallel aligned leads a scattering region consisting of a 8 atom super cell, constructed from two 4-spin blocks separated by a gap Δ (cf. Figure 6.21) and for antiparallel alignment a 16 atoms in the super cell with 4-spin (up), 8-spin (down) and 4-spin (up) blocks, separated by two gaps Δ with the spin blocks aligned antiparallel to each other at each side of the gap.

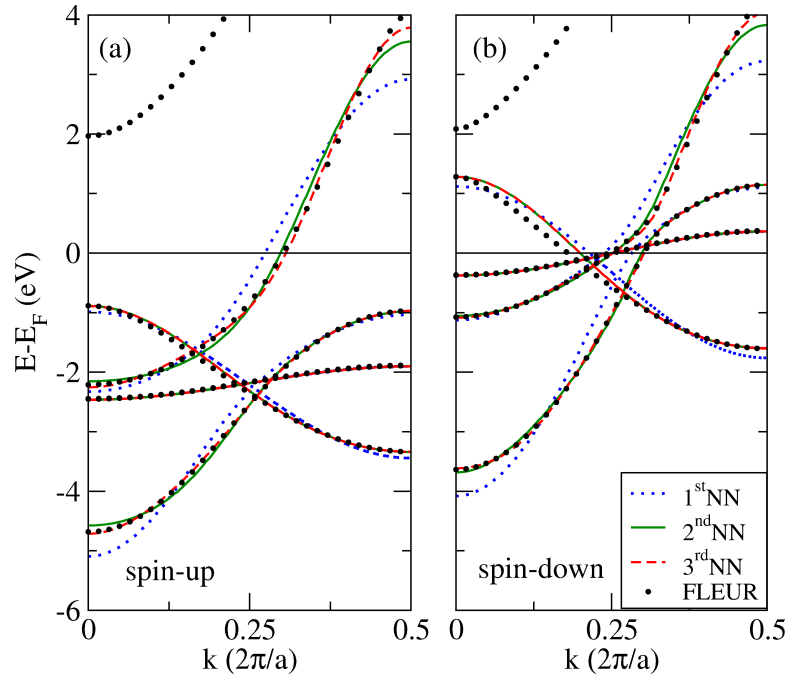


Figure 6.22: (a) Majority and (b) minority bandstructure for a ferromagnetic Co monowire with $d_{\text{Co}} = 4.15$ bohr calculated within FLAPW (big dots) and FSFWs in 1st (dotted lines), 2nd (dashed lines) and 3rd NN (solid lines) approximation.

The perfect lead was calculated as a ferromagnetic Co monowire with 24 k -points in the whole BZ, using a G_{max} of 4.1 bohr^{-1} (≈ 220 basis functions per atom). For both 8 and 16 atom super cell calculations the irreducible part of the 1D Brillouin zone (BZ) was sampled by 8 k -points and G_{max} was chosen to be 3.7 bohr^{-1} resulting in approximately 210 basis functions per atom. The vacuum parameters D_{vac} and \tilde{D} constituted 4.3 and 6.6 bohr, respectively, in all cases. The exchange-correlation potential was treated within GGA [103]. For all quantum conductance calculations the locking technique (see chapter 6.4) to a perfect FM Co monowire was used. As trial orbitals for the FSFWs 6 s - and d -orbitals per atom and spin in the super cell were used, constructed from the solution of the radial *first-principles* potential. For the disentanglement procedure [136] the lowest 58 (110) eigenstates per k -point were used to obtain the 48 (96) WFs in the 8 (16) atom super cell calculation.

6.7.1 The Magnetoresistance

The bandstructure of the ferromagnetic Co chain exhibits, compared to the non-magnetic Pt bandstructure in section 6.6.2, a smaller band width due to more localized $3d$ -states (compared to the $5d$ -states), and a large exchange splitting (see Figure 6.22). The exchange splitting leads to a net spin moment in the unit cell of $2.13\mu_B$ and ferromagnetic order.

The bandstructure can be approximated by FSWFs in 3rd NN approximation. For the d -bands and the s - d_{z^2} bands in the interesting energy region around the Fermi energy even the 2nd NN approximation is sufficient. The main difference between the FLAPW calculation and the FSWFs description is the upper s - d_{z^2} band edge 3 eV above the Fermi level. Since at 2 eV an additional band originates at $k = 0$, not included in the chosen set of Wannier functions, the description of the system is not valid any more in that energy region. With focus on quantum transport in the vicinity of the Fermi level, representing the linear response regime, the 2nd NN approximation is fully sufficient for all quantum transport calculations. For a description of the electronic structure beyond 2 eV above the Fermi level, more Wannier functions and a larger set of NN would be necessary to describe the system precisely, but without any improvement of the accuracy for the present quantum transport scheme. From the spin-split bandstructure a larger conductance in the parallel magnetization alignment can be expected due to the presence of Δ_3 and Δ_4 minority bands at the Fermi level, as shown in Figure 6.23. In the antiparallel case the majority and minority channels are exchanged for one lead, blocking the Δ_3 and Δ_4 contributions. A positive magnetoresistance (MR) caused by Δ_3 and Δ_4 minority bands in the parallel case is therefore expected for this system.

This can be observed in Figure 6.23, where at the Fermi level the majority and minority spin conductances are $G_{\text{maj}} = 0.5 G_0$ and $G_{\text{min}} = 3 G_0$ at the Fermi level for the perfect parallel ferromagnetic Co monowire (see Figure 6.23 (a)). With increasing stretching of the central bond the minority state conductance drops rapidly because of the strong localization of the $d_{xz,yz}$ - and d_{xy,x^2-y^2} -states. The majority and the residual $s - d_{z^2}$ minority state conductance, on the other hand, decay slower due to the more delocalized $s - d_{z^2}$ -states.

In the antiparallel alignment (Fig 6.23 (b)), the conductance is equal in both spin channels. There is only a small energy window between 1 eV and 1.7 eV below the Fermi energy in which the $d_{xz,yz}$ -states overlap and contribute to the transport process. This energy window corresponds to the overlap region between the majority states and the minority states of $d_{xz,yz}$ -symmetry of the ferromagnetic leads, shown in the same Figure (Fig 6.23 (b)). Since the left and right leads are aligned antiparallel, majority and minority channels are exchanged for one lead. Transmission is therefore only possible for states, that are simultaneously present in both leads. This can be seen, i.e., at the abrupt drop of conductance below -3.5 eV for the $s - d_{z^2}$ -channel, caused by the lower minority state band edge. For the same reason, there is no d_{xy,x^2-y^2} -state transmission in the antiparallel case, the conductance is dominated by the $s - d_{z^2}$ -states and there is only $s - d_{z^2}$ -state transmission at the Fermi level.

The conductance in the antiparallel alignment can be interpreted as an inner envelope of spin-up and spin-down transmission functions calculated for the parallel ferromagnetic case, the more rounded shape of the d -state contribution originates from the non-perfect matching of orbitals from one lead to the other. In a more

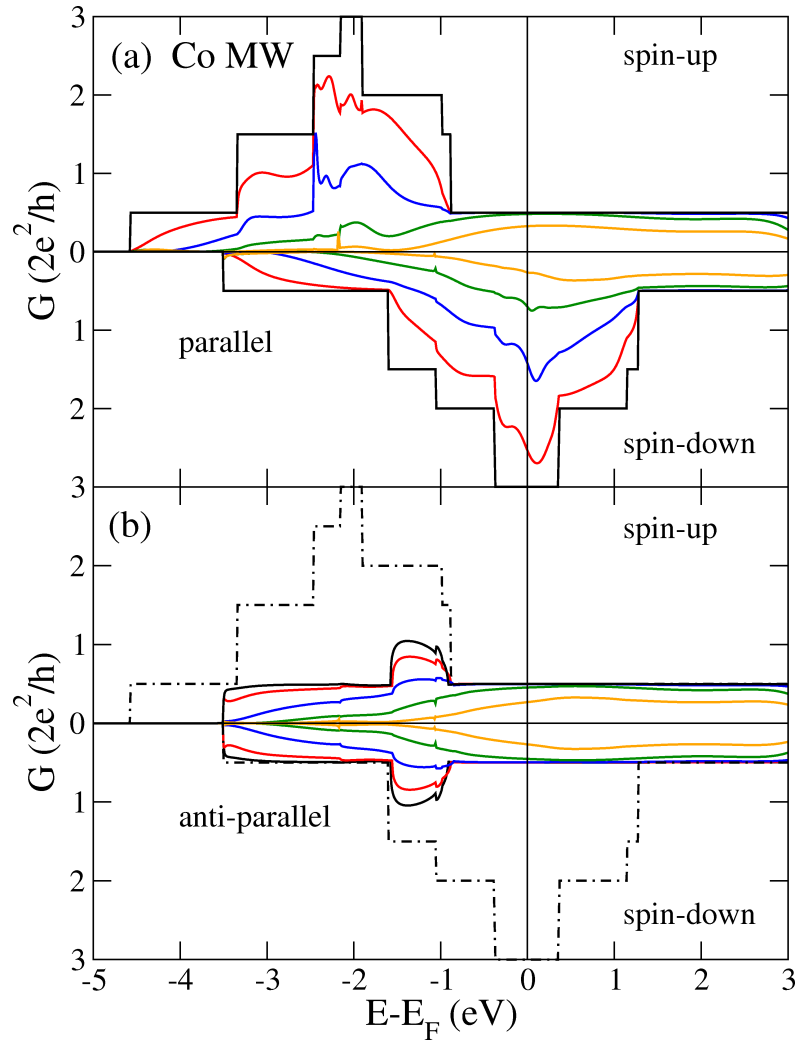


Figure 6.23: Conductance between two ferromagnetic Co monowires separated by a gap, Δ , in (a) parallel and in (b) antiparallel alignment of the magnetization. A super cell of 16 atoms has been used for the scattering region and the transport Hamiltonian was constructed based on FSWFs in the second NN approximation. From left to right: gap of $\Delta = 0.0, 0.45, 1.05, 1.85$ and 2.85 bohr. Upper and lower part of the plots show the spin-up and spin-down transmission channel, respectively.

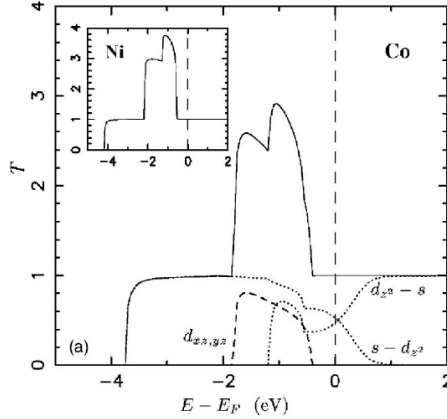


Figure 6.24: Transmission function obtained within a scattering approach in combination with a fully relativistic pseudopotential method for the electronic structure for a FM Co monowire with $d_{\text{Pt}} = 4.15$ bohr in antiparallel alignment, taken from [81]. The definition of the transmission function here is based on the definition of conductance quantum as $G'_0 = e^2/h$, in contrast to the conductance quantum defined as $G_0 = 2e^2/h$ within this thesis, resulting in the factor 2 difference to Figure 6.23 (b).

complex system, i.e., with contributing d_{xy,x^2-y^2} -states, it is necessary to orbitally decompose the conductance to identify overlapping energy regions and the orbital contributions, respectively.

The conductance found in the antiparallel configuration is in good agreement with the results reported by Smogunov *et al.* using a scattering approach and pseudopotentials [81], as shown in Figure 6.24.

Based on the obtained quantum conductance at the Fermi level, the ballistic magnetoresistance can be calculated upon stretching the central bond. The ballistic magnetoresistance is defined as the difference between the conductance in the parallel and antiparallel alignment, divided by the antiparallel conductance:

$$\text{BMR} = \frac{G_{\text{P}}(E_{\text{F}}) - G_{\text{AP}}(E_{\text{F}})}{G_{\text{AP}}(E_{\text{F}})} \times 100\% \quad (6.32)$$

Figure 6.25 displays the evolution of the spin-resolved conductance as a function of gap size between both leads for the parallel and antiparallel configurations. The ballistic MR is shown in the inset of Figure 6.25 and shows a strong dependence on the central bond length. This strong dependence can be understood by analyzing the conductance channels. The total conductance of the parallel alignment is dominated by the minority d -states near to contact and rapidly decreasing upon stretching due to localization properties of those states. For larger distances the conductance of the parallel as well as the antiparallel configurations are dominated by $s - d_{z^2}$ -states, leading to diminishing ballistic MR. The ballistic MR can be strongly modified by

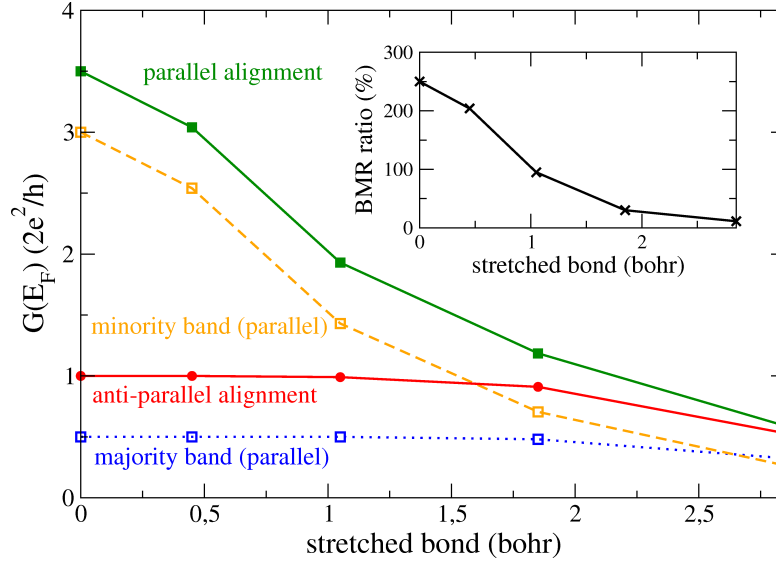


Figure 6.25: Conductance at E_F for the antiparallel (red filled circles, solid line) and the parallel (green solid squares, solid line) alignment of two ferromagnetic Co monowires as a function of separation. For the parallel case the decomposition into majority (blue open squares, dashed line) and minority (orange open squares, dotted line) contributions is given. The inset shows the ballistic MR ratio as a function of separation.

changing the distance between the two FM Co monowires and ranges from 250% in the contact regime to nearly 11.3% for a central bond length of 3.0 bohr.

These results outline the importance of resolving the conductance orbitally to completely understand the ballistic conductance of a given system. The tunneling-to-contact region, shown for the ballistic MR calculations in Figure 6.25, describes an intermediate region between the pure tunneling and the pure contact regime. It is known that the s -orbital contribution is dominant for larger distances between the leads, described, i.e., by the Tersoff-Hamann model for STM [150]. For some materials it is necessary to include d_{z^2} -orbitals to understand atomic resolution, i.e. provided by transition metal tips in (SP-)STM experiments, as shown by Chen [151].

The results in this chapter demonstrate, that for experiments in the intermediate tunneling-to-contact regime, e.g. $d_{xz,yz}$ - and d_{xy,x^2-y^2} -orbitals can play an important role in the conductance and magnetoresistance. Theoretical modeling of break-junction experiments [4] or SP-STM investigations [5–8] in the intermediate regime therefore requires an approach that is capable to describe both regimes, tunneling and contact, for a complete description of ballistic transport processes.

7 Ballistic Scattering on Impurities with SOC

In the previous chapter the new ballistic transport code was applied to systems with spin-orbit coupling (SOC) (Pt monowires in chapter 6.6) and high spin-polarization (Co monowires in chapter 6.7). It has been demonstrated, that both effects are significant for the ballistic conductance of nanoscale junctions, either due to the change of the electronic structure by the coupled spin and orbital space or due to the exchange split majority and minority states. While the latter give rise to a magnetoresistance between parallel and antiparallel aligned magnetic leads, the coupling of spin and orbital space in combination with an exchange splitting can result in ballistic anisotropic magnetoresistance (BAMR). The BAMR is not an effect of the relative alignment of lead's magnetic moments such as the magnetoresistance. Instead the coupling of the spins to the crystal field results in a difference in the conductance for different absolute spin orientations. Here, the rotation of the magnetic moments from parallel direction to perpendicular to the current (cf. Figure 7.1) results in a step-wise behavior of the conductance on the rotation angle related to the conductance quantum G_0 . This has been predicted [16] and was experimentally found in Co break junctions [14]. However, these conductance jumps are closely linked to the electronic structure of pure and locally periodic¹ nanojunctions. They can be understood in terms of bandstructure effects, where the rotation of the local quantization axis causes the opening of anti crossing band gaps and correspondingly to discrete conductance jumps due to the quantized conductance [14, 16]. Recent theoretical investigations studied the effect of a lifted local periodicity on the BAMR by introducing a broken central bond into a Ni nanojunction within density functional theory (DFT) [17]. The more complex electronic structure of such a system and the additional scattering potential were found to smooth out the step-like conductance behavior of the BAMR, resulting in a conventional anisotropic magnetoresistance (AMR) effect.

The aim of this chapter is to study the effect of spin-polarization and spin-orbit coupling on ballistic transport for model systems incorporating an impurity. Ballistic transport calculations for a similar system, a Ni impurity in a Au monowire, have been recently performed [152] without considering the effect of SOC. Two types of nanojunctions are investigated in this chapter: A magnetic Co impurity in a non-magnetic Pt monowire ($\text{Pt}_{\text{inf}} - \text{Co} - \text{Pt}_{\text{inf}}$) and a Pt-impurity in a ferromagnetic

¹Locally periodic system means that leads and scattering region can be described by e.g. perfect monowires connected with contacts which are far away. The electronic structure can then be described by the bandstructure of a perfect wire.

Co monowire ($\text{Co}_{\text{inf}} - \text{Pt} - \text{Co}_{\text{inf}}$). Both types of nanojunction combine the high spin-polarization of the Co atoms and heavy $5d$ Pt atoms, susceptible to large SOC effects due to their high nuclear charge. While for the magnetic Co impurity in a non-magnetic Pt monowire the question arises, whether a single magnetic impurity can give rise to BAMR, the focus on the investigation of the Pt-impurity in a ferromagnetic Co monowire is, whether the complex scattering potential of a Pt impurity can alter the BAMR to an AMR, similar to the previously reported Ni junctions with a stretched central bond [17].

Both model system introduced in this chapter can be seen as prototypical systems to theoretically describe contact spin-polarized scanning tunneling microscope (SP-STM) [5–8] or break junction (BJ) experiments [4, 14], where the semi-infinite leads describe the tip and sample (SP-STM) or the left and right contact (BJ) in with an central impurity atom. The direction of the magnetization could be either controlled by applying an external magnetic vector field or by exploiting a local exchange field in the junction. For example, it has been reported that the spin-direction of Co adatoms on one monolayer Mn on W(110) can be individually manipulated by SP-STM [18]. The spin-spiral state in the Mn monolayer on W(110) allows to quasi-continuously tune the spin-direction of a Co adatom due to the exchange coupling to the substrate by moving it laterally. In principle, this allows to investigate the angular dependence of the BAMR without applying an external magnetic field, even though the exchange coupling between the STM tip and the magnetic adatom might influence the outcome (cf. chapter 8.2).

This chapter provides results published in reference [79] and adds supplementary material.

7.1 Magnetic Impurity in a Non-Magnetic Wire

In this section the situation of a non-magnetic impurity in an otherwise non-magnetic monowire is considered. As a model system, a magnetic Co impurity is introduced into a non-magnetic Pt wire and the dependence of the conductance on the magnetization direction of the Co impurity is studied (cf. Figure 7.1). The Pt leads are non-magnetic and therefore do not exhibit BAMR. However, Pt can be magnetized in the scattering region due to the the magnetic Co impurity. Additionally, the influence of SOC is stronger for the heavy $5d$ Pt due to the large nuclear charge, which is certainly important for the ballistic transport properties.

The reduced symmetry in such a quasi one-dimensional junction results in a much larger magneto-crystalline anisotropy energy (MAE) as the orbital moments become more significant. E.g. freestanding and suspended chains of $4d$ - and $5d$ -transition-metals become magnetic and show giant values of the MAE [124, 125] and the effect of colossal magnetic anisotropy has been reported [126].

An important tool for the further analysis, as previously shown in chapter 6.6.4, is

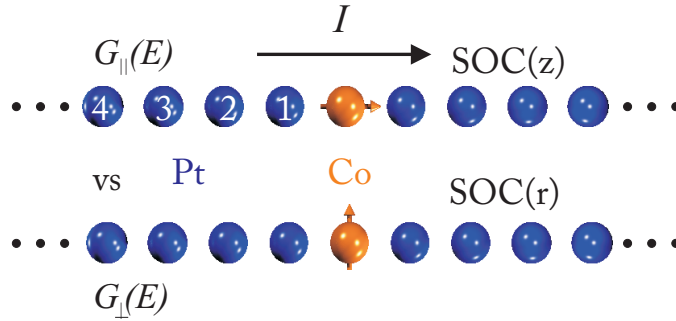


Figure 7.1: Sketch of the scattering region of the $\text{Pt}_{\text{inf}} - \text{Co} - \text{Pt}_{\text{inf}}$ junction: Pt wires (blue) with a magnetic Co (orange) impurity, possessing an in-chain quantization axis (SOC(z), upper wire) and an out-of chain quantization axis (SOC(r), lower wire). The difference between the conductances of both configurations ($G_{\parallel}(E)$ and $G_{\perp}(E)$) give raise to the ballistic anisotropic magnetoresistance or BAMR.

the locally resolved orbital decomposed transmission function and density of states (DOS), which allows to study the influence of SOC on the different transmission channels, as well as e.g. the effect of the local magnetization of Pt atoms due to the magnetic Co impurity on the conductance. These tools additionally allow to study a possible broken orbital symmetry in the chain due to e.g. an out-of-chain spin-quantization axis in case of SOC, resulting in an intermixing of spin-channels and spin-scattering processes, that do not conserve spin.

Computational Details

The electronic structure of the system was calculated within the FLEUR code [63] using a 9 atom super-cell for the scattering region consisting of one impurity Co and 4 Pt monowire atoms on both sides (cf. Figure 7.1). The interatomic distance was chosen as $d_{\text{Pt}} = 4.48 \text{ bohr}^2$ for the Pt monowire with a Co impurity. The exchange-correlation potential was treated within GGA [103] and SOC was included within second variation. In each case three calculations were performed: in the scalar-relativistic approximation, i.e. , without SOC, and for two different directions of the magnetization with SOC, namely, along the chain axis (SOC(z)) and perpendicular to it (SOC(r)). For all calculations the 1D Brillouin zone (BZ) was sampled by 16 k -points and G_{max} was set to 3.9 bohr^{-1} resulting in approximately 190 basis functions per atom for the Pt monowire with a Co impurity. The lead's electronic structure was obtained from calculations of perfect Pt monowires described in chapter 6.6. The vacuum parameters for all cases constituted 4.3 and 6.6 bohr for D_{vac} and \tilde{D} , respectively.

For all quantum conductance calculations the locking technique (cf. chapter 6.4) to the respective leads and the third nearest-neighbor approximation were employed.

²¹1 bohr = $5.2917721092 \times 10^{-11} \text{ m}$ ($\approx 0.529 \text{ \AA}$)

In the SR case FSWFs were generated on a 16 k -point mesh in the whole 1D-BZ with 1 s - and 5 d -orbitals per atom and spin, based on the radial solutions of the FLAPW potential. For the disentanglement procedure [136] the lowest 62 eigenvalues per k -point for 54 WFs for Co impurities in Pt monowires were considered. The Pt lead WFs were constructed as described in chapter 6.6. With SOC the FSWFs were generated on a 16 k -point mesh in the whole 1D-BZ with 2 s - and 10 d -orbitals per atom. For disentanglement [136] the lowest 116 eigenstates per k -point for 108 WFs were used. The Pt lead WFs with SOC was constructed as described in chapter 6.6.

7.1.1 The $\text{Pt}_{\text{inf}} - \text{Co} - \text{Pt}_{\text{inf}}$ Junction

The first system considered for ballistic scattering and transport with spin-orbit coupling on an impurity is a single magnetic Co atom in a Pt monowire. In particular, the nonmagnetic Pt leads have already been discussed with and without spin-orbit coupling in chapter 6.6. The conductance will be studied in dependence on the magnetization directions of the Co impurity atom, aligned in-chain or out of chain (cf. Figure 7.1), in order to calculate the ballistic anisotropic magnetoresistance. The BAMR is the normalized difference in conductance, when changing the magnetization direction from parallel to the current (G_{\parallel}) to perpendicular to it (G_{\perp})³:

$$\text{BAMR} = \frac{G_{\parallel} - G_{\perp}}{G_{\perp}} \times 100\%, \quad (7.1)$$

As previously mentioned, a change in the number of conducting bands results in a step-like behavior of the BAMR due to the discrete conductance jumps of G_{\parallel} or G_{\perp} , related to the conductance quantum G_0 [14, 16]. A system can only exhibit BAMR ($G_{\parallel}(E) \neq G_{\perp}(E)$) when spin- and orbital space are coupled by spin-orbit coupling and thus the direction of the spin-quantization axis becomes important.

Before the calculated conductance is discussed, the magnetic properties and the electronic structure of the system have to be studied. From the FLAPW calculations in the scalar-relativistic case a spin moment of $2.46\mu_B$ for the Co atom is obtained. The presence of a magnetic Co impurity induces spin moments of a magnitude of up to $0.27\mu_B$ in the neighboring Pt atoms, oscillating in sign and slowly decaying as a function of separation from the Co atom, as show in Table 7.1.

A very similar behavior is found upon including SOC in the calculations for both magnetization directions, with a Co spin moment of about $2.49\mu_B$. Including spin-orbit interaction into the calculations gives rise to finite values of the orbital moments of the atoms, which play an important role in determining the energetically favorable direction of the magnetization [124]. The orbital moments of the Co atoms are much larger than those of the adjacent Pt atoms, and constitute $0.12\mu_B$ and $0.19\mu_B$ for

³A more detailed discussion of the BAMR and the anisotropic magnetoresistance (AMR), which does not display conductance jumps, in nanojunctions with an impurity can be found in section 7.2.2

spin- and orbital moments (μ_B)	Pt MW	Pt ₁	Pt ₂	Pt ₃	Pt ₄	Co
scalar-relativistic	0.0	0.04	-0.17	-0.27	0.04	2.49
SOC(z) spin moment	0.0	-0.01	-0.03	0.03	0.28	2.49
SOC(z) orbital moment	0.0	0.03	-0.01	0.03	0.08	0.12
SOC(r) spin moment	0.0	0.06	-0.11	-0.19	0.09	2.48
SOC(r) orbital moment	0.0	0.03	-0.03	-0.08	0.01	0.19

Table 7.1: Spin- and orbital moments for the Pt_{inf} – Co – Pt_{inf} junction, in scalar-relativistic (SR) approximation and with the SOC quantization axis in chain (SOC(z)) and out of chain (SOC(r)), including the non-magnetic leads. The locations of Pt₁ to Pt₄ are shown in Figure 7.1.

the magnetization along the chain axis (z) and perpendicular to it (r), respectively. However, in accordance with [124], the resulting energetic preference of the in-chain magnetization direction over the out-of-chain direction, with a calculated magnetocrystalline anisotropy energy of 4.3 meV per magnetic atom, is due to the larger total sum of orbital moments, including the induced orbital moments of Pt, as shown in table 7.1.

The calculated conductance is presented in the three top panels of Figure 7.2 for the scalar-relativistic case and upon including spin-orbit coupling for the two different magnetization directions. For reference the orbitally decomposed conductance and the density of states of a perfect Pt monowire is given in each of the three plots and in the panels below, respectively. In comparison to the perfect Pt wires the introduction of a Co scatterer, that might seem as a minor modification, significantly reduces the conductance over the whole energy range. The overall reduction is due to the non-perfect matching between the spin-split Co $3d$ -states and the more delocalized Pt $5d$ -states (cf. the bandstructures in Figs. 6.8 and 6.22). In all three cases, a clear signature of the exchange-split Co Δ_3 -band can be observed in the conductance, most clearly visible in the spin- and orbital decomposition. As expected from previous results (compare chapter 6.6), the Δ_4 -bands are shifted towards the Fermi energy upon including spin-orbit coupling, but due to the energetic mismatch between the Co and Pt Δ_4 -bands (compare Figure 7.2 Pt monowire and Co monowire Δ_4 -DOS) in SR and for both magnetization directions with SOC, this band plays only a minor role in the overall conductance.

However, there is a considerable difference between the conductance at the Fermi level in the scalar-relativistic case, $G_{SR} = 1.40 G_0$, and both SOC quantization directions, either for z -magnetization, $G_{\parallel} = 2.25 G_0$, or r -magnetization, $G_{\perp} = 2.10 G_0$, as seen in Figure 7.3. The main reason for this large difference between SR and SOC conductances can be found in the Δ_1 band of SR Pt. In this channel the DOS is reduced compared to the SOC cases at the Fermi energy at the Pt NN atoms and there is a corresponding reduction of the conductance, as shown in Figure 7.2. The difference of $G_{\parallel} - G_{\perp} = 0.15 G_0$ between the two different

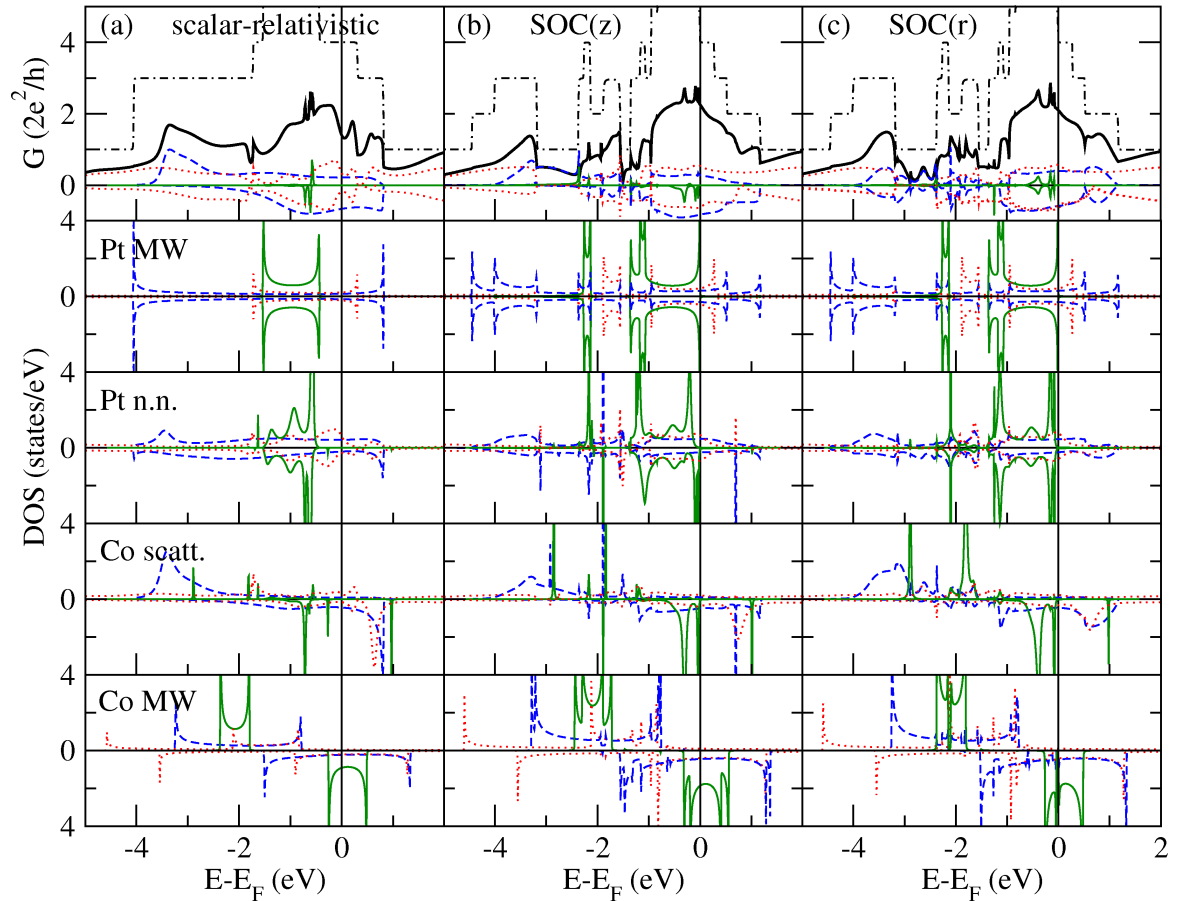


Figure 7.2: Conductance of a Pt monowire with a single Co impurity in (a) the scalar-relativistic approximation and including spin-orbit coupling for a magnetization (b) along the chain axis (z) and (c) perpendicular to it (r). In addition to the total conductance (black thick line) each panel shows the transmission for a perfect Pt monowire (dashed-dotted line) and orbital-decomposed into the Δ_1 - (red dotted line), Δ_3 - (blue dashed line), and Δ_4 -band (green solid line) contribution. The projection onto the spin-up and spin-down states is given for two different directions of the y -axis, respectively. Below each conductance panel the density of states is displayed in the corresponding electronic configuration, i.e., SR or SOC, for a perfect Pt monowire, the Pt atom adjacent to the Co impurity, the Co impurity, and a perfect Co monowire.

magnetization directions can be found in the larger minority Δ_3 -state contribution of the parallel aligned axis. Here, the SR and the parallel SOC case behave similarly. The DOS for Δ_3 majority states is small at the Fermi level, the majority state conductance is reduced in comparison to the minority state contribution, as a result of the exchange splitting of the Co scatterer.

Interestingly this is not the case for the r direction of the magnetization, for which majority and minority channels contribute equally to the total conductance. This effect also occurs for the Δ_3 minority channel between -2.8 eV and -3.9 eV as well as for the Δ_4 conductance just below the Fermi energy. While the very sharp spin-up Δ_4 -peak in the SR transmission at -0.7 eV can be traced back to a small spin-up Δ_4 peak in the DOS of the central Co atom at this energy, this is not the case for the mentioned regions in case of the r -magnetization, for which no majority Δ_3 and Δ_4 states are present at the scatterer. The origin of this effect is the broken cylindrical symmetry when the magnetization points out of chain. This broken symmetry allows for a hybridization between Δ_1 and Δ_3 orbitals with $j = \frac{1}{2}$, as well as between Δ_3 and Δ_4 orbitals with $j = \frac{3}{2}$. As a result an incident electron of $j = \frac{1}{2}$ ($\frac{3}{2}$) can be transmitted into a state with $j = \frac{1}{2}$ ($\frac{3}{2}$) of different orbital character and spin. This channel for scattering is less effective than the spin-conserving scattering for the in-chain magnetization, resulting in a larger conductance in this case.

7.1.2 The Ballistic Anisotropic Magnetoresistance (BAMR)

The changes in the ballistic conductance due to ballistic spin-scattering are important for the ballistic anisotropic magnetoresistance. The BAMR (cf. Figure 7.1) is defined similar to the ballistic magnetoresistance (BMR) (Eqn. (6.32) in chapter 6.7.1), as shown in Eqn. (7.1):

$$\text{BAMR} = \frac{G_{\parallel} - G_{\perp}}{G_{\perp}} \times 100\%, \quad (7.2)$$

where G_{\parallel} and G_{\perp} are the conductances for magnetization directions parallel to the current and perpendicular to it, respectively [16]. In contrast to the ballistic magnetoresistance, caused by a change of the relative magnetization alignment of the leads, the difference in conductance responsible for BAMR is due to the introduction of a global spin-quantization axis and the resulting changes in the electronic structure due to spin-orbit coupling. The difference of $0.15 G_0$ at the Fermi level in favor of the parallel quantization axis due to ballistic spin-scattering results in a small BAMR of the order of 7% (see inset of Figure 7.3). This might seem to be a small effect, but it is still considerably large when keeping in mind, that there is no BAMR for the pure Pt leads and the 7% are caused by a single magnetic Co scatterer and the induced spin-polarization of adjacent Pt atoms by changing the magnetization direction from in-chain to out-of-chain. Apart from this effect at the Fermi energy driven by Δ_1 - and Δ_3 -orbitals, there is another distinct BAMR con-

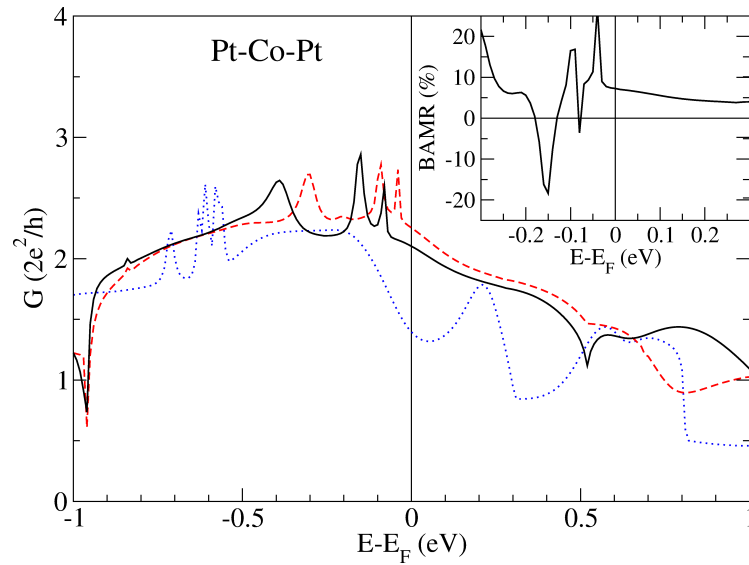


Figure 7.3: Conductance around the Fermi level for a Pt wire with a single Co impurity atom without spin-orbit coupling (dotted blue line) and including SOC for an in-chain (dashed red line) and an out-of-chain (solid black line) magnetization direction. The inset shows the ballistic anisotropic magnetoresistance as defined by Eq. 7.1.

tribution below the Fermi level due to a small shift between the Δ_4 conductances of the two magnetization directions. This shift is due to a small spin-splitting of those bands for the Pt atom neighboring the Co scatterer (cf. Figure 7.2) and results in an oscillatory behavior of the BAMR around -0.05 eV to -0.2 eV below the Fermi level, with values ranging from -20% to 25% .

The overall observed BAMR might seem to be relatively small for the $\text{Pt}_{\text{inf}} - \text{Co} - \text{Pt}_{\text{inf}}$ junction, but it is still e.g. comparable to the 11% BMR in the near tunneling regime obtained for the FM Co chain (chapter 6.7) and should constitute a measurable effect. The BAMR is solely caused by changing the magnetization direction of one single magnetic Co impurity in the center and one possibly could get an even larger BAMR effect for a larger magnetic cluster or a magnetic molecule as an impurity. Another interesting effect is the observed spin-scattering in this particular junction, mixing both incoming spin-channels and allowing a spin to flip in the scattering process due to spin-orbit coupling.

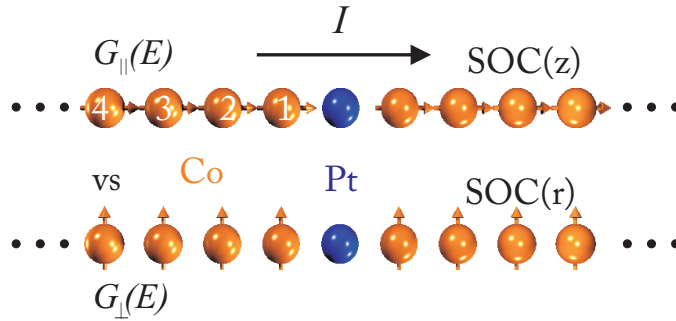


Figure 7.4: Sketch of the scattering region of the $\text{Co}_{\text{inf}} - \text{Pt} - \text{Co}_{\text{inf}}$ junction: Magnetic Co wires (orange) and a heavy Pt scatterer (blue) with an in-chain quantization axis ($\text{SOC}(z)$, upper wire) and an out-of chain quantization axis ($\text{SOC}(r)$, lower wire).

7.2 Non-magnetic Impurity in a Ferromagnetic Wire

After investigating the effect of SOC on ballistic transport through a non-magnetic chain with a single magnetic impurity in the previous sections, here a ferromagnetic Co monowire with a single Pt impurity is considered (cf. Figure 7.4) and the effect of SOC on such a system is studied. Although both systems seem at first to be very similar, they differ significantly in the observed effects, such as BAMR/AMR and the occurrence of spin-scattering. For example, in contrast to the previously described non-magnetic Pt monowire, the pure FM Co monowire exhibits a considerably large BAMR effect of 130%. BAMR has been reported by theoretical DFT calculations [16] and been confirmed by break junction experiments [14] for Co based systems. In addition, the effect of an additional heavy Pt scatterer, which has a large nuclear number and thereby a large spin-orbit interaction, is considered.

It has been reported for Ni monowires with a stretched central bond [17], that the anisotropic magnetoresistance in nanocontacts with either localized states or large orbital polarization can deviate from the BAMR of well-defined periodic systems, such as Co chains [16]. Especially the typical step-function like dependence on the angle of the quantization axis can be altered by localized states or large orbital polarization of the contact. In the previous section 7.1, the non-magnetic Pt leads did not exhibit BAMR and the found 7% BAMR, here defined as the normalized difference of conductance in respect to the magnetization direction (Eqn. (7.1) in section 7.1), was solely due to the magnetic impurity and the overall effect was small. Due to the rather large BAMR of 130% for pure FM Co wires, here the influence of a Pt impurity on this effect is studied in dependence on the angle between magnetization and current direction. This allows to determine whether the observed conductance behavior upon rotation exhibits a BAMR or rather a AMR like shape due the broken translational symmetry.

Computational Details

The electronic structure of the system was calculated within the FLEUR code [63] using a 9 atom supercell for the scattering region consisting of one Pt scatterer and 4 ferromagnetic Co monowire atoms on both sides (cf. Figure 7.4). The interatomic distance was chosen as $d_{\text{Co}} = 4.48$ bohr. The exchange-correlation potential was treated within GGA [103] and SOC was included within second variation. In each case two types of calculations were performed: in the scalar-relativistic (SR) approximation, i.e. , without SOC, and with SOC for various angles α between the wire and the magnetization direction (cf. section 7.2.2, Figure 7.9). Most prominently, the configurations with magnetic moments parallel to the chain axis ($\alpha = 0^\circ$) and perpendicular to it ($\alpha = 90^\circ$) were calculated. For all calculations the 1D Brillouin zone (BZ) was sampled by 16 k -points and G_{max} was set to 3.9 bohr^{-1} resulting in approximately 175 basis functions per atom for the Co monowire with a Pt impurity. The leads were described by a Co monowire in a 3 atom unit cell, which were treated in either the scalar-relativistic (SR) approximation or including SOC in the magnetization direction defined by α . The BZ was sampled by 24 k -points and G_{max} was set to 4.1 bohr^{-1} , resulting in approximately 210 basis functions per atom. The vacuum parameters for all cases constituted 4.3 and 6.6 bohr for D_{vac} and \tilde{D} , respectively.

For all quantum conductance calculations the locking technique (cf. chapter 6.4) to the respective leads and the third nearest-neighbor approximation was employed. In the SR case FSWFs were generated on a 16 k -point mesh in the whole 1D-BZ with 1 s - and 5 d -orbitals per atom and spin, constructed by the radial solutions of the FLAPW potential. For the disentanglement procedure [136] the lowest 64 eigenvalues per k -point for 54 WFs for Pt impurities in Co monowires were considered. The Co lead WFs were constructed as described in chapter 6.7 in this case. With SOC the FSWFs were generated on a 16 k -point mesh in the whole 1D-BZ with 2 s - and 10 d -orbitals per atom. For disentanglement [136] the lowest 116 eigenstates per k -point for 108 WFs were used. The WFs for the semi-infinite Co leads were generated on a 24 k -point mesh with the same trial functions as those used for the atoms inside the scattering region, while for disentanglement the lowest 26 eigenvalues per k -point for 18 WFs per spin (SR) and the lowest 44 eigenvalues per k -point for 36 WFs (SOC) were used.

7.2.1 The $\text{Co}_{\text{inf}} - \text{Pt} - \text{Co}_{\text{inf}}$ Junction

In chapter 7.1 for the previous system the transmission was shown to be affected by ballistic spin-scattering, leading to a small BAMR below the Fermi energy and BAMR oscillations due to a shift of the Δ_4 orbitals of the Pt atom adjacent to the Co scatterer. In this section the situation is inverted, a non-magnetic Pt impurity is placed into a ferromagnetic Co monowire. Although the resulting system might seem

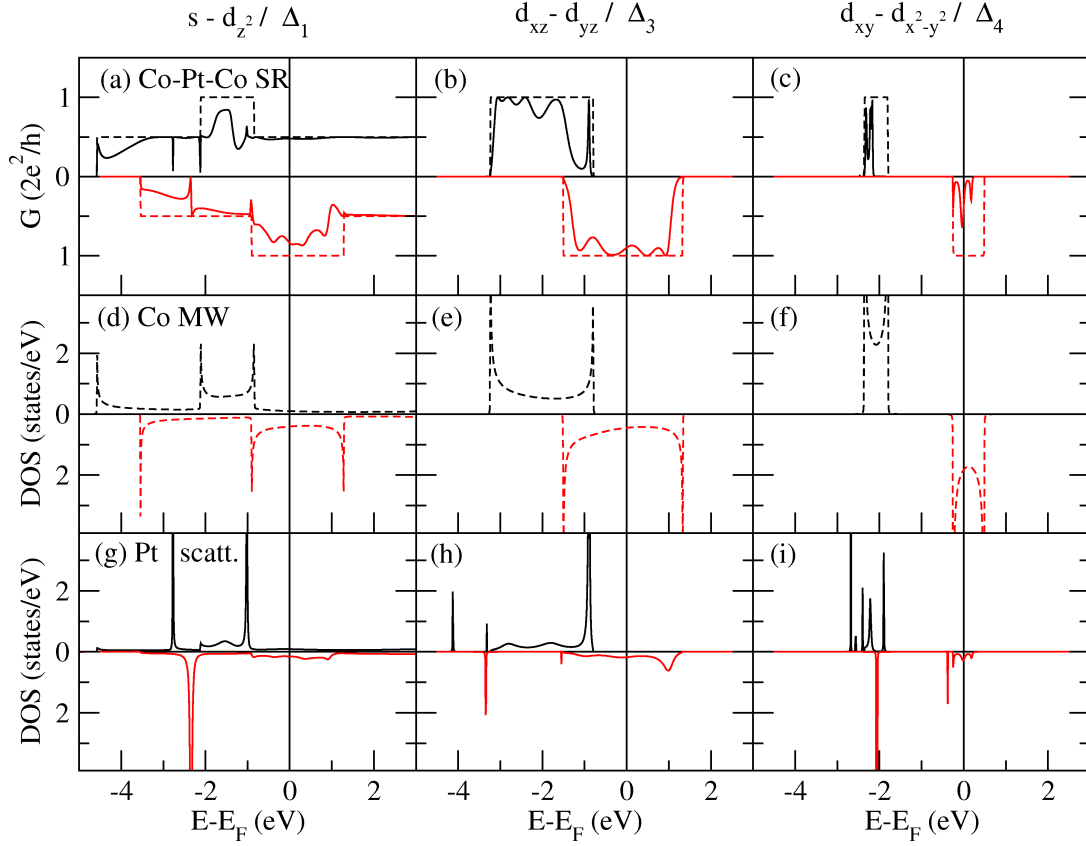


Figure 7.5: (a-c) Orbital decomposition of transmission through a ferromagnetic Co wire with a single Pt impurity (solid lines) and a perfect Co wire (dashed lines) for the Δ_1 , Δ_3 , and Δ_4 channels, respectively, for spin-up (black, upper part) and spin-down (red, lower part). (d-f) Density of states of the Co leads orbitally decomposed for spin-up (dashed black lines, upper part) and spin-down (red dashed lines, lower part) states. (g-i) Orbitally decomposed DOS of the Pt impurity atom, for spin-up (black, upper part) and spin-down (red, lower part).

very similar to the $\text{Pt}_{\text{inf}} - \text{Co} - \text{Pt}_{\text{inf}}$ junction, there are new effects to consider. For example, in case of a non-magnetic impurity in a FM wire, no ballistic spin-mixing occurs due to the large exchange splitting in the leads, prohibiting scattering between the states with opposite spin due to the shift in energy. In contrast, the presence of spin-degenerate bands in the non-magnetic Pt leads caused the spin-scattering effect in the $\text{Pt}_{\text{inf}} - \text{Co} - \text{Pt}_{\text{inf}}$ junction (cf. section 7.1).

First, the junction is described in the scalar-relativistic approximation in order to understand the main impact of the Pt scatterer on the conductance. While Co atoms in the leads carry a magnetic moment of $2.13\mu_B$, (see Table 7.2), the Co atoms in the vicinity of the Pt atom have moments in the range of $2.15-2.20\mu_B$, and the Pt atom itself is spin-polarized with a considerable moment of $0.36\mu_B$. The orbitally

spin- and orbital moments (μ_B)	FM Co MW	Co ₁	Co ₂	Co ₃	Co ₄	Pt
scalar-relativistic	2.12	2.20	2.19	2.19	2.15	0.36
SOC(z) spin moment	2.12	2.20	2.19	2.19	2.15	0.36
SOC(z) orbital moment	0.22	0.22	0.38	0.07	0.53	0.10
SOC(r) spin moment	2.12	2.20	2.19	2.19	2.14	0.36
SOC(r) orbital moment	0.17	0.20	0.20	0.15	0.14	0.09

Table 7.2: Spin- and orbital moments for the Co_{inf} – Pt – Co_{inf} junction in scalar-relativistic approximation and with the SOC quantization axis in-chain (SOC(z)) and out-of-chain (SOC(r)) direction, including the ferromagnetic leads. The locations of Co₁ to Co₄ are shown in Figure 7.4.

decomposed conductance, Figure 7.5 (a-c), displays a reduction of the conductance due to the Pt impurity atom is relatively small compared to the effect of the Co impurity on the Pt_{inf} – Co – Pt_{inf} junction in section 7.1. This general behavior can be understood from the fact that the Pt 5*d*-bands possess a larger bandwidth than the Co 3*d* states, resulting in the presence of Pt states with the same symmetry as the Co states in nearly the whole energy region. The resulting good matching between Pt and Co states allows to maintain a large fraction of the pure Co leads conductance, even with an incorporated impurity (cf. Figure 6.8 and Figure 6.22).

In the $s - d_{z^2}$ (Δ_1)-channel, the reduction of the conductance is similarly small for the majority and minority spin contributions due to the energetic alignment of the spin-split states of the Co wire with the states of the Pt impurity. In the majority spin channel, a significant reduction of transmission only occurs in a region from $E_F - 2.1$ eV to $E_F - 0.9$ eV where the perfect conductance amounts to G_0 . In the spin- and orbital-decomposed density of states, Figure 7.5 (d) and (g), there are also two resonances at the Pt impurity located at 2.8 eV, and 2.3 eV below the Fermi energy in the majority and minority spin channel, respectively. In the conductance, a Fano-type line shape is observable due to the coupling of the Δ_1 -band to these resonances.

The conductance from the Δ_3 -bands is only reduced at the bottom and top edges of the leads bands in both spin channels, due to the on-site energies of Co and Pt $d_{xz,yz}$ -states being close in energy. The density of states of the Pt atom, Figure 7.5 (h), shows that the $d_{xz,yz}$ states are spin-split and carry a significant part of the Pt moment, and align well with the Δ_3 -bands in the Co monowire resulting in an efficient transport channel. The most severe change in the conductance upon introducing a Pt impurity occurs in the Δ_4 -band. Here, a large decrease due to scattering at the Pt impurity can be observed. For both, the $d_{xz,yz}$ and d_{xy,x^2-y^2} channels, bound states on the Pt atom can be found due to the lower on-site potential at the Pt site. For the Δ_3 -symmetry there are such states at -4.1 eV for the majority band and at -3.3 eV for both spin channels, which do not contribute to the conduction as they are below the Δ_3 -band of the Co leads. For the Δ_4 symmetry

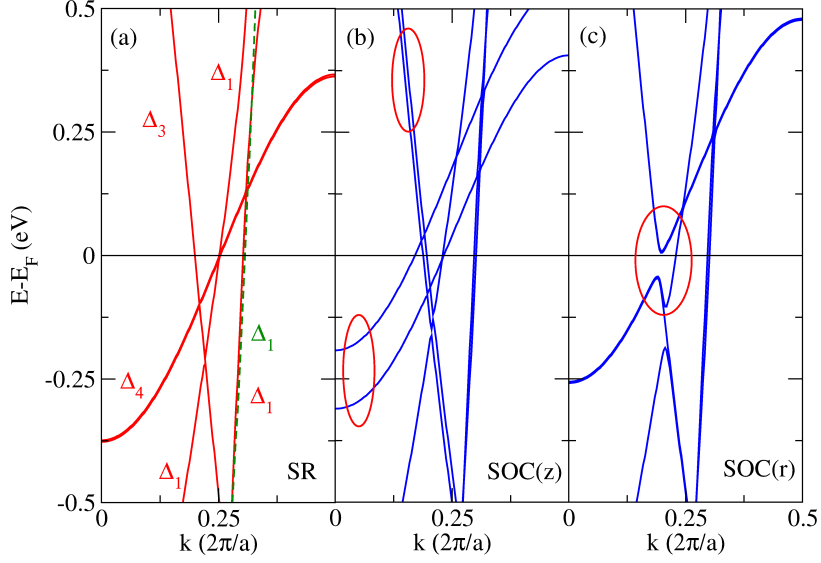


Figure 7.6: Origin of the BAMR for a perfect FM Co monowire: (a) orbitally resolved scalar-relativistic bandstructure (spin up, solid red lines, spin down, dashed green line) of a FM Co MW in the vicinity of the Fermi level in comparison to bandstructures with SOC and an in-chain (SOC(z)) and out-of-chain (SOC(r)) quantization direction. All bandstructures calculated in a 3rd NN approximation MLWFs tight-binding Hamiltonian. Red circled areas: Bands responsible for the BAMR effect, due to spin-splitting (SOC(z)) and a lack of bands at the Fermi level due to an anti-crossing (SOC(r)).

there are majority states around -2.5 eV and a paired state at -2 eV with respect to the Fermi level, not contributing to the majority channel transmission.

Δ_4 electrons are only transmitted in the small overlap region around -2.1 eV for majority and around Fermi level for minority states, where a very narrow band is formed in both cases. The shape of the transmission function follows the two-peak (majority band) and three-peak (minority band) shape of the DOS of the central Pt atom.

The effect of spin-orbit coupling on the magnetic and transport properties of the $\text{Co}_{\text{inf}} - \text{Pt} - \text{Co}_{\text{inf}}$ junction can now be discussed. For the perfect Co monowire there is a magneto-crystalline anisotropy energy (MAE), i.e., the difference in energy for the magnetization in the chain axis and perpendicular to it, of 0.8 meV per magnetic atom in favor of an out-of-chain magnetization and orbital moments of $0.17\mu_B$ for out-of-chain and $0.22\mu_B$ for in-chain direction. Although the MAE might be small for the perfect FM Co MW, SOC induces a giant BAMR (Eqn. (7.1) in chapter 7.1) of 130% (cf. Figure 7.6). The BAMR is caused by the change of hybridization in respect to the quantization axis. For an in-chain axis, the Δ_3 and Δ_4 band experience an energy splitting due to the two possible spin alignments relative to

the orbital moment, resulting in $|m_j| = 1/2$ and $3/2$ (Δ_3) and $|m_j| = 3/2$ and $5/2$ (Δ_4), respectively. For an out-of chain quantization axis it is possible for Δ_3 and Δ_4 bands to hybridize, resulting in an anti-crossing gap at the Fermi level. The BAMR can now be determined by simply counting the bands at the Fermi level, resulting in 7 bands for a magnetization along the chain axis and 3 bands for a magnetization perpendicular to it at the Fermi level and therefore in a BAMR of 130%⁴ (cf. Figure 7.6). The large exchange splitting also prevents mixing the two spin-channels due to SOC.

Upon introducing a Pt impurity, the previously mentioned MAE value is reduced to 0.5 meV per magnetic atom in favor of an out-of-chain magnetization. The magnetic moment (cf. table 7.2) of the Pt atom is $0.36\mu_B$ for both magnetization directions with very similar orbital moments of $0.09\mu_B$ (out-of-chain) and $0.10\mu_B$ (in-chain). Characteristically, as in the case of the Co leads, the orbital moments of the Co atoms adjacent to the Pt impurity are significantly larger for the in-chain direction (reaching as much as $0.53\mu_B$ for the nearest Co atom), than for the out-of-chain direction (at most $0.2\mu_B$). Despite the larger orbital moments of in-chain magnetization, the out-of-chain magnetization remains energetically favorable, in accordance with the previously found results of the pure Co leads.

Compared to a perfect Co wire in the scalar-relativistic approximation, a reduction by roughly a factor of two can be observed in the overall conductance over the entire energy range with SOC, due to the less efficient coupling between the Co wire and the Pt impurity, especially for the Δ_3 - and Δ_4 -orbitals (cf. Figure 7.7). For the transport properties including SOC the orbitals with Δ_3 and Δ_4 symmetry are therefore essential, depending on the quantization axis defined by the magnetization direction, e.g. the spin-degeneracy of these orbitals is lifted (cf. Figure 7.7 (b)).

At the Fermi energy the majority and minority spin contributions from the Δ_1 -band are about 0.5 and $1.0 G_0$ for both magnetic directions (cf. Figure 7.7). Only the minority states of the other two orbital symmetries are present due to the exchange splitting. The minority Δ_3 band contributes almost $1.0 G_0$ for the in-chain magnetization, while it reveals a depletion at E_F for the out-of-chain magnetization, as shown in Figure 7.7 (b). Accordingly, the Δ_4 -band conductance also changes significantly upon switching the magnetization direction, owing to the changes in the details of hybridization between Δ_3 and Δ_4 states when the direction of the magnetization is changed, see Figure 7.7 (b) and Figure 7.2 (cf. DOS of the Co monowires for the two different magnetization directions). These changes in the energetic structure of Δ_3 and Δ_4 states lead to a large difference between the in-chain and out-of-chain conductances, also visible for the pure Co chain in the Figure 7.7.

In Figure 7.8, the conductance is displayed in a small energy window around the Fermi energy for the two different magnetization directions. It is apparent that the changes arise due to the modifications of the Δ_4 -band conductance between Fermi

⁴Due to the lifted spin-degeneracy each band contributes $1/2 G_0$ to the conductance.

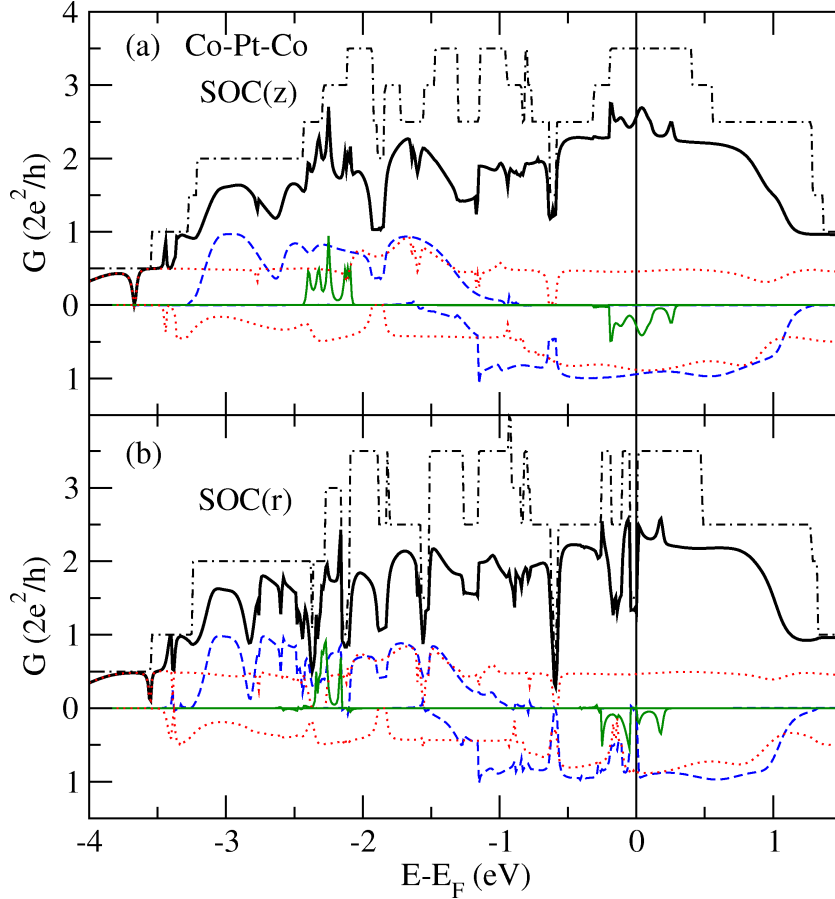


Figure 7.7: Conductance including SOC for a Co monowire with a Pt impurity atom for (a) magnetization along the wire axis and (b) perpendicular to the axis. The decomposition of transmission into Δ_1 (dotted red lines), Δ_3 (dashed blue lines) and Δ_4 (solid green lines) channels for majority spin (positive y -axis) and minority spins (negative y -axis) shows the presence of a Δ_4 minority band channel at the Fermi level. Black dashed-dotted lines display the transmission of the perfect infinite Co leads.

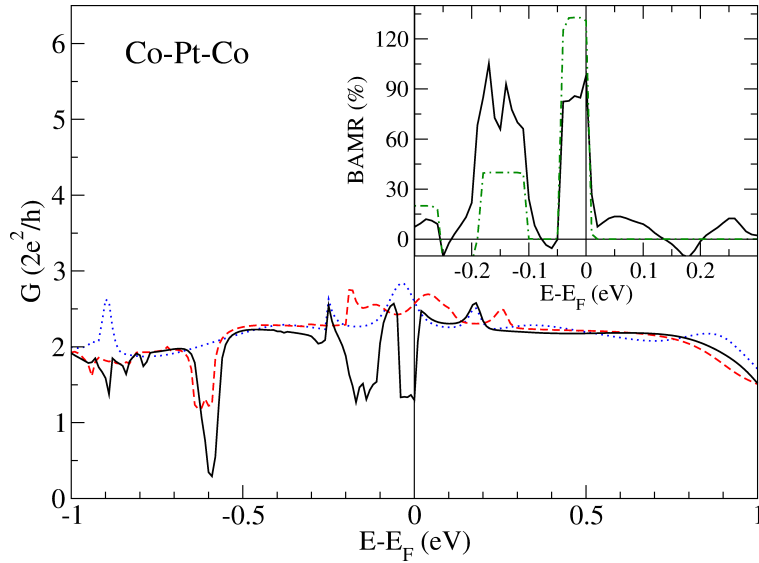


Figure 7.8: Conductance around the Fermi level for a Co monowire with a Pt impurity atom in the scalar-relativistic approximation (blue dotted line) and including SOC for a magnetization along the chain axis (dashed red line) and perpendicular to the axis of the wire (solid black line). The inset shows the BMR as defined by Eq. (7.8) for the Co monowire with a Pt impurity (solid black line) and for a perfect infinite Co monowire (dashed-dotted green line).

level and -0.05 eV, and Δ_3 -band conductance around E_F and -0.15 eV which are subject to different band mixing from spin-orbit coupling.

As a result of the fine structure of the Δ_4 and Δ_3 conductances (see Figure 7.7 (b)), the obtained BMR, shown in the inset of Figure 7.8, displays a strong variation with energy. Compared to the BMR of a perfect Co MW of 130% a Pt scatterer reduces this effect to 80–100%, which is still considerably high. An enhanced BMR can be found for the second peak below the Fermi Energy, where a Δ_4 conduction peak for the in-chain direction in coincidence with a Δ_3 conduction depletion result in a BMR increase from 40% for the perfect Co MW to 60–100% when a Pt scatterer is introduced.

7.2.2 Magnetoresistance: BMR vs AMR

As previously shown, the BMR is lowered at the Fermi level upon introduction of a heavy Pt scatterer into a FM Co chain, but it is still a significant effect. The question arises, how the Pt scatterer affects the typical step-like behavior of the conductance [14, 16] on the angle of the quantization axis relative to the current direction (cf. Figure 7.9).

The origin of this step-function like behavior of the BMR can be found in the bandstructures of the pure FM Co chain with an angle α between the quantization

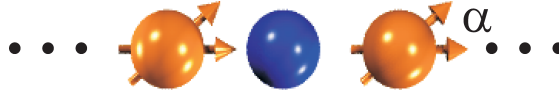


Figure 7.9: Definition of the quantization axis by introducing an angle α between the z -axis and the spin-quantization axis. $\alpha = 0^\circ$ corresponds to SOC(z) (in-chain direction) and $\alpha = 90^\circ$ to SOC(r) (out-of-chain direction) in the previous notation.

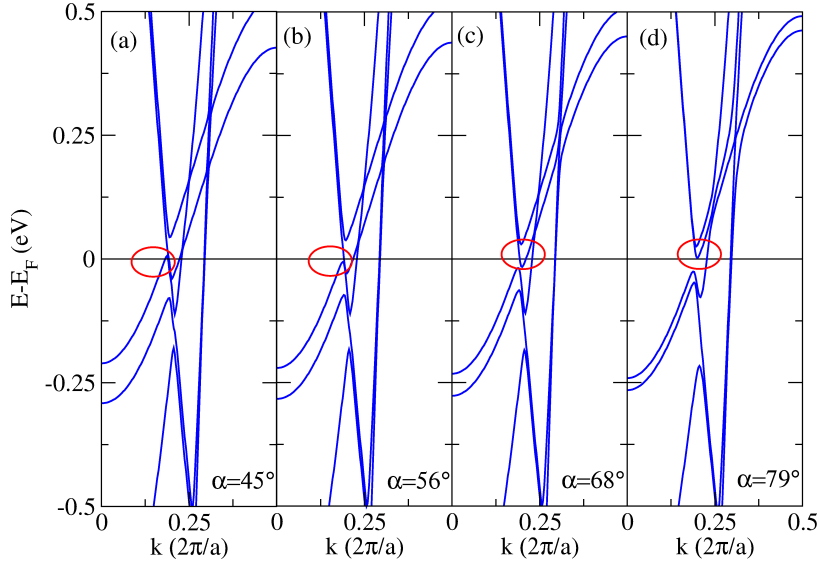


Figure 7.10: Bandstructures of FM Co monowires including SOC for an angle α between z -axis and spin quantization axis. (a) $\alpha = 45^\circ$ (b) $\alpha = 56^\circ$ (c) $\alpha = 68^\circ$ and (d) $\alpha = 79^\circ$. All bandstructures based on a 3rd NN approximation MLWFs tight-binding Hamiltonian. The red circled areas indicate the bands responsible for the BAMR conductance jumps moving away from the Fermi level.

axis and the z -direction [14, 16]. $\alpha = 0^\circ$ corresponds here to an in-chain quantization axis and 90° to an out-of-chain quantization axis, as previously shown in Figure 7.6.

In Figure 7.10 (a-d) the bandstructures for the angles $\alpha = 45^\circ$, $\alpha = 56^\circ$, $\alpha = 68^\circ$ and $\alpha = 79^\circ$ are shown. Increasing α induces a gradual change from in-chain to out-of-chain quantization axis, resulting in an anti-crossing band that moves below the Fermi level for $\alpha > 56^\circ$, as shown in Figure 7.10 (b). For $\alpha > 79^\circ$, another anti-crossing band moves above the Fermi level for as shown in Figure 7.10 (d). Due to the reduction of bands at the Fermi level the conductance exhibits two steps of G_0 upon rotation of the magnetization, resulting in a step-like angular dependence of the conductance of the pure FM Co monowire, shown in Figure 7.11.

The introduction of a Pt scatterer lifts the translational symmetry of the FM Co wires. Since the BAMR is defined for pure locally periodic systems, the question

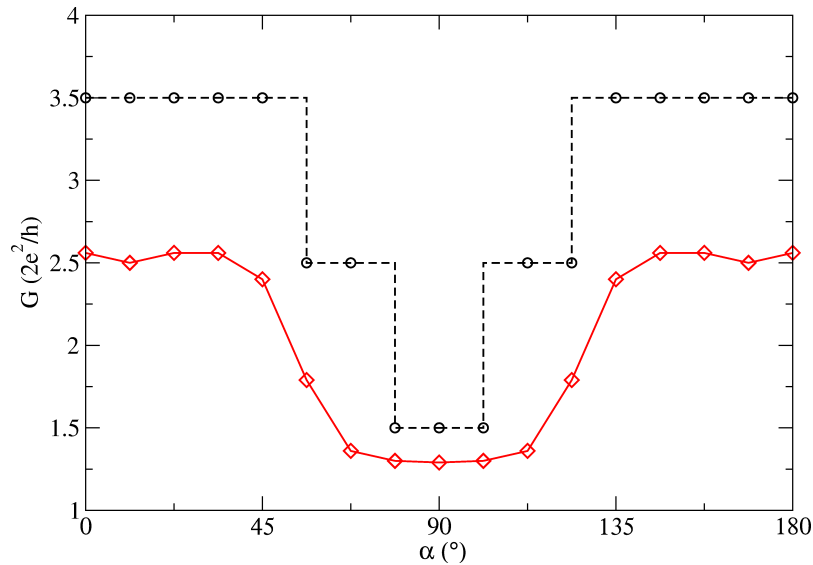


Figure 7.11: Conductance at the Fermi level for a perfect Co MW (dashed black line, open black circles) and a $\text{Co}_{\text{inf}} - \text{Pt} - \text{Co}_{\text{inf}}$ junction (solid red lines, open red diamonds) in dependence of the angle α between z -axis and spin quantization axis. All results in 3rd NN MLWFs (Co-MW) and MLWFs/FSWFs (leads/ $\text{Co}_{\text{inf}} - \text{Pt} - \text{Co}_{\text{inf}}$ junction) description.

arises whether conductance of the system exhibits a BAMR or AMR angular dependence of the conductance, where AMR does not show step-like features. The Pt impurity induces an additional scattering potential, which leads an overall reduction of the conductance at the Fermi level for the $\text{Co}_{\text{inf}} - \text{Pt} - \text{Co}_{\text{inf}}$ junction compared to the pure FM Co monowires, as shown in Figure 7.11. In addition, the angular dependence does not exhibit the typical step-like behavior of the BAMR, it is rather smoothed out like the AMR.

The dependence of the conductance for a larger energy region is displayed in Figure 7.12. Here, the effect of the opening of bandstructure gaps in the FM Co leads (cf. Figure 7.10) is shown to mainly affect the region in the vicinity of the Fermi level. While for $\alpha = 0^\circ$ expectably no such gap exists, for larger angles α the gap opens above the Fermi level ($\alpha = 45^\circ$) and moves below the Fermi level upon further rotation ($\alpha > 56^\circ$). For $\alpha > 79^\circ$ another band moves above the Fermi level (cf. Figure 7.10), resulting in a further decrease of the conductance, which is already very similar to the previously obtained out of chain result ($\alpha = 90^\circ$).

The effect of a Pt scatter on the conductance upon rotation of the magnetization constitutes a significant change from the BAMR of pure FM Co monowires to an AMR behavior, as shown in Figure 7.11. However, the change from BAMR to AMR still conserves the general conductance behavior, compared to a FM Ni monowire with one elongated central Ni bond, the effect of the Pt impurity is in the order

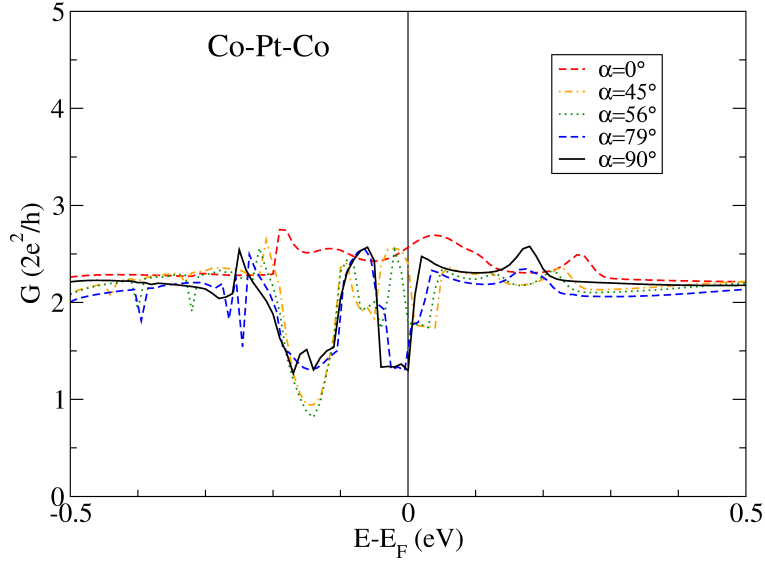


Figure 7.12: Conductance for the $\text{Co}_{\text{inf}} - \text{Pt} - \text{Co}_{\text{inf}}$ junction with different quantization axes α : In-chain quantization axis $\alpha = 0^\circ$ (SOC(z)) (red dashed line), $\alpha = 45^\circ$ (orange dash-dotted line), $\alpha = 56^\circ$ (green dotted line), $\alpha = 79^\circ$ (dashed blue line) and out-of-chain quantization axis $\alpha = 90^\circ$ (SOC(r)) (solid black line) All conductances in 3rd NN MLWFs/FSWFs (leads/ $\text{Co}_{\text{inf}} - \text{Pt} - \text{Co}_{\text{inf}}$ junction) approximation.

of a 10%-20% stretching of the central bond [17]. As pointed out in reference [17], the introduction of scatterers in the nanocontacts with either localized states or large orbital polarization, such as e.g. magnetic molecules, could result in an even stronger effect and possibly more dramatic changes of the angular behavior of the conductance.

8 Ballistic Transport in Nanojunctions with Non-Collinear Magnetic Order

In this chapter, the developed ballistic transport code is used to calculate the conductance in magnetic nanojunctions with non-collinear spin structures from first-principles. Such junctions can be realized e.g. by break junction experiments, which have allowed to perform transport studies on nanoscale metallic contacts in which the mean free path of the electrons is much larger than the junction length. The observation of quantized conductance in such systems is a hallmark of ballistic transport and opened new vistas to study the scaling of electronic devices down to the atomic length scale [153]. A drawback of such experiments is the limited control of the microscopic arrangement in the junction which hinders a straight forward interpretation of the data and makes a comparison with theoretical calculations difficult [9]. In this respect, a great advantage is given by the use of scanning tunneling microscopy (STM) experiments, in which a tip can approach and contact single atoms or molecules on a surface [5–8, 12, 154]. In such experiments, it has been possible to measure the conductance as a function of tip-sample distance from the tunneling to the contact regime. A recent focus of such contact measurements has been magnetic systems, e.g. spin-valve behavior has been observed in single magnetic molecules or atoms on surfaces [154, 155] and the occurrence of the Kondo effect has been found in ferromagnetic atomic contacts [8].

It has been emphasized that the low coordination of the contact atoms in nanoscale junctions leads to an enhanced tendency towards magnetism, e.g. magnetic moments are formed in systems of otherwise non-magnetic materials [125, 126, 156–158]. Naturally, transport phenomena in such magnetic low-dimensional systems have raised a lot of attention and triggered many theoretical studies, which mainly focused on systems with collinear magnetic order, considering also the effect of magnetoresistance [79, 81, 159–162]. It was also recently realized that, if the magnetization direction of the two electrodes is opposite, a domain wall can form in the contact between them and the non-collinear order in the domain strongly affects the conductance and the magnetoresistance [76, 163, 164].

Recently, the transition regime from tunneling to contact in a spin-polarized STM geometry has been studied based on density functional theory in order to explain e.g. the conductance of a single magnetic atom,[12] and to analyze the contribution from different conduction channels [162]. As a magnetic STM tip approaches a single magnetic atom on a surface an exchange interaction with the tip apex atom

occurs. In principle, it is possible to switch the magnetic moment of the adatom in such a way [165]. If the magnetic moment of the adatom is exchange coupled to the substrate there is a competition of exchange interactions which can result in a canting of the spins close to contact [154]. Non-collinear spin alignment in such an atomic contact can also occur if the adatom spin is canted due to exchange coupling on a substrate with a spin spiral structure [18, 166]. The effect of such a non-collinearity in the spin direction of the tip apex and the adatom on the conductance is the focus of the present work.

The approach taken in this chapter differs from recent investigations of the effect of non-collinear magnetism on ballistic transport. In the present literature the focus of theoretical investigations on ballistic transport through non-collinear nanojunctions is on domain wall structures and the spin-torque effect [74–76]. Theoretical investigations in a similar geometry as proposed in this chapter were performed on the electron transport through nanojunctions including electrically switchable molecules [72] based on the $s - d$ model for the non-collinear electronic structure. Within the same $s - d$ model transport approach, based on a slightly different geometric setup, where a magnetic Mn chain is considered to be situated perpendicular to nonmagnetic leads, spectroscopic SP-STM features of Mn nanowires including inelastic spin-flip processes were investigated [73].

In contrast to the reported studies, in this chapter the influence of competing exchange interactions between two magnetic apex atoms is investigated, as e.g. present in a SP-STM or break junction geometry, performed in the transitional regime from tunneling to contact. As a model system, two Co monowires are considered to each of which a single apex Mn atom is attached. The distance between the two Mn atoms is varied in order to calculate the conductance from the tunneling to the contact regime. The magnetization direction of the two Co electrodes is chosen either parallel (P) or antiparallel (AP) which allows to obtain the distance-dependent magnetoresistance. Upon approaching the two Mn atoms in P electrode alignment can experience frustration close to contact due a change from ferro- to antiferromagnetic Mn-Mn coupling, previously reported on perfect Mn monowires [167], and the resulting competing exchange interactions in the junction. As a result, a stable non-collinear spin-arrangement can become the magnetic ground state, resulting in distinctive distance dependent conductance and magnetoresistance signatures.

This chapter provides results published in Ref. [80] and includes supplementary material.

8.1 Non-Collinear Magnetism in Mn Monowires

Before proceeding to more complex nanojunctions, the characteristics of non-collinear WFs (cf. chapter 5.7) are discussed on various non-collinear magnetic states of a freestanding Mn monowires. Freestanding Mn monowires have been reported to

exhibit a complex dependence of the magnetic order on the lattice constant [168], including e.g. non-collinear spin-states and a remarkable transition from FM to AFM coupling at a lattice constants of 4.75 bohr^1 [167]. Therefore, they represent an ideal starting point to investigate the characteristics of a non-collinear Wannier functions. It will be shown, that a mapping to non-collinear WFs lead to an equally accurate description of the electronic structure of the underlying FLAPW calculations. The accuracy is only limited by the applied nearest neighbor (NN) approximation.

Computational Details

The Mn monowires were calculated within the FLEUR code [63] with an interatomic distance of $d_{\text{Mn}} = 5.0 \text{ bohr}$. The collinear FM and AFM configurations were performed in unit cells consisting of 1 (FM) and 2 (AFM) atoms and the non-collinear magnetic Mn wires were treated in unit cells consisting of 1,2,3,4 and 6 atoms. The angles between the magnetic moments of adjacent atoms were chosen as 0° (1 atom unit cell), 60° (6 atom unit cell), 90° (4 atom unit cell), 120° (3 atom unit cell) and 180° (2 atom unit cell), respectively. The single atom unit cell calculations were performed on a mesh of 24 k -points on the z axis in a super cell geometry. All other calculations were performed on a mesh of 12 k -points on the z axis in a super cell geometry with a inter-wire distance of 10 bohr in x - and y -direction. In all calculations, G_{max} was chosen to be 3.7 bohr^{-1} , which corresponds to approximately 440 basis functions per atom. The generalized gradient approximation (GGA) was applied to the exchange-correlation potential [103]. The spin moments of all calculated freestanding Mn wires in direction of the local spin axis were found to be within $4.00 \pm 0.04 \mu_B$.

The collinear and non-collinear MLWFs were generated on a mesh of 24 k -points in the whole BZ starting from one s - and 5 d -orbitals per atom obtained from the radial solutions of the FLAPW potential as trial functions. In the calculations including non-collinear magnetism, MLWFs were generated on a 24 k -point mesh in the whole BZ based on 2 s - and 10 d -orbitals per atom due to the coupled spin channels. The energy bands were disentangled using the procedure described in [136]. For the collinear calculations, the lowest 9/16 energy states per k -point were used to determine 6/12 WFs in the FM/AFM case. For the non-collinear calculations the lowest 15/82/52/40/16 energy states per k -point for 12/72/48/36/24 WFs with angles of $0^\circ/60^\circ/90^\circ/120^\circ/180^\circ$ between the spin moments of adjacent atoms were used.

8.1.1 Non-Collinear MLWFs of Mn Monowires

As the first step, shown in Figure 8.1, the bandstructures of freestanding FM and AFM Mn monowires are compared based on collinear and the according non-

¹1 bohr = $5.2917721092 \times 10^{-11} \text{ m}$ ($\approx 0.529 \text{ \AA}$)

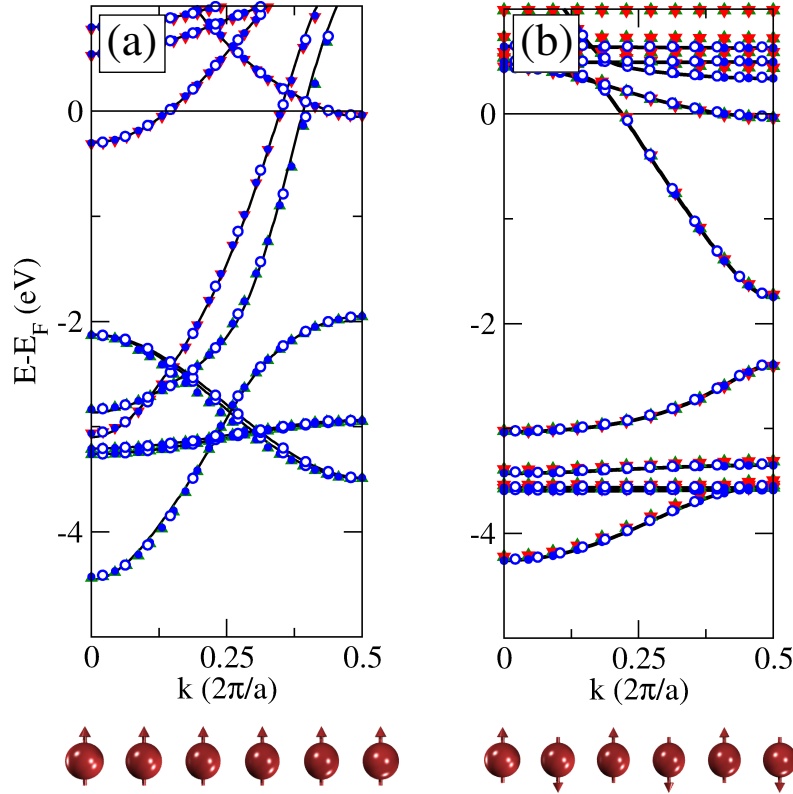


Figure 8.1: Bandstructures of Mn monowires for the (a) ferromagnetic and (b) antiferromagnetic configuration based on collinear FLAPW calculations (green up-triangles for spin up, red down-triangle for spin down) non-collinear FLAPW calculations (full blue circles, both spin channels) and the non-collinear MLWFs representation (open blue circles). The interpolated bandstructures (black solid lines) are based on a 3rd NN (FM) and 4th NN (AFM) description of the non-collinear MLWFs Hamiltonians.

collinear FLAPW calculations with angles of 0° (FM) and 180° (AFM) (cf. sketches in Figure 8.1) between adjacent spin moments. Both representations are in excellent agreement with each other for the occupied states. However, there is a shift between the Δ_4 band energies 0.3 eV above the Fermi level in case of AFM order, shown in Figure 8.1) (b). This shift might be due to numerical difficulties to exactly decouple both spin channels in a non-collinear FLAPWs description for AFM-type spin-order. Significant differences between those AFM-like collinear and non-collinear FLAPW calculations have only been found well above the Fermi level and therefore such differences do not limit the applicability of the transport method or the accuracy of non-collinear WFs. The non-collinear MLWFs representations of the bandstructures (open blue circles) for both cases, FM and AFM, as shown in Figure 8.1, are in excellent agreement with the non-collinear FLAPW calculations, as well as the

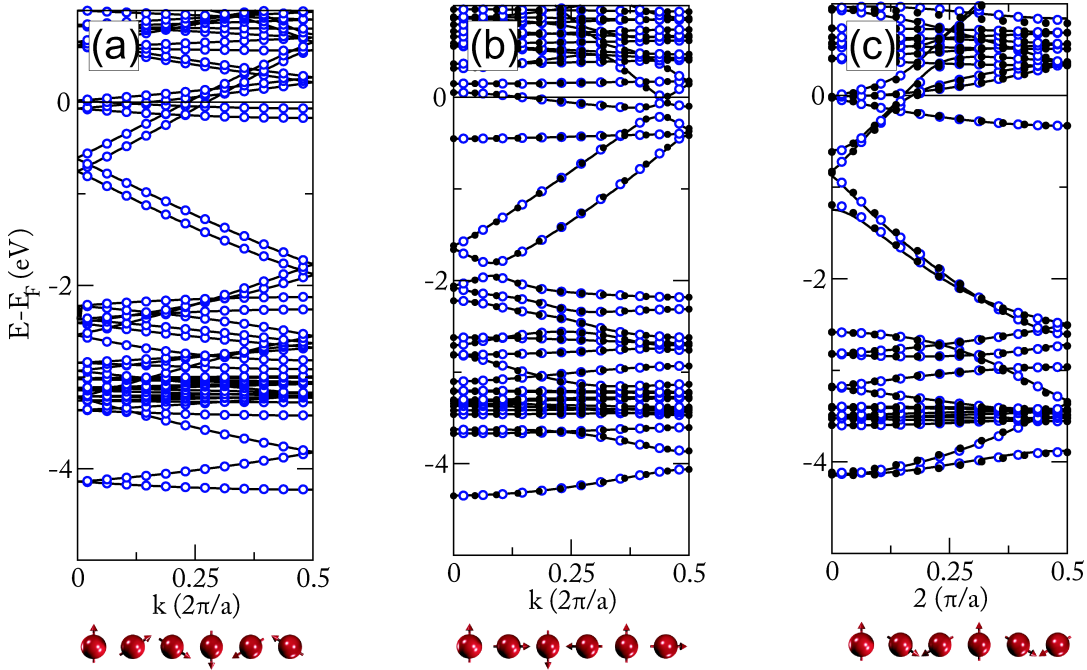


Figure 8.2: Bandstructures of Mn monowires with angles of (a) 60° , (b) 90° and (c) 120° between the spin moments of adjacent atoms, determined by non-collinear FLAPW calculations (full black circles) mapped to a non-collinear MLWFs (open blue circles) representation and the 3rd NN (60°), 4th NN (90°) and 3rd NN (120°) interpolated bandstructures (black solid lines) based on the non-collinear MLWFs.

interpolated bandstructures performed within 3rd (FM)/4th NN (AFM) approximation (cf. Eqn. (5.31) in chapter 5.5), similar to the results found for collinear WFs (see chapter 6.6).

Figure 8.2 shows the bandstructures of non-collinear spin states of freestanding Mn monowires for angles of $\alpha = 60^\circ$, 90° and 120° between adjacent spin moments (cf. sketches in Figure 8.2). The bands based on the FLAPW calculation and on the MLWFs representation are again in excellent agreement with each other, even though the bandstructures become more complex due to backfolding and mixing of the spin channels. The interpolated bandstructures in Figure 8.2 show a similar dependence on the NN approximation as previously found for collinear systems (see chapter 6.6, indicating similar localization properties). For ballistic transport of these non-collinear systems even 2nd or 3rd NN would be sufficient due to the absence of $s - d_{z^2}$ band edges in the vicinity of the Fermi level, which usually require a larger number of NN (cf. chapter 6.6).

The spreads of collinear and non-collinear MLWFs with Δ_1 , Δ_3 and Δ_4 orbital symmetry are shown in Table 8.1 for all considered spin structures in the Mn monowire. The spreads and therefore the localization properties are very similar

Ω_{MLWFs} (bohr ²)	FM	AFM	0° (FM)	60°	90°	120°	180° (AFM)
$\Delta_1(s)$	7.9	7.8	8.5	8.6	8.6	8.4	7.9
$\Delta_1(d_{z^2})$	2.5	4.2	2.8	2.5	4.7	2.4	2.3
Δ_3	2.1	2.0	2.5	2.2	2.2	2.2	2.0
Δ_4	1.7	1.7	1.8	1.8	1.7	1.7	1.7

Table 8.1: MLWFs Spreads (Ω) for collinear (FM and AFM) and non-collinear spin-structures (angles of 0° (FM)/60°/90°/120°/180° (AFM) between adjacent spin moments) in a perfect Mn monowire with $d_{\text{Mn}} = 5.0$ Bohr of orbitals belonging to the Δ_1 , Δ_3 and Δ_4 symmetry groups.

in both representations, indicating the presence of well-localized MLWFs for non-collinear systems with similar characteristics as have been previously obtained for nonmagnetic Pt wires (cf. chapter 6.6.1). The results for FSWFs, found in that chapter, can be transferred to systems with non-collinear spin-structures in most cases.

In conclusion, Wannier functions are capable of describing the electronic structure of freestanding Mn monowires exhibiting non-collinear spin-structures with comparable accuracy and localization properties as for collinear calculations (cf. chapter 6.6), resulting in overall excellent agreement with the underlying FLAPW calculations. While collinear MLWFs are known for their real-valuedness, non-collinear Wannier functions do not conserve this very useful characteristic. Non-collinear Wannier functions are mostly real-valued if they are used to describe systems with collinear magnetic order, this is not the case for the general non-collinear case. Calculations based on non-collinear WFs have to deal with complex numbers, similarly to FSWFs and MLWFs including spin-orbit coupling.

In general, the information of the spin direction is lost in case of a non-collinear Wannier representation. It is in principle possible to regain this information for special cases (cf. chapter 5.7) with identical global and local spin frames, such as e.g. the FM and AFM bandstructures in the non-collinear representation (see Figure 8.1). For more general cases, such as e.g. the non-collinear spin configurations with angles of 60°, 90° and 120° between adjacent spin moments (see Figure 8.2), global and local spin frames differ significantly (cf. chapter 4.7), prohibiting further decomposition into individual spin-channels.

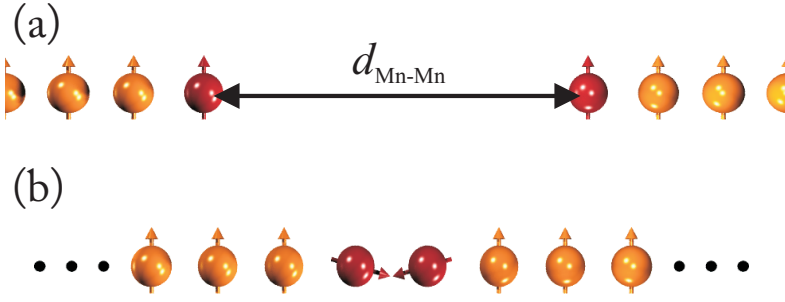


Figure 8.3: Sketch of the $\text{Co}_{\text{inf}} - \text{Mn} - \text{Mn} - \text{Co}_{\text{inf}}$ junction brought from the tunneling regime (a) to the contact regime (b) by decreasing $d_{\text{Mn-Mn}}$. While in the tunneling regime the magnetic order is collinear, in the near contact regime the Mn-Mn exchange interaction can possibly lead to non-collinear magnetic order, such as e.g. the shown state (b) with an angle of $\pm 105^\circ$ between the magnetic moments Co (orange) and Mn (red).

8.2 The $\text{Co}_{\text{inf}} - \text{Mn} - \text{Mn} - \text{Co}_{\text{inf}}$ Junction

In the following section, the ballistic transport properties of collinear and non-collinear magnetic configurations of a $\text{Co}_{\infty}\text{-Mn-Mn-Co}_{\infty}$ junction are investigated, consisting of semi-infinite ferromagnetic Co monowires with magnetic Mn "tip" atoms, see sketch of the structure in Figure 8.3. The effect of non-collinear magnetism on ballistic transport through such a junction is discussed, specifically in connection with tunneling-to-contact spin-polarized scanning tunneling microscope (SP-STM) [5–8, 12, 154] and mechanically-controllable break-junction [4] experiments. In particular, the changes in the transport properties are investigated upon changing the distance between the two Mn atoms, while keeping all other interatomic distances fixed at their equilibrium "semi-infinite" values. Upon bringing the leads together, the non-collinearity in this system will be shown to emerge as a result of competing Mn-Mn and Mn-Co exchange interactions. The influence of non-collinear magnetism on ballistic transport is then explored for various collinear and non-collinear configurations.

The nomenclature for the magnetic states in the $\text{Co}_{\infty}\text{-Mn-Mn-Co}_{\infty}$ junction includes the alignment of the magnetization directions of the leads, parallel (P) or antiparallel (AP) to each other (cf. Figure 8.4 (a) and (e)) and the ballistic magnetoresistance calculations for magnetic Co wires in chapter 6.7.1), and the directions of the two Mn spins. Without loss of generality, these directions are denoted with respect to the left lead which has magnetization "up". The Mn spins can point "up" (\uparrow), "down" (\downarrow) or in a direction which makes an angle α with the direction "up". In the latter case the symmetric configuration is considered, denoted as $\text{P}\alpha$ (cf. Figure 8.4 (b)), in which the spins of the Mn atoms make an angle of 2α between each other. For all considered non-collinear $\text{P}\alpha$ states fixed the direction of

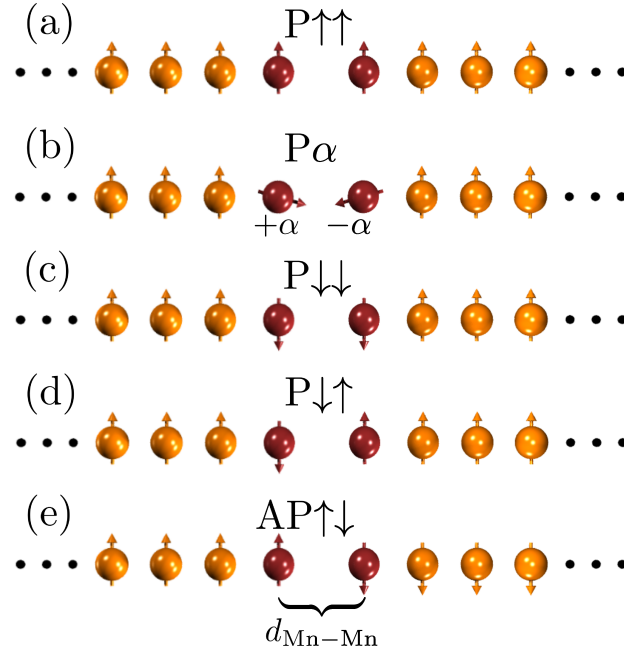


Figure 8.4: Calculated magnetic configurations in the Co-Mn-Mn-Co junction. The magnetic moments of the FM Co leads (orange) can be aligned parallel (P) or antiparallel (AP), the magnetic moments of the Mn adatoms (red) are denoted as up (u), down (d) or by an angle $\pm\alpha$ with respect to the magnetization direction of the left lead. Nomenclature for the displayed states: (a) P uu, (b) P 105° , (c) P dd (d) P du and (e) AP ud.

all Co atoms are fixed either up or down, depending on the magnetization direction of the corresponding lead. The energy differences between different magnetic states are given per Mn atom.

Computational Details

The $\text{Co}_{\text{inf}} - \text{Mn} - \text{Mn} - \text{Co}_{\text{inf}}$ junction was structurally optimized by the relaxation of the interatomic Co-Mn distance $d_{\text{Co-Mn}}$. The relaxation was performed by calculating the forces on the Mn atom within the FLAPW method [169] in an asymmetric wire consisting of 6 Co atoms and one Mn atom at one end. The wires were calculated in a tetragonal 3D super-cells running in z -direction with separations of $d_{x,y} = 12.5$ bohr and $d_z \approx 18.5$ bohr between the wires. The 3D BZ was sampled by $1 \times 1 \times 12$ k -points on the z -axis. GGA was used as approximation to the exchange-correlation potential. G_{max} was chosen to be 3.7 bohr^{-1} , which corresponds to approximately 740 basis functions per atom. Two collinear magnetic configurations were considered: "up" (\uparrow), "down" (\downarrow) pointing spin moment of the Mn atom with respect to the ferromagnetic Co wire, resulting in a relaxed inter-atomic distance of

$d_{\text{Co-Mn}} = 4.48$ bohr in favor of the up (\uparrow) alignment.

For all other collinear and non-collinear electronic structure calculations density functional theory within generalized gradient approximation (GGA) to the exchange-correlation potential [103] was used, as implemented in the FLEUR code [63]. The wires were calculated in three-dimensional super-cells, with an interchain separation in the x - y -plane of 13 bohr. The super-cell setup along the chain's axes (z -direction) is described in detail below. The Brillouin zone (BZ) was sampled by 12 or 24 k -points along the z -axis, depending on the size of the super-cell. All calculations were performed with an LAPW basis cut-off parameter k_{max} of 3.7 bohr^{-1} , resulting in approximately 625 LAPW basis functions per atom.

The parallel magnetic configuration (P) of Co_{∞} -Mn-Mn- Co_{∞} junctions was investigated in an 8-atom super-cell along the chain direction, consisting of six Co atoms with an equilibrium interatomic distance of the Co infinite monowire of $d_{\text{Co}} = 4.15$ bohr, and two attached Mn atoms, see Figure. 8.4. For all considered magnetic configurations, with parallel or antiparallel alignment of the magnetization of the leads, as well as non-collinear magnetic states, irrespective of the separation between the leads, the Co-Mn distance $d_{\text{Co-Mn}}$ is fixed to 4.48 bohr, which corresponds to the equilibrium distance between the ferromagnetic Co and Mn atoms at a very large separation between the leads, as mentioned above. For the $\text{P}\uparrow\uparrow$ and $\text{P}\downarrow\downarrow$ -states of the junction inter-Mn separations of $d_{\text{Mn-Mn}} = 5.0, 5.5, 7.0, 8.5, 10.0, 12.5, 15.0, 17.5$ and 20.0 bohr were considered. The antiparallel magnetic configuration (AP) of Co_{∞} -Mn-Mn- Co_{∞} junctions was calculated in a 16-atom super-cell, consisting of six \uparrow -Co atoms and two Mn atoms on one side, and six \downarrow -Co atoms and two Mn atoms at another end of the junction. In this case $d_{\text{Mn-Mn}}$ was set to 4.5, 5.0, 5.5, 7.0 and 8.5 bohr.

For the conductance calculations the locking technique (cf. chapter 6.4) was applied to a perfect monowire to describe the semi-infinite leads. In all cases the Wannier functions were generated on a $1 \times 1 \times 24$ k -point grid in the BZ. For the collinear cases the FSWFs were generated from one $4s$ - and five $3d$ -orbitals per atom for each spin separately, which were constructed from the radial solutions for the FLAPW potential. In non-collinear calculations the spin channels are mixed, and two $4s$ - and ten $3d$ -orbitals per atom were used to construct the FSWFs per atom. The energy bands were disentangled using the procedure described in reference [136]. For the collinear calculations the lowest 58 eigenvalues per k -point were used to obtain 48 WFs for the 8 atom super-cell and the lowest 104 eigenvalues per k -point for 96 WFs for the 16 atom super-cell calculations. With non-collinearity of the magnetization included the the lowest 103 eigenvalues per k -point were used to obtain 96 WFs for the 8 atom unit cell. For testing purposes, for several non-collinear configurations the electronic structure of the system is compared calculated with FLEUR and with corresponding FSWFs, finding that a very good description of the electronic structure can be achieved with FSWFs within the 3rd nearest-neighbor approximation, while for FSWFs calculations of the transmission in the

vicinity of the Fermi level already the 2nd nearest-neighbor approximation to the FSWFs Hamiltonian provides very reliable results.

8.2.1 The Tunneling-to-Contact Regime

The investigation of the $\text{Co}_\infty\text{-Mn-Mn-Co}_\infty$ junction starts with both leads positioned far away from each other. To mimic a tip-sample approach, the Mn-Mn distance $d_{\text{Mn-Mn}}$ is decreased, the calculated energies of collinear states $\text{P}\uparrow\uparrow$, $\text{P}\downarrow\downarrow$ and $\text{P}\downarrow\uparrow$ are shown in Figure 8.5 (a). The energy difference between $\text{P}\uparrow\uparrow$ and $\text{P}\downarrow\downarrow$ states when the distance is varied in the tunneling regime from $d_{\text{Mn-Mn}} = 20$ bohr down to 10 bohr remains relatively constant and constitutes around 27 meV per atom, indicating weak interaction between both sides of the junction and a weak ferromagnetic coupling between the Mn atom and its nearest Co neighbor (NN Co). After a small reduction of the energy difference between the $\text{P}\uparrow\uparrow$ and $\text{P}\downarrow\downarrow$ states, the FM Mn-Co coupling becomes more stable for decreasing $d_{\text{Mn-Mn}}$, expressed in an increasing energy difference. In the contact regime the energy difference is slightly decreased from 93.5 meV at $d_{\text{Mn-Mn}} = 5.0$ bohr down to 77 meV per atom at $d_{\text{Mn-Mn}} = 4.5$ bohr. This decrease in energy can be correlated with strong changes in the Mn and NN Co spin moments, S_{Mn} and S_{Mn} , respectively, upon decreasing the distance, see Figure 8.5 (b) and (c) (see also discussion in section 8.2.3).

While in all cases the spin moments of the Co atoms, not neighboring the Mn atoms directly ($\approx 2.09 \mu_B$) are very similar to the spin moments of the Co atom in an infinite lead ($\approx 2.07 \mu_B$), the spin moments of Mn atoms and the NN Co atoms can be strongly affected by $d_{\text{Mn-Mn}}$ and spin configuration of the junction. Namely, for the $\text{P}\downarrow\downarrow$ state S_{Mn} decreases from $4.3 \mu_B$ to $3.9 \mu_B$, while NN S_{Co} increases from $1.4 \mu_B$ to $1.8 \mu_B$, as $d_{\text{Mn-Mn}}$ is varied from 5.5 to 4.5 bohr. On the other hand, if the Mn spin moment exhibits a similar variation as a function of distance for the $\text{P}\uparrow\uparrow$ state, the spin moment of the NN Co atoms remains relatively constant ($\approx 2 \mu_B$). This interplay between structure and magnetism already indicates that the intra-atomic as well as inter-atomic exchange, given by the Stoner parameter I and the Heisenberg exchange constants J , respectively, may be of importance for the further understanding of the magnetic properties of this system.

The change from FM coupling at larger interatomic distances to an AFM coupling at smaller $d_{\text{Mn-Mn}}$ in an infinite Mn chain has been predicted based on DFT calculations [167]. In the vicinity of this crossover point the Mn spins favor non-collinear magnetic order [168, 170, 171]. To demonstrate a strong tendency of Mn spin moments to AFM coupling at smaller values of $d_{\text{Mn-Mn}}$ the energy difference is plotted between the $\text{P}\uparrow\uparrow$ and $\text{P}\downarrow\uparrow$ states in Figure 8.5 (a). Reversing one the Mn spin moments in the $\text{P}\uparrow\uparrow$ configuration is clearly energetically more favorable than the $\text{P}\uparrow\uparrow$ state when the distance between the Mn atoms is below ≈ 5.2 bohr. In this case the gain in energy due to switch of the Mn spin moment can be explained only by the strong AFM coupling of the two Mn atoms for this regime of interatomic

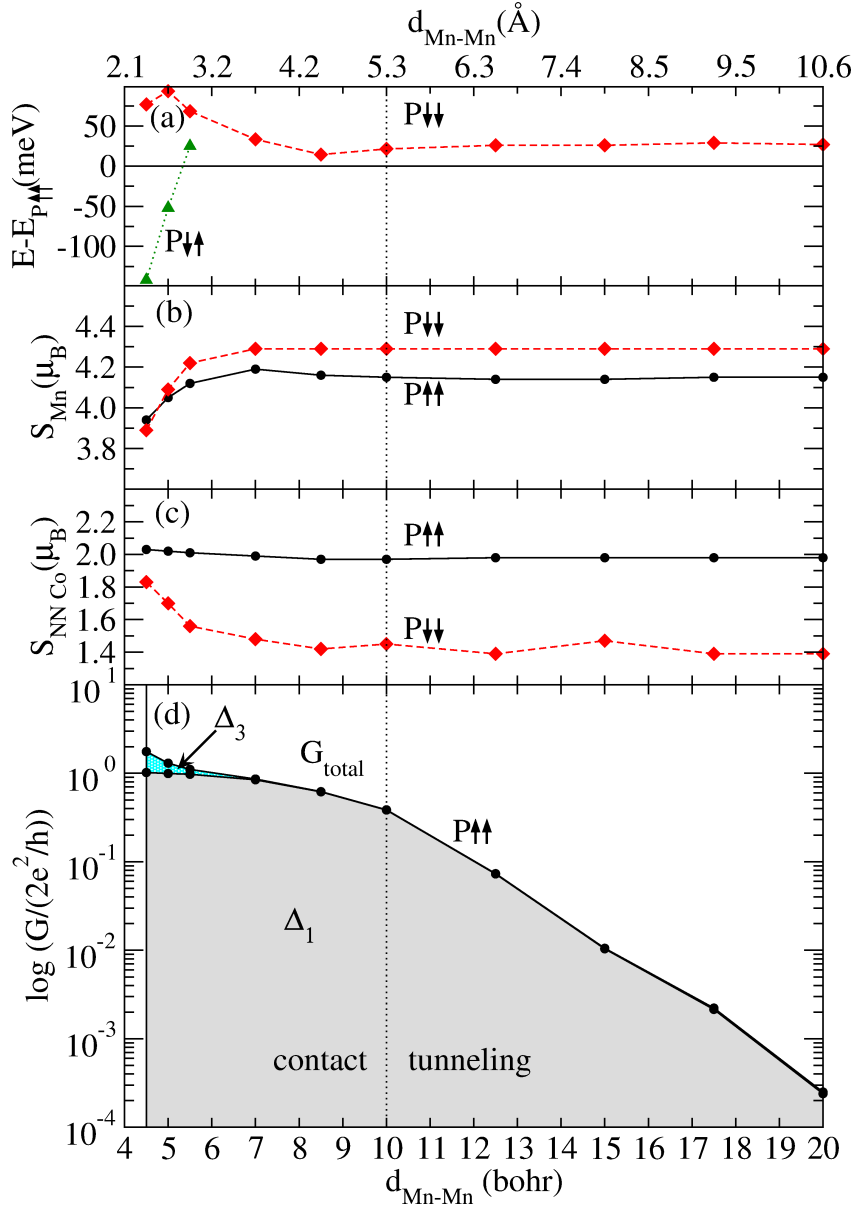


Figure 8.5: (a) Energy of the $\text{P}\downarrow\downarrow$ state (red diamonds, dashed line) and $\text{P}\downarrow\uparrow$ state (green triangles, dotted line) with respect to the energy of the $\text{P}\uparrow\uparrow$ state, as a function of the Mn-Mn interatomic distance $d_{\text{Mn-Mn}}$. Spin moment of the Mn atoms, S_{Mn} , (b), and NN Co atoms, S_{Co} , (c), for $\text{P}\uparrow\uparrow$ (black circles, solid line) and $\text{P}\downarrow\downarrow$ (red diamonds, dashed line) configurations are given as a function of $d_{\text{Mn-Mn}}$. (d) Total conductance at the Fermi level, $G_{\text{total}}(E_F)$ (upper line) and Δ_1 conductance $G_{\Delta_1}(E_F)$ (lower line) on a logarithmic scale for the $\text{P}\uparrow\uparrow$ -state. Gray shaded area is associated with the Δ_1 conductance, while cyan shaded area with the Δ_3 conductance.

distance, since the coupling of the Mn atom with its NN Co atom is ferromagnetic. The spin moments in the $P\downarrow\uparrow$ state at $d_{\text{Mn-Mn}} = 4.5$ bohr constitute $4.1 \mu_B$ for Mn and $1.5 \mu_B$ for its NN Co on the AFM side, and $3.7 \mu_B$ for Mn and $1.9 \mu_B$ for the NN Co on the FM side. For larger $d_{\text{Mn-Mn}}$ values the $P\uparrow\uparrow$ state is the lowest in energy state as compared to all possible collinear states of the junction in which the magnetization direction of the left and right leads is the same, which is indicative of the FM Mn-Mn coupling for larger distances.

In Figure 8.5 (d) the results of the calculations are presented for the evolution of the ballistic conductance of a $P\uparrow\uparrow$ junction when going from tunneling to contact regime. The main contribution to the conductance at large Mn-Mn distances is coming solely from the Δ_1 channel, owing to the overlap between the $s-d_{z^2}$ orbitals of the neighboring Mn atoms across the barrier. Within the introduced approach, the expected exponential behavior of the conductance at very large distances is very nicely reproduced. At a distance of $d_{\text{Mn-Mn}} \approx 10$ bohr the conductance approaches the magnitude of the conductance quantum, reaching saturation upon further decreasing the distance. For the distances below 7 bohr more localized d -orbitals of Δ_3 symmetry start contributing to the total conductance, as can be seen in Figure 8.5 (d). The Δ_3 contribution to the conductance increases with decreasing distance. As can be seen in the following, the details of hybridization between the Δ_3 orbitals are very sensitive to the magnetic state of the junction. On the other hand, in all considered cases the d -states of Δ_4 symmetry do not contribute to the conductance due to an energetic mismatch between the states of this symmetry of NN Co and Mn atoms, see discussion in section 8.2.3.

Before continuing to investigate non-collinear magnetic order in the $\text{Co}_{\text{inf}} - \text{Mn} - \text{Mn} - \text{Co}_{\text{inf}}$ junction, the quality of non-collinear transport calculations is confirmed. As a reference, the conductance of the collinear $P\uparrow\uparrow$ and $P\downarrow\downarrow$ configurations are obtained within a collinear and within a non-collinear representation, as shown in Figure 8.6. While both descriptions do not result in identical conductances, both are in very good agreement with each other, particularly in the linear response regime in the vicinity of the Fermi level. There are differences between both descriptions, e.g. at the lower band edges (Figure 8.6 (a) at -4.5 eV and Figure 8.6 (b) at -3.6 eV) due to the known issues in the description of the $s - d_{z^2}$ -orbitals (cf. chapter 6.8) and well above the Fermi level (Figure 8.6 (b) at 1.5 eV) due to differing collinear and non-collinear FLAPW bandstructures. (cf. chapter 8.1, Figure 8.1 (b)). For critical systems with band edges of $s - d_{z^2}$ -origin at the Fermi level, other than the present system, the NN approximation would have to be increased to resolve the first issue. The second issue only occurs for unoccupied states and in case of antiparallel aligned spin moments due to numerical difficulties to decouple both spin-channels in a non-collinear FLAPW calculation, as discussed in section 8.1. this regime is typically situated outside of the range of validity of FLAPW and NEGF ballistic transport methods. All occupied states and states slightly above the Fermi level have been found to be captured well for all similar

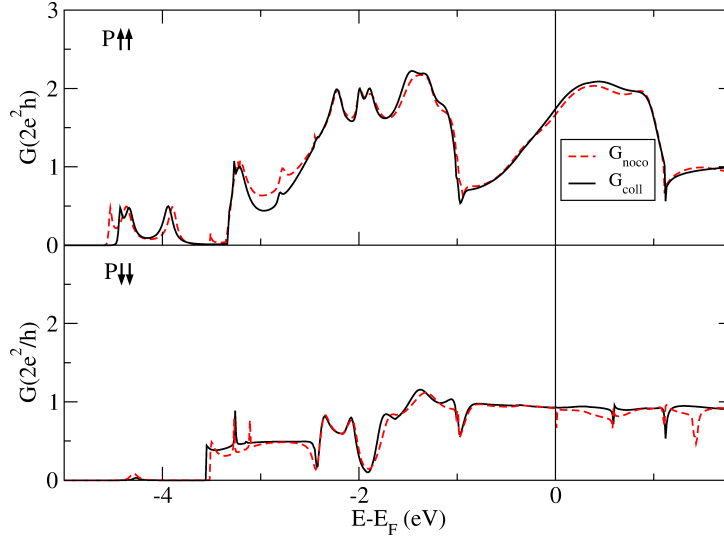


Figure 8.6: Comparison between the conductances of the (a) $\text{P}\uparrow\uparrow$ and (b) $\text{P}\downarrow\downarrow$ configurations of the $\text{Co}_{\text{inf}} - \text{Mn} - \text{Mn} - \text{Co}_{\text{inf}}$ junction in collinear (dashed red lines) and non-collinear (solid black lines) WF representation obtained within the 2nd NN FSWFs approximation.

systems investigated in this thesis.

8.2.2 Non-Collinear Magnetic States of the Junction in Contact Regime

According to the findings presented above, the Mn spin moments are expected to experience a frustration in the contact regime, when the magnetizations of the leads are parallel to each other. In this case, when Mn atoms are close enough, FM coupling of Mn spins with NN Co atoms and AFM Mn-Mn coupling can possibly lead to a stable non-collinear magnetic state. In order to consider this situation, an angle α is introduced between the spin moments of the Mn and the NN Co atoms, rotating the first Mn spin moment by $+\alpha$ and the second one by $-\alpha$, while keeping the moments of the Co atoms fixed, see Figure 8.4 (b), which constitutes a symmetric $\text{P}\alpha$ -state. The distance is chosen to be 4.5 bohr between the Mn atoms as a representative of the contact regime at which the Mn-Mn coupling is strongly antiferromagnetic.

The results of the calculations for the total energy of the $\text{P}\alpha$ state, $E_{\text{P}\alpha}$, in relation to the energy of the $\text{P}\uparrow\uparrow$ state are shown in Figure 8.7 (a) as a function of the angle α . From this plot can be observed that the minimum of the total energy is acquired for the non-collinear $\text{P}105^\circ$ state, which is 137 meV lower in energy than corresponding collinear $\text{P}\uparrow\uparrow$ state. The failure of straightforward description of the $E_{\text{P}\alpha}$ in terms of a simple Heisenberg model which assumes just the nearest-neighbor Co-Mn and Mn-Mn exchange coupling, given by antiferromagnetic $J_{\text{Mn}} < 0$ and ferromagnetic

$J_{\text{Co}} > 0$, respectively, can be understood from noticing that the expression for the energy within this approximation, given by

$$E_{\text{P}\alpha}(\alpha) = -\frac{1}{2}(J_{\text{Mn}} \cos(2\alpha) + 2J_{\text{Co}} \cos(\alpha)), \quad (8.1)$$

where the prefactor $\frac{1}{2}$ accounts for the energy per Mn atom, acquires a minimum for angles α below 90° , in contradiction to the calculations.

The solution to this deficiency of the Heisenberg model can be given by lifting the assumption that the exchange interaction between the Mn and Co spins, given by J_{Co} , is ferromagnetic. As can be seen from Figure 8.7 (b) and (c), while the Mn spin moment remains relatively constant upon changing α , S_{Co} for values of α below 60° is by as much as $0.2 \mu_B$ larger than for $\alpha > 90^\circ$. Owing to the intra-atomic Stoner exchange, the non-collinear states with small α therefore acquire a negative contribution to the total energy in addition to that proportional to J_{Co} , as compared to larger angles.

If accounting for the energy gain due to creation of the NN Co spin moments by a Stoner parameter of Co, $I \approx 990$ meV [172], and subtract the energy gain $E_{\text{Stoner}} = \frac{1}{2}IS_{\text{Co}}^2$ from the calculated DFT dispersion, the resulting energy dispersion (squares in Figure 8.7(a)), includes only for exchange interactions between the atoms. If this curve is now fitted according to Eqn. (8.1) (dashed line in Figure 8.7(a)), "non-renormalized" Heisenberg exchange constants are obtained of $J_{\text{Co}} = -170$ meV and $J_{\text{Mn}} = -266$ meV. Including the biquadratic interaction (cf. chapter 3.8, Eqn. (3.66)), which is either stabilizing or destabilizing collinear magnetic moments in general ($E_{\text{biq}} \propto (\mathbf{S}_i \mathbf{S}_j)^2$), is not found to provide a significant improvement of the description or to resolve this problem, the term is therefore neglected further on. It becomes clear now, that, although the "pure" exchange coupling between the Mn and Co spins is expectedly antiferromagnetic, the larger spin moment of Co when the Mn spin is aligned in parallel to it, tips the balance in favor of ferromagnetic coupling between the spins, which can be observed for a large range of distances $d_{\text{Mn-Mn}}$, c.f. Figure 8.5(a).

From Figure 8.5(a) can also be observed that, judging from the energies, in the close contact regime the collinear $\text{P}\downarrow\uparrow$ -state is competing with the non-collinear $\text{P}\alpha$ -state for the global ground state of the system. Indeed, the calculations show that at the $d_{\text{Mn-Mn}}$ of 4.5 bohr the $\text{P}\downarrow\uparrow$ -configuration is by tiny 5 meV lower in energy than the $\text{P}105^\circ$ solution. However, the $\text{P}\downarrow\uparrow$ -state is not very likely to appear in experiments, given that the Co electrodes are identical. In this case, the adiabatic rise of the intrinsically asymmetric $\text{P}\downarrow\uparrow$ -configuration via symmetric non-collinear states cannot happen, as the electrodes, initially being in the $\text{P}\uparrow\uparrow$ -state when very far from each other, are brought together (see also discussion at the beginning of section 8.2.5). Nevertheless, it seems plausible, that such state, if observed in experiment, is created via a rapid flip of one of the Mn atoms in the contact regime, during, e.g., a reformation of the lead geometry, or an inelastic current-induced spin-

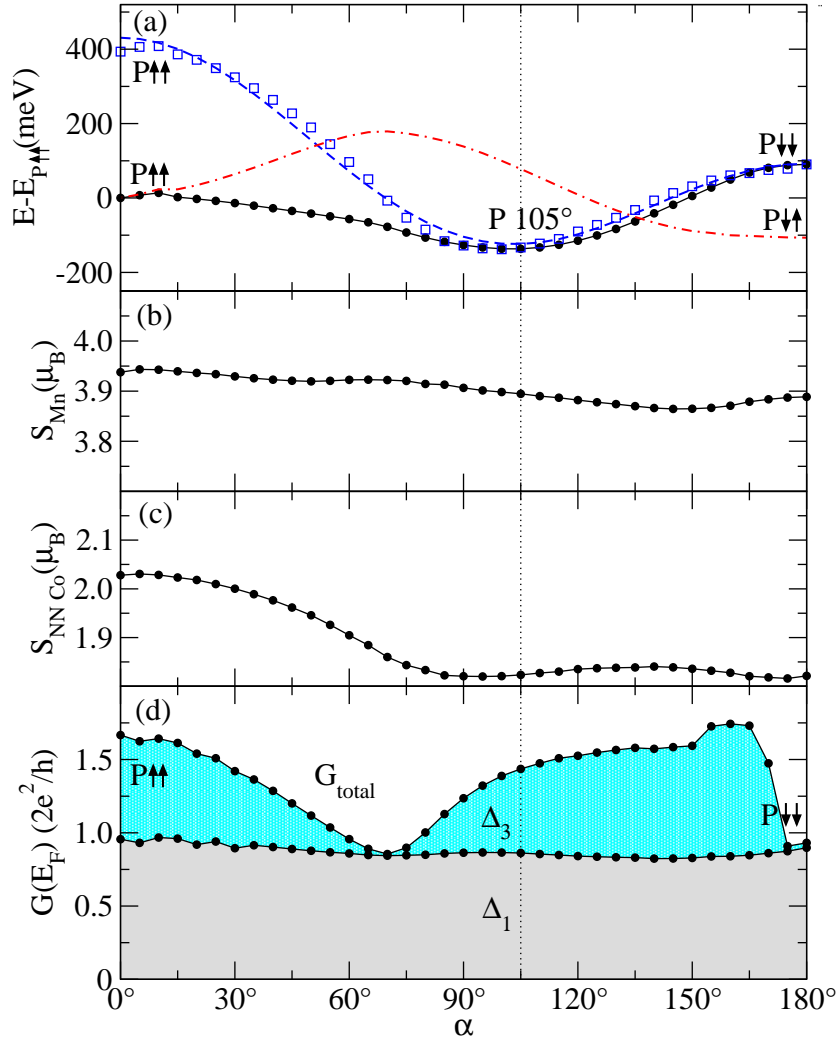


Figure 8.7: a) Total energy of the $P\alpha$ state obtained with DFT with respect to the $P\uparrow\uparrow$ state as a function of angle α (solid line, filled circles). With open black squares the total energy of the $P\alpha$ state is shown from which the Stoner energy due to creation of the NN Co spin moments is subtracted. The corresponding fit of the corrected energy within the Heisenberg model is shown with a dashed blue line. With the red dotted line the total energy of the $P\uparrow\downarrow$ state is shown with only the \downarrow -Mn spin rotated by an angle α , calculated within the Heisenberg model and incorporating also the Stoner exchange. (b) Mn spin moment as a function of angle α . (c) NN Co spin moment as a function of angle α . (d) Ballistic conductance at the Fermi level for the $P\alpha$ state as a function of angle α : total conductance $G_{\text{total}}(E_F)$ (upper line), the Δ_3 conductance contribution (cyan shaded area) and Δ_1 conductance $G_{\Delta_1}(E_F)$ (lower line, gray shaded area).

flip process. The calculations, shown with a dash-dotted line in Figure 8.7(a), based on the Heisenberg model introduced above which includes the Stoner term reflecting the modifications of one of Co moments, indicate, that once the system enters the $P\downarrow\uparrow$ -state, it is effectively "trapped" there, since the \downarrow -Mn is energetically quite stable versus deviations in the angle its spin makes with the rest of the spins in the system. Thus, no non-collinear states are considered associated with the $P\downarrow\uparrow$ -state in the following.

8.2.3 Ballistic Conductance of Non-Collinear Magnetic States of the Junction

In this section a detailed analysis is performed of the ballistic conductance $G(E_F)$ of the $P\alpha$ state at fixed distance between Mn atoms of 4.5 bohr. At this distance, $G(E_F)$ is calculated as a function of angle α and the results are presented in Figure 8.7 (d). From this plot can be observed that the conductance exhibits a very non-trivial dependence on α , originating mainly from the Δ_3 -orbitals ($d_{xz,yz}$), while the Δ_1 contribution ($s - d_{z^2}$) to the conductance, G_{Δ_1} , remains almost perfectly constant. Surprisingly, the Δ_3 -conductance almost vanishes for α of about 70° , away from any high-symmetry spin configuration in the junction, suggesting, that the dependence of the details of hybridization and electronic structure on the angle between the Mn spins can be rather delicate. In order to analyze this dependence in more detail, as a function of α , the energy-dependent conductance, $G(E)$, is plotted versus the local densities of states (LDOS) of Mn and NN Co atoms resolved into spin-up and spin-down contributions with respect to the global spin quantization z -axis, Figure 8.8. The further analysis is focused mainly on the Δ_3 -contribution to the conductance and the LDOS, although in the upper ($P\uparrow\uparrow$) and lower ($P\downarrow\downarrow$) panels of Figure 8.8 also show the total LDOS of the atoms.

The conductance at a given energy E depends on the presence of available states in the LDOS of the atoms at E , and on the coupling between these states across the junction – both of which depend on the orientation of the spins with respect to each other. By looking at the LDOS of the atoms presented in Figure 8.8 for $\alpha = 0^\circ$ the absence of the Δ_4 contribution to the conductance can be explained: The localized Δ_4 (dashed line) states of the Co atoms, which can be seen as pronounced peaks in the LDOS marked with the dashed line in Figure 8.8 (b), are positioned at about -2 eV for spin-up channel and directly at the Fermi energy for spin-down channel, while the corresponding Mn Δ_4 states are positioned below -2.5 and above $+1$ eV, prohibiting thus the hybridization between the Co and Mn orbitals of Δ_4 symmetry across the junction. Noticeably, the LDOS of both atoms for the up-spin in a wide region of energies around E_F is absent, leading to a negligible \uparrow -conductance. Here, it is important to remark, that the LDOS of the NN Co atoms around the Fermi energy overall resembles quite well the LDOS of a Co atom in a Co monowire (cf. Figure 6.22 in chapter 6.7), or even of a Co atom deposited on a noble-metal surfaces [173]. This means that the results should be rather stable with respect

to the geometry of the Co leads, manifesting that the main influence on the Δ_3 conductance at E_F would come from the hybridization of the Mn and NN Co states.

Turning now to comparatively delocalized Δ_3 -states (solid line) on both Co and Mn atoms, it can be observed that they hybridize directly at the Fermi energy, which leads to a significant Δ_3 contribution to the conductance. Specifically, while the Δ_3^\downarrow subband of Co spreads from -1.8 to $+1$ eV, the Δ_3 -down states of Mn atoms are distinctly split into wide bonding ("b") states at the Fermi energy and narrow anti-bonding ("a") states at $+1.8$ eV. Very importantly for the transport properties of the system, the hybridization of the Δ_3^\downarrow band of Co with the Δ_3^\downarrow states of Mn is non-trivial. (i) The Δ_3^\downarrow states of Co exhibit a dip at the position of the maximal density of bonding states of Mn due to the fact that these Mn states are localized mainly in between the Mn atoms prohibiting strong overlap with the Co states. (ii) The upper, antibonding, part of the Co Δ_3^\downarrow band hybridizes stronger with the bonding states of Mn, since the antibonding states of Co atoms have a larger overlap with the Mn orbitals, which results in a larger Δ_3 -conductance above E_F . (iii) Analogously, for energies below E_F the conductance is suppressed, since the bonding-like Δ_3^\downarrow Co states have smaller overlap with the Mn bonding states.

Following the evolution of the electronic structure upon increasing the angle between the Mn spins, two trends in the LDOS can be clearly observed in Figure 8.8. Firstly, with increasing α the splitting between the bonding and antibonding Mn states decreases owing to the mixed spin character of the states. At the angle of 90° , when Mn spins are antiparallel to each other, both types of states transform into degenerate Δ_3 -orbitals of the "isolated" Mn atoms, since the hybridization between the Mn states of the same spin is almost absent due to large exchange splitting. On the other hand, the dip in the \downarrow -LDOS of the NN Co atoms follows the position of the bonding state of the Mn dimer, moving from the Fermi energy at $\alpha = 0^\circ$ to $+0.2$ eV for $\alpha = 90^\circ$ (indicated by filled triangles in Figure 8.8). Overall, such redistribution of the LDOS of the atoms combined with the effect of decreasing LDOS of Mn atoms for spin-down channel at the Fermi energy when the angle α is varied, results first in a decrease of the conductance at E_F for $\alpha \approx 70^\circ$, followed by a consequent increase with increasing angle.

When the angle α increases further beyond 90° , the bonding and anti-bonding Mn states eventually acquire their initial splitting at $\alpha = 180^\circ$ ($\text{P}\downarrow\downarrow$ -state), when the Mn spins are collinear again. Simultaneously, with increasing angle, it can be observed that the Mn states around the Fermi energy become sharper, since the hybridization with the Co leads decreases as the Mn states become predominantly spin-up in character. Interestingly, while for $90^\circ < \alpha < 120^\circ$ a large value of the Δ_3 -conductance is due to a significant amount of delocalized Co and bonding Mn states at the Fermi energy in the spin-down channel, for larger angles the value of $G_{\Delta_3}(E_F)$ is due to a sharp resonant Co state in the spin-up channel at the Fermi energy, coupled to a bonding Mn state at E_F . When further increasing α above 170° , this resonance becomes more localized and decoupled from the states in the

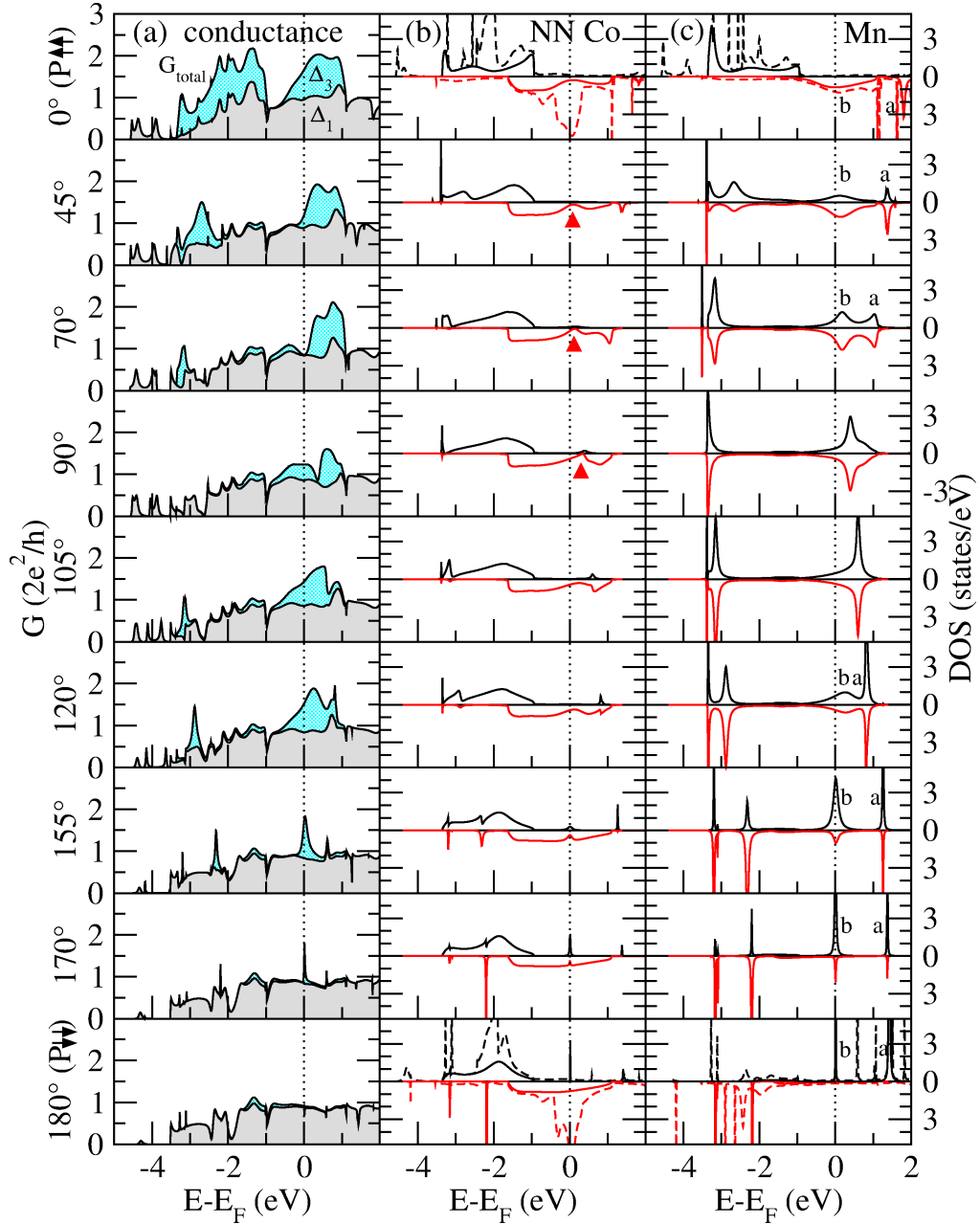


Figure 8.8: Transport properties and electronic structure of the P_α -state at $d_{\text{Mn-Mn}}$ of 4.5 bohr as a function of angle α (indicated on the left). (a) Total conductance G_{total} (upper line) decomposed into the Δ_3 - (cyan shaded area) and Δ_1 -contributions (G_{Δ_1} , lower line, gray shaded area). The spin-resolved local density of states (LDOS) of the NN Co atom and Mn atom are given in columns (b) and (c), respectively. For both (b) and (c) the LDOS spin-decomposition is performed with respect to the global frame, with spin-up and spin-down LDOS presented in the upper and lower parts of each plot. In both (b) and (c), the Δ_3 -contribution is indicated with solid lines, while for $\alpha = 0^\circ$ and $\alpha = 180^\circ$ also the total LDOS is shown with dashed lines. The red triangles in (b) follow the development of the dip in the LDOS of the NN Co atom as the angle α is varied. In (c), the bonding and anti-bonding unoccupied Mn states are marked with "b" and "a", respectively. For details see text.

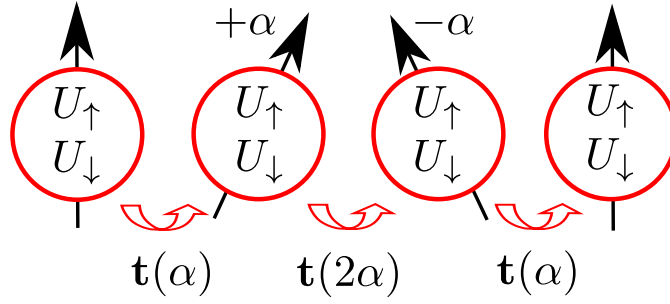


Figure 8.9: Scattering region of the simple tight-binding model consisting of 4 atoms with on-site hopping elements of $U_{\downarrow} = 0$ eV (minority states), $U_{\uparrow} = -2.1$ eV (majority states). The two central spin moments are rotated by applying the spin-rotation matrices \mathbf{U}_{α} , resulting in angle dependent hopping matrices $\mathbf{t}(\alpha)$ and $\mathbf{t}(2\alpha)$, respectively. The matrix elements of $\mathbf{t}(0^{\circ})$ are $t_{\uparrow\uparrow} = t_{\downarrow\downarrow} = -0.5$ eV and $t_{\uparrow\downarrow} = t_{\downarrow\uparrow} = 0$ eV between NN atoms.

leads, while the Mn LDOS at the E_F in the minority spin-channel vanishes, causing a sharp drop in the Δ_3 -conductance. By looking at the total LDOS of the NN Co atom in the $\text{P}_{\downarrow\downarrow}$ -state it can be observed that it remains basically unaffected, as compared to the $\text{P}_{\uparrow\uparrow}$ -configuration, while the Mn states become pronouncedly decoupled from the states of the NN Co owing to the energetical mismatch for both spin channels.

8.2.4 Model-Based Analysis of the Non-Collinear Ballistic Conductance

A further understanding of the previously observed complex non-collinear conductances, shown in Figure 8.8, can be obtained from a simple tight-binding model. While the constant Δ_1 channel contribution is rather easy to explain, the aim of this section is to provide further insights into the more complex conductance behavior of the Δ_3 channel upon the rotation of the two central spin moments by $\pm\alpha$. Therefore, the effect of non-collinear spin order is included into a simple tight binding model of two exchange-split bands by applying spin-rotation matrices \mathbf{U}_{α} (chapter 4.7, Eqn. (4.30)). The Hamiltonian of the tight-binding model is constructed (see Figure 8.9) of a perfect and magnetic four atom monowire with on-site hopping elements of $U_{\downarrow} = 0$ eV (minority states), $U_{\uparrow} = -2.1$ eV (majority states), chosen to reproduce two exchange split bands. The spin-dependent hopping elements are expressed by the matrix \mathbf{t} with the matrix elements $t_{\uparrow\uparrow} = t_{\downarrow\downarrow} = -0.5$ eV and $t_{\uparrow\downarrow} = t_{\downarrow\uparrow} = 0$ eV between NN atoms. In the upper panels of Figure 8.10 it is shown, that without considering the spin-rotation matrices, such a model Hamiltonian results two uniform, decoupled and exchange-split bands with minority states at the Fermi energy and a step-like conductance behavior. The results are obtained within the transport code based on the model tight-binding Hamiltonian defined above.

Now, two central spin moments are rotated by $\pm\alpha$ due to spin-rotation matrices, mimicking the rotation of Mn atoms in a $P\alpha$ $\text{Co}_\infty\text{-Mn-Mn-Co}_\infty$ junction. The \mathbf{U}_α matrices are applied to the hopping elements \mathbf{t} , which then depend on the *relative* angle between adjacent spin-moments: The hopping elements $\mathbf{t}(\alpha)$ between unrotated and rotated atoms depend on α and the hopping elements $\mathbf{t}(2\alpha)$ between the two rotated atoms on 2α , as shown in Figure 8.9. As a result, the off-diagonal elements $t_{\uparrow\downarrow} = t_{\downarrow\uparrow}$ can become non-zero, coupling thereby both spin channels.

Here, angles from $\alpha = 30^\circ$ to 180° are considered, transforming the model Hamiltonian from its $P\uparrow\uparrow$ to its $P\downarrow\downarrow$ configuration. Due to the reduced hybridization upon rotating the central spin moments by $\pm\alpha$ the states in the rotated atoms become more localized, resulting in peaks in the LDOS, e.g. at 0.1 eV for $\alpha = 90^\circ$, as can be seen in Figure 8.10 (c). The reduced coupling of those localized states to the states in the unrotated NN atom leads to corresponding dips in the LDOS, shown in Figure 8.10 (b). The vanishing LDOS in the NN atom results again in no transmission at that particular energy, as displayed in Figure 8.10 (a). A similar behavior can be found in the $\text{Co}_\infty\text{-Mn-Mn-Co}_\infty$ junction, e.g. at 70° (Figure 8.10).

Upon further rotating the spin moments of the central atoms, two peaks appear in the LDOS of those atoms, similar to the findings in the $\text{Co}_\infty\text{-Mn-Mn-Co}_\infty$ junction (Figure 8.8 (c)), which become sharper for larger angles α (see Figure 8.10 (c)). This indicates a further localization due to the reduced hybridization across the junction. The influence of those localized states on the LDOS of the unrotated NN atoms, as shown in Figure 8.10 (b), results in minor dips in the same spin channel and small peaks in the channel with opposite spin due their coupling into both spin channels. These small dips and peaks in the LDOS can be as well observed in the Δ_3 -states of the NN Co atoms in the $\text{Co}_\infty\text{-Mn-Mn-Co}_\infty$ junction, as shown in Figure 8.8 (b) and (c). The conductance, shown in Figure 8.10 (a), mainly follows the peaks of the localized states of the atoms with rotated spin moments. Finally, the conductance vanishes for the $P\downarrow\downarrow$ configuration at 180° , where the majority and minority states are decoupled across the junction, in accordance with the $\text{Co}_\infty\text{-Mn-Mn-Co}_\infty$ junction (Figure 8.8 (a)). However, in the real system, a small fraction of Δ_3 conductance survives due to electron tunneling across the Mn atoms.

In Figure 8.11, the angular dependence of the conductance of the tight-binding model is compared to the Δ_3 conductance of the $\text{Co}_\infty\text{-Mn-Mn-Co}_\infty$ junction. Here, the tight-binding model contains two degenerate channels (d_{xz} and d_{yx}). The conductance of the $\text{Co}_\infty\text{-Mn-Mn-Co}_\infty$ junction is overall reduced compared to the tight-binding model due electron scattering caused by the more complex chemical composition and geometrical shape, not captured by the model. As pointed out before, the first minimum of the conductance at the Fermi level of the tight-binding model is located at $\alpha = 90^\circ$ in contrast to the found 70° in the $\text{Co}_\infty\text{-Mn-Mn-Co}_\infty$ junction, which is due to the details of the electronic structure (compare LDOS in Figure 8.8 (b) and 8.10 (b)). The consecutive rise of the conductance can be qualitatively achieved within the tight-binding model up to angles of 120° . Beyond 120° , the

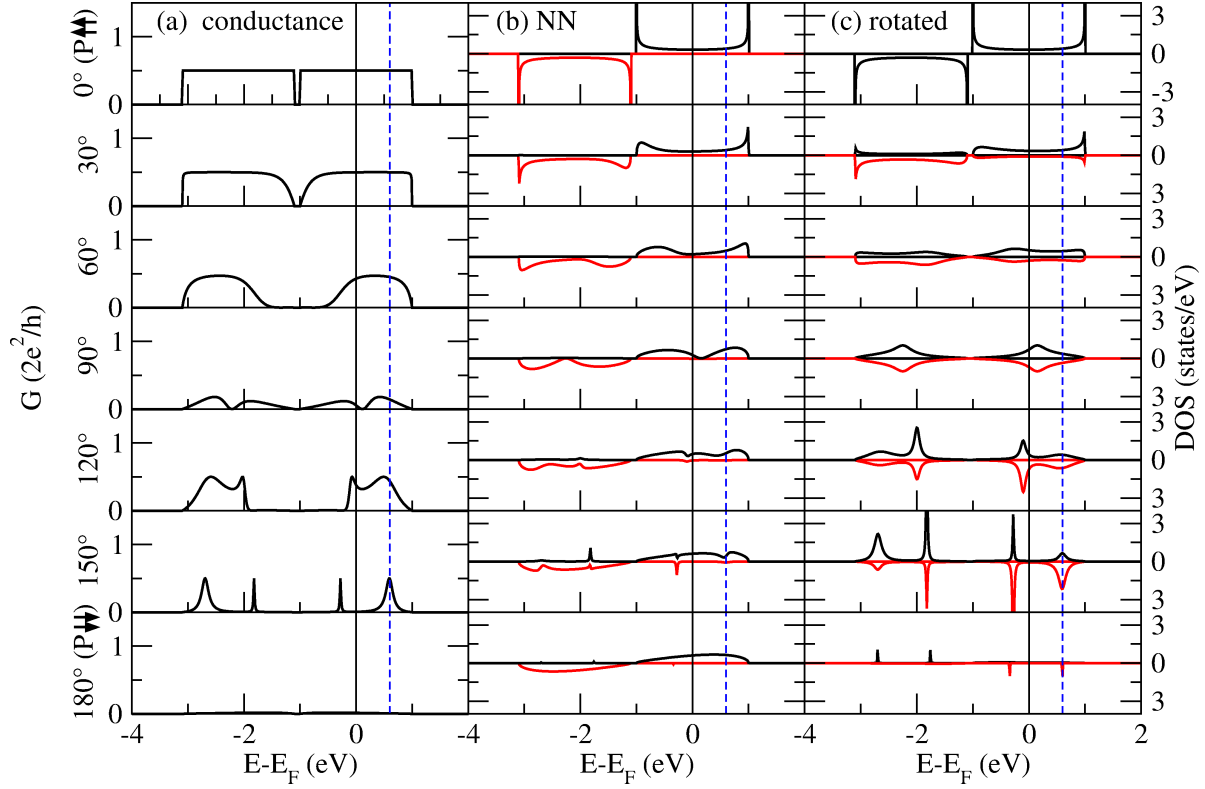


Figure 8.10: Transport properties and electronic structure of a two-channel tight-binding model Hamiltonian including the spin-rotation matrices as a function of angle α (indicated on the left). (a) Total conductance G_{total} . The spin-resolved (majority bands black upper curves; minority bands red lower curves) local density of states (LDOS) of the NN atom and a rotated atom (cf. Figure 8.8) are given in columns (b) and (c), respectively. For both (b) and (c) the LDOS spin-decomposition is performed with respect to the global frame, with spin-up and spin-down LDOS presented in the upper and lower parts of each plot. For details see text.

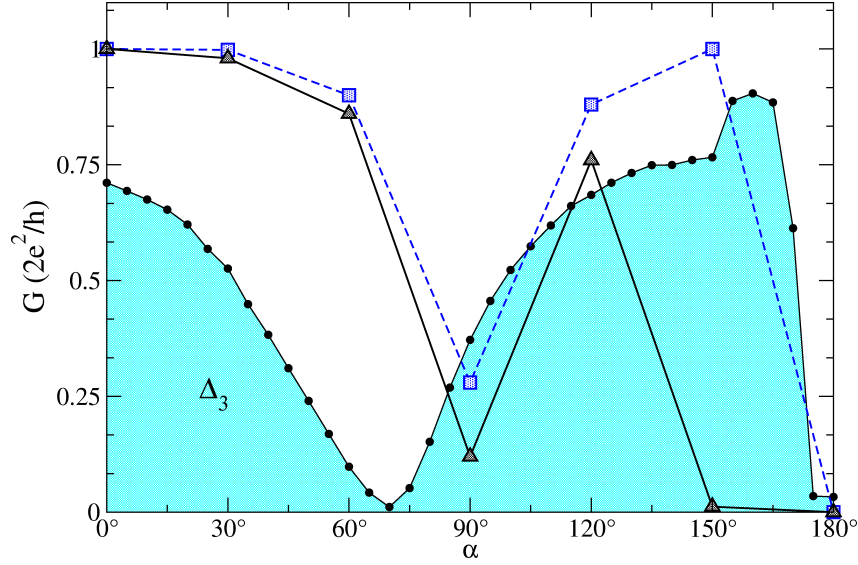


Figure 8.11: Ballistic Δ_3 channel conductance for the $P\alpha$ states as a function of angle α : The $\text{Co}_\infty\text{-Mn-Mn-Co}_\infty$ junction (filled black circles, cyan shaded area) and the tight-binding model (black triangles, thick black line) at E_F ; the tight-binding model at 0.6 eV.

tight-binding model and the $\text{Co}_\infty\text{-Mn-Mn-Co}_\infty$ junction differ significantly due to the energetical position of the localized states (compare LDOS-peaks in Figure 8.8 (c) and 8.10 (c)). To regain a qualitative correspondence between the conductances for larger angles, the localized states of the tight-binding Hamiltonian have to be shifted to the Fermi level. This can be done by either reducing the on-site matrix of the tight-binding Hamiltonian elements by -0.6 eV or by evaluating the conductance at 0.6 eV (blue dashed lines in Figure 8.11). In this case, the high conductance for larger angles α is captured well by the model.

In conclusion, the details of the angular dependence of the conductance strongly depend on the electronic structure of the investigated system and the energetical location of the Fermi level. However, the key features of the Δ_3 conductance of the $\text{Co}_\infty\text{-Mn-Mn-Co}_\infty$ junction can be qualitatively explained by the introduced simple tight-binding model and spin-rotation matrices.

8.2.5 Fingerprints of Non-Collinear Magnetic States in Ballistic Conductance Experiments

Here, the evolution of the conductance of different magnetic states of the junction is investigated, mimicking thus a typical STM or break junction experiment. This approach is partly motivated by the fact that a non-trivial behavior of magnetoresistance when going from tunneling to contact has been recently observed in STM experiments [154]. At a very large separation between the leads (or, the tip and the

sample in the language of STM experiments), owing to the FM coupling of the Mn atom to the Co chain, one can imagine only two possible magnetic configurations – $\text{P}\uparrow\uparrow$ and $\text{AP}\uparrow\downarrow$. The conductance of these two magnetic states in the tunneling regime, arising mainly from the s -orbitals, is orders of magnitude smaller than in the contact regime, for which the dependence of $G(E_F)$ on the distance can be non-trivial due to the large contribution of the d -states.

In the case of the $\text{AP}\uparrow\downarrow$ configuration, the starting collinear arrangement of the spins will survive over the whole range of the separation between the leads, since in the contact regime, when the Mn atoms are close to each other, both exchange preferences of the Mn spins, that is, FM coupling to the NN Co spins and AFM coupling among each other, are fulfilled. Small possible deviations from the collinear arrangement of the Mn spins, which can affect the details of the distribution of the Δ_3 -states and their coupling to the leads, would not manifest in a conductance measurement, owing to the antiparallel magnetizations of the leads, and corresponding complete dominance of the Δ_1 channel for conductance at E_F in this case, Figure 8.12. As can be seen from this Figure, $G(E_F)$ lies in between 0.5 and $1.0 G_0$, when the distance between the Mn atoms is varied from 8.5 to 4.5 bohr. This is very similar to the behavior of the conductance at the Fermi energy of pure AP Co leads without Mn atoms, see Figure 6.23 in chapter 6.7. The evolution of the $\text{AP}\uparrow\downarrow$ conductance upon stretching the Mn-Mn bond is shown in Figure 8.13. For the $\text{AP}\uparrow\downarrow$ configuration only Δ_1 states, which are present in both leads, contribute to the conductance, since the majority and minority channels (thin dash-dotted lines in Figure 8.13) are exchanged for the right lead. In contrast to the AP FM Co wire (cf. chapter 6.7.1), where a small Δ_3 contribution exists below the Fermi energy, this contribution is blocked in the Co_{∞} -Mn-Mn- Co_{∞} junction due to the smaller bandwidth and therefore missing overlap of the Mn Δ_3 states across the gap, as can be seen from the upper LDOS panel in Figure 8.8 (c).

Owing to the magnetic frustration of the Mn spins of the junction in the contact regime, for the $\text{P}\uparrow\uparrow$ initial configuration, the $\text{P}\alpha$ and $\text{P}\downarrow\uparrow$ states are considered in addition to the $\text{P}\uparrow\uparrow$ state when the Mn-Mn distance is relatively small. Here, as discussed in the preceding section, the conductance at the Fermi energy can be very strongly influenced by the details of hybridization between the Δ_3 -orbitals. On the other hand, since very often experimentally transport measurements serve as the only insight into the magnetic structure of the system, it is very important to coin each of the possible magnetic states with a unique fingerprint which can be related to the experimental data. Below, it is suggested that indeed three distinct spin states in a Co_{∞} -Mn-Mn- Co_{∞} junction – which can occur in an experiment due to various reasons such as structural details, temperature fluctuations, external magnetic field, etc. – lead to different transport fingerprints.

As already shown in Figure 8.5 (d), the conductance of the collinear $\text{P}\uparrow\uparrow$ state rapidly rises towards a value of $1.8 G_0$ as the distance between the leads is decreased. Compared to other possible magnetic configurations of the junction, $G_{\text{P}\uparrow\uparrow}(E_F)$ is

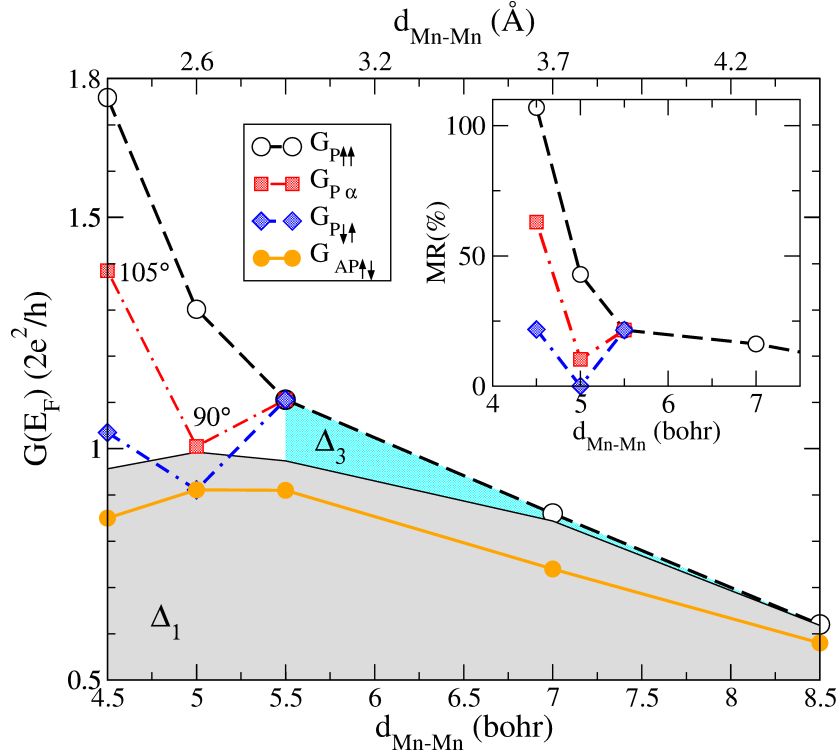


Figure 8.12: Conductance at the Fermi energy of various possible magnetic states of the $\text{Co}_\infty\text{-Mn-Mn-Co}_\infty$ junction as a function of the distance between the Mn atoms. Following magnetic states are considered: $\text{AP}\downarrow\uparrow$ (filled circles, solid line), $\text{P}\uparrow\uparrow$ (open circles, dashed line), $\text{P}\downarrow\downarrow$ (diamonds, dash-dash-dotted line), and $\text{P}\alpha$ (squares, dot-dashed line). The Δ_1 contribution for the $\text{P}\uparrow\uparrow$ -state is shown with a thin solid line and grey shaded area, while the Δ_3 part is shaded in cyan. For the $\text{P}\alpha$ states the state which is lowest in energy among all possible angles α at a fixed distance is considered. In the inset the values of the magnetoresistance for different P-states are shown.

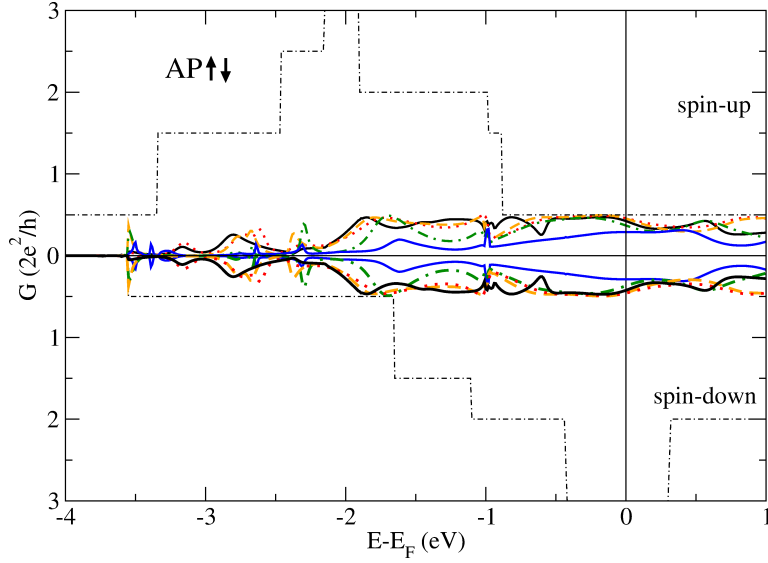


Figure 8.13: Spin-resolved conductance of the $\text{AP}\uparrow\downarrow$ configuration versus the Mn-Mn interatomic distance $d_{\text{Mn-Mn}} = 4.5$ bohr (solid black line), 5.0 bohr (dotted red line), 5.5 Bohr (dashed orange line), 7 bohr (dash-dotted green line), 8 bohr (solid blue line) and the conductance of the left perfect lead (thin black dash-dotted lines). Conductances obtained within 2nd NN FSWFs approximation in collinear representation.

significantly larger in value, see Figure 8.12, because of the alignment of the minority s - and d -states of Co electrodes and Mn atoms at the Fermi energy, which ideally favors perfect transmission. In contrast, the conductance of the collinear $\text{P}\downarrow\uparrow$ -state is significantly suppressed, reaching only $1.0 G_0$ at the separation of 4.5 bohr, due to the large exchange splitting of the Δ_3 states of the Mn atoms with antiparallel spin moments which hinders the Δ_3 conductance. On the other hand the conductance of the non-collinear ground-state $\text{P}\alpha$ -state lies in between the values for both limiting collinear configurations. In the close contact regime, at $d_{\text{Mn-Mn}}$ of 4.5 bohr, the conductance of the $\text{P}\alpha$ -state of $1.4 G_0$ is exactly in between the values of $G_{\text{P}\uparrow\uparrow}(E_F)$ and $G_{\text{P}\downarrow\uparrow}(E_F)$. Clearly, the difference of $0.4 G_0$, stemming from the variation in the Δ_3 -conductance with the spin state, can be easily detected in experiment, allowing for a way to distinguish between different possible magnetic configurations.

At a distance of 5.0 bohr the equilibrium state among the $\text{P}\alpha$ states is the $\text{P}90^\circ$ state, with an energy gain of 43 meV compared to the $\text{P}\uparrow\uparrow$ configuration. The corresponding conductances of the $\text{P}90^\circ$ and the $\text{P}\downarrow\uparrow$ states at 5.0 bohr are show in Figure 8.14 in comparison to the $\text{P}\downarrow\uparrow$ and $\text{P}105^\circ$ states at 4.5 bohr. Besides a decrease in the conductance due to the larger Mn-Mn distance, e.g. visible for the $\text{P}\downarrow\uparrow$ configurations in Figure 8.14 (c) and (d), the Δ_3 conductance of the $\text{P}90^\circ$ state at 5.0 bohr is significantly reduced compared to the $\text{P}105^\circ$, owing to the antiparallel

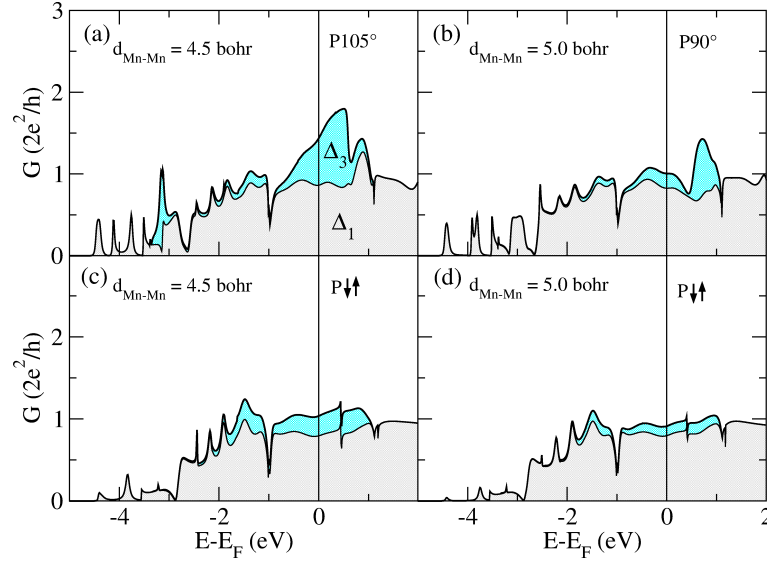


Figure 8.14: Total conductance (G_{total} , upper black line), Δ_3 channel contribution (cyan shaded area) and Δ_1 channel conductance (G_{Δ_1} , lower black line, grey shaded area) obtained within the 2nd NN FSWFs approximation in non-collinear representation, for (a) the non-collinear P105° state at $d_{\text{Mn-Mn}} = 4.5$ bohr, (b) the non-collinear P90° state at $d_{\text{Mn-Mn}} = 5.0$ bohr, c) the collinear P $\uparrow\uparrow$ state at $d_{\text{Mn-Mn}} = 4.5$ bohr and (d) the collinear P $\downarrow\uparrow$ state at $d_{\text{Mn-Mn}} = 5.0$ bohr.

alignment of both Mn spin moments.

For larger distances above 5.5 bohr, the system converges to a collinear configuration. The angle α in the lowest in energy P α state decreases smoothly with increasing the separation, and it can be assumed, that owing to the non-monotonous behavior of the conductance as a function of α , seen in Figure 8.7(d), the conductance as a function of $d_{\text{Mn-Mn}}$, can exhibit several features similar to that at $d_{\text{Mn-Mn}}$ of 5.0 bohr, although no calculations were performed to support this statement owing to the required computational effort.

According to recent experiments [154], the conductance of the junction with the parallel (P) and antiparallel (AP) orientation of the lead's magnetization can be related to each other via measuring the magnetoresistance (MR). From the values presented in Figure 8.12 the MR of the junction is calculated, defined as (cf. Eqn. (6.32) in chapter 6.7.1):

$$\text{MR} = \frac{G_{\text{P}}(E_F) - G_{\text{AP}}(E_F)}{G_{\text{AP}}(E_F)} \times 100\%, \quad (8.2)$$

and present the MR as a function of separation between the electrodes in the inset of Figure 8.12, where $G_{\text{AP}\uparrow\downarrow}$ is chosen for $G_{\text{AP}}(E_F)$, and values of $G_{\text{P}\uparrow\uparrow}(E_F)$, $G_{\text{P}\downarrow\uparrow}(E_F)$ and $G_{\text{P}\alpha}(E_F)$ for $G_{\text{P}}(E_F)$. The overall smaller AP $\uparrow\downarrow$ conductance as compared the

P-configurations results in positive magnetoresistance values. The MR curves as a function of the distance generally resemble those of the conductance, with the values of the MR of 22, 62 and 105% at the distance of 4.5 bohr for the $\text{P}\downarrow\uparrow$, $\text{P}\alpha$ and $\text{P}\uparrow\uparrow$ -states, respectively. Much more pronounced in the MR is the feature characteristic to the $\text{P}\downarrow\uparrow$ and $\text{P}\alpha$ -configurations – a dip around the distance of 5.0 bohr, also present in the conductance curves. As can be seen from Figure 8.12, at this distance, the MR almost completely vanishes when the Mn spins exhibit a different configuration as the FM configuration.

As a final conclusion, even such a simple setup as formed by two semi-infinite Co electrodes with a single apex Mn atom, brought from tunneling to contact regime, allows to draw some general conclusions concerning the interplay of structure and magnetism for the transport through such atomic-sized contacts. It has been shown, that it is necessary to consider Heisenberg exchange constants as well as Stoner-type creation of spin moments to capture non-collinear spin-order in this junction, such as the found stable $\text{P}105^\circ$ configuration close to the contact regime, where the Mn spins are tilted by an angle $\alpha = \pm 105^\circ$. While in the tunneling regime the conductance G is solely coming from the overlap between the Δ_1 (s - d_{z^2} -orbitals) of the contacts and the Mn spins prefer to order ferromagnetically with respect to the magnetization of the leads, the hybridization between the Δ_3 (d_{xz} , d_{yz} -orbitals) states of the junction starts to provide a sizable contribution to G that delicately depends on the Mn spin-directions. This dependence on the spin configuration results in distinctive conductance fingerprints, or by comparing parallel and antiparallel lead magnetizations, to a pronounced difference in the shape and magnitude of the MR curves, which can vary in the contact regime between 20 and 100%, depending on the spin arrangement. Those conductance or magnetoresistance fingerprints might also be used in experiments to shed light onto the complex magnetism in this type of systems. However, there might be further effects to consider, such as structural relaxation of the junction in the near contact regime or non-collinearity of the spin moments of the NN Co atoms.

9 Summary

The present thesis introduces a new state-of-the-art *first-principles* ballistic transport method for one-dimensional two-terminal magnetic nanojunctions [79, 80].

The central aspect of the approach is the combination of a non-equilibrium Green's functions (NEGF) method [84] to treat non-equilibrium open quantum systems and the *first-principles* density functional theory (DFT) [94–96], based on the all-electron full-potential augmented plane wave (FLAPW) method, as implemented in the FLEUR-code [63], which ranks among the most accurate schemes to describe the ground state properties of a large class of material systems. The FLEUR-code allows to incorporate complex magnetic phenomena such as non-collinear magnetic order [67] and subtle effects such as SOC [66] and can be additionally tailored to efficiently treat one-dimensional systems [64]. All these qualities make the FLEUR-code an excellent choice for a description of complex electronic and magnetic nanojunctions.

The combination of both methods imposes a significant problem, since the Green's functions rely on a tight-binding like description of the Hamiltonian matrices and the FLAPW method uses intrinsically delocalized Bloch type wave functions as a basis set, prohibiting to combine both methods in a straight-forward way. The approach taken in this work is to map the delocalized FLAPW wave functions onto a localized tight-binding like basis set are Wannier functions (WFs) [61]. Wannier suggested a Fourier-like transformation from delocalized Bloch basis functions to positional space, providing a localized basis set. Wannier functions cannot be defined uniquely due to an arbitrary phase factor applicable to any Bloch state. However, this phase factor can be used to impose additional constraints, e.g. by requiring maximal spatial localization of the Wannier orbitals. The resulting maximally localized Wannier functions (MLWFs) [62] are unique, real-valued for most systems (excluding SOC and non-collinear magnetic systems) and decay exponentially in real space. Thus, MLWFs constitute an optimal and minimal basis set, which was demonstrated to maintain the FLAPW accuracy in NEGF ballistic transport calculations in this thesis. A computationally less demanding Wannier function approach are first-shot Wannier functions (FSWFs). FSWFs are obtained by projecting the FLAPW basis functions onto localized trial orbitals [68] and are commonly used as a starting point for MLWFs localization. It was demonstrated in this thesis, that FSWFs, although depending strongly on the shape of the trial orbitals, can maintain the FLAPW accuracy for reasonable choices of trial orbitals. For practical ballistic transport calculations, FSWFs can even be regarded superior to MLWFs, especially

for calculations including coupled spin channels (SOC or non-collinear spin structures), due to the easier access to the spin and orbital quantum numbers of WF orbitals, helping to avoid systematical errors in the construction of the WFs Hamiltonian matrices. The implementation of WFs within the FLEUR-code [68] uses an interface to the publicly available Wannier90-code [137] and can be extended to successfully map the FLAPW electronic structure of complex magnetic and electronic phenomena such as SOC [68] or non-collinear spin-structures [80] on a localized tight-binding like Hamiltonian.

The introduced method treats the single electron ballistic transport in a Landauer-Büttiker approach [19–21], in which the conductance is related to the quantum mechanical transmission probability of an electron to pass the junction, carrying a conductance quantum of $G_0 = \frac{2e^2}{h} = (12.9k\Omega)^{-1}$. Here, a nanojunction is described as a two-terminal junction, consisting of three regions: A central scattering region and two semi-infinite leads. This approach already includes the contact resistance caused by the coupling of a scattering region to macroscopic reservoirs by its leads. The quantum conductance calculations are performed in the linear-response regime for small applied bias voltages. Within this regime, the Hamiltonian matrices are based on the equilibrium electronic structure ($V = 0$), as provided by the combined FLAPW and WFs approach. The challenge is to construct the Hamiltonian matrices for the scattering region and the semi-infinite leads in an efficient and computationally inexpensive way. The FLAPW unit cell of the scattering region has to be chosen to be sufficiently large to include the scatterer and a scatterer-lead interface region, but small enough to remain computationally feasible. As became clear in this work, it is nearly impossible to achieve an adequate precision of the electronic structure of the leads from one reasonably-sized FLAPW calculation. A solution of this problem, the "locking-technique", was introduced in chapter 6, where leads were constructed from separate FLAPW calculations of perfect periodic structures. Based on these, the effect of the leads on the scattering region were incorporated by finite sized self-energy matrices, obtained within a surface Green's function approach.

Other important tools, provided by the introduced method, were the locally and orbitally resolved density of states (DOS) and the orbital decomposition of the conductance. The main result of a ballistic transport calculation is the conductance, which is rather difficult to understand on its own. Since the electron transmission can be strongly influenced by the geometrical shape, orbital symmetries and the magnetic order, these tools can provide additional insights into the nanojunction and can help to understand quantum transport.

As test systems for the NEGF transport method within FLAPW Wannier functions, non-magnetic Pt monowires and two ferromagnetic Co monowires with parallel and antiparallel aligned magnetic moments were investigated in chapter 6. Key aspects of the new method, such as e.g. the locking-technique, the orbital decomposition of conductance and DOS and the convergence of the conductance with respect of the nearest neighbor (NN) tight-binding approximation were demonstrated on

these systems. Further, the impact of SOC on the conductance of a Pt monowire and the magnetoresistance of the magnetic Co wires were studied, compared to results obtained within a fully relativistic ultrasoft pseudopotential method and a scattering approach to obtain the conductance [69, 81] and found to be in excellent agreement.

In chapter 7, the new method was applied to study the effect of spin-orbit scattering at an impurity atom in a monowire. Here, two model cases were considered: (i) a magnetic atom in a non-magnetic wire, Co in a Pt monowire, and (ii) a non-magnetic heavy element in a ferromagnetic wire, Pt in a Co monowire. For both cases a distinct dependence of the conductance on the magnetization direction was observed with respect to the wire axis.

For a Co impurity in a Pt chain it was found, that due to the broken cylindrical symmetry for an out-of-chain magnetization direction the hybridization between states of different angular character and spin but with identical quantum number j leads to scattering processes that do not conserve spin. Those ballistic spin-scattering processes and the magnetic polarization of Pt due to the introduction of a magnetic impurity are shown to result in a ballistic anisotropic magnetoresistance (BAMR) [14, 16] of 7%. The relatively moderate values are caused by the large background conductance from bands originating from $s-d_{z^2}$ - and $d_{xz,yz}$ -states which are not modified much upon switching the magnetization. For a Pt impurity in a Co chain it was found, that the impurity reduces the BAMR of the pure Co chain from 130% to 100%. In this case, the magnetoresistance originates from hybridization between the Δ_3 and Δ_4 states moderated via SOC by the direction of the magnetization. It was demonstrated, that the impurity smooths out the typical conductance jumps upon rotating the magnetization direction from parallel to perpendicular to the current direction, resulting into conventional anisotropic magnetoresistance (AMR) [17].

As a first application to study the effect of non-collinear spin structures on ballistic transport, the properties of a single-atom junction formed by two semi-infinite Co electrodes with a single apex Mn atom were investigated in chapter 8. The conductance as a function of the separation between the two Mn atoms from the tunneling to the contact regime was taking into account the complex magnetic interaction in the junction. It was demonstrated, that even such a simple setup allows to draw some general conclusions concerning the interplay of structure and magnetism for the transport through such atomic-sized contacts which are in the focus of today's research. The ballistic conductance of the junction was analyzed with lead magnetizations in parallel and antiparallel alignment. The tunneling and contact regimes of the junction were considered separately, and it was demonstrated that in the tunneling regime the conductance G is solely coming from the overlap between the Δ_1 ($s-d_{z^2}$ -orbitals) of the contacts. In this case it was shown, that the Mn spins prefer to order ferromagnetically with respect to the magnetization of the leads. On the other hand, upon reaching the close contact regime, the hybridization between the

Δ_3 (d_{xz}, d_{yz} -orbitals) states of the junction starts to provide a sizable contribution to G .

In the close contact regime it was found when the hybridization between the Mn atoms is significant, that Mn spins experience a frustration due to the FM coupling with the leads and an AFM Mn-Mn coupling. The competition between the two gives rise to a stable non-collinear solution which can be characterized by a tilting angle of the Mn spins, α . General for this type of junction is the sensitivity of the d -orbital conductance on the angle α , which is due to a delicate interplay between the hybridization details of the Mn and Co states at the Fermi energy, as well as spin-asymmetry in their distribution. This gives rise to a non-trivial α -dependence of the conductance of the d -states. It was shown that the complicated Δ_3 -channel conductance arising on the background of almost constant Δ_1 contribution can be used in order to distinguish between different magnetic states of the contact via either a direct conductance measurement, or via measuring the magnetoresistance, which, according to the presented calculations, can vary in the contact regime between 20 and 100%, depending on the spin arrangement.

Finally, the approximation for the monowire-geometry of the junctions, assumed in this work, shall be commented on. Albeit being very simple, it allowed to capture the key features which govern the transport properties of the system, while keeping the computational burden reasonable. Namely, within this geometry: (i) the transition from tunneling to contact can be naturally studied; (ii) the effect of SOC and the magnetic frustration of the spins in the junction, and (iii) the delicate details of the hybridization of impurities or adatoms with the lead reservoirs are taken into account; (iv) the sensitive dependence of the spin moments on the magnetic configuration in the nanocontact is included into the considerations. Of course, in order to achieve a quantitative agreement of the calculated values to the experimentally measured ones in this type of junction beyond the major trends, all details of the structure and structural reformation upon approaching should be ideally accounted for. Such a challenging study lies, however, outside of the scope of the current work, and has to be left for future studies.

The general quantum transport approach is open for future extensions, such as e.g. including a finite bias voltage within WFs [91], more complex geometries beyond monowires or an extension to two-dimensional planar junctions within the efficient interpolation method based on Wannier functions (cf. chapter 5). The latter allows to e.g. refine the \mathbf{k} -mesh without recalculating the DFT electronic structure and is therefore suitable for e.g. planar tunnel junctions, known for large conductance contributions of single \mathbf{k} -points ("hot spots"), as reported e.g. for the Fe/MgO/Fe(001) junction [174, 175]. Ideally, for such geometrically more complex calculations an improved layer-wise Wannier representation would be required, assigning a distinct subset of Wannier functions to a fixed layer as used in the construction of the transport Hamiltonian and, thus, resulting in a much more convenient way of evaluating the Wannier function Hamiltonian for geometrically challenging systems. The

construction of the transport Hamiltonian (cf. chapter 6) allows to locally include inelastic scattering processes, such as e.g. the scattering on vibrations [35, 36] or consider electron correlation effects [37], which have been reported to be important e.g. for the conductance through benzenedithiol and benzenediamine molecules in Au nanojunctions [176]. Furthermore, given a Wannier representation for non-collinear magnetic order including SOC, studying the effect of the chirality of non-collinear spin-structures on ballistic transport in nanojunctions lacking inversion symmetry is within reach.

In conclusion, a new method has been developed and implemented that allows to describe electronic transport in the ballistic regime with FLAPW accuracy. This particular method has been demonstrated to be applicable to systems, exhibiting a strong SOC influence or non-collinear spin structures. The provided tools of this method, namely the orbital decomposition of conductance and DOS, has been demonstrated to be valuable to study the complex electronic details of various nanojunctions and their conductances.

Bibliography

- [1] GRÜNBERG, P. ; SCHREIBER, R. ; PANG, Y. ; BRODSKY, M. B. ; SOWERS, H.: Layered Magnetic Structures: Evidence for Antiferromagnetic Coupling of Fe Layers across Cr Interlayers. In: *Phys. Rev. Lett.* 57 (1986), Nov, S. 2442–2445
- [2] BAIBICH, M. N. ; BROTO, J. M. ; FERT, A. ; VAN DAU, F. N. ; PETROFF, F. ; ETIENNE, P. ; CREUZET, G. ; FRIEDERICH, A. ; CHAZELAS, J.: Giant Magnetoresistance of (001)Fe/(001)Cr Magnetic Superlattices. In: *Phys. Rev. Lett.* 61 (1988), Nov, S. 2472–2475
- [3] <http://www.itrs.net/Links/2011ITRS/Home2011.htm>
- [4] KIZUKA, T.: Atomic configuration and mechanical and electrical properties of stable gold wires of single-atom width. In: *Phys. Rev. B* 77 (2008), Apr, Nr. 15, S. 155401
- [5] NÉEL, N. ; KRÖGER, J. ; BERNDT, R.: Quantized Conductance of a Single Magnetic Atom. In: *Phys. Rev. Lett.* 102 (2009), Feb, Nr. 8, S. 086805
- [6] KRÖGER, J. ; NÉEL, N. ; LIMOT, L.: Single-atom contacts with a scanning tunnelling microscope. In: *J. Phys. Cond. Mat.* 20 (2008), S. 223001
- [7] CHOPRA, H. D. ; SULLIVAN, M. R. ; ARMSTRONG, Jason N. ; HUA, Susan Z.: The quantum spin-valve in cobalt atomic point contacts. In: *Nature Materials* 4 (2005), S. 832–837
- [8] CALVO, M. R. ; FERNÁNDEZ-ROSSIER, J. ; PALACIOS, J. J. ; JACOB, D. ; NATELSON, D. ; UNTIEDT, C.: The Kondo effect in ferromagnetic atomic contacts. In: *Nature* 458 (2009), S. 1150–1153
- [9] THIESS, A. ; MOKROUSOV, Y. ; BLÜGEL, S. ; HEINZE, S.: Theory and Application of Chain Formation in Break Junctions. In: *Nano Letters* 8 (2008), Nr. 8, S. 2144–2149
- [10] HASMY, A. ; PÉREZ-JIMÉNEZ, A. J. ; PALACIOS, J. J. ; GARCÍA-MOCHALES, P. ; COSTA-KRÄMER, J. L. ; DÍAZ, M. ; MEDINA, E. ; SERENA, P. A.: Ballistic resistivity in aluminum nanocontacts. In: *Phys. Rev. B* 72 (2005), Dec, Nr. 24, S. 245405

- [11] BURTON, J. D. ; SABIRIANOV, R. F. ; VELEV, J. P. ; MRYASOV, O. N. ; TSYMBAL, E. Y.: Effect of tip resonances on tunneling anisotropic magnetoresistance in ferromagnetic metal break-junctions: A first-principles study. In: *Phys. Rev. B* 76 (2007), Oct, Nr. 14, S. 144430
- [12] TAO, K. ; RUNGGER, I. ; SANVITO, S. ; STEPANYUK, V. S.: Quantum conductance of a single magnetic atom: An ab initio study. In: *Phys. Rev. B* 82 (2010), Aug, Nr. 8, S. 085412
- [13] OLESEN, L. ; LAEGSGAARD, E. ; STENSGAARD, I. ; BESENBACHER, F. ; SCHIOTZ, J. ; STOLTZE, P. ; JACOBSEN, K. W. ; NORSKOV, J. K.: Quantized conductance in an atom-sized point contact. In: *Phys. Rev. Lett.* 72 (1994), Apr, S. 2251–2254
- [14] SOKOLOV, A. ; ZHANG, C. ; TSYMBAL, E.Y. ; REDEPENNING, J. ; DOUDIN, B.: Quantized magnetoresistance in atomic-size contacts. In: *Nature Nanotechnology* 2 (2007), S. 171–175
- [15] COSTA-KRÄMER, J. L. ; GARCIA, N. ; OLIN, H.: Conductance quantization histograms of gold nanowires at 4 K. In: *Phys. Rev. B* 55 (1997), May, S. 12910–12913
- [16] VELEV, J. ; SABIRIANOV, R. F. ; JASWAL, S. S. ; TSYMBAL, E. Y.: Ballistic Anisotropic Magnetoresistance. In: *Phys. Rev. Lett.* 94 (2005), Mar, Nr. 12, S. 127203
- [17] JACOB, D. ; FERNÁNDEZ-ROSSIER, J. ; PALACIOS, J. J.: Anisotropic magnetoresistance in nanocontacts. In: *Phys. Rev. B* 77 (2008), Apr, Nr. 16, S. 165412
- [18] SERRATE, D. ; FERRIANI, P. ; YOSHIDA, Y. ; HLA, S.-W. ; MENZEL, M. ; BERGMANN, K. von ; HEINZE, S. ; KUBETZKA, A. ; WIESENDANGER, R.: Imaging and manipulating the spin direction of individual atoms. In: *Nature Nanotechnology* 5 (2010), S. 350 – 353
- [19] LANDAUER, R.: Spatial Variation of Currents and Fields Due to Localized Scatterers in Metallic Conduction. In: *IBM Journal of Research and Development* 1 (1957), July, S. 223
- [20] LANDAUER, R.: Spatial Variation of Currents and Fields Due to Localized Scatterers in Metallic Conduction. In: *IBM Journal of Research and Development* 32 (1988), May, S. 306
- [21] BÜTTIKER, M. ; IMRY, Y. ; LANDAUER, R. ; PINHAS, S.: Generalized many-channel conductance formula with application to small rings. In: *Phys. Rev. B* 31 (1985), May, Nr. 10, S. 6207–6215

- [22] DARANCET, P. ; OLEVANO, V. ; MAYOU, D.: Quantum transport through resistive nanocontacts: Effective one-dimensional theory and conductance formulas for nonballistic leads. In: *Phys. Rev. B* 81 (2010), Apr, Nr. 15, S. 155422
- [23] MEIR, Y. ; WINGREEN, N. S.: Landauer formula for the current through an interacting electron region. In: *Phys. Rev. Lett.* 68 (1992), Apr, Nr. 16, S. 2512–2515
- [24] SAUTET, P. ; JOACHIM, C.: Electronic transmission coefficient for the single-impurity problem in the scattering-matrix approach. In: *Phys. Rev. B* 38 (1988), Dec, Nr. 17, S. 12238–12247
- [25] EMBERLY, E. G. ; KIRCZENOW, G.: Theoretical study of electrical conduction through a molecule connected to metallic nanocontacts. In: *Phys. Rev. B* 58 (1998), Oct, Nr. 16, S. 10911–10920
- [26] HIROSE, K. ; TSUKADA, M.: First-Principles Theory of Atom Extraction by Scanning Tunneling Microscopy. In: *Phys. Rev. Lett.* 73 (1994), Jul, Nr. 1, S. 150–153
- [27] JOON CHOI, H. ; IHM, J.: Ab initio pseudopotential method for the calculation of conductance in quantum wires. In: *Phys. Rev. B* 59 (1999), Jan, Nr. 3, S. 2267–2275
- [28] KOBAYASHI, N. ; BRANDBYGE, M. ; TSUKADA, M.: First-principles study of electron transport through monatomic Al and Na wires. In: *Phys. Rev. B* 62 (2000), Sep, Nr. 12, S. 8430–8437
- [29] WORTMANN, D. ; ISHIDA, H. ; BLÜGEL, S.: *Ab initio* Green-function formulation of the transfer matrix: Application to complex band structures. In: *Phys. Rev. B* 65 (2002), Mar, S. 165103
- [30] LANG, N. D.: Resistance of atomic wires. In: *Phys. Rev. B* 52 (1995), Aug, Nr. 7, S. 5335–5342
- [31] DALGLEISH, H. ; KIRCZENOW, G.: Theoretical study of spin-dependent electron transport in atomic Fe nanocontacts. In: *Phys. Rev. B* 72 (2005), Oct, Nr. 15, S. 155429
- [32] KHOMYAKOV, P. A. ; BROCKS, G. ; KARPAN, V. ; ZWIERZYCKI, M. ; KELLY, P. J.: Conductance calculations for quantum wires and interfaces: Mode matching and Green’s functions. In: *Phys. Rev. B* 72 (2005), Jul, Nr. 3, S. 035450

- [33] KELDYSH, L. V.: Quantum transport equations for high electric fields. In: *JETP-USSR* 20 (1965), S. 1018
- [34] KADANOFF, L.P. ; BAYM, B.: *Quantum Statistical Mechanics*. Benjamin, 1962
- [35] FREDERIKSEN, T. ; BRANDBYGE, M. ; LORENTE, N. ; JAUHO, A.-P.: Inelastic Scattering and Local Heating in Atomic Gold Wires. In: *Phys. Rev. Lett.* 93 (2004), Dec, Nr. 25, S. 256601
- [36] FREDERIKSEN, T. ; PAULSSON, M. ; BRANDBYGE, M. ; JAUHO, A.-P.: Inelastic transport theory from first principles: Methodology and application to nanoscale devices. In: *Phys. Rev. B* 75 (2007), May, Nr. 20, S. 205413
- [37] THYGESEN, K. S. ; RUBIO, A.: Conserving *GW* scheme for nonequilibrium quantum transport in molecular contacts. In: *Phys. Rev. B* 77 (2008), Mar, Nr. 11, S. 115333
- [38] BARANGER, H. U. ; STONE, A. D.: Electrical linear-response theory in an arbitrary magnetic field: A new Fermi-surface formation. In: *Phys. Rev. B* 40 (1989), Oct, Nr. 12, S. 8169–8193
- [39] EVERS, F. ; WEIGEND, F. ; KOENTOPP, M.: Conductance of molecular wires and transport calculations based on density-functional theory. In: *Phys. Rev. B* 69 (2004), Jun, Nr. 23, S. 235411
- [40] BAGRETS, A. ; PAPANIKOLAOU, N. ; MERTIG, I.: Ab initio approach to the ballistic transport through single atoms. In: *Phys. Rev. B* 73 (2006), Jan, Nr. 4, S. 045428
- [41] MAVROPOULOS, P. ; PAPANIKOLAOU, N. ; DEDERICHS, P. H.: Korringa-Kohn-Rostoker Green-function formalism for ballistic transport. In: *Phys. Rev. B* 69 (2004), Mar, S. 125104
- [42] SANVITO, S. ; LAMBERT, C. J. ; JEFFERSON, J. H. ; BRATKOVSKY, A. M.: General Green's-function formalism for transport calculations with *spd* Hamiltonians and giant magnetoresistance in Co- and Ni-based magnetic multilayers. In: *Phys. Rev. B* 59 (1999), May, Nr. 18, S. 11936–11948
- [43] HÄFNER, M. ; VILJAS, J. K. ; FRUSTAGLIA, D. ; PAULY, F. ; DREHER, M. ; NIELABA, P. ; CUEVAS, J. C.: Theoretical study of the conductance of ferromagnetic atomic-sized contacts. In: *Phys. Rev. B* 77 (2008), Mar, Nr. 10, S. 104409
- [44] NARDELLI, M. B.: Electronic transport in extended systems: Application to carbon nanotubes. In: *Phys. Rev. B* 60 (1999), Sep, Nr. 11, S. 7828–7833

-
- [45] TAYLOR, J. ; GUO, H. ; WANG, J.: Ab initio modeling of quantum transport properties of molecular electronic devices. In: *Phys. Rev. B* 63 (2001), Jun, Nr. 24, S. 245407
- [46] NARDELLI, M. B. ; FATTEBERT, J.-L. ; BERNHOLC, J.: $O(N)$ real-space method for ab initio quantum transport calculations: Application to carbon nanotube–metal contacts. In: *Phys. Rev. B* 64 (2001), Dec, Nr. 24, S. 245423
- [47] XUE, Y. ; DATTA, S. ; RATNER, M. A.: First-principles based matrix Green's function approach to molecular electronic devices: general formalism. In: *Chemical Physics* 281 (2002), Nr. 2-3, S. 151 – 170. – ISSN 0301–0104
- [48] BRANDBYGE, M. ; MOZOS, J.-L. ; ORDEJÓN, P. ; TAYLOR, J. ; STOKBRO, K.: Density-functional method for nonequilibrium electron transport. In: *Phys. Rev. B* 65 (2002), Mar, Nr. 16, S. 165401
- [49] THYGESEN, K. S. ; BOLLINGER, M. V. ; JACOBSEN, K. W.: Conductance calculations with a wavelet basis set. In: *Phys. Rev. B* 67 (2003), Mar, Nr. 11, S. 115404
- [50] CALZOLARI, A. ; MARZARI, N. ; SOUZA, I. ; NARDELLI, M. B.: Ab initio transport properties of nanostructures from maximally localized Wannier functions. In: *Phys. Rev. B* 69 (2004), Jan, Nr. 3, S. 035108
- [51] KE, S.-H. ; BARANGER, H. U. ; YANG, W.: Electron transport through molecules: Self-consistent and non-self-consistent approaches. In: *Phys. Rev. B* 70 (2004), Aug, Nr. 8, S. 085410
- [52] HEURICH, J. ; CUEVAS, J. C. ; WENZEL, W. ; SCHÖN, G.: Electrical Transport through Single-Molecule Junctions: From Molecular Orbitals to Conduction Channels. In: *Phys. Rev. Lett.* 88 (2002), Jun, Nr. 25, S. 256803
- [53] DEROSA, P. A. ; SEMINARIO, J. M.: Electron Transport through Single Molecules: Scattering Treatment Using Density Functional and Green Function Theories. In: *J. Phys. Chem. B* 105 (2001), S. 471â481
- [54] PALACIOS, J. J. ; PÉREZ-JIMÉNEZ, A. J. ; LOUIS, E. ; VERGÉS, J. A.: Fullerene-based molecular nanobridges: A first-principles study. In: *Phys. Rev. B* 64 (2001), Aug, Nr. 11, S. 115411
- [55] PALACIOS, J. J. ; PÉREZ-JIMÉNEZ, A. J. ; LOUIS, E. ; SANFABIÁN, E. ; VERGÉS, J. A.: First-principles approach to electrical transport in atomic-scale nanostructures. In: *Phys. Rev. B* 66 (2002), Jul, Nr. 3, S. 035322

- [56] THYGESEN, K. S. ; JACOBSEN, K. W.: Molecular transport calculations with Wannier functions. In: *Chemical Physics* 319 (2005), Nr. 1-3, S. 111 – 125. – ISSN 0301–0104
- [57] PAULY, F. ; VILJAS, J.K. ; HUNIAR, U. ; HÄFNER, M. ; WOHLTHAT, S. ; BÜRKLE, M. ; CUEVAS, J.C. ; SCHÖN, G.: Cluster-based density-functional approach to quantum transport through molecular and atomic contacts. In: *New J. Phys.* 10 (2008), S. 125019
- [58] WORTMANN, D. ; ISHIDA, H. ; BLÜGEL, S.: Embedded Green-function approach to the ballistic electron transport through an interface. In: *Phys. Rev. B* 66 (2002), Aug, S. 075113
- [59] INGLESFIELD, J. E.: A method of embedding. In: *J. Phys. C: Solid State Phys.* 14 (1981), S. 3795
- [60] ROCHA, A. R. ; GARCÍA-SUÁREZ, V. M. ; BAILEY, S. ; LAMBERT, C. ; FERRER, J. ; SANVITO, S.: Spin and molecular electronics in atomically generated orbital landscapes. In: *Phys. Rev. B* 73 (2006), Feb, Nr. 8, S. 085414
- [61] WANNIER, G. H.: The Structure of Electronic Excitation Levels in Insulating Crystals. In: *Phys. Rev.* 52 (1937), Aug, Nr. 3, S. 191–197
- [62] MARZARI, N. ; VANDERBILT, D.: Maximally localized generalized Wannier functions for composite energy bands. In: *Phys. Rev. B* 56 (1997), Nov, Nr. 20, S. 12847–12865
- [63] www.flapw.de
- [64] MOKROUSOV, Y. ; BIHLMAYER, G. ; BLÜGEL, S.: Full-potential linearized augmented plane-wave method for one-dimensional systems: Gold nanowire and iron monowires in a gold tube. In: *Phys. Rev. B* 72 (2005), Jul, Nr. 4, S. 045402
- [65] KRAKAUER, H. ; POSTERNAK, M. ; FREEMAN, A. J.: Linearized augmented plane-wave method for the electronic band structure of thin films. In: *Phys. Rev. B* 19 (1979), Feb, Nr. 4, S. 1706–1719
- [66] LI, C. ; FREEMAN, A. J. ; JANSEN, H. J. F. ; FU, C. L.: Magnetic anisotropy in low-dimensional ferromagnetic systems: Fe monolayers on Ag(001), Au(001), and Pd(001) substrates. In: *Phys. Rev. B* 42 (1990), Sep, Nr. 9, S. 5433–5442
- [67] KURZ, Ph. ; FÖRSTER, F. ; NORDSTRÖM, L. ; BIHLMAYER, G. ; BLÜGEL, S.: *Ab initio* treatment of noncollinear magnets with the full-potential linearized augmented plane wave method. In: *Phys. Rev. B* 69 (2004), Jan, S. 024415

-
- [68] FREIMUTH, F. ; MOKROUSOV, Y. ; WORTMANN, D. ; HEINZE, S. ; BLÜGEL, S.: Maximally localized Wannier functions within the FLAPW formalism. In: *Phys. Rev. B* 78 (2008), Jul, Nr. 3, S. 035120
- [69] DAL CORSO, A. ; SMOGUNOV, A. ; TOSATTI, E.: Ab initio ballistic conductance with spin-orbit coupling: Application to monoatomic wires. In: *Phys. Rev. B* 74 (2006), Jul, Nr. 4, S. 045429
- [70] SMOGUNOV, A. ; DAL CORSO, A. ; TOSATTI, E.: Magnetic phenomena, spin-orbit effects, and Landauer conductance in Pt nanowire contacts: Density-functional theory calculations. In: *Phys. Rev. B* 78 (2008), Jul, Nr. 1, S. 014423
- [71] HÄFNER, M. ; VILJAS, J. K. ; CUEVAS, J. C.: Theory of anisotropic magnetoresistance in atomic-sized ferromagnetic metal contacts. In: *Phys. Rev. B* 79 (2009), Apr, Nr. 14, S. 140410
- [72] SHUKLA, S. K. ; SANVITO, S.: Electron transport across electrically switchable magnetic molecules. In: *Phys. Rev. B* 80 (2009), Nov, S. 184429
- [73] HURLEY, A. ; BAADJI, N. ; SANVITO, S.: Spin-flip inelastic electron tunneling spectroscopy in atomic chains. In: *Phys. Rev. B* 84 (2011), Jul, S. 035427
- [74] SEDLMAYR, N. ; DUGAEV, V. K. ; BERAKDARA, J. ; VIEIRA, V. R. ; ARAÚJO, M. A. N. ; BARNAS, J.: Spin and charge transport through non-collinear magnetic nanowires. In: *Journal of Magnetism and Magnetic Materials* 322 (2010), S. 1419â1421
- [75] YAVORSKY, B. Y. ; MERTIG, I.: Noncollinear interface magnetism and ballistic transport in Fe/FeO/MgO/Fe tunnel junctions: *Ab initio* calculations using the KKR method. In: *Phys. Rev. B* 74 (2006), Nov, S. 174402
- [76] BURTON, J. D. ; SABIRIANOV, R. F. ; JASWAL, S. S. ; TSYMBAL, E. Y. ; MRYASOV, O. N.: Magnetic Moment Softening and Domain Wall Resistance in Ni Nanowires. In: *Phys. Rev. Lett.* 97 (2006), Aug, S. 077204
- [77] www.wien2k.at
- [78] KUNEŠ, J. ; ARITAC, R. ; WISSGOTTE, P. ; TOSCHIE, A. ; IKEDAF, H. ; HELDE, K.: Wien2wannier: From linearized augmented plane waves to maximally localized Wannierfunctions. In: *Comput. Phys. Commun.* 181 (2010), S. 1888
- [79] HARDRAT, B. ; WANG, N.-P. ; FREIMUTH, F. ; MOKROUSOV, Y. ; HEINZE, S.: One-dimensional ballistic transport with FLAPW Wannier functions. In: *Phys. Rev. B* 85 (2012), Jun, S. 245412

- [80] HARDRAT, B. ; FREIMUTH, F. ; HEINZE, S. ; MOKROUSOV, Y.: Conductance fingerprints of noncollinear magnetic states in single-atom contacts: A first-principles Wannier-functions study. In: *Phys. Rev. B* 86 (2012), Oct, S. 165449
- [81] SMOGUNOV, A. ; DAL CORSO, A. ; TOSATTI, E.: Ballistic conductance of magnetic Co and Ni nanowires with ultrasoft pseudopotentials. In: *Phys. Rev. B* 70 (2004), Jul, Nr. 4, S. 045417
- [82] OHM, G. S.: *Die galvanische Kette, mathematisch bearbeitet*. T. H. Riemann, 1827
- [83] WEES, B. J. ; HOUTEN, H. van ; BEENAKKER, C. W. J. ; WILLIAMSON, J. G. ; KOUWENHOVEN, L. P. ; MAREL, D. van d. ; FOXON, C. T.: Quantized conductance of point contacts in a two-dimensional electron gas. In: *Phys. Rev. Lett.* 60 (1988), Feb, S. 848–850
- [84] DATTA, S.: *Quantum Transport: Atom to Transistor*. Cambridge University Press, 2005
- [85] DRUDE, P.: Zur Elektronentheorie der Metalle. In: *Annalen der Physik* 306 (1900), S. 566
- [86] DRUDE, P.: Zur Elektronentheorie der Metalle; II. Teil. Galvanomagnetische und thermomagnetische Effecte. In: *Annalen der Physik* 308 (1900), S. 369
- [87] DATTA, S.: *Electronic Transport in Mesoscopic Systems*. Cambridge University Press, 1995
- [88] SANVITO, S.: Ab-initio methods for spin-transport at the nanoscale level. In: *arXiv:cond-mat/0503445v2 [cond-mat.mes-hall]* (2005)
- [89] BOZEC, D. ; HOWSON, M. A. ; HICKEY, B. J. ; SHATZ, S. ; WISER, N. ; TSYMBAL, E. Y. ; PETTIFOR, D. G.: Mean Free Path Effects on the Current Perpendicular to the Plane Magnetoresistance of Magnetic Multilayers. In: *Phys. Rev. Lett.* 85 (2000), Aug, S. 1314–1317
- [90] NOLTING, W.: *Grundkurs Theoretische Physik 5/1: Quantenmechanik - Grundlagen*. Springer, 2008
- [91] WANG, N.-P.: Electronic transport calculations using maximally-localized Wannier functions. In: *Commun. Theor. Phys.* 55 (2011), Jan, S. 158
- [92] ASHCROFT, N. W. ; MERMIN, N. D.: *Solid State Physics*. Holt, Rinehart and Wilson, 1976

-
- [93] KOHN, W.: Nobel Lecture: Electronic structure of matter-wave functions and density functionals. In: *Rev. Mod. Phys.* 71 (1999), Oct, Nr. 5, S. 1253–1266
- [94] HOHENBERG, P. ; KOHN, W.: Inhomogeneous Electron Gas. In: *Phys. Rev.* 136 (1964), Nov, Nr. 3B, S. B864–B871
- [95] KOHN, W. ; SHAM, L. J.: Self-Consistent Equations Including Exchange and Correlation Effects. In: *Phys. Rev.* 140 (1965), Nov, Nr. 4A, S. A1133–A1138
- [96] LEVY, M.: Universal Variational Functionals of Electron Densities, First-Order Density Matrices, and Natural Spin-Orbitals and Solution of the v -Representability Problem. In: *Proc. Natl. Acad. Sci. USA* 76 (1972), S. 6062
- [97] NOLTING, W.: *Grundkurs Theoretische Physik 5/2*. Springer, 2004
- [98] THOMAS, L. H.: The calculation of atomic fields. In: *Proc. Cambridge Phil. Soc.* (1927), Nr. 23, S. 542
- [99] FERMI, E.: Un metodo statistico per la determinazione di alcune priorieta dell'atome. In: *Rend. Accad. Naz. Linzei* (1927), Nr. 6, S. 602
- [100] SHELDON, J. W.: Use of the Statistical Field Approximation in Molecular Physics. In: *Phys. Rev.* 99 (1955), Aug, Nr. 4, S. 1291–1301
- [101] FRIEDRICH, C. ; BLÜGEL, S. ; SCHINDLMAYR, A.: Efficient implementation of the GW approximation within the all-electron FLAPW method. In: *Phys. Rev. B* 81 (2010), Mar, S. 125102
- [102] STIXRUDE, L. ; COHEN, R. E. ; SINGH, D. J.: Iron at high pressure: Linearized-augmented-plane-wave computations in the generalized-gradient approximation. In: *Phys. Rev. B* 50 (1994), Sep, S. 6442–6445
- [103] ZHANG, Y. ; YANG, W.: Comment on Generalized Gradient Approximation Made Simple. In: *Phys. Rev. Lett.* 80 (1998), Jan, Nr. 4, S. 890
- [104] VOSKO, S. H. ; WILK, L. ; NUSAIR, M.: Accurate spin-dependent electron liquid correlation energies for local spin density calculations: a critical analysis. In: *Canadian Journal of Physics* 58 (1980), Nr. 8, S. 1200–1211
- [105] BARTH, U. von ; HEDIN, L.: A lokal exchange-correlation potential for the spin polarised case. In: *J. Phys. C.* (1972), Nr. 5, S. 1629
- [106] WEINERT, M. ; WIMMER, E. ; FREEMAN, A. J.: Total-energy all-electron density functional method for bulk solids and surfaces. In: *Phys. Rev. B* 26 (1982), Oct, Nr. 8, S. 4571–4578

- [107] JOHNSON, D. D.: Modified Broyden's method for accelerating convergence in self-consistent calculations. In: *Phys. Rev. B* 38 (1988), Dec, Nr. 18, S. 12807–12813
- [108] BLÜGEL, S. ; BRÜCKEL, T. ; SCHNEIDER, C. M. ; (EDS.): *Magnetism goes Nano*. Jülich : Schriften des Forschungszentrum Jülich, Reihe Materie und Material Nr. 26, 2005
- [109] HEISENBERG, W.: Zur Theorie des Ferromagnetismus. In: *Zeitschrift für Physik* 49 (1928), S. 619
- [110] MACDONALD, A. H. ; GIRVIN, S. M. ; YOSHIOKA, D.: $\frac{t}{V}$ expansion for the Hubbard model. In: *Phys. Rev. B* 37 (1988), Jun, S. 9753–9756
- [111] BODE, M. ; HEIDE, M. ; BERGMANN, K. von ; FERRIANI, P. ; HEINZE, S. ; BIHLMAYER, G. ; KUBETZKA, A. ; PIETZSCH, O. ; BLÜGEL, S. ; WIESENDANGER, R.: Chiral magnetic order at surfaces driven by inversion asymmetry. In: *Nature* 447 (2007), S. 190–193
- [112] HEIDE, M. ; BIHLMAYER, G. ; BLÜGEL, S.: Dzyaloshinskii-Moriya interaction accounting for the orientation of magnetic domains in ultrathin films: Fe/W(110). In: *Phys. Rev. B* 78 (2008), Oct, S. 140403
- [113] HEINZE, S. ; BERGMANN, K. von ; MENZEL, M. ; KUBETZKA, A. ; BREDE, J. ; WIESENDANGER, R. ; BIHLMAYER, G. ; BLÜGEL, S.: Spontaneous atomic-scale magnetic skyrmion lattice in two dimensions. In: *Nature Physics* 7 (2011), S. 713–718
- [114] SLATER, J. C.: A Simplification of the Hartree-Fock Method. In: *Phys. Rev.* 81 (1951), Feb, Nr. 3, S. 385–390
- [115] ANDERSEN, O. K.: Linear methods in band theory. In: *Phys. Rev. B* 12 (1975), Oct, Nr. 8, S. 3060–3083
- [116] KOELLING, D. D. ; ARBMAN, G. O.: Use of energy derivative of the radial solution in an augmented plane wave method: application to copper. In: *J. Phys. F: Met. Phys.* 5 (1975), S. 2041–2054
- [117] MARCUS, P. M.: Variational methods in the computation of energy bands. In: *Int. J. Quantum Chem., Issue Suppl. S1* (1967), Nr. 1, S. 567
- [118] KOELLING, D. D.: Alternative Augmented-Plane-Wave Technique: Theory and Application to Copper. In: *Phys. Rev. B* 2 (1970), Jul, Nr. 2, S. 290–298
- [119] HAMANN, D. R.: Semiconductor Charge Densities with Hard-Core and Soft-Core Pseudopotentials. In: *Phys. Rev. Lett.* 42 (1979), Mar, Nr. 10, S. 662–665

-
- [120] WIMMER, E. ; KRAKAUER, H. ; WEINERT, M. ; FREEMAN, A. J.: Full-potential self-consistent linearized-augmented-plane-wave method for calculating the electronic structure of molecules and surfaces: O_2 molecule. In: *Phys. Rev. B* 24 (1981), Jul, Nr. 2, S. 864–875
- [121] WEINERT, M.: Solution of Poisson’s equation: Beyond Ewald-type methods. In: *Journal of Mathematical Physics* 22 (1981), November, Nr. 11, S. 2433–2439
- [122] RAJAGOPAL, A. K. ; CALLAWAY, J.: Inhomogeneous Electron Gas. In: *Phys. Rev. B* 7 (1973), Mar, Nr. 5, S. 1912–1919
- [123] KOELLING, D. D. ; HARMON, B. N.: A technique for relativistic spin-polarised calculations. In: *J. Phys. C* (1977), Nr. 10, S. 3107
- [124] MOKROUSOV, Y. ; BIHLMAYER, G. ; HEINZE, S. ; BLÜGEL, S.: Giant Magnetocrystalline Anisotropies of 4d-Transition-Metal Monowires. In: *Phys. Rev. Lett.* 96 (2006), S. 147201
- [125] THIESS, A. ; MOKROUSOV, Y. ; HEINZE, S.: Competing magnetic anisotropies in atomic-scale junctions. In: *Phys. Rev. B* 81 (2010), Feb, S. 054433
- [126] SMOGUNOV, A. ; DAL CORSO, A. ; DELIN, A. ; WEHT, R. ; TOSATTI, E.: Colossal magnetic anisotropy of monatomic free and deposited platinum nanowires. In: *Nature Nanotechnology* 3 (2008), S. 22
- [127] CHADI, D. J. ; COHEN, Marvin L.: Special Points in the Brillouin Zone. In: *Phys. Rev. B* 8 (1973), Dec, Nr. 12, S. 5747–5753
- [128] MONKHORST, H. J. ; PACK, J. D.: Special points for Brillouin-zone integrations. In: *Phys. Rev. B* 13 (1976), Jun, Nr. 12, S. 5188–5192
- [129] RESTA, R.: Macroscopic Electric Polarization as a Geometric Quantum Phase. In: *EPL (Europhysics Letters)* 22 (1993), Nr. 2, S. 133
- [130] WU, X. ; DIÉGUEZ, O. ; RABE, K. M. ; VANDERBILT, D.: Wannier-Based Definition of Layer Polarizations in Perovskite Superlattices. In: *Phys. Rev. Lett.* 97 (2006), Sep, S. 107602
- [131] KING-SMITH, R. D. ; VANDERBILT, D.: Theory of polarization of crystalline solids. In: *Phys. Rev. B* 47 (1993), Jan, S. 1651–1654
- [132] SILVESTRELLIA, P. L. ; MAZARI, N. ; VANDERBILT, D. ; PARRINELLO, M.: Maximally-localized Wannier functions for disordered systems: Application to amorphous silicon. In: *Solid State Communications* 107 (1998), May, S. 7â11

- [133] PAVARINI, E. ; BIERMANN, S. ; POTERYAEV, A. ; LICHTENSTEIN, A. I. ; GEORGES, A. ; ANDERSEN, O. K.: Mott Transition and Suppression of Orbital Fluctuations in Orthorhombic $3d^1$ Perovskites. In: *Phys. Rev. Lett.* 92 (2004), Apr, S. 176403
- [134] ANISIMOV, V. I. ; KONDAKOV, D. E. ; KOZHEVNIKOV, A. V. ; NEKRASOV, I. A. ; PCHELKINA, Z. V. ; ALLEN, J. W. ; MO, S.-K. ; KIM, H.-D. ; METCALF, P. ; SUGA, S. ; SEKIYAMA, A. ; KELLER, G. ; LEONOV, I. ; REN, X. ; VOLLHARDT, D.: Full orbital calculation scheme for materials with strongly correlated electrons. In: *Phys. Rev. B* 71 (2005), Mar, S. 125119
- [135] LECHERMANN, F. ; GEORGES, A. ; POTERYAEV, A. ; BIERMANN, S. ; POSTERNAK, M. ; YAMASAKI, A. ; ANDERSEN, O. K.: Dynamical mean-field theory using Wannier functions: A flexible route to electronic structure calculations of strongly correlated materials. In: *Phys. Rev. B* 74 (2006), Sep, S. 125120
- [136] BIRKENHEUER, U. ; IZOTOV, D.: Localization of Wannier functions for entangled energy bands. In: *Phys. Rev. B* 71 (2005), Mar, Nr. 12, S. 125116
- [137] MOSTOFI, A. A. ; YATES, J. R. ; LEE, Y.-S. ; SOUZA, I. ; VANDERBILT, D. ; MARZARI, N.: Wannier90: A Tool for Obtaining Maximally-Localised Wannier Functions. In: *Comput. Phys. Commun.* 178 (2008), May, S. 158
- [138] Y. Mokrousov; personal communication
- [139] WANG, X. ; YATES, J. R. ; SOUZA, I. ; VANDERBILT, D.: *Ab initio* calculation of the anomalous Hall conductivity by Wannier interpolation. In: *Phys. Rev. B* 74 (2006), Nov, S. 195118
- [140] YATES, J. R. ; WANG, X. ; VANDERBILT, D. ; SOUZA, I.: Spectral and Fermi surface properties from Wannier interpolation. In: *Phys. Rev. B* 75 (2007), May, S. 195121
- [141] WANG, X. ; VANDERBILT, D. ; YATES, J. R. ; SOUZA, I.: Fermi-surface calculation of the anomalous Hall conductivity. In: *Phys. Rev. B* 76 (2007), Nov, S. 195109
- [142] CAROLI, C. ; COMBESCOT, R. ; NOZIERES, P. ; SAINT-JAMES, D.: Direct calculation of the tunneling current. In: *J. Phys. C: Solid State Phys.* 4 (1971), S. 916
- [143] LAKE, R. ; KLIMECK, R. ; BOWEN, R.C. ; JOVANOVIC, D.: Single and Multiband Modeling of Quantum Electron Transport Through Layered Semiconductor Devices. In: *J.Appl.Phys.* 81 (1971), S. 7845–7869

-
- [144] GUINEA, F. ; TEJEDOR, C. ; FLORES, F. ; LOUIS, E.: Effective two-dimensional Hamiltonian at surfaces. In: *Phys. Rev. B* 28 (1983), Oct, Nr. 8, S. 4397–4402
- [145] LEE, Y.-S. ; NARDELLI, M. B. ; MARZARI, N.: Band Structure and Quantum Conductance of Nanostructures from Maximally Localized Wannier Functions: The Case of Functionalized Carbon Nanotubes. In: *Phys. Rev. Lett.* 95 (2005), Aug, S. 076804
- [146] ROCHA, A. R. ; ROSSI, M. ; FAZZIO, A. ; SILVA, Antonio J. R.: Designing Real Nanotube-Based Gas Sensors. In: *Phys. Rev. Lett.* 100 (2008), Apr, S. 176803
- [147] SHELLEY, M. ; MOSTOFI, A. A.: Prediction of high zT in thermoelectric silicon nanowires with axial germanium heterostructures. In: *EPL (Europhysics Letters)* 94 (2011), Nr. 6, S. 67001
- [148] SVIZHENKO, A. ; ANANTRAM, M. P. ; GOVINDAN, T. R. ; BIEGEL, B. ; VENUGOPAL, R.: Two-dimensional quantum mechanical modeling of nanotransistors. In: *Journal of Applied Physics* 91 (2002), Feb, S. 2343
- [149] MARZARI, N. ; MOSTOFI, A. A. ; YATES, J. R. ; SOUZA, I. ; VANDERBILT, D.: Maximally localized Wannier functions: Theory and applications. In: *arXiv:1112.5411v1 [cond-mat.mtrl-sci]* (2011)
- [150] TERSOFF, J. ; HAMANN, D. R.: Theory and Application for the Scanning Tunneling Microscope. In: *Phys. Rev. Lett.* 50 (1983), Jun, S. 1998–2001
- [151] CHEN, C. J.: Origin of atomic resolution on metal surfaces in scanning tunneling microscopy. In: *Phys. Rev. Lett.* 65 (1990), Jul, S. 448–451
- [152] MIURA, Y. ; MAZZARELLO, R. ; DAL CORSO, A. ; SMOGUNOV, A. ; TOSATTI, E.: Monatomic Au wire with a magnetic Ni impurity: Electronic structure and ballistic conductance. In: *Phys. Rev. B* 78 (2008), Nov, Nr. 20, S. 205412
- [153] YANSON, A. I. ; BOLLINGER, G. R. ; BROM, H. E. d. ; AGRAIT, N. ; RUITENBEEK, J. M.: Formation and manipulation of a metallic wire of single gold atoms. In: *Nature* 395 (1998), S. 783–785
- [154] ZIEGLER, M. ; NÉEL, N. ; LAZO, C. ; FERRIANI, P. ; HEINZE, S. ; KRÖGER, J. ; BERNDT, R.: Spin-valve effect in single-atom contacts. In: *New J. Phys.* 17 (2011), S. 085011
- [155] SCHMAUS, S. ; BAGRETS, A. ; NAHAS, Y. ; YAMADA, T. K. ; BORK, A. ; BOWEN, M. ; BEAUREPAIRE, E. ; EVERS, F. ; WULFHEKEL, W.: Giant

- magnetoresistance through a single molecule. In: *Nature Nanotechnology* 6 (2011), S. 185
- [156] DELIN, A. ; TOSATTI, E.: Magnetic phenomena in 5d transition metal nanowires. In: *Phys. Rev. B* 68 (2003), Oct, S. 144434
- [157] DELIN, A. ; TOSATTI, E. ; WEHT, R.: Magnetism in Atomic-Size Palladium Contacts and Nanowires. In: *Phys. Rev. Lett.* 92 (2004), Feb, S. 057201
- [158] THIESS, A. ; MOKROUSOV, Y. ; HEINZE, S. ; BLÜGEL, S.: Magnetically Hindered Chain Formation in Transition-Metal Break Junctions. In: *Phys. Rev. Lett.* 103 (2009), Nov, S. 217201
- [159] SMOGUNOV, A. ; DAL CORSO, A. ; TOSATTI, E.: Ballistic conductance and magnetism in short tip suspended Ni nanowires. In: *Phys. Rev. B* 73 (2006), Feb, S. 075418
- [160] BAGRETS, A. ; PAPANIKOLAOU, N. ; MERTIG, I.: Magnetoresistance of atomic-sized contacts: An *ab initio* study. In: *Phys. Rev. B* 70 (2004), Aug, S. 064410
- [161] BAGRETS, A. ; PAPANIKOLAOU, N. ; MERTIG, I.: Conduction eigenchannels of atomic-sized contacts: *Ab initio* KKR Green's function formalism. In: *Phys. Rev. B* 75 (2007), Jun, S. 235448
- [162] POLOK, M. ; FEDOROV, D. V. ; BAGRETS, A. ; ZAHN, P. ; MERTIG, I.: Evaluation of conduction eigenchannels of an adatom probed by an STM tip. In: *Phys. Rev. B* 83 (2011), Jun, S. 245426
- [163] CZERNER, M. ; YAVORSKY, B. Y. ; MERTIG, I.: Fully relaxed magnetic structure of transition metal nanowires: First-principles calculations. In: *Phys. Rev. B* 77 (2008), S. 104411
- [164] CZERNER, M. ; YAVORSKY, B. Y. ; MERTIG, I.: The role of noncollinear magnetic order and magnetic anisotropy for the transport properties through nanowires. In: *Phys. Status Solidi B* 247 (2010), S. 2594
- [165] TAO, K. ; STEPANYUK, V. S. ; HERGERT, W. ; RUNGGER, I. ; SANVITO, S. ; BRUNO, P.: Quantum conductance of a single magnetic atom: An *ab initio* study. In: *Phys. Rev. Lett.* 103 (2009), S. 057202
- [166] MENZEL, M. ; MOKROUSOV, Y. ; WIESER, R. ; BICKEL, J. E. ; VEDMEDENKO, E. ; BLÜGEL, S. ; HEINZE, S. ; BERGMANN, K. von ; KUBETZKA, A. ; WIESENDANGER, R.: Information Transfer by Vector Spin Chirality in Finite Magnetic Chains. In: *Phys. Rev. Lett.* 108 (2012), May, S. 197204

-
- [167] MOKROUSOV, Y. ; BIHLMAYER, G. ; BLÜGEL, S. ; HEINZE, S.: Magnetic order and exchange interactions in monoatomic 3d transition-metal chains. In: *Phys. Rev. B* 75 (2007), Mar, S. 104413
- [168] SCHUBERT, F. ; MOKROUSOV, Y. ; FERRIANI, P. ; HEINZE, S.: Noncollinear magnetism in freestanding and supported monatomic Mn chains. In: *Phys. Rev. B* 83 (2011), Apr, S. 165442
- [169] YU, R. ; SINGH, D. ; KRAKAUER, H.: All-electron and pseudopotential force calculations using the linearized-augmented-plane-wave method. In: *Phys. Rev. B* 43 (1991), Mar, S. 6411–6422
- [170] ZELENÝ, M. ; ŠOB, M. ; HAFNER, J.: Noncollinear magnetism in manganese nanostructures. In: *Phys. Rev. B* 80 (2009), Oct, S. 144414
- [171] ATACA, C. ; CAHANGIROV, S. ; DURGUN, E. ; JANG, Y.-R. ; CIRACI, S.: Structural, electronic, and magnetic properties of 3d transition metal monatomic chains: First-principles calculations. In: *Phys. Rev. B* 77 (2008), Jun, S. 214413
- [172] GUNNARSSON, O.: Band model for magnetism of transition metals in the spin-density-functional formalism. In: *Journal of Physics F: Metal Physics* 6 (1976), Nr. 4, S. 587
- [173] NONAS, B. ; CABRIA, I. ; ZELLER, R. ; DEDERICHS, P. H. ; HUHNE, T. ; EBERT, H.: Strongly Enhanced Orbital Moments and Anisotropies of Adatoms on the Ag(001) Surface. In: *Phys. Rev. Lett.* 86 (2001), Mar, S. 2146–2149
- [174] MATHON, J. ; UMERSKI, A.: Theory of tunneling magnetoresistance of an epitaxial Fe/MgO/Fe(001) junction. In: *Phys. Rev. B* 63 (2001), May, S. 220403
- [175] BUTLER, W. H. ; ZHANG, X.-G. ; SCHULTHESS, T. C. ; MACLAREN, J. M.: Spin-dependent tunneling conductance of Fe|MgO|Fe sandwiches. In: *Phys. Rev. B* 63 (2001), Jan, S. 054416
- [176] STRANGE, M. ; ROSTGAARD, C. ; HÄKKINEN, H. ; THYGESEN, K. S.: Self-consistent GW calculations of electronic transport in thiol- and amine-linked molecular junctions. In: *Phys. Rev. B* 83 (2011), Mar, S. 115108

Veröffentlichungen und Konferenzbeiträge

Veröffentlichungen

Teile der vorliegenden Arbeit wurden veröffentlicht in:

- B. Hardrat, N.-P. Wang, F. Freimuth, Y. Mokrousov and S. Heinze
One-dimensional ballistic transport with FLAPW Wannier functions
Physical Review B **85**, 245412 (2012)
- B. Hardrat, F. Freimuth, Y. Mokrousov and S. Heinze
Conductance fingerprints of non-collinear magnetic states in single atom contacts: a first-principles Wannier functions study
submitted to Physical Review B.;
Physical Review B **86**, 165449 (2012)

Weitere Veröffentlichungen:

- B. Hardrat, A. Al-Zubi, P. Ferriani, S. Blügel, G. Bihlmayer, and S. Heinze
Complex magnetism of iron monolayers on hexagonal transition metal surfaces from first principles
Physical Review B **79**, 094411 (2009)

Konferenzbeiträge und Poster

Vorträge

- **26.02.2008** B. Hardrat, P. Ferriani, and S. Heinze
Unique playground for non-collinear magnetism : Fe monolayers on hexagonal transition-metal surfaces
DPG Frühjahrstagung, 02/2008, Berlin
- **31.07.2008** B. Hardrat, A. Al-Zubi, P. Ferriani, S. Blügel, G. Bihlmayer, and S. Heinze
Unique playground for non-collinear magnetism : Fe monolayers on hexagonal transition-metal surfaces
European conference on Surface Science (ECOSS), 07/2008, Liverpool, England

- **21.03.2010** B. Hardrat, N.-P. Wang, Y. Mokrousov, F. Freimuth, and S. Heinze
Ballistic transport in 1D magnetic systems based on the FLAPW Method and Wannier functions
DPG Frühjahrstagung, 03/2010, Regensburg
- **17.03.2011** B. Hardrat, N.-P. Wang, F. Freimuth, Y. Mokrousov, and S. Heinze
First-principles calculation of transport through magnetic impurities in metallic wires with strong spin-orbit coupling
DPG Frühjahrstagung, 03/2011, Dresden

Poster

- **08.09.2008** B. Hardrat, A. Al-Zubi, P. Ferriani, S. Blügel, G. Bihlmayer, and S. Heinze
Unique playground for complex magnetism: Fe on hexagonal transitionmetal surfaces
 Ψ_k -Summer School: Nanomagnetism and Spintronics, 09/2008, Prag, Tschechien
- **08.10.2008** B. Hardrat, N.-P. Wang, Y. Mokrousov, F. Freimuth, and S. Heinze
Ballistic Transport in 1D Magnetic Systems using Wannier Functions obtained within the FLAPW Method
Workshop: Quantum Transport in Nanostructures, 10/2008, Hamburg
- **03.06.2009** B. Hardrat, N.-P. Wang, Y. Mokrousov, F. Freimuth, and S. Heinze
Ballistic Transport in 1D Systems using Wannier Functions obtained within the FLAPW Method
CECAM Workshop: Theoretical Modeling of Transport in Nanostructures, 06/2009, Lausanne, Schweiz
- **15.09.2010** B. Hardrat, N.-P. Wang, F. Freimuth, Y. Mokrousov, and S. Heinze
One-dimensional ballistic transport with FLAPW Wannier functions
 Ψ_k -Konferenz, 09/2010, Berlin

Seminarvorträge

- **16.06.2009** B. Hardrat, N.-P. Wang, Y. Mokrousov, F. Freimuth, and S. Heinze
Ballistic Transport in 1D Systems using Wannier Functions obtained within the FLAPW Method
Institut für Festkörperforschung, Forschungszentrum Jülich, 06/2009, Jülich
- **18.09.2009** B. Hardrat, N.-P. Wang, F. Freimuth, Y. Mokrousov, and S. Heinze
Ab-Initio Calculation of Ballistic Transport in 1D Magnetic Nanostructures
Sehlendorf-Seminar: Strukturforschung an Werkstoffen, Universität Kiel, 09/2009, Sehlendorf

Wissenschaftliche Aktivitäten

- **09.03-20.03.2009** 40th IFF Springschool
Spintronics - From GMR to Quantum information
Forschungszentrum Jülich, 03/2009, Jülich

Lebenslauf

PERSÖNLICHE DATEN

Björn Hardrat
Eppendorfer Weg 23B
20259 Hamburg
Geb. am 25.08.1980 in Hamburg
Ledig, deutsch

SCHULAUSBILDUNG

1987 – 1991 Grundschule Schenefeld
1991 – 2000 Gymnasium Schenefeld

06/2000 Allgemeine Hochschulreife

ERSATZDIENST

09/2000 – 07/2001 Kindertagesstätte der Paulskirche Schenefeld

STUDIUM

10/2001 – 10/2003 Grundstudium Physik an der Universität Hamburg
10/2003 – 03/2007 Hauptstudium Physik an der Universität Hamburg

02/2006 – 03/2007 Diplomarbeit am Institut für Angewandte Physik, Universität
Hamburg
Magnetische Ordnung und Austauschwechselwirkung in Fe Mono-
lagen auf hexagonalen Übergangsmetalloberflächen

03/2007 Diplom Physik

PROMOTION

04/2007 – 11/2012 Promotion Physik
Ballistic transport in one-dimensional magnetic nanojunctions: A
first-principles approach

04/2007 – 12/2009 am Institut für Angewandte Physik
Universität Hamburg

01/2010 – 11/2012 am Institut für Theoretische Physik und Astrophysik
Christian-Albrechts Universität zu Kiel

Danksagung

Am Ende dieser Arbeit möchte ich mich bei all jenen bedanken, die mich während der zurückliegenden Jahre begleitet und deren Anregungen, Hilfe, Unterstützung, Förderung, und Freundschaft diese Arbeit erst ermöglichten.

Als erstes möchte ich Prof. Dr. Stefan Heinze danken. Ich bin unglaublich froh, dass ich die Möglichkeit zur Forschung in seiner Gruppe in Kiel und in Hamburg hatte. Seine Motivationsfähigkeit, seine Begeisterung für Elektronentransport und Spintronik und die intensive Betreuung haben maßgeblich zum Erfolg dieser Arbeit beigetragen.

Bei Assistant Professor Dr. Yuriy Mokrousov möchte ich mich für die Diskussionen, seine Vorschläge und Anmerkungen zu den Veröffentlichungen und der Dissertation und die Aufenthalte am Forschungszentrum Jülich bedanken. Es war eine wirklich hochinteressante und wunderschöne Zeit und ich werde mich, unter anderem, immer an die Parkplatz-Fußballspiele erinnern.

Ich danke Dr. Neng-Ping Wang für seine Hilfe und Unterstützung bei der Beschreibung des ballistischen Transports mit Hilfe von Nichtgleichgewichts-Greensfunktionen.

Ohne Dr. Frank Freimuth wären mir wohl einige Geheimnisse der Wannierfunktionen verborgen geblieben. Vielen Dank für die Anregungen, Tipps und Tricks und den trockenen Humor, der den Anmerkungen und Verbesserungsvorschlägen zu den Veröffentlichungen innewohnte.

Ich möchte mich auch bei Prof. Dr. Stefan Blügel für wertvolle Anregungen zur Interpretation von Quantentransportrechnungen und die Möglichkeit, meine Ergebnisse am Forschungszentrum Jülich vorzutragen, bedanken.

Silke Schröder, Dr. Paolo Ferriani, Dr. Cesar Lazo danke ich für die beste Fahrge-
meinschaft, die ich jemals hatte, und für die freundschaftliche Arbeitsatmosphäre in
Kiel und in Hamburg. Paolo danke ich insbesondere für das Korrekturlesen meiner
Arbeit.

Desweiteren danke ich allen anderen MitarbeiterInnen aus der Gruppe Spintronics, die ich über die Jahre kennenlernen durfte: Fabian Otte, Dr. Bertrand Dupé, Dr. Nuala Caffrey, Maren Kaluza, Alexander Thiess, Gregor Michalicek, Franziska Schubert und Urs Wilke. Vielen Dank für die Diskussionen, auch abseits der Physik, und die Unterstützung. Bertrand danke ich zudem für das Korrekturlesen meiner Arbeit.

Ich danke den Mitarbeitern am Instituts für theoretische Physik und Astrophysik an der Universität Kiel für die gute Arbeitsatmosphäre.

Der Gruppe Rastersonormethoden des Instituts für Angewandte Physik an der Universität Hamburg danke ich für eine ganz besondere Zeit an der Schnittstelle zwischen Theorie und Experiment.

Ich möchte auch den Mitgliedern der Gruppe Quantum Theory of Materials des Peter-Grünberg-Instituts danken, durch die meine Aufenthalte am Forschungszentrum Juelich so interessant und lehrreich geworden sind.

Mein besonderer Dank gilt meinen Eltern, meiner Familie und meinen Freunden. Vielen Dank für die Unterstützung, die Aufmunterung und den Rückhalt.